Isolated Elusive Fullerene and Lanthanoid Complex Species: Optical Spectroscopy in Cryogenic Matrixes and Low-Temperature STM

Zur Erlangung des akademischen Grades eines
Doktors der Naturwissenschaften
(Dr. rer. nat.)

bei der Fakultät für Physik
des Karlsruher Instituts für Technologie (KIT)

genehmigte
DISSERTATION

von
Dipl.-Phys. Bastian Kern
aus
Heilbronn-Neckargartach

Datum der mündlichen Prüfung: 23. Oktober 2015
Referent: Prof. Dr. Wulf Wulfhekel
Korreferent: Prof. Dr. Manfred M. Kappes

Contents

1 Introduction

Since the 1950s, when the first species were trapped in cryogenic noble gas matrixes [1], matrix isolation spectroscopy has become a well-established and widely used experimental technique to determine the optical properties (vibrations and electronic transitions) of isolated species. For matrix isolation, the species of interest is co-condensed onto a cold surface with an excess of matrix gas. The surface temperature has to be below 7 K for neon, and below 36 K for argon [2, 3]. Thus a solid noble gas crystal is created, in which the deposited species are isolated from each other. At these low temperatures, the species are usually in their electronic and vibrational ground state, which, in combination with suppressed rotation for most species [4], greatly simplifies the assignment of the observed absorptions.

In the isolating noble gas environment, it is also possible to store ionic species. In the simplest experiments, the ions are generated by discharge in the gas phase close to the cold surface and subsequently co-condensed, or they are generated in the matrix from trapped precursor molecules by photoionization [5]. However, while the generation of charged species is possible in such experiments, one always obtains a mixture of different species and charge states. To distinguish the different species, mass-to-charge selection prior to the isolation in the matrix is necessary.

In the 1990s, the first such experiments have been reported [6, 7]. However, only ions could be measured, for which high intensity ion beams (several tens on nano-Amperes of ion current) could easily be achieved. Furthermore, for the species studied, the low ion current of the mass-selected species prevented the determination of many spectroscopic properties. In principle, low ion currents can be compensated by increased deposition time. Since no degradation of the isolated species inside the cryogenic matrix occurs, deposition times of several days are possible. However, such prolonged depositions demand a clean UHV environment to prevent the accumulation of impurities in the matrix, which greatly reduce the quality of the noble gas crystal and hinder the spectroscopic characterization of the deposited species. In most matrix isolation experiments, this demand is not met, deposition of molecules or ions is only possible for a relatively short time, preventing the accumulation of rare species. The combination of mass-selection and matrix isolation spectroscopy of ions is still not widely used today because of the difficult sample preparation, i.e. the required high intensity ion beam and the clean UHV environment.

The standard ionization technique used in most experiments for deposition of mass-selected molecular ions into noble gas matrixes is electron impact ionization (EI) of sublimated molecules. With EI, high ion currents of up to several tens of nano-Amperes can be generated, and since the molecules can be sublimed in UHV, it is a very clean technique. It is also possible to generate fragments of the parent ions, or multiply charged ions, albeit with lower intensity than the singly charged parent ion. Still, in previous matrix isolation experiments of fullerene ions, only the C_{60} and C_{70} cations have been investigated, the C_{60} cation in the IR and NIR, the C_{70} cation only in the visible range as its ion current was not sufficient for IR measurements [8, 9].

In electron impact ionization, only stable species survive the sublimation, and the subsequent electron bombardment. Large and fragile species cannot be ionized by EI. One of the actively developing methods for the generation of large and fragile molecular ions from solution is electrospray ionization (ESI) [10]. The solution containing the species of interest is sprayed from a thin needle at high bias voltages via a capillary into the vacuum setup. Subsequent mass-to-charge separation allows the selection of specific ionic species.

One of the drawbacks of ESI is that the produced ion current is inherently low, typically below 100 pA, and can be much lower for some species. Even with highly sensitive spectroscopic methods such as laser induced photoluminescence, the deposited amount of ions is critical. Additionally, the ions are generated at ambient pressure from a solution and then transferred into the vacuum setup. To generate a high quality matrix, it is imperative to efficiently reduce the contamination by residual air and solvent molecules prior to deposition: from the ion source to the deposition region, the pressure has to be reduced by a factor of 10^{12}. No combination of ESI and matrix isolation spectroscopy has been reported so far.

In this thesis, the improvement of a setup for matrix isolation of mass-selected ions is reported, especially regarding the ion beam intensity, and the residual background pressure. The improved setup allows for the IR spectroscopy of ionic species with a low production rate, for the first time fullerene multications and fullerene fragments are studied with optical spectroscopy. The combination of electrospray ionization and matrix isolation spectroscopy is reported for the first time.

Similar to matrix isolation, isolated molecular monomers at low temperatures can be studied by scanning tunneling microscopy (STM) [11]. A sharp metal tip (ideally the apex has to consist of a single metal atom) is positioned above the molecules of interest, which are adsorbed on a metallic substrate. Measuring the tunneling current through the molecule not only allows to study the electronic and magnetic properties, but also the vibrational excitations of molecules can be probed by inelastic electron tunneling spectroscopy (IETS). In contrast to matrix isolation spectroscopy, in which always an ensemble of molecules or complexes is probed, STM allows the study of specific single and addressable molecules.

However, the spatial selectivity of single molecule measurements comes at a price: the species of interest is adsorbed on a substrate. While for most species this is not a drawback, and even is desired for others, some elusive species cannot be prepared on surfaces. For example, the molecular geometry relaxes, charge transfer to the surface occurs, or, as is the case for the hydrogen molecule, the excited spin state is unstable.

Isolation of metal atoms [12, 13], metal complexes [14, 15], and molecules [16, 17] from the surface is possible by incorporating these species into fullerene cages. STM studies of metal atoms and clusters inside fullerene cages have shown that the electronic properties of the fullerene cage are modified by the endohedral species. For example, La@C_{60} shows a metallic behavior at room temperature and is semiconducting below 28 K [18], while Sc_3N@C_{80} exhibits conductance switching due to induced transitions between different conformers of the endohedral Sc_3N complex [19]. For Gd@C_{82}, a strong dependency of the DFT calculated vibrational excitations on the position of the metal atom inside the cage has been predicted [20].

While metal atoms and complexes show a strong hybridization with the carbon cage, endohedral hydrogen only interacts by weak van der Waals forces with the fullerene [21]. In this thesis, a system is created by deposition of H_2@C_{60} onto surfaces, in which the fullerene is physisorbed on the surface, while the endohedral molecular hydrogen is quasi-free. In this way, while being addressable, weakly interacting hydrogen molecules are studied by STM.

First, a short introduction to the research methods is given in this thesis. The fundamentals of density functional theory (DFT) are explained, followed by a description of on the experimental methods used, matrix isolation spectroscopy and scanning tunneling microscopy. The experimental setups, which were used for the measurements, are presented.

The measurement results are presented in three chapters. In chapter 3, optical spectroscopy measurements of different charge states of the fullerenes C_{60} and C_{70} are presented, for the first time absorptions of $C_{60}^{2+/3+}$ and C_{70}^{2+} are identified. IR spectra of the reactive non-IPR fullerene C_{58} and its ions are reported. The azafullerene $C_{59}N$ was studied as stable dimer and radical monomer, and IR absorptions of the monomer ions are identified. In chapter 4, the capability of the combination of matrix isolation and electrospray ionization is demonstrated with laser-induced photoemission spectroscopy of rare and elusive lanthanoid diketonate species, which could not be studied in the gas phase or in condensed phase mixtures. STM measurements vibronic excitations of C_{60} and of *ortho*- and *para*-hydrogen isolated in fullerene C_{60} cages are reported in chapter 5.

A summary of the experimental results and some suggestions for further measurements and for improvements of the measurement equipment is given in chapter 6.

2 Methods

2.1 Density Functional Theory Calculations

2.1.1 Density Functional Theory

According to Hohenberg and Kohn [22], the ground state properties of a molecular system are unambiguously assigned by functionals of the position dependent electron density $\rho(\vec{r})$. Therefore, knowledge of $\rho(\vec{r})$ allows the determination of the ground-state potential of the system, and of all other observables $\hat{O}$ by

$$O_0 = O[\rho_0] = \langle \Psi[\rho_0] | \hat{O} | \Psi[\rho_0] \rangle$$

with the ground state density ρ_0, as a functional of the electron density. The most important observable is the ground state energy $E[\rho_0]$.

Density functional theory (DFT) is a widely used method, nowadays applied for large systems with up to a hundred atoms, or even more. DFT allows the calculation of properties, e.g. the binding energy, electronic states, structure, and excitations of molecules. For molecular energies, the accuracy of DFT calculations is often within 0.2 eV [23, 24], and can be better for small or highly symmetric systems.

Calculation of the IR excitation spectra of molecules in their electric ground state is possible in DFT, including relative intensities of the transitions. Second order derivatives of the total molecular energy with respect to nuclear displacements characterize vibrational frequencies [25, 26, 27].

Electronic excitation energies, and hence the electronic spectrum, can be obtained from the response of a molecule to a time dependent external field (time dependent density functional theory, TD-DFT) [28].

Standard DFT treats systems within the Born-Oppenheimer approximation. However, molecules and their ions often exhibit properties which cannot be accurately described within the Born-Oppenheimer approximation. Most of the time, electronic excitations cannot be decoupled from a change in structure, for example the Renner-Teller effect in linear molecules, the static and dynamic Jahn-Teller effect, where a structural change induces a change in the electronic states, and vice

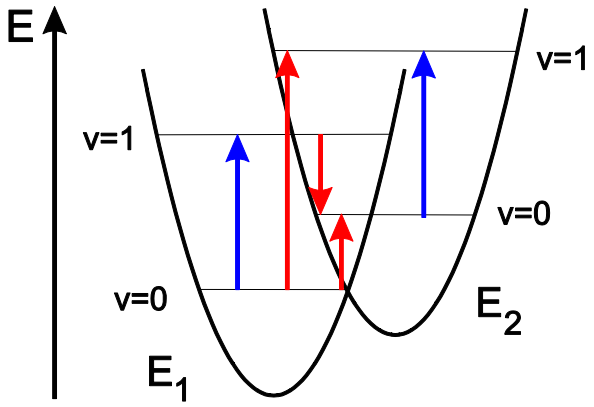

Figure 2.1: Two electronic potential surfaces E_1 and E_2. A vibrational excitation from the lower state E_1 can lead to a crossing to E_2. The graph is only for illustration.

versa, and the Teller-Herzberg intensity borrowing. The latter two will be briefly addressed in the following paragraph.

2.1.2 Beyond Born-Oppenheimer: Jahn-Teller and Teller-Herzberg Effect

In the Born-Oppenheimer approximation, the equations for electronic motions are solved under the assumption of stationary nuclei. This provides the adiabatic potential energy surface (APES), which is the effective potential for the vibrational states. If the lowest energy APES is well separated from all other potential surfaces, the influence of these potentials can be ignored. However, if two or more APES intersect at energies, which are within the range of vibrational levels, all low lying potentials have to be included [29].

The dynamic Jahn-Teller effect originates from the coupling of electronic states to vibrational modes. In short, intersections of different APES (E_1, E_2) enable the transition from the electronic state E_1 to E_2 by vibrational excitation. This results in a broadening of the spectral features. Additionally, vibrational excitations are possible in E_2, resulting in a deviation from the ground state vibrations. This can lead to further broadening, or to the emergence of new vibrational tranisitons. Normal vibrational modes, which allow crossing of the intersections, and hence couple electronic excitations to vibrations, are called Jahn-Teller active modes. A simplified scheme of the Jahn-Teller effect is shown in figure 2.1.

In IR spectra, the presence of Jahn-Teller distortions is inferred from the broadening of vibrational transitions [30]. If the Jahn-Teller effect is large for a molecule, simple DFT calculations are insufficient to accurately describe the corresponding electronic states, and in particular to describe transitions between them.

The Herzberg-Teller effect explains, why some weak or symmetry-forbidden vibronic transitions are observed in the experiment. This 'intensity borrowing' is understood as a dependence of the dipole moment of the electronic transition on the nuclear displacement of the vibration. In the measurement, additional transitions appear which are not expected, or gain in strength in comparison to the calculations. Some examples of the importance of the associated non-adiabatic effects are shown in Domcke *et al.* [31].

The described effects are not taken into account in the theoretical calculations presented in this work. If the effects are small, as in the case of $C_{60}^{0/+/-}$ [32], simple DFT calculations are still reliable (see chapter 3.2). However, if the spectra of the studied species are affected strongly by the interaction of electronic and vibrational states, no meaningful results of DFT calculations were obtained, as in the case of the vibrational spectra of $C_{70}^{+/-}$ (see chapter 3.3). The calculations presented in this work are performed with the Turbomole program package [33]. Following the geometry optimization, the vibrational energies are calculated with the resolution of identity approach (RI-DFT). The electronic transitions are calculated with time dependent DFT (TD-DFT). Unless stated otherwise, the generalized gradient approximation functional used is BP86 [34, 35], and the basis set used is def-SVP [36].

2.2 Matrix Isolation Spectroscopy

In the 1950s, cryogenic matrixes comprising inert noble gases were first used to enable infrared (IR) [1, 37, 38] and electronic spectroscopy [39] of elusive species such as radicals, undercoordinated or weakly bound complexes, and molecular ions. Basically, all species that can be produced in gas-phase can be co-condensed with matrix gas [3, 40]. Even though other techniques, such as supersonic expansion, also allow for spectroscopy of reactive species [41, 42], matrix isolation still remains a versatile and widely used method for structural and electronic characterization of such species [43, 44, 45, 46]. Its advantages include chemical, physical, and electrical isolation, low temperature environments to reduce the ambient energy and dissipate absorbed energy, the suppression of rotation for most species [4], and the storage of deposited species for several days. Even a rough control of reactions can be provided by annealing the matrixes to temperatures close to their melting points, thus enabling thermal diffusion and reaction of stored species [47, 45].

Noble gas matrixes are transparent for optical spectroscopy over a wide spectral range. In the UV, the transmission is limited by the optical excitation of electrons to the conduction band. The cut-off energy is determined by the energy gap of the solid. In the far-IR, lattice phonon excitations in the matrix occur at certain frequencies [48]. The phonon energy is independent of the guest species, the onset of the phonon modes is given by the Debye frequency of the matrix material. For

neon and argon at 0 K the frequencies are 75 cm^{-1} and 93 cm^{-1}, respectively [2]. These phonon absorptions complicate the measurement, but do not prevent the FIR range to be investigated by matrix isolation spectroscopy.

In the solid matrix, perturbations of the observed spectra occur, such as matrix shifts due to interactions with the polarizable surroundings and line splitting due to different adsorptions sites. A detailed discussion of the different interactions can be found in Ref. [2].

Matrix shifts of vibrational modes are usually smaller than 1% relative to gas phase values [43]. While this is sufficient for the comparison with calculations to assign the specific vibrational modes, it is inadequate for the accurate prediction of unknown gas-phase frequencies. Therefore, experiments are typically performed on species embedded in a variety of different matrixes with different polarizabilities. Plotting the observed frequencies versus the polarizability of the solid matrix, the gas-phase values can be estimated by extrapolating to $\alpha_{Vacuum} = 0$. Frequencies obtained by this approach are in good agreement with measured gas-phase values.

The adsorption of molecules in different sites on the surface of the growing inert gas matrix results in different local environments. Spectroscopic features originating from these different adsorption sites can be identified by annealing of the matrix, or deposition of the species at elevated sample temperatures (still below the melting point of the respective matrix). For larger species, the energy barrier between different adsorption geometries is usually higher than the thermal energy available at annealing temperatures, even more so since the rotation of the species is hindered in the matrix. However, the larger a molecule is in relation to the matrix atoms or molecules, the smaller the influence of different adsorption sites on its spectrum. In most cases, a direct identification of different adsorption geometries is not pursued. Instead, close-lying features are typically assigned to the same transition.

Charge balance of anions and cations has to be maintained upon deposition of charged species into cryogenic matrixes. Noble gases do not screen the ion charge sufficiently to prevent incoming ions from being deflected, which would hinder the accumulation of sufficient material for spectroscopy. A simple way to study ions in neutral matrixes is the generation of ions from trapped precursor molecules by photoionization, either directly or for example by charge transfer from photoionized alkali atoms [5]. However, these approaches do not allow for mass separation of the studied species.

Generation of ions in external sources enables mass-selection prior to deposition in the matrix [6, 7]. However, the formation of counter-ions is then more complicated [49]. Even in matrixes containing high concentrations of cations (around 10^{16} cm^{-3}), counter-ions have typically not been observed spectroscopically [50]. Nevertheless, they are present.

It has been shown that during deposition of cations, counter-ions are formed via electron capture of secondary electrons. The secondary electrons are generated by the impact of the incoming and deflected ions onto metal parts of the vacuum chamber [49], or from the ion gauge. The molecules capturing the electrons are usually contaminations of the matrix, mostly CO, CO_2, and H_2O, which are present in the residual gas of the vacuum chamber [49]. Neutralization and even counter-charging (after pick-up of two electrons) of the deposited ions is also possible [50, 8, 51], as illustrated in figure 2.2 a.

Neutralization of the deposited species can be avoided by the use of so-called electron scavengers during deposition. Species with positive electron affinities are added to the matrix gas. The generated secondary electrons readily recombine with the scavenger molecules, thus forming the anions needed for neutrality. This process is illustrated in figure 2.2 b.

While the generation of matrixes from the deposition of cations was achieved in 1992 [7], the deposition of anions remains a challenge. Upon deposition of anions, the neutrality of the matrix cannot be achieved by the generation of secondary electrons. Instead, two ion beams of opposite charge must be directed onto the matrix. Early experiments to simultaneously deposit CS_2^+ and Cl^- did not produce detectable amounts of stored ions, even with highly sensitive laser-induced fluorescence measurements [52]. Only in 2013 was the successful co-deposition of copper cluster anions with argon cations reported [46].

In summary, matrix isolation of elusive and reactive species is a viable technique for absorption and emission spectroscopy from the UV to the far-IR. With its basically infinite storage time it allows for the investigation of transient species, which cannot be produced in sufficient quantities for direct gas phase measurements. The combination with gas-phase mass selection enables the fabrication of clean samples of anions or cations. The downside of this technique is the evident interaction of the guest species with the matrix, although the use of different matrix gases allows for the estimation of unperturbed gas-phase absorption frequencies.

2.2.1 Absorption Spectroscopy

Infrared (IR) spectroscopy probes the vibrational modes of the molecules of interest. Within the harmonic approximation, the intensity $I_{nm,\,IR}$ of the vibrational transition $n \rightarrow m$ is given by

$$I_{nm,\,IR} \propto \sum_q \left(\sum_{k=1}^{3N-6} \left(\frac{\partial \mu_q}{\partial Q_k} \right)_0 \langle \psi_m | Q_k | \psi_n \rangle \right)^2$$

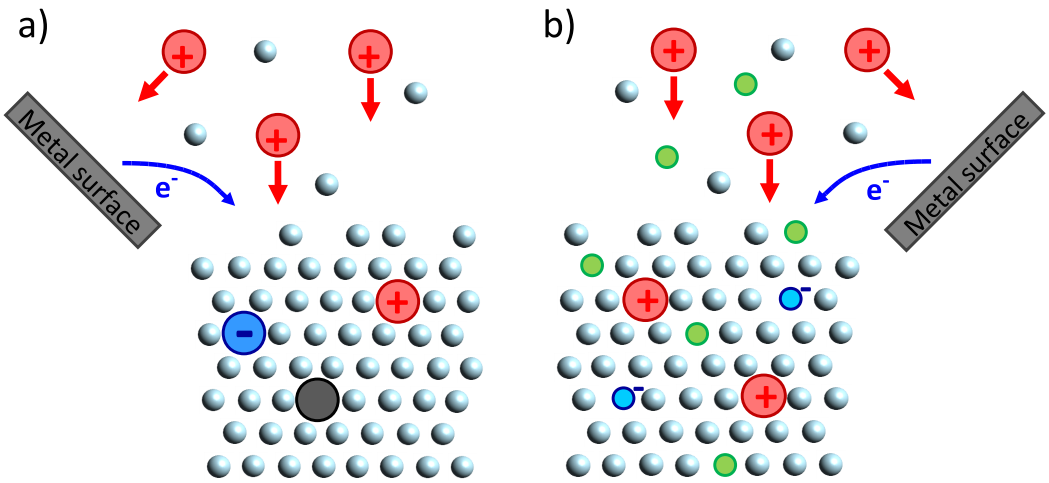

Figure 2.2: (a) Generation of secondary electrons leads to neutralization of the deposited ions in the matrix. The mass-selected ions are shown as large red circles, neutralized and anionic species as black and blue circles, respectively. (b) Addition of electron scavengers to the matrix gas prevents neutralization of the species of interest. The electron scavengers are shown as small green circles, the counterions formed from the electron scavenger are shown a small blue circles.

with the Carthesian coordinates q, the normal coordinates Q_k, the dipole moment μ_q, and the orthogonal wavefunctions ψ_n and ψ_m. The transition only has a non-zero intensity if two conditions are met. Firstly, the derivative of the dipole moment with respect to the normal coordinate Q_k has to be non-zero, which means that the normal mode has to induce a change of the dipole moment. Secondly, the vibrational quantum numbers n and m have to differ by $\Delta n = \pm 1$ for the integral to be non-zero.

Considering anharmonicities of the potential, the selection rules are weakened to $\Delta n = \pm 1, \pm 2, ...$ with decreasing intensity of the higher order transitions.

Allowed transitions and their IR intensities depend on the structure of the molecule, enabling the assignment of the observed absorptions to specific vibrational transitions and structural motifs by comparison to theoretical calculations.

The absorption of light in the UV-vis range is not as sensitive to minute structural changes of the molecule as IR spectroscopy. While vibrational transitions typically show a full width at half maximum (*fwhm*) of only around $1 \ldots 10\,\mathrm{cm}^{-1}$, some electronic transitions exhibit a *fwhm* of several hundreds to thousands of wavenumbers. However, other electronic transitions, for example from long-lived triplet states, exhibit a narrow *fwhm* of just some tens of wavenumbers, and can be used as well for the structural determination of the species.

2.2.2 Laser-induced Luminescence Spectroscopy

For laser-induced luminescence spectroscopy, the species of interest is irradiated with a laser (often in the UV range) and excited to a real electronic state[1]. Through relaxation and internal conversion via energy redistribution or interaction with the environment the system typically reaches the vibrational ground-state of the electronic excited state [53]. From there, de-excitation is possible by the emission of a photon. This process happens on timescales of nanoseconds to microseconds. For some systems, intersystem crossing into a long-lived triplet state occurs, with lifetimes up to several seconds and an emission that is shifted to significantly lower energy. Instead of light emission it is also possible for the molecule to de-excite by energy transfer to phonon modes of the environment.

Repeated photoexcitation of the molecules close to their photofragmentation threshold values can be a problem in gas phase measurements. In particular, if the energy dissipation is slow compared to the absorption rate, fragmentation of the molecule and a loss of signal may occur. In matrixes, this is not such a severe problem because of the much higher energy dissipation rates.

Due to the negligible background, laser-induced luminescence spectroscopy allows to probe weak transitions, or dilute samples of rare species.

2.2.3 Experimental Setup

The experimental setup is dedicated to the spectroscopy of molecular ions isolated in cryogenic noble gas matrixes. It enables the investigation of rare or unstable species by infrared (IR) and UV-vis absorption spectroscopy, as well as laser induced luminescence spectroscopy. The general layout is shown in figure 2.3.

In short, the ions are generated by either electron impact ionization or electrospray ionization (fig. 2.4 and 2.5). A wide range of molecular ions can be produced and subsequently investigated by these two methods, from polyaromatic hydrocarbon ions and their fragments to ions of large and fragile molecular complexes.

Following the ion generation in the source region, separation of the residual neutrals from the ionic beam is achieved using an electrostatic quadrupole bender (fig. 2.3 b). The species of interest are then mass-selected with a quadrupole mass filter (QMS), unwanted side-species such as ionic impurities, fragments, or ions with solvent adducts are removed. The mass selected ions are subsequently co-deposited in the presence of an excess of matrix gas onto a cold ($T \geq 5$K) metal coated sapphire substrate (fig. 2.3 c). Deposition of the ionic species over several days without sample degradation is possible. Once sufficient material for optical spectroscopy is deposited in the matrix, the deposition is stopped and the sample analyzed.

[1] In Raman spectroscopy, in contrast, the molecule is excited to a virtual electronic state.

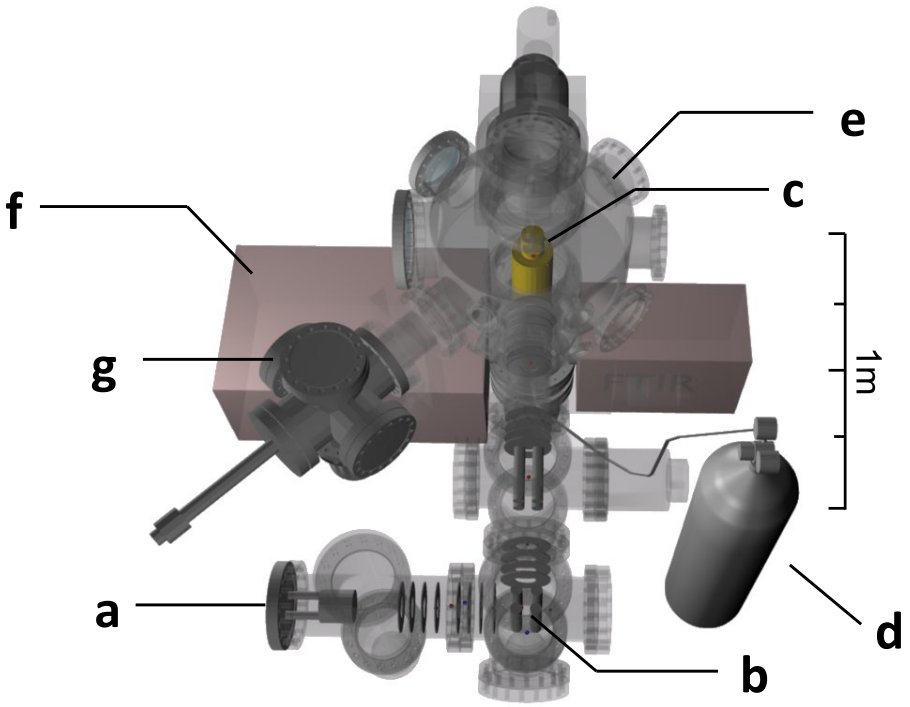

Figure 2.3: General layout of the matrix isolation experiment with attached electron impact ionization source (exchangeable with an electrospray ionization source). (a) Ion source region, (b) ion optics with electrostatic quadrupole bender and quadrupole mass filter, (c) cold substrate ($T \geq 5$K), (d) matrix gas reservoir (Ne, Ar, with possible addition of electron scavenger CO_2, CCl_4), (e) viewport for UV-vis and laser-induced luminescence spectroscopy, (f) FT-IR spectrometer, attached to lower chamber, (g) load-lock chamber. Details see text.

A detailed description of the main components and of recent improvements of the experimental setup is provided in the following sections. Further details about the apparatus can be found in Ref. [54].

Ion Sources

Two different ionization techniques are used in this experiment. Electron impact induced ionization allows for the generation of ions from sublimable molecules, which do not fragment easily upon electron impact. Electrospray ionization is known as a soft ionization method for large, unsublimable, but soluble molecules. The source region, consisting of the ion source and a first series of electrostatic lenses (fig. 2.4 and 2.5), can be disconnected from the following ion optics and pumping stages by a gate valve. Switching between the two sources is thus possible without breaking the vacuum in the main chamber.

Electron Impact Induced Ionization Source

The impact of electrons with kinetic energies of several tens of electronvolts leads to the ionization and fragmentation of gaseous molecules. These processes will be illustrated for the example of C_{60}: Low kinetic energies of the electrons ($E_{kin} \leq 40\,\text{eV}$) lead predominantly to ionization of the molecule [55], higher electron energies, or multiple impacts, allow for fragmentation by C_2 emission on a mass spectrometric timescale of less than 100 µs [55, 56, 57].

For slow electrons ($E_{kin} \sim 10\,\text{eV}$), direct electron capture by the molecule is also possible, though with a small cross-section, and a resulting low current (approximately 5% of the cationic current observed for fullerenes under the same conditions). To realize high intensity ion beams of sublimable species, a setup previously used for the ionization of polycyclic aromatic hydrocarbons has been adapted [58]. As a result, the previously used source setup is improved [59, 54]: the ion current intensity is increased by a factor of 5, the time necessary for refilling the source is reduced, and temperature adjustment is facilitated, which makes the sublimation of molecules more easily controllable.

As shown in figure 2.4 b, the electron impact induced ionization source (EI source) consists of a filament (F), from which the electrons are emitted, a grid (G) to further accelerate the electrons and repel the formed ions, an electron reflector (R), the sublimation source itself (S), and an extraction lens (E) for the ions. All voltages listed are for the generation of cations.

A thoriated tungsten wire (d=0.25 mm, l∼5 cm) is used as filament. It is operated at 10 V/8 A with a negative bias of 100-150 V to eject the electrons. The central grid is taken from a nude Bayard-Alpert ion gauge (Vacuum Generators, now VG Scienta),

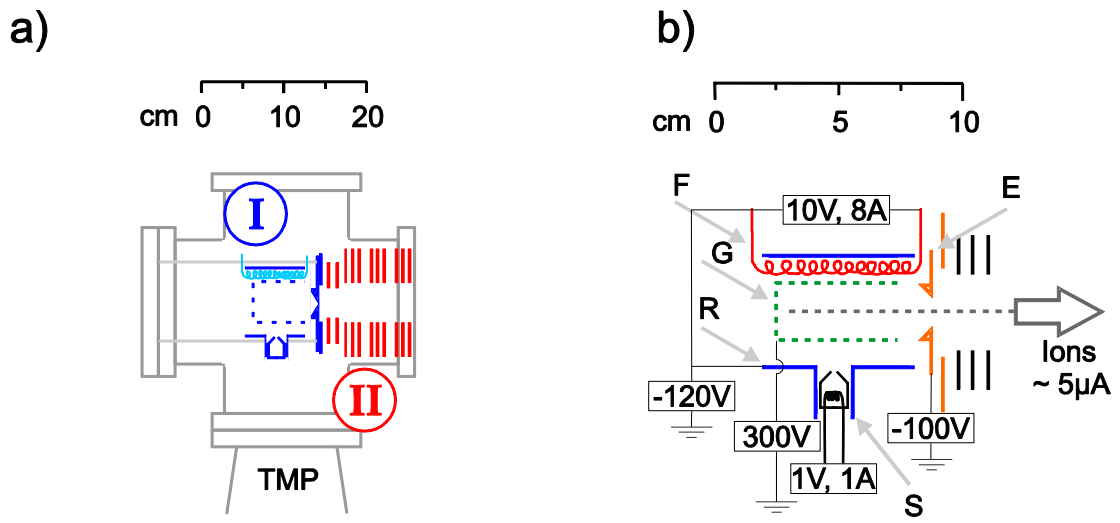

Figure 2.4: a) Schematic of the EI source region, (I) electron impact induced ionization region, (II) ion optics. b) Detail of the EI source, F: hot filament, G: central grid, R: electron repeller, S: sublimation source, E: extraction lens. Details see text.

its length is 5 cm with a diameter of 2.3 cm. The top end of the grid is removed to make space for the extraction electrode. The bottom of the grid is closed. As a result, the internal electric field is approximately constant, thus reducing the kinetic energy spread of the ions. Typically, a positive bias voltage of 200 V is applied to the grid. A stainless steel cylinder (d=45 mm, l∼6 cm) surrounding the grid is biased at a negative voltage (100-150 V) to reflect the electrons, thereby increasing their path length.

Attached to the electron reflector is the sublimation source. The sublimation source used is a halogen bulb (50-100 W, operated at 1-4 W). The top of the bulb is removed, creating a small opening (ca. 1 mm diameter), through which the source is filled, and through which the neutral molecules are effused when heating the bulb. To ensure a uniform temperature distribution, the halogen bulb is wrapped in aluminum foil. The sublimation source is aligned perpendicular to the ion extraction direction, thus the contamination of the ion optics by neutral molecules is minimized. An additional halogen bulb (100 W, usually operated at 20 W) attached to the electron reflector can be used to increase the rate of resublimation of the molecules not yet ionized. The ions are extracted from the ionization region by a lens with a narrowing conical aperture, held at negative bias (-100 V), and guided by the following electrostatic ring electrodes.

The entire EI source and the subsequent ion optics are installed in a CF DN160 6-way-cross and pumped by a turbomolecular pump to approximately 10^{-6} mbar under operating conditions.

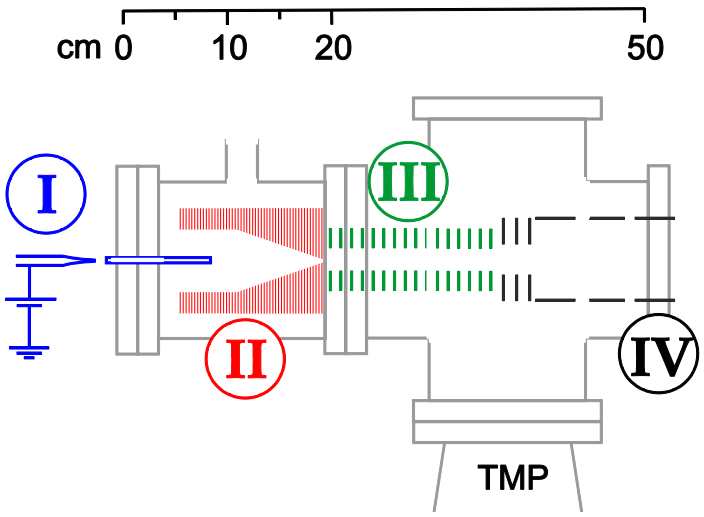

Figure 2.5: Schematic of the nanoES, (I) borosilicate glass needle and desolvation capillary, (II) RF ion funnel, (III) RF ion guide, (IV) electrostatic lenses.

Nano-Electrospray Ionization Source

Electrospray ionization is known to be a soft ionization technique enabling the transfer of large and complex species as ions from the solution to the gas phase [10]. It enables deposition of mass selected molecules, DNA strands, and peptides on metal surfaces and self-assembled monolayers [60, 61, 62].

In this setup, ions are produced from a home-build nano-electrospray ionization source (nanoES), operated at 5-14 kV needle voltage in positive or negative mode, depending on the desired ions. The setup is illustrated in figure 2.5. The prepared solution containing the desired species is inserted into a thin borosilicate glass needle, which is directed at a heated desolvation capillary (l =100 mm, 0.5 mm i.d., 150 °C, 350-500 V), through which the transfer into the vacuum setup is achieved (fig 2.5 (I)). To reduce the flow of neutral solvent int the vacuum chamber, the desolvation capillary is aligned slightly off the ion beam axis.

Collisional focusing of the ions in low vacuum is achieved by a home-build RF ion funnel [63]. The ion funnel is composed of a series of 73 ring electrodes (0.5 mm thick stainless steel plates), forming a 27 mm drift region and a 45 mm focusing region with progressively decreasing inner diameters (from 25 to 3 mm, fig. 2.5 (II)). 0.5 mm thick teflon spacers are used to insulate the electrodes from each other. The ion funnel 'empties' into an RF ion guide consisting of 43 ring electrodes, with a constant inner diameter of 8 mm and which are separated by 2.8 mm viton spacers to allow for differential pumping. The ion guide electrodes are evenly spaced over a total length of 140 mm (2.5 (III)). To provide the DC potential gradient (∼130 V over the entire length), all of the electrodes of the funnel and the ion guide are

connected by 1 MΩ resistors. Each electrode is connected to one of the two alternating outputs of the RF power supply (home-built, 500 kHz, $V_{pp,\,max} = 330$ V) with a 200 pF capacitor, such that the phase difference between adjacent electrodes is 180°. Following the RF ion guide, a series of electrostatic lenses is used to direct the ions to the quadrupole bender (fig. 2.5 (IV)).

The nanoES and the subsequent ion optics are installed in a CF DN160 6-way-cross and an CF DN160 nipple, the low vacuum region of the ion funnel is pumped by a roots pump ($p \sim 4 \times 10^{-1}$ mbar) with the funnel exit lens separating the differentially pumped stages. The subsequent ion optics are pumped by a turbomolecular pump ($p \sim 10^{-5}$ mbar under operating conditions).

Ion Optics and Mass Separation

Following the source region, the ions are guided and focused by cylindrical electrostatic electrodes to the electrostatic quadrupole bender, which prevents contamination of the sample by residual neutral molecules from the ion source by deflecting the ion beam at a right angle (fig. 2.6 (II)). The deflected ions of the desired charge are focused into a quadrupole mass filter to select the desired ion species [64] (fig. 2.6 (III)). The quadrupole mass filter consists of four parallel cylindrical metal rods, opposing rods are connected in pairs. Applying a superposition of DC and AC voltages with $U_0 = \pm 1/2 (U + V\cos(\omega t))$ to the rod pairs leads to the separation of ion trajectories into stable and unstable ones, depending on the mass-to-charge ratio of the ions. In mass resolving mode, only ions within a defined $^{(m \pm \Delta m)}/_{z}$ range are transmitted, the range is adjusted by the ratio of AC to DC voltage. In 'RF only' mode, the DC voltage is switched off and only the AC voltage is applied: All ions with a $^{m}/_{z}$ ratio above a threshold, which is adjusted by the AC amplitude, are transmitted.

The quadrupole mass filter (QMS) used is an Extrel 19 mm QMS with pre- and post-filter assembly driven by a 880 kHz power supply, allowing for a mass range of up to 1000 $^{\mathrm{amu}}/_{\mathrm{e}}$ in mass resolving mode. To achieve high transmission, the mass resolution $^{\Delta m}/_{m}$ is tuned down to about 30, which is enough to separate fragment ions or ions with attached solvent molecules and allows for high intensity ion beams. Following the QMS, several einzel lenses focus the mass selected ion beam onto the cold ($T \geq 5$ K) target (fig. 2.6 (IV, V)). Prior to the deposition, the ion current can be monitored with a picoamperemeter (Keithley, Model 6485). All voltages and currents can be adjusted and monitored with LabView (National Instruments).

The total ion output of the ion sources is measured to be approximately 7 µA for EI, and 5 nA for nanoES. The ion current, measured on the deposition position for a mass selected ion beam, can reach up to 300 nA or 350 pA, respectively, but strongly depends on the ion species. This corresponds to a maximum transmission of roughly 5% for the complete ion optics setup, including mass selection.

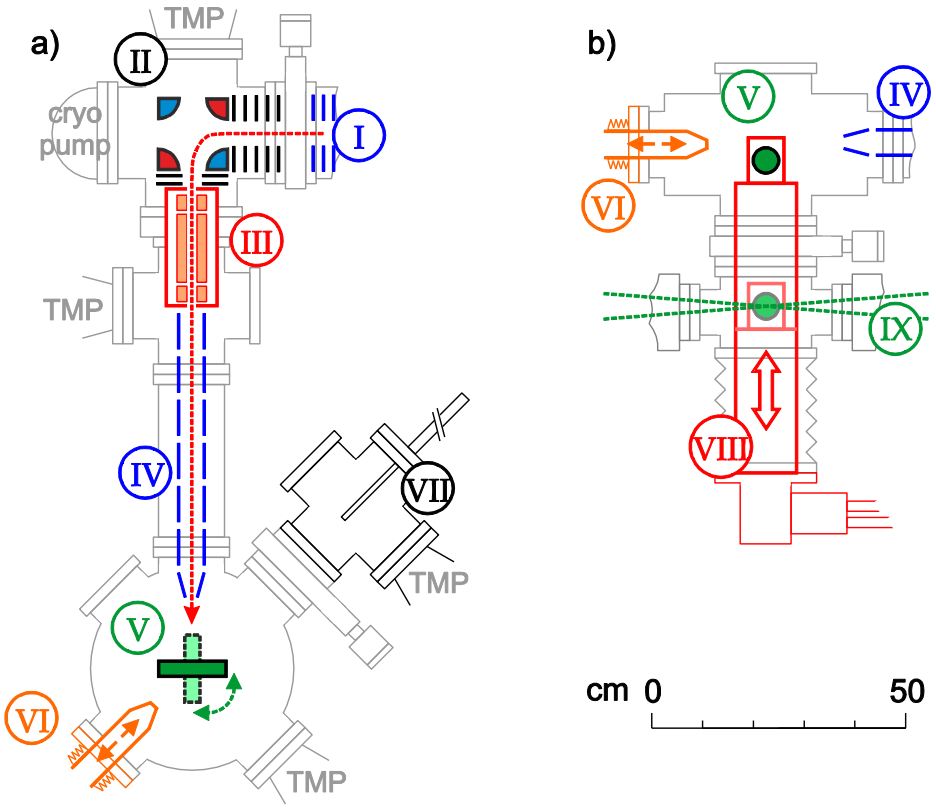

Figure 2.6: Schematic of the experimental setup (a) top view, b) side view), showing (I) source region (EI or nanoES), (II) electrostatic quadrupole bender, (III) quadrupole mass filter, (IV) ion optics, (V) sample ($T \geq 5\,\mathrm{K}$, position vertically adjustable), (VI) UV-vis viewport for absorption and photoluminescence spectroscopy, (VII) load-lock chamber, (VIII) closed cycle cryocooler, and (IX) FT-IR spectrometer beam path (sample in lower position).

Vacuum Setup

To transfer the ions from the source region to the sample, two differentially pumped chambers are used in addition to the source region, which itself is differentially pumped by one (EI source) or two (nanoES) stages. The source region can be separated from the following setup by a gate valve when no deposition is performed, keeping the contamination and gas load to a minimum. An aperture of 10 mm diameter forms the transition from the source region to the electrostatic bender, behind which, in direct line of sight from the ion source, a cryogenic pump (Sumitomo CP-8LP, $T_{1st\ stage}$=60 K, $T_{2nd\ stage}$=10 K) is placed to trap residual solvent molecules. Additionally, a turbomolecular pump is used to further reduce pressure and contamination. Between the electrostatic bender and the endmost deposition chamber, the housing of the QMS acts as an aperture with an opening of 15.24 mm (fig. 2.6). With the source region connected, base pressure in the deposition chamber is below 10^{-8} mbar (EI source) or below 5×10^{-8} mbar (nanoES). During deposition the pressure increases to approximately 10^{-5} mbar due to the excess of matrix gas.

While UV-vis and laser induced luminescence measurements are performed in the deposition chamber (fig. 2.6 (VI)), the sample is transferred *in vacuo* to the lower measurement chamber for IR measurements (fig. 2.6 (IX)). Deposition and measurement chamber can be separated by a gate valve.

A load-lock chamber attached to the deposition chamber allows for changing of the substrate without breaking the vacuum (fig. 2.6 (VII)).

Additional vacuum TMPs are used to evacuate a mixing chamber, in which gas mixtures for sample preparation are produced, and for the liquid helium cooled IR detectors: the CuGe detector and the bolometer (both from Infrared Laboratories). The FT-IR spectrometer is pumped by rough pumps to reduce water vapor impurities in the optical path.

Sample Preparation

To prepare the samples, the ion beam is co-deposited with an excess of matrix gas ($p_{matrix\ gas} \approx 10^{-5}$ mbar) onto a cold metal coated (aluminum for UV-vis, gold for IR measurements) sapphire substrate at a nominal kinetic energy of less than 50 eV. The kinetic energy of the incoming ions is further reduced by the electrostatic retardation potential from the positively charged sample. The charge leads to a deflection of the ions, on the sample they are deposited into a spot of roughly 1 cm diameter with approximately Gaussian shape.

The ion current directed at the substrate has an intensity between 1 pA and 300 pA for nanoES, and between 5 nA and 300 nA for EI, depending on the species of interest. For samples produced with the EI source, the total number of ions typically amounts to 10^{13} to 10^{14} ions at a ratio of matrix to guest molecule of about 5×10^3

to 1, effectively isolating the deposited ions from each other. From the nanoES, roughly a factor of 10^{-3} fewer ions are deposited. The reduced matrix gas pressure for low ion currents leads to a ratio of matrix to guest molecules of about 5×10^5 to 1.

The substrate is cooled by a closed-cycle cryostat (SHI Cryogenics, RDK-415D) to 5-6 K, measured at the sample holder with a Si diode. The low temperatures allow for the use of neon as matrix gas, best suited for absorption measurements and laser induced fluorescence spectroscopy, because of the high optical quality of solid neon [65].

In all matrix isolation experiments of ionic species, partial neutralization of the matrix via counterions has to take place, in order to reduce deflection of the incoming ions from the sample by the accumulated charge. In case of deposited cations, formation of counterions is induced via electron capture of either impurities in the matrix or the deposited ions themselves [49]. The formation of counterions can be facilitated by adding an electron scavenger with a positive electron affinity, like CO_2 or CCl_4.[2] This leads to an increase of the cation:neutral ratio, or, if the ion forms its own counterion, the cation:anion ratio. The use of electron scavengers can also lead to the formation of complexes or Coulomb pairs, and thus influence the spectrum. By using different matrix gases (pure Ne, Ne + CO_2, Ne + CCl_4), these and other matrix effects can be assessed. For reference, spectra of neutral molecules are obtained from deposition of neutral molecules directly from a sublimation source, if possible.

Furthermore, the use of inert matrix gases with different polarizabilities (Ne: α_{Ne}= 0.395 Å^3 or Ar: α_{Ar}= 1.641 Å^3, [2]) allows to estimate the shift of spectral features in respect to gas phase measurements by extrapolation of the shift to the gas phase with $\alpha_{vac} = 0$.

Annealing of the sample to 8 K or 20 K for neon or argon matrixes, respectively, increases the mobility of the stored species and enables additional neutralization [69]. From the decrease of the cationic/anioic and the increase of the neutral absorbances the relative absorption cross sections can be estimated.

Measurement Setup

When the sample is prepared, it can be studied with IR and UV-vis absorption spectroscopy, as well as with laser induced emission spectroscopy. UV-vis absorptions and laser induced emissions are measured in the deposition chamber (fig. 2.6 (VI)). The experimental setup requires the prepared matrix to be turned by an angle of 90° for absorption measurements, or by 80° for emission measurements (to

[2]Electron affinity (EA) of CCl_4: 0.8 eV [66], CCl_3 (formed in the matrix [67]): 2.2 eV [68]; EA of CO_2: -0.6 eV (gas phase); on surfaces, CO_2 has a bent structure and a positive EA [49]

prevent the reflected excitation laser beam from entering the spectrometer). For IR absorption spectroscopy, the as-prepared sample mounted in its sample holder is transferred into the lower measurement chamber. To prevent contamination, all measurements are performed under UHV conditions ($p < 5 \times 10^{-9}$ mbar). Sample rotation and transfer into the lower measurement chamber is possible without measurably raising the sample temperature or the pressure in the vacuum chambers.

Infrared spectra are measured in reflection geometry at 60° incidence angle relative to the surface normal with a Bruker IFs66v spectrometer (resolution 0.25 cm^{-1}, experimental accuracy is 0.1 cm^{-1}). Three different detectors are used: a liquid nitrogen cooled mercury-cadmium-telluride (MCT) detector (7000 - 800 cm^{-1}), a liquid helium cooled copper-germanium (CuGe) detector (2000 - 400 cm^{-1}), and a liquid helium cooled bolometer (1000 - 50 cm^{-1}). MCT and CuGe measurements are done using a potassium bromide (KBr) beamsplitter, and thallium bromo-iodide (KRS5) windows to separate the spectrometer from the measurement chamber. For bolometer measurements, the beamsplitter has to be changed to a 50 µm mylar beamsplitter, and silicon windows are used. Changing the detectors from CuGe to the bolometer requires several days of adjustment of the optical path, as well as baking of the measurement chamber, thus most samples are investigated in the MCT and CuGe spectral range only. For each spectrum, 1200 to 3600 single scans are averaged, resulting in a total measurement time of 20 to 60 minutes.

In the UV-vis to near infrared (NIR) range (200 - 1100 nm), absorption and emission spectra are measured. For absorption measurements, the sample is irradiated with a deuterium discharge lamp (200 to 450 nm) and with a halogen lamp (450 to 1100 nm). Typically, 100 spectra are acquired and summed up. The acquisition time for each single spectrum is 500 ms.

Laser induced luminescence of deposited ions is measured upon laser-excitation at 375 nm (diode laser, Thorlabs, P_{max}= 20 mW, bandwidth 1 nm) or at 405 nm (diode laser, Lasever, P_{max}= 250 mW, bandwidth 1 nm). The irradiated area is around 1 mm^2, approximately 2% of the deposited ions are probed. The emitted light is collected using a focusing lens ($d = 1.4$ cm), positioned about 50 mm from the surface, and transferred through an optical fiber bundle to a spectrometer, leading to a collection efficiency of roughly 1%. The measurement time for each spectrum shown ranged from 300 to 2400 s. All emission spectra shown in this work are intensity corrected.

The spectrometers used in the UV-vis-NIR range are an ARC SpectraPro-500 spectrograph equipped with an EG&G PARC 1456A detector (resolution up to 0.08 nm), a Princeton Instruments IsoPlane SCT320 spectrograph with a PIXIS 256 OE camera (resolution up to 0.12 nm), both with entrance aperture slits of 50 µm, and an RXN1 Kaiser Optics process-Raman spectrometer with the excitation laser turned off, which is optimized for measurements in the NIR range (resolution 0.4 nm). The experimental accuracy for UV-NIR measurements is 0.1 nm (0.4 nm for the RXN1 Raman spectrometer).

2.3 Scanning Tunneling Microscopy

The basic principle of scanning tunneling microscopy (STM) is described by tunneling junctions. For these junctions, the current through an insulating barrier is measured as a function of external parameters, for example of barrier height and thickness, external magnetic or electric fields, or temperature. In STM, developed in 1982 [11], one electrode of the junction is substituted with a sharp tip and moved across a sample. The tunneling current, or a derived parameter, is plotted primarily as a function of the tip position, but also of other parameters.

The description of the current through a planar tunneling junction in one dimension is quite straightforward. Taking the tip into account for STM, Tersoff and Hamann [70] calculated a tunneling conductance σ given by

$$\sigma \propto \rho(\vec{r}_0, E_F)$$

with the tip position $\vec{r}_0$, the Fermi energy E_F, and the local density of states (LDOS) $\rho(\vec{r}_0, E) = \sum_\nu |\Psi_\nu(\vec{r}_0)|^2 \delta(E_\nu - E)$. The z-position of the tip at constant current will thus follow lines of constant LDOS. However, this so-called s-wave model does not account for the resolution of the STM. To get an accurate description of the STM tunneling junction, the electronic states of the tip have to be taken into consideration [71]. Atomic resolution of the STM is only possible with localized metallic p_z or d_{z^2} states, which are formed e.g. by tungsten, platinum, or iridium, or some semiconductors.

The measured current is typically of the order of several tens to hundreds of nanoamperes and has to be amplified for processing.

2.3.1 Inelastic Tunneling Spectroscopy

For inelastic tunneling spectroscopy (IETS), the tip is set to a fixed z-position above a molecule that is introduced into the tunneling junction, and an AC voltage is applied in addition to the DC bias of the tip. Vibrational excitations of the molecule can be measured.

The molecule modifies the roughly exponential change of the current with increased voltage ($I-V$ curve) in the junction by allowing additional non-resonant tunneling processes. The process is illustrated in figure 2.7. The conductivity of the tunneling junction with the introduced molecule increases, if the energy of the tunneling electrons is above the excitation energy of molecular vibrations. This effect can be seen in the $I - V$ curve by a sudden, but small, increase in the conductivity. Looking at the second derivative $\mathrm{d}I^2/\mathrm{d}^2V$ of the measured current, the molecular excitation is seen as a sharp peak in the signal and more easily identified. To increase the

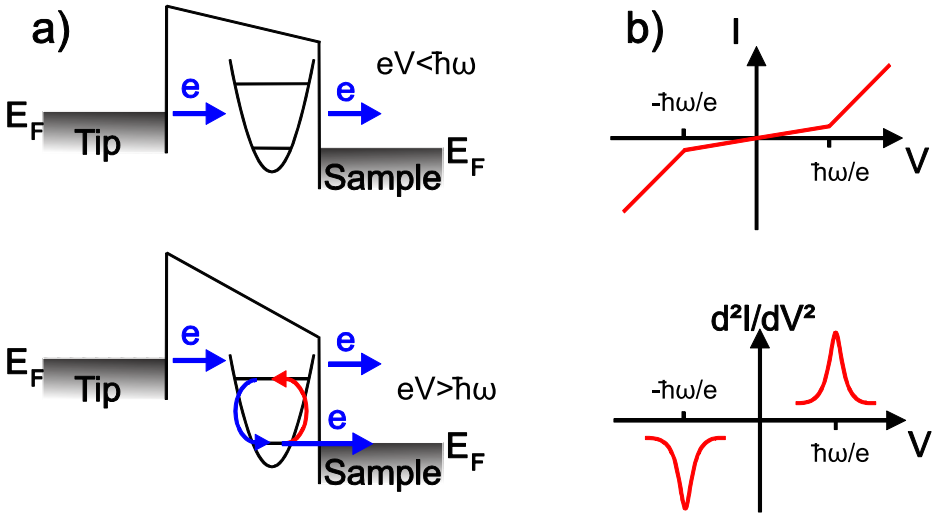

Figure 2.7: Increasing the energy of the tunneling electron above the excitation energy of the molecule in the gap gives rise to additional tunneling channels (a). Excitation of the molecule is identified by kinks in the $I-V$ curve and peaks in the $^{\mathrm{d}I^2}/_{\mathrm{d}V^2}$-$V$ spectrum (b).

signal, the $^{\mathrm{d}I^2}/_{\mathrm{d}^2V}-V$ spectrum is measured at the 2nd harmonic of the modulation frequency via a lock-in amplifier.

The lineshape of the IETS signal is broadened by the finite lifetime of the excitation, accounted for by the parameter Γ, the non-zero temperature T, and the amplitude of the applied AC voltage ΔV^{rms}. The result is a Gaussian with an effective width of

$$W_{tot} = \sqrt{\Gamma^2 + (5.4k_BT)^2) + (1.7\Delta V^{rms})^2}$$

limiting the energy resolution of IETS [72, 73].

Theoretical models of the inelastic spectra of molecules predict the inelastic signal to be enhanced for resonances in proximity of the Fermi level, and specify excitation selection rules [74, 75]. In actual experiments, these predictions often do not fully apply. Instead, the so-called IETS propensity rules were defined, based on the comparison of theoretical predictions and experimental results [76]. Especially C_{60} has been used to study the selection rules of IETS on different substrates [77, 78, 79, 80, 81].

2.3.2 Experimental Setup

The STM used in the measurements presented is a home-built machine, developed by Zhang *et al* [82, 83]. Low temperatures of the sample are realized by a Joule-

Thompson (JT) stage, the complete setup will therefore be referred to as JT-STM in the following chapters.

The JT-STM consists of three UHV chambers: a measurement chamber with the microscope and the cryostat, a preparation chamber where the metallic substrates are cleaned and prepared, and a load-lock chamber for transferring samples from and to ambient suroundings. The load-lock chamber is also used for the deposition of the molecules.[3] To vibrationally decouple the apparatus from the laboratory, it is lifted by four pneumatic feet (Newport S-2000 series). During measurement, the STM and preparation chamber are pumped by ion pumps to avoid vibrations from turbomolecular pumps (TMPs).

Load-Lock Chamber

The load-lock chamber consists of a CF-40 6-way-cross with an attached TMP and a transfer rod. Additionally, a molecular evaporator filled with the molecules of interest is attached to this chamber. The molecular evaporator is composed of a ceramic crucible, which can be heated up to 500 °C by resistive heating. The temperature is controlled through a thermal sensor and adjusted by a PID controller. During deposition of the molecules the pressure in the load-lock chamber is around 10^{-7} mbar.

Preparation Chamber

In the preparation chamber, the single crystalline metallic substrates are cleaned and prepared prior to deposition of molecules. It is pumped by a titanium sublimation pump, an ion getter pump, and a TMP. The base pressure of this chamber is typically 10^{-10} mbar. A differentially pumped ion gun with two leak valves, for argon and nitrogen sputtering, is also mounted. The pressure during sputtering does not exceed 5×10^{-8} mbar. Following the sputtering procedure, the substrate is annealed at around 600 to 1000 K (depending on the metal substrate used) by means of electron impact heating, with its temperature monitored with a pyrometer.

Freshly etched tungsten tips are also sputtered with argon and tempered for some seconds ('flashed') in the preparation chamber to remove residual oxides.

Characterization of the sample in the preparation chamber can be done by LEED and Auger spectroscopy. Several electron beam evaporators are available to deposit different metals on the sample or the tip.

[3] For the measurements presented, neutral molecules were deposited directly on the substrate without mass selection. For other measurements, mass selected ions were soft-landed on the substrate, and the sample was subsequently vacuum transferred to the STM [84].

STM Chamber

The STM chamber contains the liquid helium cryostat and JT stage, the actual low temperature scanning tunneling microscope unit, and an additional electron beam evaporator for *in situ* preparation at low temperatures. It is pumped by an ion getter pump and a TMP, allowing for a pressure of less than 10^{-10} mbar. The cold cryostat, cryoshield, and STM act as an additionl cryogenic pump, decreasing the pressure inside the microscope considerably, and enabling long measurement times without sample degradation.

The cryostat system consists of a liquid nitrogen and a liquid helium bath cryostat. In the Joule-Thompson expansion stage, a He_3/He_4 mixture is used. The helium bath is used for precooling, pressure reduction with a TMP from 500 mbar to $\sim 3\times10^{-1}$ mbar results in a temperature as low as 800 mK for the STM.

A superconducting coil surrounding the STM can generate magnetic fields up to 3 Tesla in the sample region.

The STM is operated via Nanonis SPM control hardware and the Nanonis SPM Control Software V4. For scanning tunneling spectroscopy, two external analog dual-channel lock-in amplifiers (EG&G 5210) are used to simultaneously measure the first and second derivative of the signal. The tunneling current is pre-amplified (Femto DLPCA 200), the gain setting of the preamplifier is adjusted to the signal intensity and the frequency range of the spectroscopy mode. Pre-amplifier gain values and associated bandwidths (attenuation -3 dB) for the measurements are 10^9 V/A with 1 kHz and 10^8 V/A with 7 kHz, limiting the frequency of second derivative measurements to approximately 0.5 kHz and 3.5 kHz, respectively.

2.3.3 Sample Preparation and Measurement

The species studied in this work are C_{60} and endohedral $H_2@C_{60}$ adsorbed on insulating Cu_2N on Cu(100).

For sample preparation, the Cu(100) surface is sputtered with Ar^+ (U=3 keV, I=3 μA, t=30 min) to remove surface adsorbants. Subsequent annealing at 720 K reduces surface defects. Copper nitride (Cu{100}-$c(2 \times 2)$N, CuN) is produced by sputtering the pre-cleaned Cu(100) surface with nitrogen ions (U=0.65 keV, I=0.15 μA, t=20 min) and ensuing annealing at 570 K, resulting in a insulating Cu_2N layer. Following the preparation of the CuN substrate, the molecules are deposited. For this, the sample is transferred into the load-lock chamber. Prior to this, the solid samples comprising the molecules to be sublimed (C_{60} or $H_2@C_{60}$) have been degassed at elevated temperature (T = 570 K) for roughly one hour to remove residual solvents. For deposition, the temperature is raised to 610 - 630 K, and the substrate is kept in direct line of sight of the molecular evaporator for two to five minutes.

The sample with the deposited molecules is then transferred back to the STM and investigated.

Topography is measured in constant current mode, typical settings for the bias and the current set point are 0.5 - 2 V and 0.05 - 1 nA. When a suitable location is scanned, the tip is placed above the region of interest and ITS is performed in the desired energy range (from -110 to +110 mV or from -700 to -400 mV at 1-20 nA). In chapter 5, detailed settings are listed for all presented measurements.

3 Spectroscopy of Isolated Fullerenes, Azafullerenes, and their Ions

3.1 Introduction

Carbon molecules with a spheroidal structure and a closed cage are called fullerenes, after the 19th century architect R. Buckminster Fuller and his geodesic domes. Mathematically, fullerenes are polyhedrons with the carbon atoms forming the corners and the C−C or C=C bonds the edges. In the simplest case, the cage consists of hexagons and pentagons. In this case, the n-atom structure can be described by the Euler theorem, which states that a closed cage can be formed from 12 pentagons and $n/2$ - 10 hexagons [85]. Fullerenes, which can be described by this rule are called classical fullerenes. If the molecular structure contains different motifs, like heptagons, octagons, or squares, the fullerene is called non-classical.

An additional classification of fullerenes is the so-called *isolated pentagon rule* (IPR) [86]. In fullerenes following this rule, the pentagons are surrounded by hexagons. Non-IPR fullerenes do not obey this rule, at least two pentagons are adjacent. These non-IPR fullerenes show an enhanced reactivity, easily form covalent bonds with other fullerene molecules, and cannot be solvated. Endohedral encapsulation of metal clusters or exohedral derivatization, for example with halogens, can stabilize non-IPR fullerenes [87, 88].

So far, no experiments to directly determine the molecular structure of bare, isolated non-IPR fullerenes have been reported due to the difficulty of separating them in amounts large enough for spectroscopy.

The curvature of IPR fullerenes leads to a mixed hybridization of the carbon orbitals, resulting in a α[sp^2]+β[sp^3] state. The hybridization of planar graphene is sp^2, whereas diamond is sp^3. Re-hybridization of the carbon orbitals to sp^3 and the associated steric strain reduce the stability of IPR cages relative to non-IPR cages [89].

Fullerenes were first generated by laser ablation of graphite in a low pressure helium atmosphere [90]. Time-of-flight mass spectrometry measurements showed the

presence of C_n clusters (with even n), with C_{60} and C_{70} the most abundant clusters. The high intensity of C_{60} and C_{70} was interpreted by the high stability of these clusters [91, 92]. While this new form of carbon generated great interest, the yield from laser ablation was too low for other than mass spectrometric studies.

The amount of available material was greatly increased by the Krätschmer- Huffmann process [93]. Carbon soot, containing fullerenes, is produced by an arc discharge between graphite electrodes in a helium or argon atmosphere. Approximately 15% of this soot consists of fullerenes and can be dissolved in organic solvents, the residual material is mainly amorphous carbon. Two mechanisms leading to the formation of closed carbon cages have been suggested, the 'bottom up' and the 'top down' model. In both laser ablation and arc discharge production, both processes are expected to co-exist.

The 'bottom up' model starts with linear chains ($n < 10$), which close to single and multiple rings as they grow larger. At $n > 30$, the formation of fullerene-like structures takes over, the planar ring structures are less stable [94, 95]. Growth of fullerenes takes place via fusion of smaller units, or addition or incorporation of C, C_2, or C_3 units [96, 97, 98]. A detailed description of the growth process can be found in an article by Khan and Ahmad [99].

In the 'top down' model, fullerenes are formed from small graphene flakes [100]. Loss of carbon atoms from the edge of the flake and subsequent relaxation of the structure lead to the formation of curved graphene sheets with pentagons. Further loss of carbon atoms results in the formation of closed carbon cages. Fullerenes formed from graphene flakes have a narrow range of average diameter of around 1 nm, consistent with the dominant formation of C_{60} and C_{70} in the experiment.

The properties of fullerenes, for example their electronic and vibrational spectrum, their reactivity or their stability, strongly depend on their structure and structure. Their properties can also be changed by replacing a carbon atom with a heteroatom in the cage [101], or by introducing a molecule or cluster into the cavitiy of the fullerene [12].

3.2 C_{60} and its Ions

Since its discovery in 1985 [90] and the following development of a route to macroscopic quantities of C_{60} [93], it has become a well-studied system, theoretically and experimentally. The great interest in C_{60} arises from its high symmetry (I_h, see figure 3.1), its unique electronic and chemical properties, and its detection in space in 2010 [102].

At the same time, spectroscopic measurements of the ions of C_{60} are scarce, due to the reactivity of these species and the difficulty in producing quantities necessary

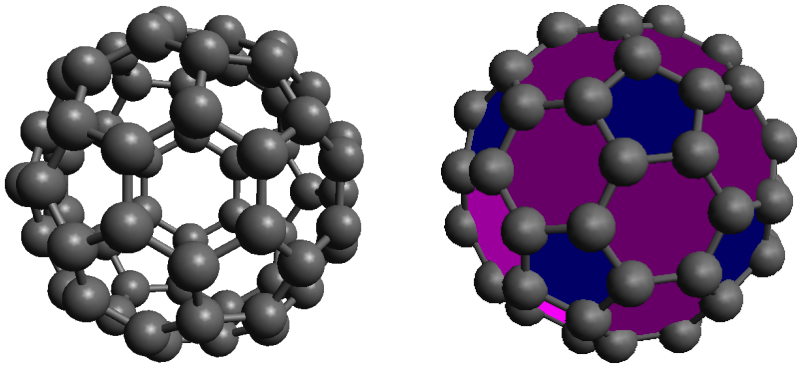

Figure 3.1: Left: The structure of C_{60}. Right: Rotated molecule with hexagons and pentagons marked.

for gas-phase experiments. The great interest in the ions of C_{60} can be seen in the long-standing discussion concerning C_{60}^+ as carrier of diffuse interstellar bands [103, 104, 105, 106]. Even so, gas phase measurements of the NIR absorptions of C_{60}^+ were only achieved in 2015, and as a result, C_{60}^+ was confirmed as the carrier of two diffuse interstellar bands at 9 632 and 9 577 Å [107].

Other spectroscopic measurements of isolated C_{60} ions include matrix isolation measurements of cations and anions [8, 108], measurement in organic solvents and crystals [109, 110], and measurement of the ions in gas phase [111, 112, 113, 107]. However, these measurements are limited by the studied frequency range, by a non-negligible interaction of the ions with their surroundings, or the presence of uncontrolled charge states and contaminating molecules.

In the following sections, measurements on matrix isolated C_{60} and its ions are presented. New absorptions of C_{60}^+ and C_{60}^- are identified, the gas phase absorption frequencies are estimated from different matrix environments, and the integrated molar absorptivities are measured. The first spectroscopic measurements of C_{60}^{2+} and C_{60}^{3+} are reported.

3.2.1 Neutral and Monoionic C_{60}

C_{60} cations are generated with the electron impact ionization source, as described in detail in section 2.2.3. With mass selection, an ion current of 200 - 300 nA can be achieved. The ions are co-deposited with an excess of matrix gas onto the gold coated sapphire substrate, held at roughly 5 K, the deposition time is five to ten hours. For C_{60} cations, neutralization of the matrix occurs via electron capture of deposited C_{60}^+, resulting in the formation of neutral C_{60} and anionic C_{60}^-. To differentiate between the charge states, matrixes are also formed by the addition of 1% CO_2 or 0.15% CCl_4, which act as electron scavengers and suppress the formation of neutral and anionic C_{60}. CO_2 and CCl_4 are used as electron scavengers because

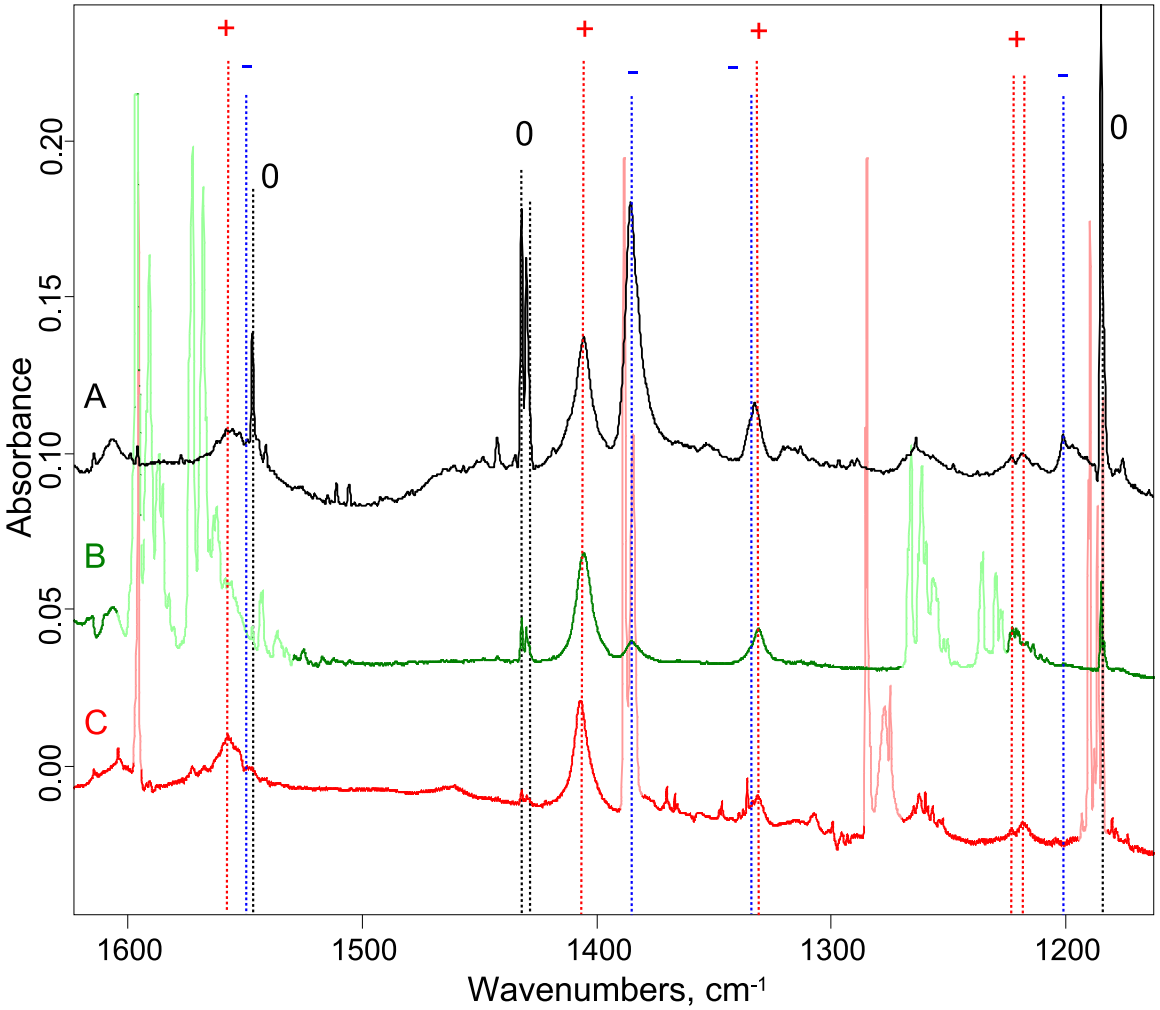

Figure 3.2: Matrixes composed of different ratios of neutral C_{60}, C_{60}^{+}, and C_{60}^{-}, (A) pure neon matrix, (B) Ne + 0.15% CCl_4, (C) Ne + 1% CO_2. Spectra are scaled to similar absorption intensities at 1405 cm^{-1} (C_{60}^{+}). Strong neutral and anionic absorptions of CCl_4 and CO_2 are shown with reduced contrast.

their infrared absorptions, obscuring some regions of the spectrum, only coincide in narrow regions. The reference spectrum of neutral C_{60} is obtained from direct deposition of C_{60} from a Knudsen cell without mass selection.

The spectra of C_{60} and its ions are measured, starting from the UV at 200 nm, through the vis, NIR, and IR range to the FIR at 200 cm^{-1}. Annealing of the matrixes and neutralization of the isolated species allows for an estimation of the integrated molar absorptivities. From measurements of the absorption positions in neon and argon matrixes the gas-phase absorption frequencies are estimated.

Results

Vibrational Spectra

IR spectra of matrixes containing only neutral C_{60} show the four well-known IR active T_{1u} absorptions [114], and one combination mode at 1547.0 cm^{-1} [115]. After deposition of mass selected C_{60}^+ into neon matrixes, several previously unidentified absorptions of C_{60}^+ and C_{60}^- can be observed [8], as well as absorptions from neutral C_{60}. Adding the electron scavenger CO_2 or CCl_4 to the matrix gas leads to a decrease in the relative intensity of the C_{60} and C_{60}^- absorptions compared to absorptions of C_{60}^+.

The IR absorption spectra are measured in argon matrixes containing only neutral C_{60} [116], and a mixture of C_{60}, C_{60}^-, and C_{60}^+ from deposition of mass-selected C_{60}^+. As can be seen in figure 3.3, the absorptions of the neutral, as well as most of the ionic C_{60} absorptions, exhibit a larger linewidth and a shift in the absorption position in argon matrixes due to the stronger interaction of the argon environment with the guest molecules [117]. However, some absorptions are narrower in argon matrixes than they are in neon. While this is unusual, the same effect has been observed in some other matrix isolation experiments, for example in Ref. [118]. Almost all identified IR and near-IR absorptions in neon matrixes are detected in argon matrixes.

Electronic Spectra

In the NIR, no absorption can be observed after deposition of neutral C_{60} into a neon matrix. Deposition of C_{60}^+ into pure neon matrixes leads to the presence of absorptions in the range from 1060 to 900 nm, while matrixes formed by adding electron scavengers only exhibit absorptions from 970 to 900 nm. Features in the range of 970 to 900 nm result from C_{60}^+, in the range of 1060 to 900 nm from C_{60}^- absorptions [8]. The band origins are found at 964.5 and 958 nm for cations, and at 1057 nm for anions. As can be seen in figure 3.3 a, both species exhibit a rich vibronic spectrum. The assignment of the vibronic features is given in Fulara *et*

Table 3.1: Assignment of the identified experimental absorption lines of $C_{60}^{0/+/-}$ according to their frequency, full width at half maximum (*fwhm*) and integrated molar absorptivity A_{Ne} in neon matrix at 5 K by comparison to DFT calculated frequency and integrated molar absorptivity A_{calc}.[a]

		experiment			*theory*	
	mode	ν[b], cm^{-1}	*fwhm*, cm^{-1}	A_{Ne}, $km{\cdot}mol^{-1}$	ν, cm^{-1}	A_{calc}, $km{\cdot}mol^{-1}$
C_{60}^{0}	comb.[c]	1547.0	0.7	2±0.2		
C_{60}^{0}	$T_{1u}(4)$	1432.1; 1430.1 [d]	1	11±1	1448.9	33
C_{60}^{0}	$T_{1u}(3)$	1184.8	0.8	10.4±0.8 [e]	1195.8	26.6
C_{60}^{0}	$T_{1u}(2)$	577.8	0.9	11±0.9	576.2	46.0
C_{60}^{0}	$T_{1u}(1)$	530.4	0.7	27±2	512.8	68.4
C_{60}^{+}	$E_{1u}(17)$	1557.6	10.3	33±9	1560.1	103.0
C_{60}^{+}	$E_{1u}(15)$	1405.3	8.6	70±19	1429.4	77
C_{60}^{+}	$E_{1u}(14)$	1331.1	5	20±5	1328.8	35.3
C_{60}^{+}	$A_{2u}(7)$	1223.2	1.9	6±2	1241.8	15.3
C_{60}^{+}	$E_{1u}(12)$	1218.1	3.1	11±3	1224.2	17.1
C_{60}^{+}	$E_{1u}(10)$	958.2	1.7	4±1	959.2	20.4
C_{60}^{+}	$E_{1u}(7)$	785.7	1.2	4±1	700.8	6.8
C_{60}^{+}	$E_{1u}(5)$	580.0	0.8	1.6±1	576.6	6.3
C_{60}^{+}	$A_{2u}(2)$	529.7	0.8	20±10 [f]	517.5	17.9
C_{60}^{+}	$E_{1u}(3)$	526.6	0.7	7±2	514.4	10.5
C_{60}^{+}	$E_{1u}(2)$	395.0; 398.5 [d]	1	10±3	388.8	9.7
C_{60}^{+}	$E_{1u}(1)$	347.2	0.9	5±2	340.0	3.8
C_{60}^{-}	$E_{u}(28)$	1546.1	13.9	16±4	1531.8	54.1
C_{60}^{-}	$E_{u}(25)$	1385.5	7.5	128±14	1418.3	258.6
C_{60}^{-}	$E_{u}(24)$	1351.6	7.1	5±1.5	1349.0	2.1
C_{60}^{-}	$E_{u}(23)$	1333.6	5.5	8±3	1334.2	30.5
C_{60}^{-}	$E_{u}(19)$	1200.7	5.4	16±4	1199.5	38.0
C_{60}^{-}	$A_{2u}(10)$	1175.6	1.6	1.3±0.5	1191.5	6.5
C_{60}^{-}	$E_{u}(17)$	964.3	2.6	0.9±0.4	972.1	2.9
C_{60}^{-}	$E_{u}(11)$	729.2	2.3	6±2	682.3	11.2
C_{60}^{-}	$A_{2u}(4)$	576.4	0.9	8±3	575.9	28.3
C_{60}^{-}	$E_{u}(8)$	575.3	1	39±4	574.1	77.6
C_{60}^{-}	$E_{u}(3)$	397.2	0.9	0.8±0.3	391.6	5.8

[a] C_{60}^{0} is calculated in I_h (singlet) symmetry, C_{60}^{+} in D_{5d} (doublet) symmetry, and C_{60}^{-} in D_{3d} (doublet) symmetry; [b] Experimental error (for all IR measurements): 0.1 cm^{-1}; [c] Combination mode [115]; [d] Site effect in Ne matrix; [e] The value was taken from Iglesias-Groth *et al.* [119]; [f] C_{60}^{+} $A_{2u}(2)$ and C_{60}^{0} $T_{1u}(1)$ absorptions coincide, therefore $A_{Ne}(A_{2u}(2))$ has a larger error.

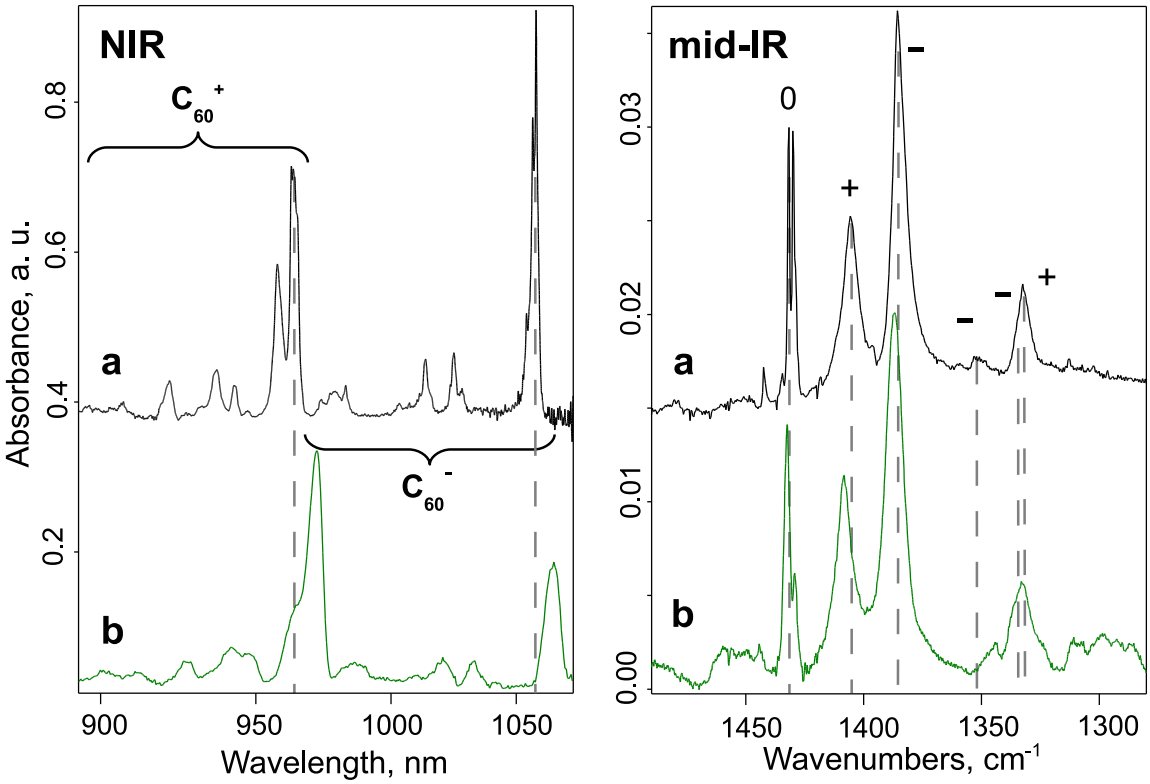

Figure 3.3: Detail of the NIR (left) and mid-IR (right) spectrum of different samples of $C_{60}^{0/+/-}$ in neon (a, black) and argon (b, green) matrixes. Dashed lines indicate the absorption frequencies in neon matrixes. Ionic NIR and neutral absorptions are broader in argon matrixes, whereas the *fwhm* of the shown mid-IR absorptions of $C_{60}^{+/-}$ is essentially independent of the matrix gas.

al [8]. However, while the absorption wavelengths are identical to the presented measurements, the determined oscillator strengths differ. This will be addressed in the following section.

In the UV-vis range, the well-known strong absorptions at 250 and 322 nm, as well as some weaker ones, can be seen after deposition of neutral C_{60} [93]. Due to scattering of the matrix, the absorptions below 250 nm cannot be observed in every sample. Attention should be paid to the absorption features around 600 nm (figure 3.8, inset), which are characteristic for neutral C_{60}.

Matrixes additionally containing C_{60}^+ and C_{60}^- do not show new absorption features in the UV range, only a slight broadening of the absorptions is visible. The formation of neutral C_{60} can be suppressed by deposition of C_{60}^+ into Ne + CO_2 and Ne + CCl_4. In these samples, the main absorption features in the UV range are still present, the UV absorptions of neutral C_{60} and C_{60}^+ coincide. Only a small shift is detectable, which is explained by interactions with the matrix environment.

Discussion

Vibrational Spectra

The spectral range of the IR absorption data for matrix isolated $C_{60}^{0/+/-}$, which was previously published by Fulara *et al.* [8], is limited to the mid-IR region (i.e. $>600\,cm^{-1}$). Furthermore, the assignment of weaker absorptions is rendered impossible by the experimental procedure followed by these authors.

To assign the detected IR absorption in the experiment, the most intense absorptions of C_{60}^+ ($1405.3\,cm^{-1}$) and of C_{60}^- ($1385.5\,cm^{-1}$) serve as reference [8]. Correlating the intensities of the absorptions measured in different matrixes allows assignment of weaker absorption features.

In detail, to assign all C_{60}^+ absorptions, we start with the spectra in Ne + 1% CO_2 and Ne + 0.15% CCl_4 matrixes (spectrum I and II). By comparing the intensities of the ionic reference absorptions at $1405.3\,cm^{-1}$ (C_{60}^+) and $1385.5\,cm^{-1}$ (C_{60}^-), only traces of C_{60}^- are identified in matrixes with electron scavengers (fig. 3.2 b, c). In the next step, the spectrum in Ne matrix (spectrum III), containing $C_{60}^{0/+/-}$ at the same time, is subtracted from spectrum I (Ne + 1% CO_2) and spectrum II (Ne + 0.15% CCl_4), respectively. In the resulting spectra, no absorptions of C_{60}^- are present. The remaining absorptions of neutral C_{60}^0 are subtracted with the reference spectrum of neutral C_{60} in Ne. Thus, we obtain spectra, in which the absorptions of C_{60}^+ are identified by correlation of absorption intensities to the $1405.3\,cm^{-1}$ (C_{60}^+) feature.

This procedure is based on the fact, that the corresponding starting spectra are constituted by a linear combination of different relative amounts of C_{60}^0, C_{60}^+, and C_{60}^-.

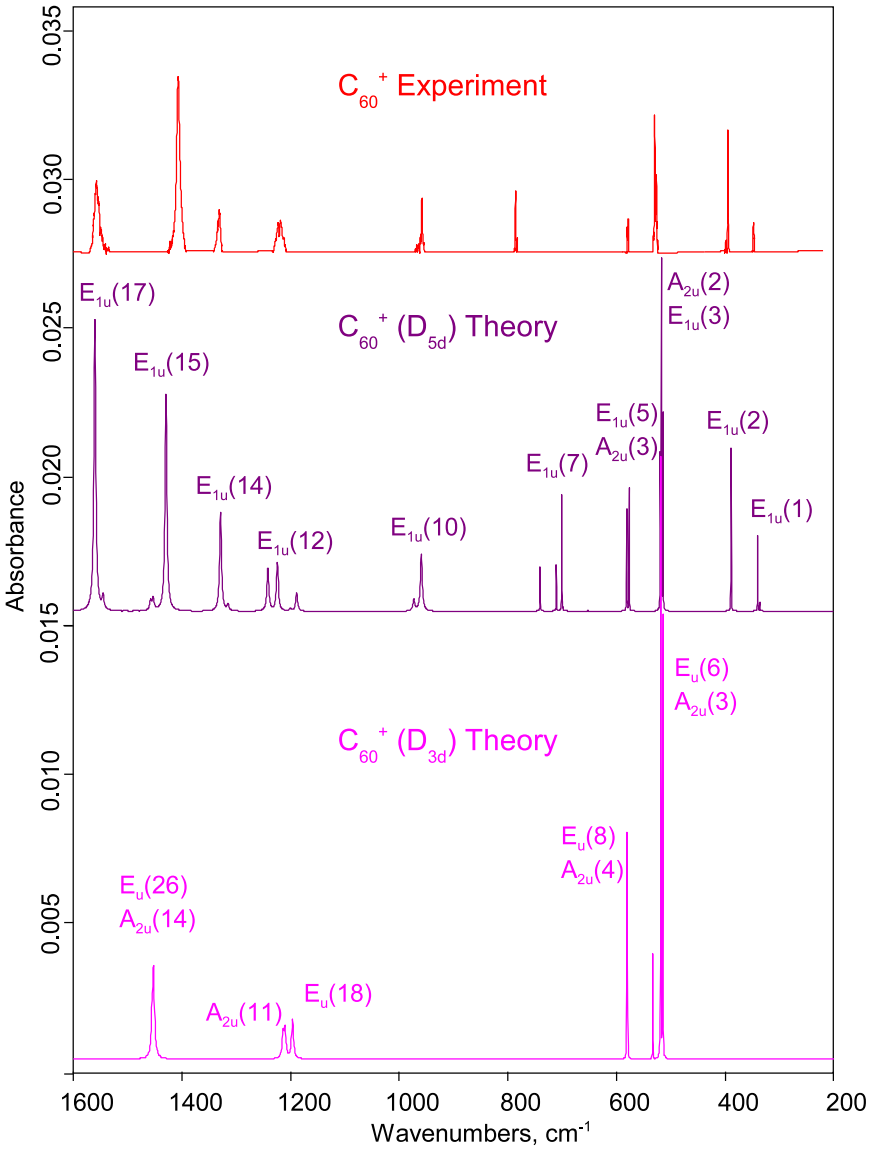

Figure 3.4: Comparison of the extracted C_{60}^+ IR absorption spectrum in neon (top) and simulated spectrum from RI-DFT calculations for D_{5d} and D_{3d} symmetry. Calculated frequencies are unscaled. Details see text.

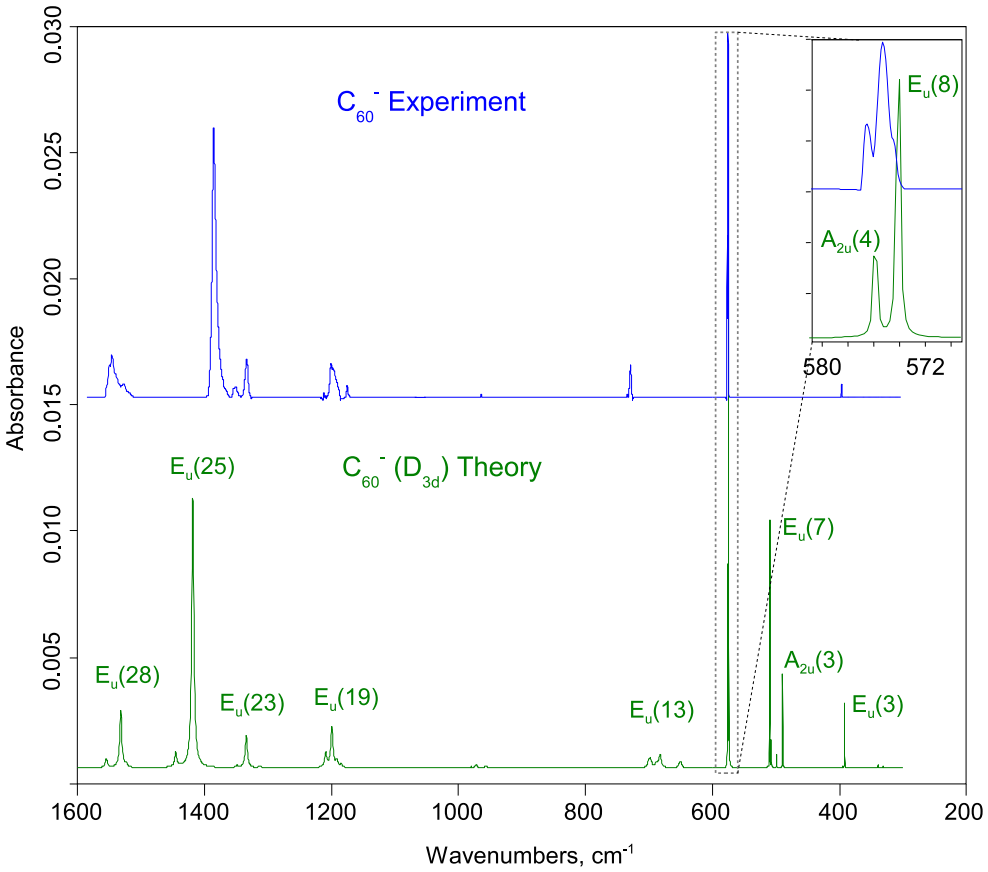

Figure 3.5: Extracted experimental IR spectrum of C_{60}^- in neon (top) and simulated spectrum from RI-DFT calculations for D_{3d} symmetry (bottom). Frequencies of the calculation are unscaled. Details see text.

A similar approach is applied for C_{60}^-. The neutral spectrum and the spectra obtained with Ne + 1% CO_2 and Ne + 0.15% CCl_4 matrixes are subtracted from the spectrum measured in a pure neon matrix in such a way, that neutral and previously identified cationic absorptions vanish. The intensities of the remaining absorptions are compared for spectra obtained from different measurements (see previous paragraph for details). Absorptions with correlating intensities in all measured spectra, and for which no other origin is identified, are assigned to C_{60}^-.

Close-lying and overlapping absorptions of C_{60}^0, C_{60}^+, and C_{60}^- are disentangled and assigned by this procedure.

To simplify the comparison with DFT calculations, regions between the identified absorptions of the C_{60} ions are next substituted by straight baselines. The absorptions themselves are taken from the original data, frequency, intensity, linewidth, and splitting are unchanged. These 'extracted' spectra are compared to calculated spectra in figure 3.4 and 3.5.

The integrated molar absorptivity of each vibrational mode is determined by relat-

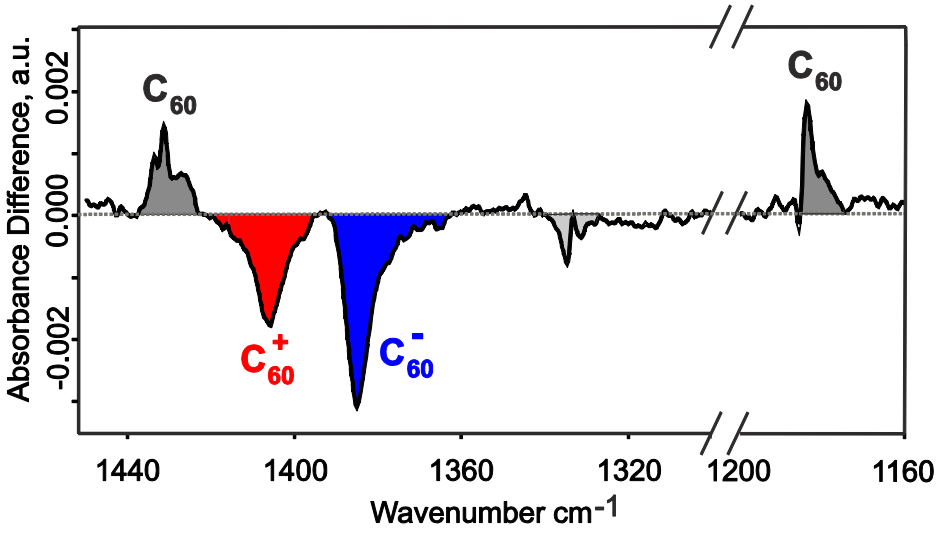

Figure 3.6: Difference spectra of neutral C_{60}, C_{60}^+, and C_{60}^- after annealing of an argon matrix at 30 K for 2 minutes. Neutral absorption features show a gain, ionic absorption features a decrease in intensity.

ing the loss of absorption intensity of the ionic lines to the gain in intensity of the neutral lines after annealing of the matrix. The intensity loss of ionic lines and the gain of neutral lines can be seen in figure 3.6. Assuming that the neutralization process is dominated by the direct neutralization of C_{60} ions via $C_{60}^+ + C_{60}^- \rightarrow 2\, C_{60}^0$, the relative absorptivity of all absorptions can be calculated. For absolute values of the absorptivity, previously published data for the integrated molar absorptivity of the four T_{1u} absorptions of neutral C_{60} in KBr pellets at different temperatures are used [119]. The absorptivity of the $T_{1u}(3)$ mode at 1184 cm^{-1} is not strongly influenced by temperature effects, therefore its absorptivity is used as a reference value. The experimental uncertainty of the intensities is 7 - 50%, depending on the signal-to-noise ratio of the absorption feature, and possible close-lying absorptions of a different charge state.

While the intensities of most absorptions can be reproduced to within 5% in different experiments, the $T_{1u}(1)$ absorption of neutral C_{60} shows a larger variation in intensity for different experiments. A comparison of different samples is shown in figure 3.7. This effect has not been reported for C_{60} isolated in Ar or H_2 matrixes [120, 121], and remains to be explained. The measured intensity of the $E_{1u}(3)$ mode of C_{60}^+ at 529.7 cm^{-1}, coinciding with the C_{60} $T_{1u}(1)$ absorption, is therefore uncertain. A similar effect is not observed for other absorption features of C_{60} and its ions, or for other fullerenes.

For C_{60}^+, DFT calculations (Turbomole [33], BP86/def2-SV(P)) are performed for D_{3d} symmetry, as suggested by gas phase photoelectron spectroscopy experiments [122], and for D_{5d} symmetry, which is the lowest-energy structure from DFT. For comparison with the experiment, no scaling was used. As shown in figure 3.4, the

calculated spectrum for D_{5d} symmetry fits the experimental spectrum more accurately. The frequencies of most of the lines are predicted within 3% of the measured value for D_{5d} symmetry, with the exception of the $E_{1u}(7)$ and $E_{1u}(15)$ modes. These deviations are probably due to large anharmonicities of the vibrations, or a shift by dynamic Jahn-Teller effects. Most of the integrated molar absorptivities are correctly predicted within a factor of 2. Nevertheless, some of the calculated intensities are overestimated, for example for the $E_{1u}(10)$ and $E_{1u}(17)$ modes. Some weaker modes predicted by DFT are probably not identified because of their low experimental intensity. For D_{3d} symmetry, only absorptions close to the T_{1u} modes of neutral C_{60} are predicted, most of the predicted vibrations are not present in the experiment. Therefore, the D_{5d} ground state is assigned to C_{60}^+ in neon matrixes.

For C_{60}^-, DFT calculations (Turbomole [33], BP86/def2-SV(P)) are performed for D_{3d} symmetry, the lowest-energy structure from DFT. No scaling was used for comparison with the experiment. As for the spectrum of C_{60}^+, the spectrum of C_{60}^- can be reproduced within 3% for the frequencies and a factor of 2 for the integrated molar absorptivities (figure 3.5). Larger deviations for the $E_u(25)$ mode can be explained by large anharmonicities of the vibrations, or a shift due to dynamic Jahn-Teller effects. The calculated intensities of the $A_{2u}(3)$ and $E_u(7)$ modes are most likely overestimated, no corresponding absorptions can be identified in the experiment.

An overview of the identified absorptions is given in table 3.1. The assignment of the identified absorption features according to DFT, their experimental frequency, full width at half-maximum, and integrated molar absorptivity, and the calculated frequency and integrated molar absorptivity are summarized there.

$C_{60}^{+/-}$ absorptions in the 1600 - 900 cm^{-1} region are broadened, indicating a faster relaxation of tangential vibrations in contrast to radial cage vibrations in the 900 - 200 cm^{-1} region. This may be due to electron-vibration coupling of the C_{60} ions, and thus a dynamic Jahn-Teller distortion of the cage symmetry. The excitation energy for electron-vibration coupling was calculated to be 69 meV/ 560 cm^{-1} (C_{60}^+) and 80 meV/ 645 cm^{-1} (C_{60}^-) [123]. Excitations above this energy are expected to induce dynamic Jahn-Teller distortions. The calculated energies are close to the measured energy of roughly 1000 cm^{-1}, above which a broadening of the absorptions is detected.

IR spectra of C_{60} and its ions measured in argon matrixes exhibit a frequency shift of up to 5 cm^{-1} compared to neon matrix frequencies. By plotting the absorption frequency versus the polarizability of the matrix gas (α_{Ne}=0.395 Å^3, α_{Ar}=1.641 Å^3, $\alpha_{GP} = 0$ [2]), the gas-phase position of the absorption line can be estimated. Absorption frequencies of $C_{60}^{0/+/-}$ in argon and neon matrixes, and the linearly extrapolated gas phase frequencies, are listed in table 3.2 (IR) and table 3.3 (NIR).

The extrapolated absorption frequencies of neutral C_{60} show good agreement with experimental gas-phase emission frequencies [124], the deviation is less than 0.6% for all features. Also, one has to keep in mind that the experimental gas-phase data

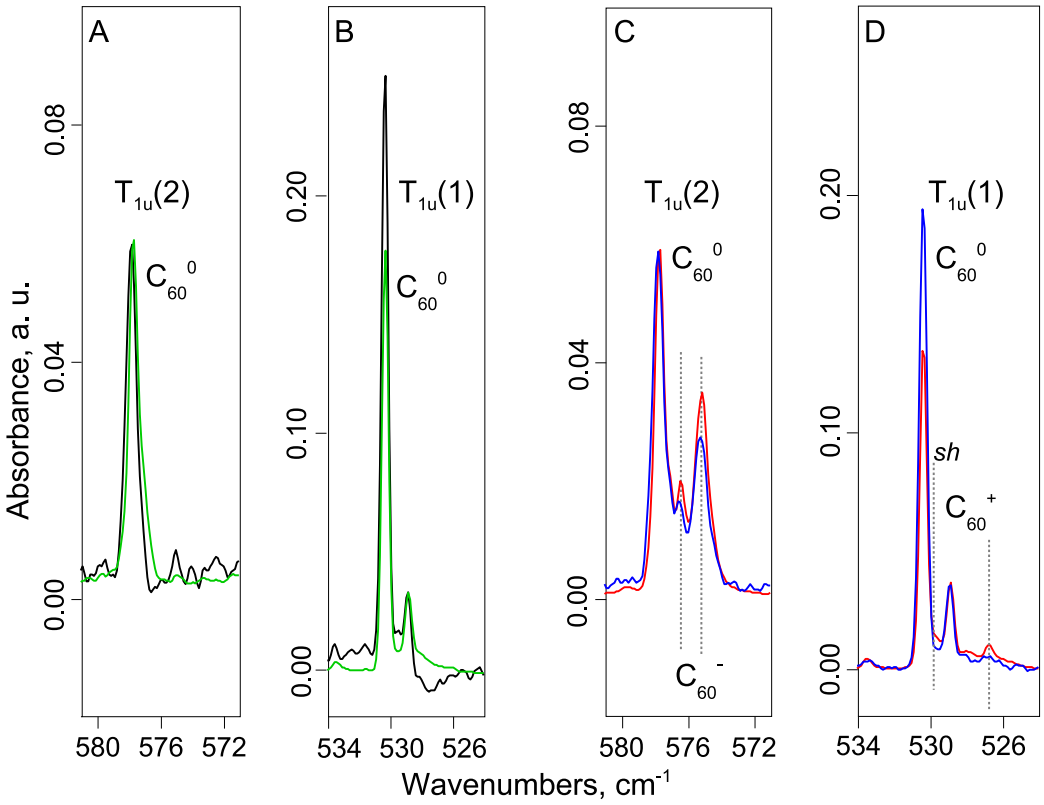

Figure 3.7: Two different samples of neutral C_{60} in a neon matrix, (A) $T_{1u}(2)$ and (B) $T_{1u}(1)$ mode. The same regions ((C) $T_{1u}(2)$ and (D) $T_{1u}(1)$) of two samples containing different ratios of C_{60}, C_{60}^{+}, and C_{60}^{-} in a neon matrix. Spectra are scaled to have similar $T_{1u}(2)$ intensities, the $T_{1u}(1)$ intensities vary. The ionic absorptions are marked (*sh*: C_{60}^{+} absorption forms a shoulder of the C_{60}^{0} $T_{1u}(1)$ mode).

are emission measurements, a shift from emission to absorption is expected, particularly as the gas-phase data were recorded at high temperatures (930 to 1230 K) and the temperature shift of the emission frequencies was extrapolated with a linear function to 0 K. This does not take possible effects due to anharmonicities properly into account.

For C_{60}^-, gas-phase absorption data was measured by multiple photon absorption and subsequent electron detachment. The exact temperature of the ions in this experiment is unknown due to the several hundred IR photons absorbed, but higher than 300 K. A shift of the absorption frequencies is known for resonance multiphoton ionization compared to low temperature absorption data [125]. The temperature shift can explain the deviation of almost 1% for the extrapolated frequencies. Also, only two absorptions were identified in the gas-phase measurements.

No gas-phase IR measurements of C_{60}^+ have yet been reported in the literature.

While the extrapolated absorption frequencies of $C_{60}^{+/-}$ are likely to show a deviation from the actual gas-phase frequencies, the error is estimated to be less than 0.6%. This result is consistent with measurements of other species isolated in noble gas matrixes [126]. Even so, calculated frequencies are not as reliable as absorption frequencies extrapolated from matrix measurements.

Gas-phase absorption frequencies and intensities, especially of C_{60}^+, over a wide spectral range are of interest for astronomical observations. IR emissions of neutral C_{60} have been detected in several stellar objects. For C_{60}^+ only two tentative IR observations have been reported [127, 128]. Emissions of C_{60}^+ could explain the intensity of some features reported by Sloan *et al.* [129] at 17.41 and 18.88 μm (574 and 530 cm^{-1}). While these observed emissions coincide with the C_{60} $T_{1u}(1)$ and $T_{1u}(2)$ modes, the relative intensity of the emissions is different in different stellar objects. A quantitative analysis is complicated by sulfur [S III] and S^{2+} emissions at 18.71 μm, which are superimposed with the fullerene emission at 18.9 μm. The change in relative intensities of these observed emissions could be due to different contributions from the C_{60}^+ $A_{2u}(2)$ mode, which coincides with the C_{60} $T_{1u}(1)$ mode.

However, it has to be taken into account that the astronomical data are emission spectra of molecules at higher temperatures (probably around 300 K [102]). A corresponding temperature shift from the absorption to the emission spectrum is expected.

A detailed discussion of the astronomical implications of C_{60}^+ lab measurements is given in Strelnikov *et al.* [130].

Table 3.2: Identified absorptions of $C_{60}^{0/+/-}$ in argon and neon matrixes at 5 K: frequency ν_{Ar} and ν_{Ne}, full width at half maximum (*fwhm*) in argon matrixes, extrapolated and measured gas phase values and deviation Δ of extrapolation.

		matrix			*gas phase*		
	mode	ν_{Ar}, cm^{-1}	*fwhm*(Ar), cm^{-1}	ν_{Ne}, cm^{-1}	extrapol. cm^{-1}	measured, cm^{-1}	Δ, cm^{-1}
C_{60}^{0}	$T_{1u}(4)$	1432.5 [a]	3	1432.1 [a]	1432.0	1435.5 ± 1 [b]	3.5 (0.25%)
C_{60}^{0}	$T_{1u}(3)$	1184.9	2.2	1184.8	1184.8	1180.75 ± 0.97 [b]	4 (0.35%)
C_{60}^{0}	$T_{1u}(2)$	578.8	1.9	577.8	577.5	574.37 ± 0.6 [b]	3.1 (0.54%)
C_{60}^{0}	$T_{1u}(1)$	529.8	— [c]	530.4	530.6	531.22 ± 0.24 [b]	0.6 (0.12%)
C_{60}^{+}	$E_{1u}(17)$	1558.1	7.4	1557.6	1557.4		
C_{60}^{+}	$E_{1u}(15)$	1408.3	6.5	1405.3	1404.3		
C_{60}^{+}	$E_{1u}(14)$	1331.5	7	1331.1	1331.0		
C_{60}^{+}	$A_{2u}(7)$	1223.2	1.6	1223.2	1223.2		
C_{60}^{+}	$E_{1u}(12)$	1219.1	2.9	1218.1	1217.8		
C_{60}^{+}	$E_{1u}(10)$	958.2	3.1	958.2	958.2		
C_{60}^{+}	$E_{1u}(7)$	784.8	1.6	785.7	786.0		
C_{60}^{+}	$E_{1u}(5)$	— [c]	— [c]	580.0	—		
C_{60}^{+}	$A_{2u}(2)$	— [c]	— [c]	529.7	—		
C_{60}^{+}	$E_{1u}(3)$	526.3	1.1	526.6	526.7		
C_{60}^{+}	$E_{1u}(2)$	395.1	0.9	395.0 [a]	395.0		
C_{60}^{+}	$E_{1u}(1)$	348.1	0.8	347.2	346.9		
C_{60}^{-}	$E_{u}(28)$	1542.2	30	1546.1	1547.3		
C_{60}^{-}	$E_{u}(25)$	1386.9	8.4	1385.5	1385.1	1374 [d]	11.1 (0.8%)
C_{60}^{-}	$E_{u}(24)$	1344.2	4.8	1351.6	1353.9		
C_{60}^{-}	$E_{u}(23)$	1334.8	4.4	1333.6	1333.2		
C_{60}^{-}	$E_{u}(19)$	1202.5	5.3	1200.7	1200.1		
C_{60}^{-}	$A_{2u}(10)$	1176.5	2.7	1175.6	1175.3		
C_{60}^{-}	$E_{u}(17)$	— [c]	— [c]	964.3	—		
C_{60}^{-}	$E_{u}(11)$	728.5	1.3	729.2	729.4		
C_{60}^{-}	$A_{2u}(4)$	577.8	— [c]	576.4	576.0		
C_{60}^{-}	$E_{u}(8)$	576.6	1.6	575.3	574.9	570 [d]	4.9 (0.9%)
C_{60}^{-}	$E_{u}(3)$	397.3	— [c]	397.2	397.2		

[a] Splitting, strongest line; [b] Emission wavelength reported from Nemes *et al.*, extrapolated to 0 K [124]; [c] No value could be determined in argon matrixes; [d] Multiphoton absorption from Kupser *et al.* [111], temperature not known.

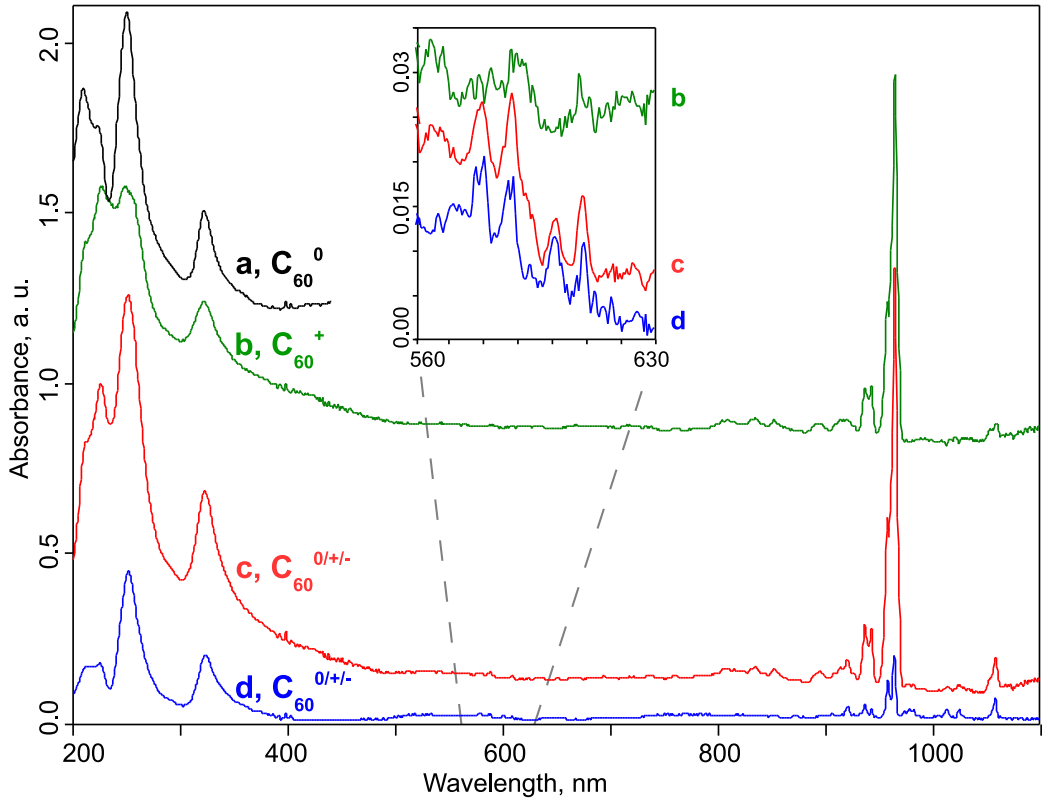

Figure 3.8: UV-vis spectra of different ratios of C_{60}:C_{60}^+:C_{60}^- in neon and Ne + 1% CO_2 matrixes, ratios are established from IR measurements. (a) neutral C_{60} in Ne + 1% CO_2, (b) extracted spectrum of C_{60}^+, (c) mixture of $C_{60}^{0/+/-}$ in Ne + 1% CO_2, (d) mixture of $C_{60}^{0/+/-}$ in Ne, features of C_{60}^- are around 1050 nm. In the inset the absence of neutral absorptions in the extracted spectrum is illustrated.

Electronic Spectra

With the ground state symmetry determined from IR absorption measurements and DFT calculations, the ionic NIR absorptions of matrix isolated $C_{60}^{+/-}$ can be assigned. The C_{60}^+ (D_{5d}) feature at 964.3 nm is assigned to the $^2E_g \leftarrow {}^2A_{1u}$ transition, the C_{60}^- (D_{3d}) feature at 1058.5 nm is assigned to the $^2E_g \leftarrow {}^2A_{2u}$ transition. The second transition of C_{60}^+ at 958.7 nm is discussed as either a different electronic state or a spin-orbit component [108, 131].

The oscillator strengths of the NIR transitions of C_{60}^+ and C_{60}^- are inferred from the measured integrated molar absorptivities of the IR vibrations (table 3.1) and measurements with a broad band MCT detector (14 000 to 1000 cm^{-1}). Here both IR and NIR absorptions are obtained within one spectrum. The oscillator strength of the NIR absorptions of C_{60}^+ is measured to be $f = 0.015 \pm 0.005$ for the 964.3 nm absorption, and $f = 0.01 \pm 0.003$ for the 958.7 nm absorption. The oscillator strength

Table 3.3: Absorption wavelength of C_{60}^+ and C_{60}^- in argon and neon matrixes, extrapolated gas phase value (linear and 2^{nd} order extrapolation, details see text), and gas phase absorption wavelength from direct measurements.

	matrix				*gas phase*
	λ_{Ar}, nm	λ_{Ne}, nm	extrapol., nm linear	extrapol., nm 2^{nd} order	gas phase value, nm
C_{60}^+	972.4	964.3	961.8	963.5	963.3 [a]
C_{60}^+	964.1	958.7	957.0	957.9	957.8 [a]
C_{60}^+	948.6	943.6	942.0	942.9	942.9 [a]
C_{60}^+	942.2	937.1	935.5	936.4	936.6 [a]
C_{60}^-	1066.8	1058.5	1055.9		1072 [b]

[a] Value from Campbell *et al.* [107], 5.8 K; [b] Value from Tomita *et al.* [112], room temperature.

of the C_{60}^- absorption at 1058.5 nm is $f = 0.022 \pm 0.005$. Previous measurements of the C_{60}^+ oscillator strength [8] give a value which is about one order of magnitude smaller, probably because the reference value of the NIR oscillator strength of C_{60}^- is taken from measurements in a glassy matrix [132], where the absorptions are much broader than in neon matrixes.

NIR spectra of C_{60}^+ and C_{60}^- isolated in solid neon and argon allow the estimation of the gas-phase absorption frequencies (fig. 3.3). In table 3.3 the absorption frequencies in argon and neon matrixes, and the extrapolated gas-phase frequencies of the NIR absorptions of $C_{60}^{+/-}$ are listed.

Compared to direct gas-phase measurements, determined by multiphoton absorption and electron emission of C_{60}^- in a storage ring [112], a shift of almost 20 nm is present for the C_{60}^- value extrapolated from matrix. Also, the trend of the absorption wavelength from argon to neon is contrary to the gas-phase position. Even though the gas-phase absorption measurements were performed at approximately 300 K, temperature effects cannot explain the huge difference of 17 nm. Apparently, the ground state and the first excited state of C_{60}^- experience different distortions from the matrix environment. For C_{60}^-, the gas-phase wavelength of the NIR absorptions cannot be extrapolated from matrix measurements.

In contrast, for C_{60}^+, extrapolation of matrix measurements can reproduce the gas-phase absorption wavelength of helium-tagged cold C_{60}^+ [107] to a high degree, the deviation is below 20 cm^{-1} (0.2%) for all absorptions. However, with a linear extrapolation function, the matrix shift is overcompensated: the absorption wavelength in neon matrixes is closer to the gas phase value than the extrapolated wave-

length. Therefore, C_{60}^{+} absorption wavelengths in matrix and gas phase are used to determine a second-order extrapolation function,

$$\nu_{GP} = \nu_{matrix} + (14 \pm 3)\ {}^{cm^{-1}}/_{\mathring{A}^3}\ \times\ \alpha_{matrix} + (18 \pm 3)\ {}^{cm^{-1}}/_{\mathring{A}^6}\ \times\ \alpha_{matrix}^2$$

with the apsorption frequencies ν in wavenumbers, and the polarizability α_{matrix} of the matrix gas used. This function may help with the extrapolation of NIR gas phase absorption wavelengths for systems similar to C_{60}^{+}. It may however be that there is also a shift in teh gas-phase data due to the He complexation.

While the exact position of gas phase NIR absorptions cannot be determined by extrapolation of matrix absorption frequencies, a very good approximation can be given. This approximation can help with the identification of molecular species generating diffuse interstellar bands, or the design of dedicated gas phase experiments.

In the UV range, the direct measurement of the oscillator strength of $C_{60}^{+/-}$ by annealing the matrix is not possible, because the matrixes always contain neutral C_{60}. The absorptions of the neutral obscure those of $C_{60}^{+/-}$. Additionally, the broad UV features with half-widths of around 3000 cm^{-1} hinder further identification of any single transition, and scattering in the UV complicates the determination of the background signal.

However, as is shown in figure 3.8, by careful subtraction of the contribution of neutral C_{60}, it is possible to estimate the oscillator strength of the 322 nm C_{60}^{+} absorption in a Ne + 1% CO_2 matrix to f =0.3±0.15 , similar to the previously reported value 0.37 for C_{60}^{0} [133]. The oscillator strength of the other absorptions of C_{60}^{+} could not be obtained, they are estimated to be comparable to the values of C_{60}^{0}. A more accurate estimation is prevented by the unknown contribution of scattering in the UV.

TD-DFT calculations predict close-lying electronic transitions in the UV range for $C_{60}^{0/+/-}$, the broad features with half-widths around 3000 cm^{-1} obscure any single transition. Plasmon-like excitations are suggested in the UV range for $C_{60}^{0/+/-}$.

3.2.2 Di- and Trications of C_{60}

The reactivity of fullerene C_{60} multications has been studied in gas phase using mass-spectroscopic methods[134]. In the condensed phase, only the preparation of a fullerenium (2+) ionic salt is reported [135]. No vibrational or electronic spectra of the reactive $C_{60}^{2+/3+}$ species have been reported, except for the measurements presented in this work [136].

C_{60} di- and trications are produced by electron impact ionization. The ion current for the di- and trications is 40 nA and 10 nA, respectively. Compared to C_{60}^+, the number of ions in the ion beam is $1/10$ and $1/50$. Due to the capture of secondary electrons, $C_{60}^{2+/3+}$ can only be investigated in matrixes containing electron scavengers. The region between 800 and 600 cm^{-1} is dominated by strong absorptions of CO_2 or CCl_4, hindering the identification of $C_{60}^{2+/3+}$ absorptions possibly present.

The high electron affinity of C_{60}^{3+}, leading to electron transfer from CO_2 and CCl_4 and the formation of C_{60}^{2+}, prevents accumulation of large amounts of this species in neon (experimental ionization energies: C_{60}: 7.6 eV (first), 11.4 eV (second), 16.6 eV (third) [137]; CO_2: 13.8 eV; CCl_4: 11.5 eV; Ne: 21.56 eV [138]).

Spectra are measured in the UV-vis (200 - 1100 nm) and the IR (4000 - 400 cm^{-1}). Due to the extensive change in the experimental setup required,[4] no FIR measurements were performed with matrixes containing fullerene C_{60} multications.

Results

Vibrational Spectra

After depositing C_{60}^{2+} into Ne + 0.15 % CCl_4 and Ne + 1% CO_2 matrixes, the characteristic absorptions of matrix isolated C_{60}^+ are observed due to electron capture of C_{60}^{2+} during deposition. Several previously not observed features are present. A detail of the mid-IR spectra is shown in figure 3.9. Additional absorption features are identified as C_{60}^{2+} absorptions by comparison with C_{60}^+ spectra from Ne + 0.15% CCl_4 and Ne + 1% CO_2 matrixes.

Electron capture of C_{60}^{3+} during deposition prevents the accumulation of sufficient C_{60}^{3+} to measure the IR absorptions of this species. Matrixes prepared from depositing C_{60}^{3+} result in IR spectra containing primarily C_{60}^{2+} and weak C_{60}^+ features. Therefore, no IR features of C_{60}^{3+} are identified.

Electronic Spectra

NIR absorption spectra are measured after deposition of C_{60}^{2+} or C_{60}^{3+} into Ne + 1% CO_2 and Ne + 0.15% CCl_4 matrixes. From IR measurements, the electron capture of the deposited ions is verified: Matrixes from deposition of C_{60}^{2+} contain additional C_{60}^+, matrixes from deposition of C_{60}^{3+} also contain C_{60}^{2+} and C_{60}^+. Traces of neutral

[4] The optical UHV windows have to be exchanged, which requires baking of the chamber, readjusting the FTIR spectrometer, and producing a new sample, while no mid-IR spectra can be measured at the same time. This cumbersome change of the measurement range was only performed for C_{60}^+, whose FIR absorptions are of special interest for astronomers.

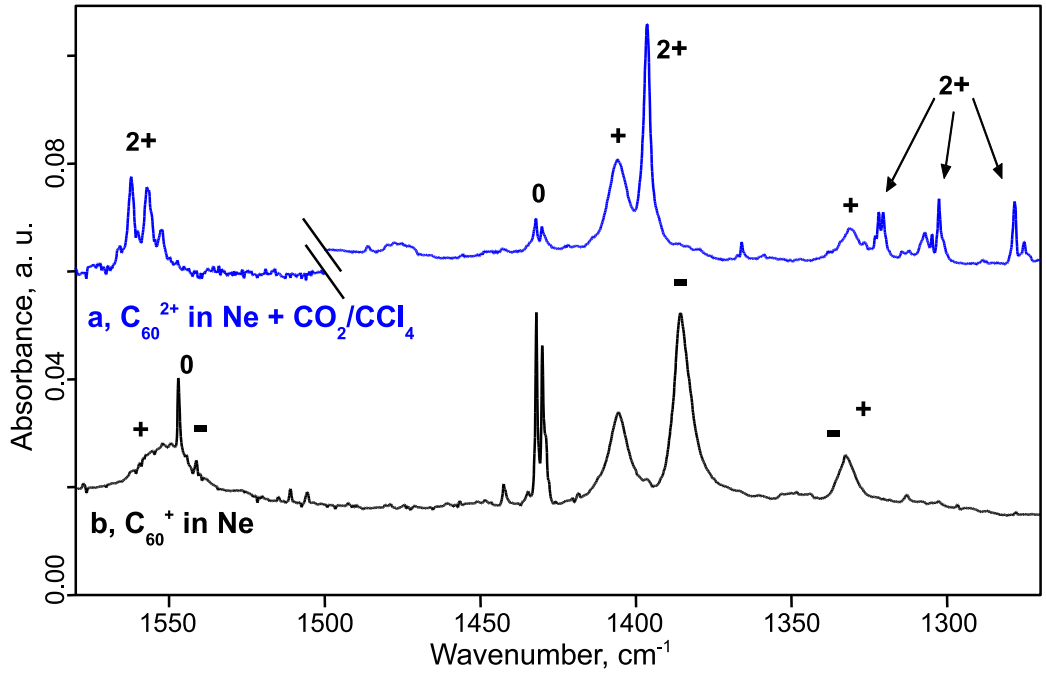

Figure 3.9: Detail of the mid-IR spectrum of $C_{60}^{0/-/+/2+}$. (a) C_{60}^{2+} co-deposited with Ne + 1% CO_2 (left region) and Ne + 0.15% CCl_4 (right). (b) C_{60}^{+} co-deposited with Ne. Spectra are scaled to similar absorption intensities at 1405 cm^{-1} (C_{60}^{+}). The spectrum of C_{60}^{2+} is reassembled in a way to exclude strong absorptions of CO_2 and CCl_4.

C_{60} and C_{60}^- can be found in all matrixes studied. In the NIR, neutral C_{60} does not exhibit any absorptions.

As shown in figure 3.10, in matrixes of C_{60}^{2+} in Ne + 1% CO_2 and Ne + 0.15% CCl_4, only the well-known absorption features of C_{60}^+ and some traces of C_{60}^- are observed in the spectrum, no additional absorptions of C_{60}^{2+} are detected. In matrixes containing C_{60}^{3+}, new absorptions are present at 899 nm and 857 nm in both Ne + 1% CO_2 and Ne + 0.15% CCl_4 matrixes. While no IR features of C_{60}^{3+} are identified, electronic transitions in the NIR are typically about three to four orders of magnitude stronger than vibrational transitions. NIR absorptions of low concentrations of C_{60}^{3+} are therefore detectable, although IR features are below the detection limit of the experimental setup.

Discussion

Vibrational Spectra

The identified IR absorptions of C_{60}^{2+} are listed in table 3.4. For comparison with DFT calculations, the IR spectrum of C_{60}^{2+} is extracted by substituting the regions between identified absorptions with zero base lines, while the frequency, intensity, linewidth, and splitting of the absorptions remains unchanged. The extracted spectrum is shown in figure 3.11.

The experimental integrated molar absorptivities of C_{60}^{2+} IR absorptions are estimated by two different approaches. First, the total amount of deposited C_{60}^{2+} is estimated from the integrated ion current and corrected for the charge state. The second approach is to use the absorption intensity of the $CCl_3 \cdot\cdot Cl^-$ counterions [67], estimated from samples of C_{60}^+ in Ne + 0.15% CCl_4, and known absorptivity values for C_{60}^+, to approximate the total charge present in the matrix. Both approaches lead to roughly the same values of the integrated molar absorptivity of C_{60}^{2+}, the overall accuracy is estimated to be approximately $\pm$ 40%.

RI-DFT calculations (Turbomole [33], BP86/def2-SV(P)) are performed for C_{60}^{2+} in singlet (D_{5d} symmetry) and triplet state (D_{5d} and C_1 symmetry). As shown in figure 3.11, the experimental IR frequencies are reproduced to within 2% by a D_{5d} singlet ground state. The calculated absorption intensities overestimate the absorptivity of all identified IR features. The D_{5d} singlet ground state is also confirmed by NIR measurements. The calculated triplet states show no agreement with the experiment.

Comparison of the broadness of the IR absorption features from C_{60}^+ and C_{60}^{2+} shows that C_{60}^{2+} features are generally narrower than those of C_{60}^+ in the same spectral region. Additionally, C_{60}^{2+} features often exhibit partially resolved fine structure due to multiple matrix sites, seen for example for the absorptions at 1562.1 , 1320.6 , 1302.7 , and 1232.3 cm^{-1}, whereas C_{60}^+ generally exhibits broad features without

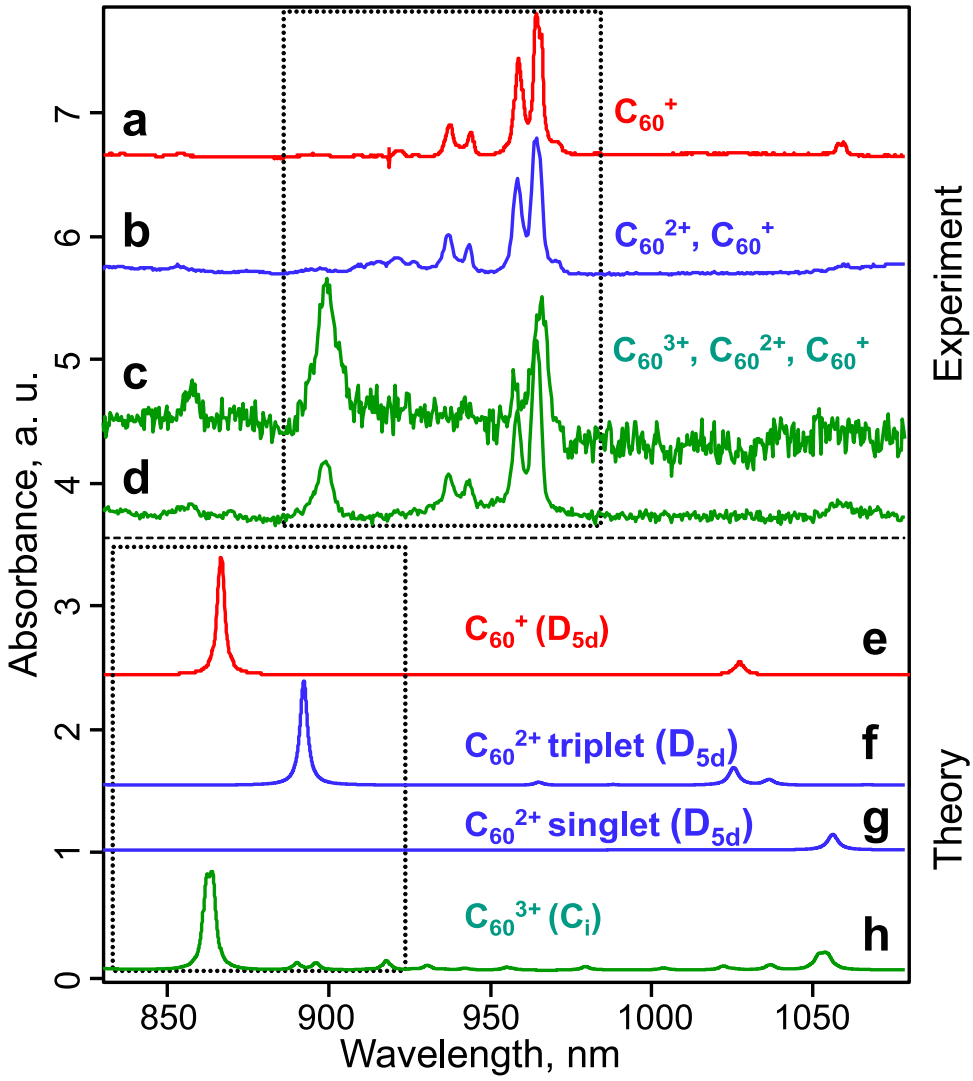

Figure 3.10: NIR absorptions of $C_{60}^{+/2+/3+}$: (a) C_{60}^{+} deposited in Ne + 0.15% CCl_4; (b) C_{60}^{2+} deposited in Ne + 0.15% CCl_4, in the IR C_{60}^{2+} and C_{60}^{+} are identified; (c) C_{60}^{3+} deposited in Ne + 1% CO_2; (d) C_{60}^{3+} deposited in Ne + 0.15% CCl_4. TD-DFT calculations of $C_{60}^{+/2+/3+}$: (e) singlet C_{60}^{+} (D_{5d}); (f) triplet C_{60}^{2+} (D_{5d}); (g) singlet C_{60}^{2+} (D_{5d}); (h) doublet C_{60}^{3+} (C_i). Experimental intensities are scaled for similar C_{60}^{+} absorbance, calculated frequencies are unscaled.

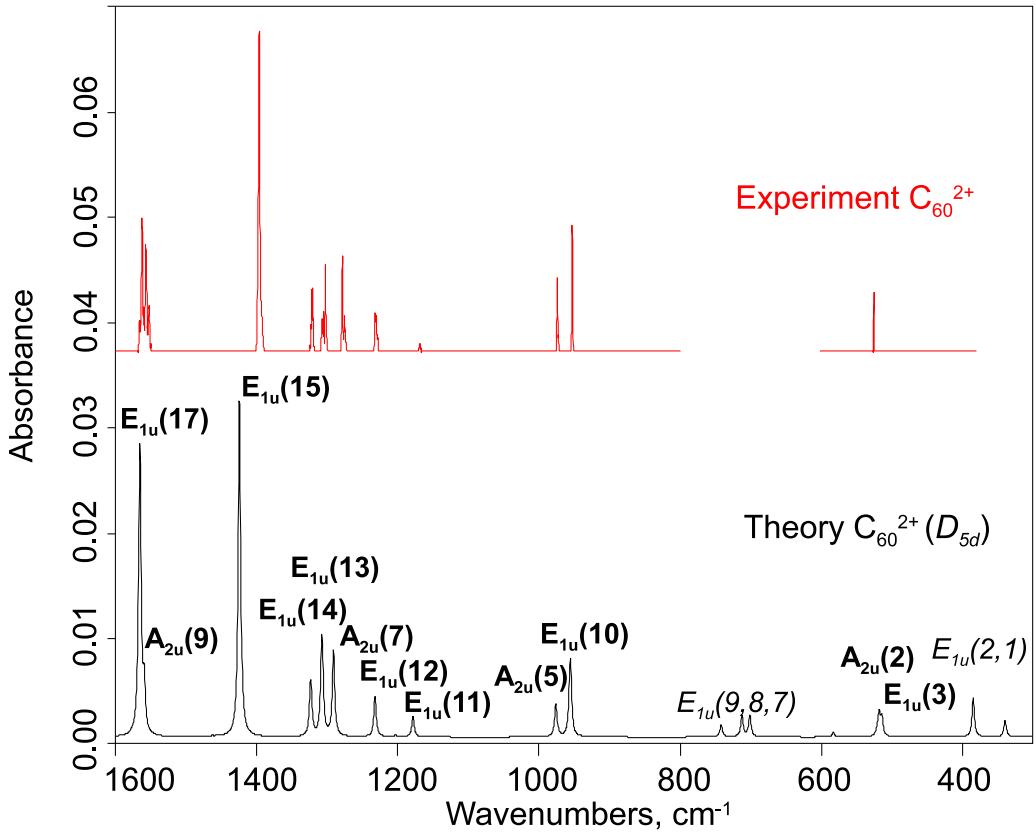

Figure 3.11: Extracted experimental IR spectrum of C_{60}^{2+} in neon (top) and simulated spectrum for DFT calculations of singlet C_{60}^{2+} (D_{5d}) (bottom). Calculated frequencies are unscaled. Dipole allowed vibrational normal modes, not observed in the experimental data are labeled in italics.

fine structure in the range from 1600 to 800 cm^{-1}. The four T_{1u} absorptions of neutral C_{60} exhibit sharp features with fine structure due to matrix sites as well. The slow relaxation of the vibrational excitations suggests a weak electron-vibration coupling in C_{60}^{2+}.

Experimental and calculated frequency, *fwhm*, and integrated molar absorptivity values of C_{60}^{2+} IR absorption features are summarized in table 3.4. For absorption features exhibiting a fine structure, the frequency ν of the most intense line is set in italics, the *fwhm* is also measured at these lines. The experimental integrated molar absorptivity in neon matrixes A_{Ne} at 5 K is derived from all absorption features. For some lines (1562.1 cm^{-1} and 525.7 cm^{-1}), it is not possible to assign specific normal vibration modes due to multiple absorption features and close-lying theoretical vibration modes.

Electronic Spectra

TD-DFT calculations of electronically excited states are performed for C_{60}^{2+} in singlet and triplet state with D_{5d} symmetry, and for C_{60}^{3+} in doublet state with C_i symmetry. The experimental and the calculated spectra are shown in figure 3.10. For triplet C_{60}^{2+} and doublet C_{60}^{3+}, strong electronic transitions are predicted close to the calculated transition of C_{60}^{+}. For singlet C_{60}^{2+}, no strong electronic transition in the NIR range is predicted. Experimentally, no NIR absorptions are detected for C_{60}^{2+}, therefore a singlet D_{5d} ground state is assigned in agreement with IR measurements.

For C_{60}^{3+}, the stronger absorption at 899 nm is assigned to the band origin of the $^2A_g \leftarrow 1^2A_u$ transition. The energy difference to the second absorption of 545 cm^{-1} is well within the range of radial vibrations of the fullerene cage. Therefore, the 857 nm absorption is assigned as a vibronic feature of the $^2A_g \leftarrow 1^2A_u$ transition at 899 nm.

The gas phase absorption wavelengths of the NIR absorptions of C_{60}^{3+} are estimated using the extrapolation function derived from the matrix shift of the C_{60}^{+} NIR absorptions (see page 44). The extrapolated gas phase wavelengths is shifted to higher energies, the absorptions of C_{60}^{3+} are expected at 898.3 and 856.4 nm. Verification of the extrapolated wavelengths is not possible, neither gas-phase nor argon matrix data is available.

The oscillator strength of the NIR absorptions of C_{60}^{3+} in Ne + 0.15% CCl_4 matrixes at 5 K is estimated. Assuming, that the overall charge of the matrix is zero, and from the known absorptivities of C_{60}^{+}, C_{60}^{2+}, and the $CCl_3 \cdot\cdot Cl^-$ counterion, the amount of C_{60}^{3+} in the matrix can be approximated. From comparison of the NIR absorptivity of C_{60}^{+} and C_{60}^{3+}, the oscillator strength of C_{60}^{3+} absorptions is estimated to be $f = 2\times10^{-3}$ for the 899 nm feature and $f = 4\times10^{-4}$ for the 857 nm feature. The error of the oscillator strength is estimated to be 50%, due to the imprecise determination of the C_{60}^{3+} amount in the matrix.

Table 3.4: Assignment of experimentally identified singlet C_{60}^{2+} (D_{5d}) absorption features by comparison to DFT calculations: frequency ν, full width at half maximum (fwhm) and integrated molar absorptivity A_{Ne} in neon matrix at 5 K, calculated frequency and integrated molar absorptivity A_{calc}.

	experiment			*theory*	
mode	ν [a], cm^{-1}	fwhm [b], cm^{-1}	A_{Ne}, $km \cdot mol^{-1}$	ν, cm^{-1}	A_{calc}, $km \cdot mol^{-1}$
$E_{1u}(17)$; $A_{2u}(9)$[c]	1565.5; *1562.1*; 1559.9; 1556.7; 1552.5	1.2	45±18	1565.5; 1559.3	160; 25.5
$E_{1u}(15)$	1396.4	3.8	50±20	1424.1	188
$E_{1u}(14)$	1323.1; 1322.6 *1320.6*	1.2	8±3	1323.2	30.7
$E_{1u}(13)$	1307.3; 1304.8; *1302.7*	1.1	12±5	1307.2	56
$A_{2u}(7)$	*1278.3*; 1275.2	1.4	11±4	1291.0	47.7
$E_{1u}(12)$	*1232.3*; 1230.6; 1228.5	1.2	7±3	1232.0	22.4
$E_{1u}(11)$	1168.9	1.9	1±0.5	1178.2	11.3
$A_{2u}(5)$	*974.1*; 972.7	1.4	5±2	976.2	18.3
$E_{1u}(10)$	*952.9*; 951.7	1.2	8±3	955.7	43.8
$A_{2u}(2)$; $E_{1u}(3)$ [c]	525.7	0.6	2±1	518.1; 514.2	12.2 10.3

[a] For site effects or other distortions in Ne matrix, the most intense line is in italics; [b] *fwhm* of the most intense absorption line; [c] The specific normal vibrational mode could not be assigned.

Spectra of matrixes containing C_{60}^{2+} and C_{60}^{3+} measured in the UV range do not exhibit any specific features that can be attributed to these ions. Similar to $C_{60}^{+/-}$, the spectra in the range from 200-500 nm are almost identical to the spectra recorded of matrixes containing only neutral C_{60}. The same effect can be observed in TD-DFT calculations, close-lying electronic transitions are predicted for all species. The broadness of the features with *fwhm* of around 3000 cm^{-1} hinders further differentiation of the absorptions. As for the other charge states of C_{60} studied in this work, a plasmon-like excitation of the delocalized electrons is suggested for $C_{60}^{2+/3+}$.

3.2.3 Summary

Electronic and vibrational spectra of neutral C_{60}, C_{60}^{-}, C_{60}^{+}, C_{60}^{2+}, and C_{60}^{3+} isolated in low temperature matrixes were recorded.

The previously measured data of C_{60}^{+} and C_{60}^{-} in neon and argon matrixes [108, 8] and of C_{60}^{-} in gas phase [111, 112] was reproduced and expanded into the FIR and UV-vis ranges. The integrated molar absorptivities were measured in the FIR to UV-vis range for C_{60}^{+} and the FIR to NIR range for C_{60}^{-}. From comparison of the experimental data and DFT calculations a D_{5d} ground state for C_{60}^{+} and a D_{3d} ground state for C_{60}^{-} was established.

For C_{60}^{2+}, optical spectra were recorded for the first time. In the IR, several vibrations were identified and the integrated molar absorptivities were estimated. From comparison with DFT calculations in the IR and NIR, a D_{5d} singlet ground state was established for C_{60}^{2+}.

Charge transfer from the electron scavengers prevented the accumulation of sufficient amounts of C_{60}^{3+} for identification in the IR range. In the NIR, for the first time the $^2A_g \leftarrow 1^2A_u$ transition at 899 nm and a vibronic sideband at 857 nm from a C_i doublet ground state were observed. The integrated molar absorptivity of the identified features was estimated. The determined NIR absorptions may be of interest for the identification of carriers of diffuse interstellar bands.

The apparent similarity of the UV spectra of different charge states of C_{60} was rationalized by plasmon-like excitations. These results were supported by TD-DFT calculations, yielding similar electronic transitions in the UV range independent of the charge of the C_{60} molecule.

The overall fit of DFT calculations for vibrational and electronic transitions in respect to position and intensity suggests that C_{60} and the studied ions show no strong non-Born-Oppenheimer effects.

A comparison of the extracted IR spectra of C_{60}^{0}, C_{60}^{+}, C_{60}^{-}, and C_{60}^{2+} is shown in figure 3.12, the NIR absorptions of C_{60}^{+}, C_{60}^{-}, and C_{60}^{3+} are compared in figure 3.13.

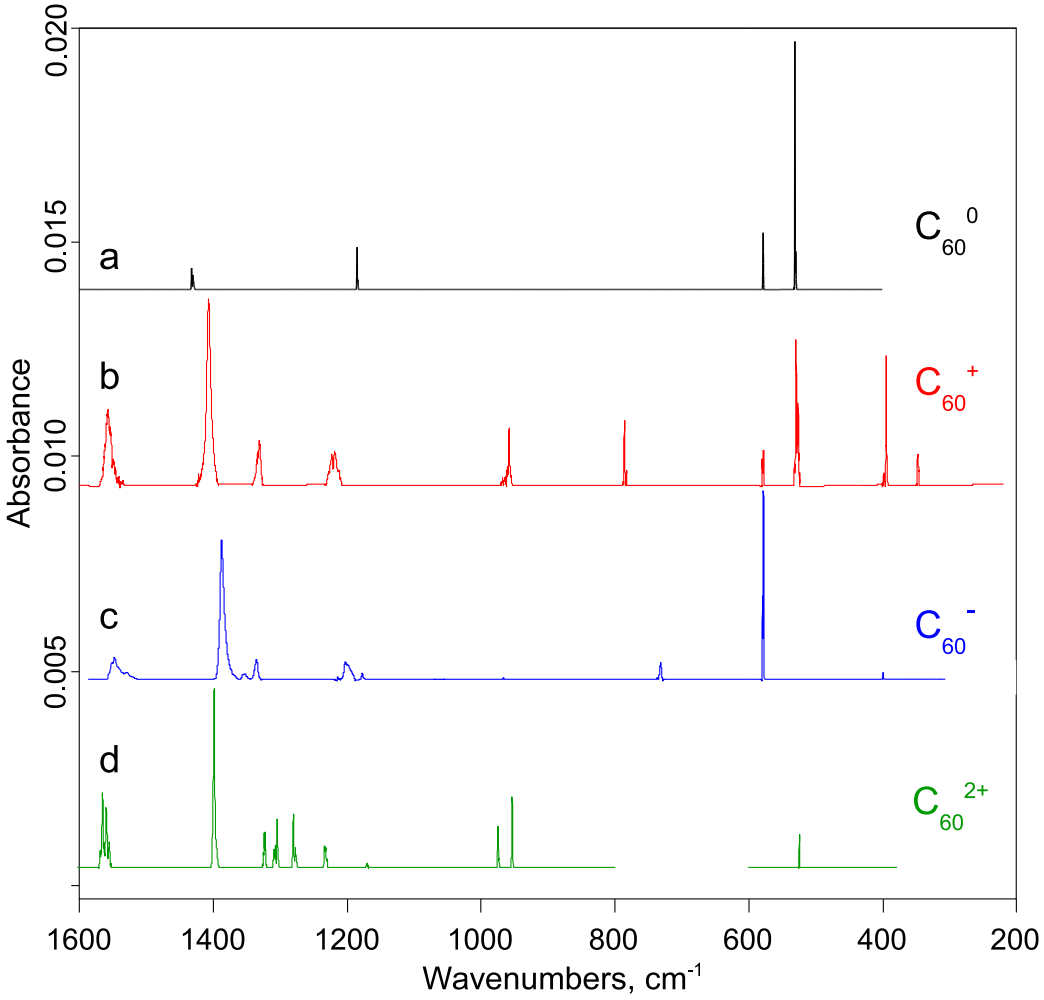

Figure 3.12: Comparison of the extracted experimental IR spectra of matrix isolated C_{60}^{0} (a), C_{60}^{+} (b), C_{60}^{-} (c), and C_{60}^{2+} (d). The spectra are scaled for similar intensities. For C_{60}^{3+}, no IR absorptions were observed.

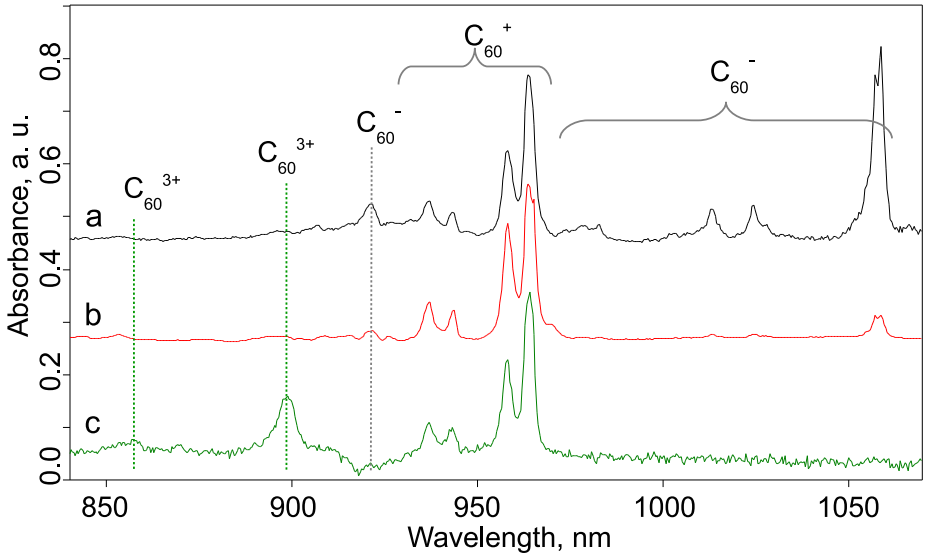

Figure 3.13: Comparison of the experimental NIR absorptions of $C_{60}^{+/-}$ in Ne (a), C_{60}^{+} in Ne + 0.15% CCl_4 (b), and $C_{60}^{+/3+}$ in Ne + 0.15% CCl_4 (c). Spectra are scaled for similar intensity of the C_{60}^{+} absorption. For C_{60}^{0} and C_{60}^{2+}, no NIR absorptions were detected.

The absorption frequencies of matrix isolated species were in good agreement with gas-phase emission and absorption frequencies, suggesting only a small influence of the matrix. Many of the identified absorptions have not previously been measured in gas phase. The frequencies and intensities of these transitions in gas phase can be estimated reasonbly well by linear (IR) or non-linear (NIR) extrapolation. The values obtained in neon matrix measurements provide a good first order prediction of the gas-phase values, in particular for cations. Due to the small shift in absorption frequency from neon matrixes to gas phase [43], the measured results can be used for the identification of C_{60} cations in space in the IR [127, 128] and their contribution to diffuse interstellar bands [107] and UV absorptions in space [139, 140].

3.3 C_{70} and its Ions

Similar to C_{60}, C_{70} has been the subject of extensive theoretical and experimental investigations. Its first detection [90] and extraction from carbon soot [93] was achieved together with C_{60}.

The structure of C_{70} is similar to C_{60}, with additional six-membered rings and a lowered symmetry (D_{5h}). A schematic drawing of C_{70} with the ten additional carbon atoms, forming five extra hexagon rings, is shown in figure 3.14. The pentagon rings are isolated from each other, making C_{70} chemically inert.

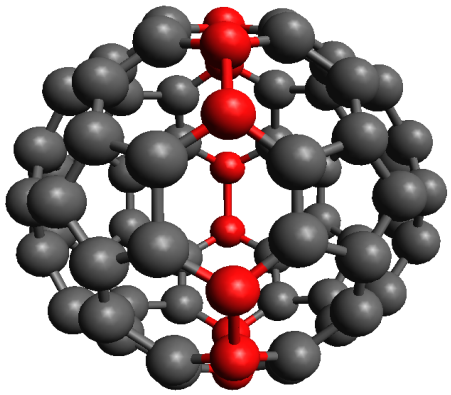

Figure 3.14: The structure of C_{70}. The ten atoms additional to the C_{60} molecule, forming five extra hexagons, are marked in red.

As is the rule for different fullerene species, C_{60} and C_{70} strongly differ in their electronic properties. For example, no superconducting phase of alkali metal intercalated C_{70} has been identified. In organic photovoltaics, C_{70} is used as electron transporter and acceptor due to its higher absorptivity in the visible range compared to C_{60} [141]. Addition of organic substituents further improves the characteristics of solar cells containing C_{70} by modifying the electron affinity.

C_{70} was identified in IR emission spectra together with C_{60} in 2010 [102]. To date, it is the largest molecule identified in space. No observation of C_{70}^{+} in IR emission or visible absorption spectra of astronomical objects has been reported.

Neutral C_{70} was studied in the gas phase by IR emission spectroscopy [124], and by absorption spectroscopy [142]. In the UV range, its spectra were measured from thin films and solution [114]. The integrated molar absorptivity of C_{70} in KBr pellets was measured for the most intense absorptions [119].

The electronic transitions of $C_{70}^{+/-}$ were studied in organic solvents, glasses, and cryogenic matrixes. Most of these experiments focused on the NIR region, where strong absorptions of C_{70}^{-} are present at 1363 nm [143, 9].

In the infrared range, C_{70}^{-} was studied in organic solvents, where it is formed by charge transfer [144]. A strong interaction of the fullerene anion with the solvent has to be assumed. For C_{70}^{+}, no IR spectroscopy measurements have been reported.

C_{70}^{2+} was studied by mass spectrometry. From electron impact ionization, the second ionization energy of C_{70} was measured to be 11.36 eV [145]. No optical spectroscopy measurements of C_{70}^{2+} have been reported in the literature.

3.3.1 Neutral and Monoionic C_{70}

C_{70} cations are produced by electron impact ionization, the setup is described in detail in chapter 2.2.3. For the experiments with mass selected ions, a current of 80 nA can be achieved. C_{70}^+ ions are co-deposited onto the gold coated sapphire substrate, which is held at approximately 5 K, with an excess of matrix gas. Deposition time for all samples is around one day, resulting in roughly 10 nmol of deposited ions in a spot size of approximately 1 cm diameter.

During deposition, the matrixes are neutralized by electron capture of the deposited C_{70}^+, resulting in the formation of neutral C_{70} and anionic C_{70}^-. In matrixes formed from Ne + 1% CO_2 or Ne + 0.15% CCl_4 as electron scavengers, the formation of neutral and anionic C_{70} is suppressed. Two different electron scavengers are used because their infrared absorptions, obscuring some regions of the spectrum, only coincide in small wavelength regions. The spectrum of neutral C_{70} is measured after direct deposition of C_{70} from a Knudsen cell without mass selection.

Annealing of the matrixes leads to neutralization of the ionic species and allows for an estimation of the integrated molar absorptivities. From measurements of the absorption wavelengths in neon and argon matrixes, the gas-phase values are estimated by linear extrapolation. Measurements are performed in the IR range from 4000 to 400 cm^{-1}, and in the UV-vis range from 250 to 1100 nm.

Results

Vibrational Spectra

IR spectra of matrixes containing only neutral C_{70} show the well-known IR absorptions of C_{70} [142]. In comparison to C_{60}, the number of vibrational modes is increased because of the additional atoms and the reduced symmetry of C_{70} (D_{5h}). Therefore the IR spectrum of C_{70} exhibits more absorptions than the highly symmetric C_{60} (I_h). The assignment of the most intense absorptions according to DFT calculations, their frequencies and integrated molar absorptivities in neon matrixes, as well as the calculated frequencies and integrated molar absorptivites are listed in table 3.5.

After deposition of mass selected C_{70}^+ into neon matrixes, absorptions of C_{70}^+ and C_{70}^- are present, as well as absorptions from neutral C_{70}. The addition of the electron scavenger CO_2 or CCl_4 to the matrix gas allows for the differentiation of absorptions of C_{70}^+ and C_{70}^-. No IR spectra of matrix isolated ions of C_{70} have been reported in the literature.

In contrast to the spectra of the ions of C_{60}, where the ionic absorptions exhibit a typical *fwhm* of less than 5 cm^{-1}, the absorption features of C_{70}^+ and C_{70}^- are generally broader, with a typical *fwhm* of 10 cm^{-1} or more, with only some sharp features.

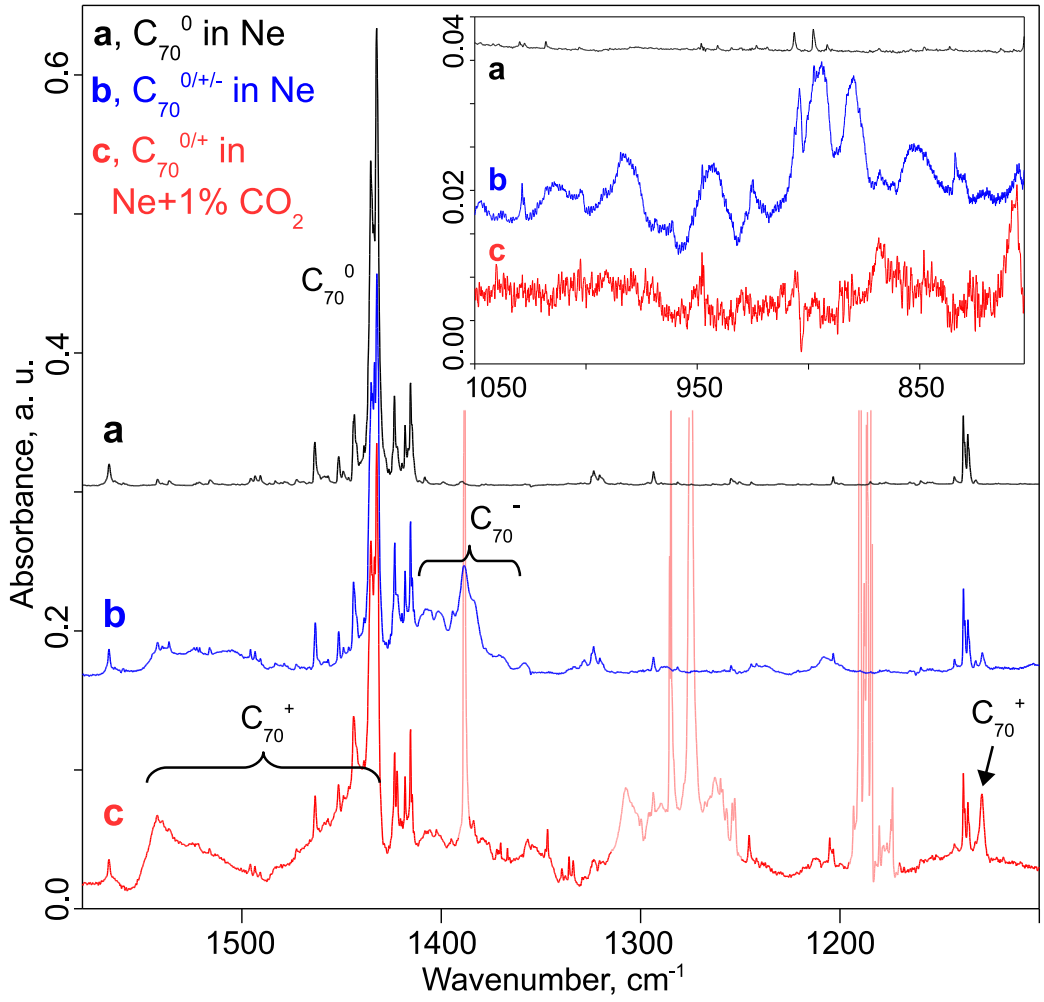

Figure 3.15: Mid-IR spectra of matrix isolated $C_{70}^{0/+/-}$. (a) Neutral C_{70} in Ne, (b) $C_{70}^{0/+/-}$ in Ne, (c) $C_{70}^{0/+}$ in Ne + 1% CO_2. The inset shows a region, where broad overlapping absorptions of C_{70}^{-} are present. Absorptions of CO_2 are shown in reduced contrast. The spectra are scaled for similar intensity of the neutral absorptions.

Table 3.5: Assignment of the most intense absorption lines of neutral C_{70} by comparison to DFT (D_{5h} singlet): experimental frequency, full width at half maximum (*fwhm*) and integrated molar absorptivity A_{Ne} in neon matrix at 5 K, calculated frequency and integrated molar absorptivity A_{calc}.

	experiment			*theory*	
mode	ν, cm^{-1}	*fwhm*, cm^{-1}	A_{Ne}, $km \cdot mol^{-1}$	ν, cm^{-1}	A, $km \cdot mol^{-1}$
$E_1'(21)$	1566.4	1.7	3.2±0.3	1555.6	3.7
$A_2''(9)$	1463.2	1.5	5.6±0.5	1477.5	11.4
$E_1'(19)$	1435.1; *1432.3* [a]	1.9	126±12	1446.2	169.4
$E_1'(18)$	1415.4	1.1	11±1	1417.8	5.3
$A_2''(6)$	*1138.1*; 1135.7 [a]	1.3	8.9±0.7 [b]	1141.6	9.9
$E_1'(13)$	1088.3	2.1	2.2±0.2	1088.9	3.1
$E_1'(10)$	799.5	0.6	9±1	706.7	5.4
$E_1'(8)$	677.5	0.9	16±2	654.6	12.7
$E_1'(7)$	644.3	0.6	6.5±0.6	628.1	10.6
$A_2''(3)$	580.7	0.7	20±2	563.8	16.4
$E_1'(6)$	565.7	1.1	7±1	557.2	18.4
$E_1'(5)$	536.1	0.7	21±2	530.9	37.4
$A_2''(2)$	458.6	0.9	8±1	446.6	7.7

[a] Site effect in Ne matrix, strongest absorption set in italics, *fwhm* of strongest feature; [b] The value was taken from Iglesias-Groth *et al.* [119].

The overlap of some features complicates the identification and assignment of the absorptions. In figure 3.15 the spectra of neutral C_{70} in Ne, and of C_{70}^+ deposited neon and Ne + 1% CO_2 are shown. In the inset, broad absorptions of C_{70}^- in the 1100 - 800 cm^{-1} range are shown.

After deposition of C_{70}^+ into pure argon matrixes, almost all absorptions of C_{70}^0, C_{70}^+, and C_{70}^- identified in neon matrixes, are also present. The spectra in two IR regions are shown in figure 3.16. As for C_{60} and its ions, the interaction with argon leads to small shifts in the absorption frequencies. Typically, the absorptions in argon are even broader than in neon matrixes. By extrapolation of the matrix shift, the gas-phase absorption frequencies of C_{70} and its ions are estimated. Absorption frequencies from argon and neon matrixes, and the extrapolated gas-phase values are listed in table 3.6.

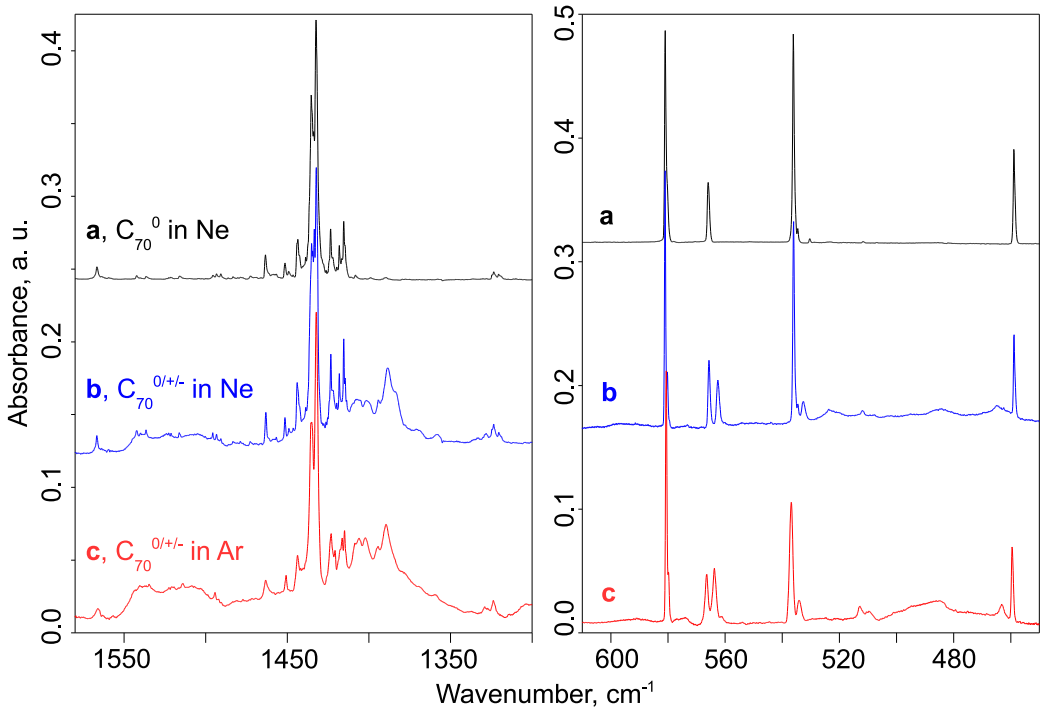

Figure 3.16: Detail of the absorptions of $C_{70}^{0/+/-}$ in Ne and in Ar matrixes. (a) Neutral C_{70} in Ne, (b) $C_{70}^{0/+/-}$ (as deposited) in Ne, (c) $C_{70}^{0/+/-}$ (as deposited) in Ar. A small shift and broadening of the absorptions is observed in Ar matrixes. The spectra are scaled for similar intensity of the C_{70}^{0} absorptions.

Electronic Spectra

The known electronic absorption spectrum of C_{70} isolated in neon matrixes [9] was obtained by deposition of neutral C_{70}. Below 570 nm, it is defined by a well-resolved vibronic structure and sharp and well-defined peaks up to approximately 700 cm^{-1} above the band origin, as well as further, broader features to the blue.

Deposition of mass-selected C_{70}^+ into neon matrixes gives rise to additional absorptions in the 645-800 nm range (fig. 3.20). Two broad and overlapping features can be distinguished. The first feature lies in the range from 690-800 nm, it has a rich vibrational structure and a band origin at 798 nm. The second feature lies in the range from 645-715 nm and does not exhibit clear vibrational features. In matrixes containing electron scavengers, these absorptions gain in relative intensity, with the exception of one sharp feature at 773.5 nm. Therefore, the two broad features are assigned as C_{70}^+ absorptions. The assignment of the first absorption region is in agreement with previous measurements [9], except that one prominent feature at 705.8 nm is missing in our spectrum. The second absorption feature in the 645-715 nm range has not been previously reported in the literature. The previously reported broad absorption of C_{70}^- at 1363 nm [9, 143] could not be detected with the measurement setup due to spectral limitations of the detector used. In the UV range, matrixes containing a mixture of C_{70}^0, C_{70}^+ and C_{70}^- do not show additional absorptions compared to matrixes containing only neutral C_{70}. UV-vis spectra of matrixes containing $C_{70}^{0/+/-}$ are shown in figure 3.20.

Discussion

Vibrational Spectra

To facilitate the identification of ionic absorptions and the comparison to DFT calculations, the absorptions of C_{70}^+ and C_{70}^- have been extracted by subtracting the (scaled) neutral or the neutral and cationic absorptions, respectively. The resulting difference spectra and the identified absorptions of C_{70}^+ and C_{70}^- are shown in figures 3.17, 3.18 (C_{70}^+), and 3.19 (C_{70}^-). The strong absorptions from the electron scavengers are shown in reduced contrast. For C_{70}^+, 9 absorption features are identified. The asymmetric shape of the absorptions at 1445 and 1542 cm^{-1} suggests several overlapping broad features.

The ionic absorptions of the fullerene C_{60} show a dynamic Jahn-Teller distortion above approximately 1000 cm^{-1}, resulting in a broadening of the absorption features. C_{70}^+ shows the same behavior. While the low energy absorption features below 550 cm^{-1} have a *fwhm* of below 3 cm^{-1}, most vibrational modes at higher energies show a halfwidth of 10 cm^{-1} or more.

Table 3.6: Absorption lines of neutral C_{70} in argon and neon matrixes at 5 K: frequency ν_{Ar} and ν_{Ne}, full width at half maximum (*fwhm*) in argon matrixes, extrapolated and measured gas phase values and deviation Δ of the extrapolation.

	matrix isolation			*gas phase*		
mode	ν_{Ar}, cm^{-1}	*fwhm* (Ar), cm^{-1}	ν_{Ne}, cm^{-1}	extrapolated, cm^{-1}	measured [a], cm^{-1}	Δ, cm^{-1}
$E_1'(21)$	1566.1	2.8	1566.4	1566.5		
$A_2''(9)$	1463.3	2.5	1463.2	1463.2		
$E_1'(19)$	1435.2; *1432.3* [b]	2.2	1435.1; *1432.3* [b]	1432.3	1432.0	0.3 (0.0%)
$E_1'(18)$	1414.9	0.9	1415.4	1415.6		
$A_2''(6)$	*1138.8*; 1136.1 [b]	1.3	*1138.1*; 1135.7 [b]	1137.9	1144.1	6.2 (0.5%)
$E_1'(13)$	1088.9	2.3	1088.3	1088.1	1099.6	11.5 (1.1%)
$E_1'(10)$	798.9	0.8	799.5	799.7	793.3	6.6 (0.8%)
$E_1'(8)$	677.1	1.2	677.5	677.6		
$E_1'(7)$	644.1	0.8	644.3	644.4	638.5	5.9 (0.9%)
$A_2''(3)$	580.6	0.8	580.7	580.7	583.1	2.4 (0.4%)
$E_1'(6)$	566.4	1.2	565.7	566.1	567.7	1.6 (0.3%)
$E_1'(5)$	536.8	1.5	536.1	535.9	545.0	9.1 (1.7%)
$A_2''(2)$	459.5	1.0	458.6	458.3		

[b] Emission wavelength reported from Nemes *et al.*, extrapolated to 0 K [124]; [b] Site effect in Ar and Ne matrixes, the most intense line is set in italics.

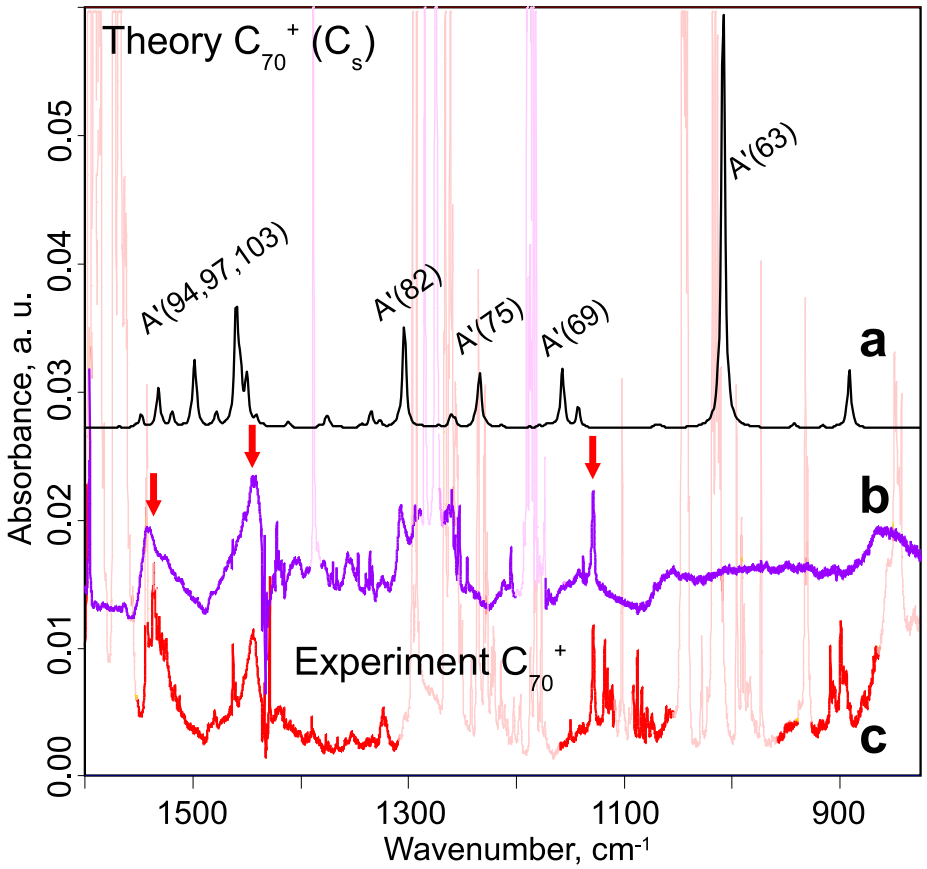

Figure 3.17: Comparison of the calculated spectrum of C_{70}^+ (C_s symmetry) (a) to the difference spectra of C_{70}^+ in Ne + 1% CO_2 (b) and in Ne + 0.15% CCl_4 (c) matrixes. The identified absorptions of C_{70}^+ are marked with red arrows, strong absorptions of the electron scavengers are shown in reduced contrast. Details see text.

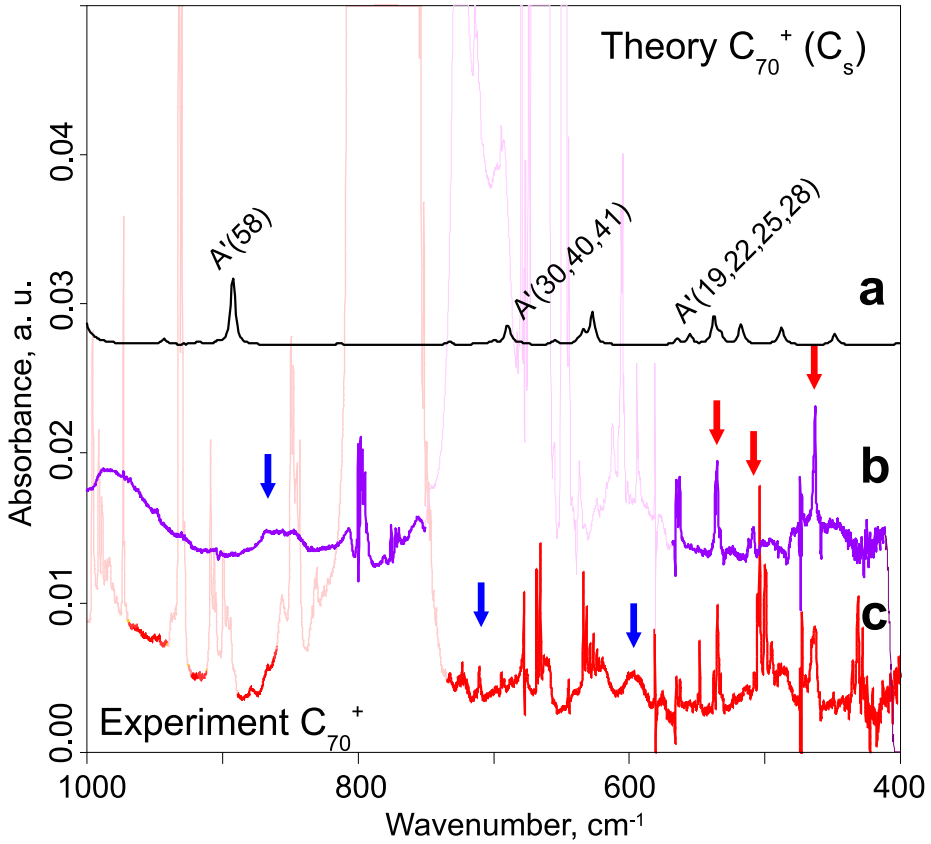

Figure 3.18: Comparison of the calculated spectrum of C_{70}^+ (C_s symmetry) (a) to the difference spectra of C_{70}^+ in Ne + 1% CO_2 (b) and in Ne + 0.15% CCl_4 (c) matrixes. The identified absorptions of C_{70}^+ are marked with red arrows, suspected absorptions with blue arrows. Strong absorptions of the electron scavengers are shown in reduced contrast. Details see text.

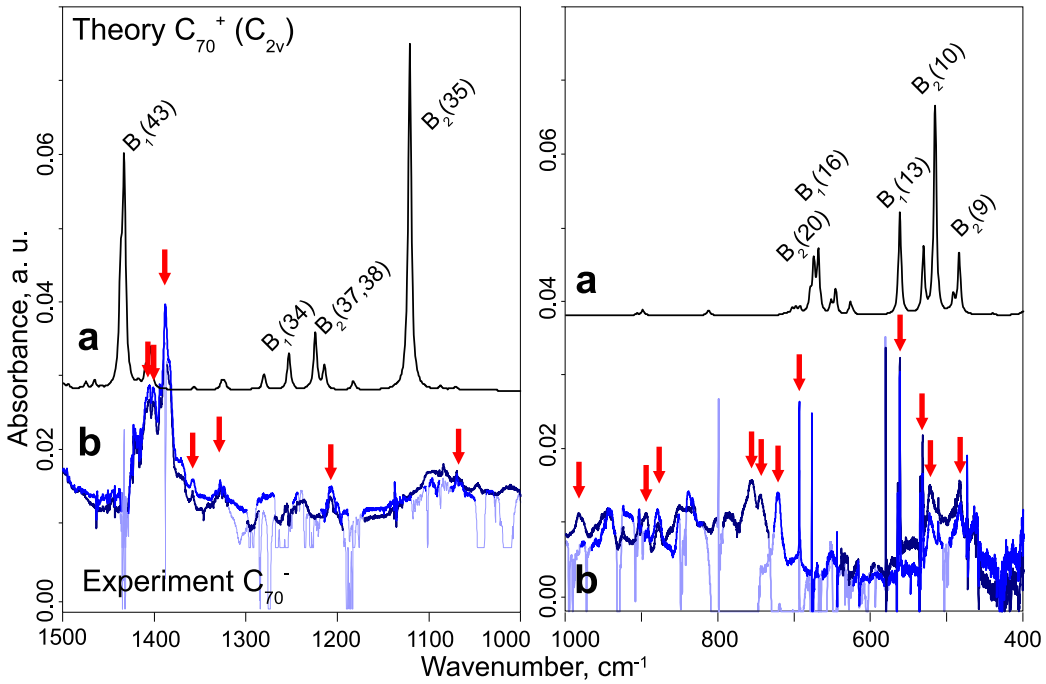

Figure 3.19: Comparison of the calculated spectrum of C_{70}^- (C_{2v} symmetry) (a) to the difference spectra of C_{70}^- (b) by subtraction of cationic spectra from Ne + 1% CO_2 (dark blue) and from Ne + 0.15% CCl_4 (light blue) matrixes. The identified absorptions of C_{70}^- are marked with red arrows. Strong features of the electron scavengers and neutral C_{70} are shown in reduced contrast. Details see text.

For C_{70}^-, broad absorptions with *fwhm* of more than 5 cm^{-1} dominate the entire spectrum, with only some sharp features around 500 cm^{-1}.The broadness of the absorptions can be rationalized by low energy dynamic Jahn-Teller distortions.

RI-DFT calculations (Turbomole [33], BP86/def-SV(P)) are performed for the ions in C_s (C_{70}^+) and C_{2v} (C_{70}^-) symmetry, the isomers with the lowest calculated ground state energy, as can be seen in figures 3.17, 3.18, and 3.19. Comparison with the experimental spectra of the ions does not show an agreement between experiment and theory.

Note, that TD-DFT calculations of C_{70}^+ and C_{70}^- predict electronic transitions at low excitation energies, in the case of C_{70}^+ at 1086 and 1271 cm^{-1}, in the case of C_{70}^- at 1177 and 1553 cm^{-1}. Therefore, the infrared activity of the system cannot be accounted for only by the displacement of the nuclei. The electronic transitions also contribute to the induced dipole, leading to a breakdown of the Born-Oppenheimer approximation. Neither the spectra calculated for C_{70}^+ and C_{70}^- in this work, nor in the calculations of C. W. Bauschlicher [146], are able to reproduce the experimental spectra.

Contrary to $C_{70}^{+/-}$, the experimental IR spectrum of neutral C_{70} is reproduced to a high degree by DFT calculations in D_{5h} symmetry.

Thermal annealing of the neon matrix containing $C_{70}^{0/+/-}$ leads to an increase of C_{70}^{0} and a decrease of C_{70}^{+} and C_{70}^{-} absorption intensities. Assuming that the dominant neutralization channel is via C_{70}^{+} + C_{70}^{-} $\rightarrow$ 2 C_{70}^{0}, and using experimental absorptivity data of neutral C_{70} in KBr pellets [119], the absolute absorptivity values of the absorptions of C_{70}^{+} and C_{70}^{-} in 5 K neon matrixes are established. Experimental determination of the integrated molar absorptivity of the ionic absorptions is hindered by the overlap of some features and their broadness. The overall accuracy of the molar absorptivities of C_{70}^{+} and C_{70}^{-}, listed in table 3.7, is therefore estimated to be roughly $\pm$40%.

The IR gas-phase absorption frequencies of $C_{70}^{0/+/-}$ are extrapolated from measurements in neon and argon matrixes. A detail of the spectra in Ar and Ne matrixes is shown in figure 3.16. The absorption frequencies and the extrapolated gas phase positions are listed in tables 3.6 and 3.7.

For neutral C_{70}, the extrapolated gas phase frequencies are compared to gas phase emission values by Nemes *et al.* [124]. Most of the extrapolated frequencies show a good agreement to the emission wavelengths with deviations of less than 1%. However, two modes ($E_1'(5)$ and $E_1'(13)$) show a larger deviation of 1.7 and 1.1%. The difference between the matrix and gas phase data can be rationalized by taking into account, that the gas phase spectra are emission frequencies measured at 930 to 1200 K, and linearly extrapolated to 0 K.

For $C_{70}^{+/-}$, no gas phase absorption or emission spectra in the IR range have yet been published. The error of the extrapolated frequencies from matrix measurements is assumed to be less than 1%, consistent with neutral C_{60}, C_{70}, and previously published results for other species [126].

Electronic Spectra

The UV-vis spectra of $C_{70}^{0/+/-}$ are shown in figure 3.20.

For neutral C_{70}, the spectra measured in this work are identical to spectra previously published. For C_{70}^{+}, an additional electronic transition is identified, and two features, previously assigned to vibronic transitions, are re-assigned as features of C_{70}^{-} and C_{70}^{2+}, respectively.

The vibronic transitions of the neutral C_{70} were assigned to the $^1A_2' \leftarrow {}^1A_1'$ (band origin at 644.2 nm), $^1E_1' \leftarrow {}^1A_1'$ (origin at 637.3 nm), and $^1A_2'' \leftarrow {}^1A_1'$ (origin at 626.3 nm) transitions [147], of which the $^1E_1' \leftarrow {}^1A_1'$ transition is the lowest energy transition

Table 3.7: Identified absorption lines of C_{70}^+ and C_{70}^-, frequency and *fwhm* in argon and neon matrixes, the integrated molar absorptivity A_{Ne} measured in neon matrixes, and the extrapolated gas phase frequency. Not all absorptions could be identified in Ar matrixes.

	matrix					*gas phase*
	ν_{Ar}, cm^{-1}	*fwhm*(Ar), cm^{-1}	ν_{Ne}, cm^{-1}	*fwhm*(Ne), cm^{-1}	A_{Ne}, $km \cdot mol^{-1}$	extrapolated, cm^{-1}
C_{70}^+	1540	20	1542	20	57±23	1543
C_{70}^+	-	-	1445	20	80±16	-
C_{70}^+	1129.3	3.8	1128.5	2.2	5±2	1128.2
C_{70}^+	-	-	868.3 [a]	9	1.2±0.5	-
C_{70}^+	709.3	2.3	710.4 [b]	1.7	0.9±0.4	710.7
C_{70}^+	591	-	595 [b]	15	10±4	596
C_{70}^+	-	-	534.9	1.2	- [c]	-
C_{70}^+	509.6	1.6	507.9	1.7	1±0.4	507.4
C_{70}^+	463.2	1.8	462.7	1.5	4±2	462.5
C_{70}^-	1508.5	20	1505.0	20	20±8	1503.9
C_{70}^-	1406.3	3.8	1406.8	6	675±270 [d]	1407.0
C_{70}^-	1402.3	3.1	1401.5	4.6	[d]	1401.2
C_{70}^-	1389.5	5.1	1388.2	5.1	[d]	1387.8
C_{70}^-	1359.1	3	1358.3	4.7	9±4	1358.0
C_{70}^-	1329.1	3.4	1328.1	2.8	4±2	1327.8
C_{70}^-	1241.4	7	1237.2	12	25±10	1235.9
C_{70}^-	1210.1	14	1208.0	10	40±16	1207.3
C_{70}^-	1070.0	2	1069.8	2.2	2±1	1069.7
C_{70}^-	986	14	981	12	34±14	979
C_{70}^-	898	10	894	10	33±13	893
C_{70}^-	884	10	880	12	29±12	879
C_{70}^-	-	-	756	8	31±12	-
C_{70}^-	747	2	746	6	11±4	746
C_{70}^-	725	15	722	9	74±30	721
C_{70}^-	694.0	0.9	694.1	0.9	20±8	694.1
C_{70}^-	563.8	1.5	562.4	1.3	31±12	562.0
C_{70}^-	534.0	1.5	532.5	1.3	11±4	532.0
C_{70}^-	-	-	523.5	6	28±11	-
C_{70}^-	485.0	10	484.2	8	27±10	483.9

[a] Absorption only measured in Ne + 1% CO_2 matrix; [b] Absorption only measured in Ne + 0.15% CCl_4 matrix; [c] Absorption coincides with neutral feature, A_{Ne} could not be determined; [d] A_{Ne} determined over whole range.

to be observed in neon matrixes. Towards higher energies, the vibronic features become broader. Broadening of the vibrational features can be explained by a shortened lifetime because of internal conversion or by an overlap with other transitions [9]. A full assignment of the absorptions is available in Sassara *et al.* [147].

Towards the blue of the vibronic transitions of neutral C_{70}, absorptions without vibrational structure are present with pronounced maxima at 468 , 378 , 360 , 331 , 236 , and 214 nm [148].

The features of C_{70}^+ in the region of 690-800 nm have been assigned to vibronic transitions of the $^2E_1' \leftarrow ^2E_1''$ electronic transition, one of four transitions expected for the assumed $^2E_1''$ ground state. The $^2A_2''$ ground state was excluded because of the energy range of the observed transitions. The measured (by photoelectron spectroscopy) and calculated position of the $^2E_1' \leftarrow ^2E_1''$ transition is roughly at 785 nm , showing good agreement with the band origin at 798 nm in neon matrixes [149, 150]. The assignment of the vibronic features of the $^2E_1' \leftarrow ^2E_1''$ electronic transition of C_{70}^+ is given in Fulara *et al.* [9].

With the exception of the features at 773.5 and 705.8 nm, all reported vibronic features are confirmed.

The absorption feature at 773.5 nm is present in samples of mass selected C_{70}^+ in pure neon matrixes, but does not occur in matrixes containing electron scavengers. This behavior is expected for anionic absorption features. The reason for its prominence in the experiments of Fulara *et al.* [9] is, that the authors used a preparation method, which creates similar amounts of cations and anions in the matrix simultaneously. The appearance of anionic absorptions is thus not surprising. TD-DFT calculations predict a transition of C_{70}^- in this energy range. Previous experiments with anions of C_{70} in organic solutions do not report features of C_{70}^- in this range [151, 152, 144]. For the C_{70}^{3-} charge state, an absorption in the range of 760 nm was identified [143]. However, the presence of this species can be ruled out in matrix environments. As only one absorption of this kind could be observed in the UV-vis range for C_{70} and its ions, our assignment remains tentative until further measurements are performed - ideally on matrixes containing only anionic C_{70}.

The absorption feature at 705.8 nm, tentatively assigned to the band origin of the $^2E_2'' \leftarrow ^2E_1''$ transition of C_{70}^+ by Fulara *et al.* [9], does not appear in any of our spectra measured after the deposition of C_{70}^+. However, the deposition of C_{70}^{2+} leads to a prominent peak at 705.7 nm. Its appearance in the measurement by Fulara *et al.* [9] can again be explained by the method used for sample preparation, where a matrix containing neutral C_{70} is illuminated with UV radiation (Ne I). Apparently, the formation of trace amounts of C_{70}^{2+} cannot be excluded by this technique. The full spectrum of C_{70}^{2+} will be discussed in the following section 3.3.2.

The newly-discovered second broad absorption feature (645-715 nm) is assigned to the $^2E_2'' \leftarrow ^2E_1''$ transition of C_{70}^+. Using ab initio calculations, the transition was

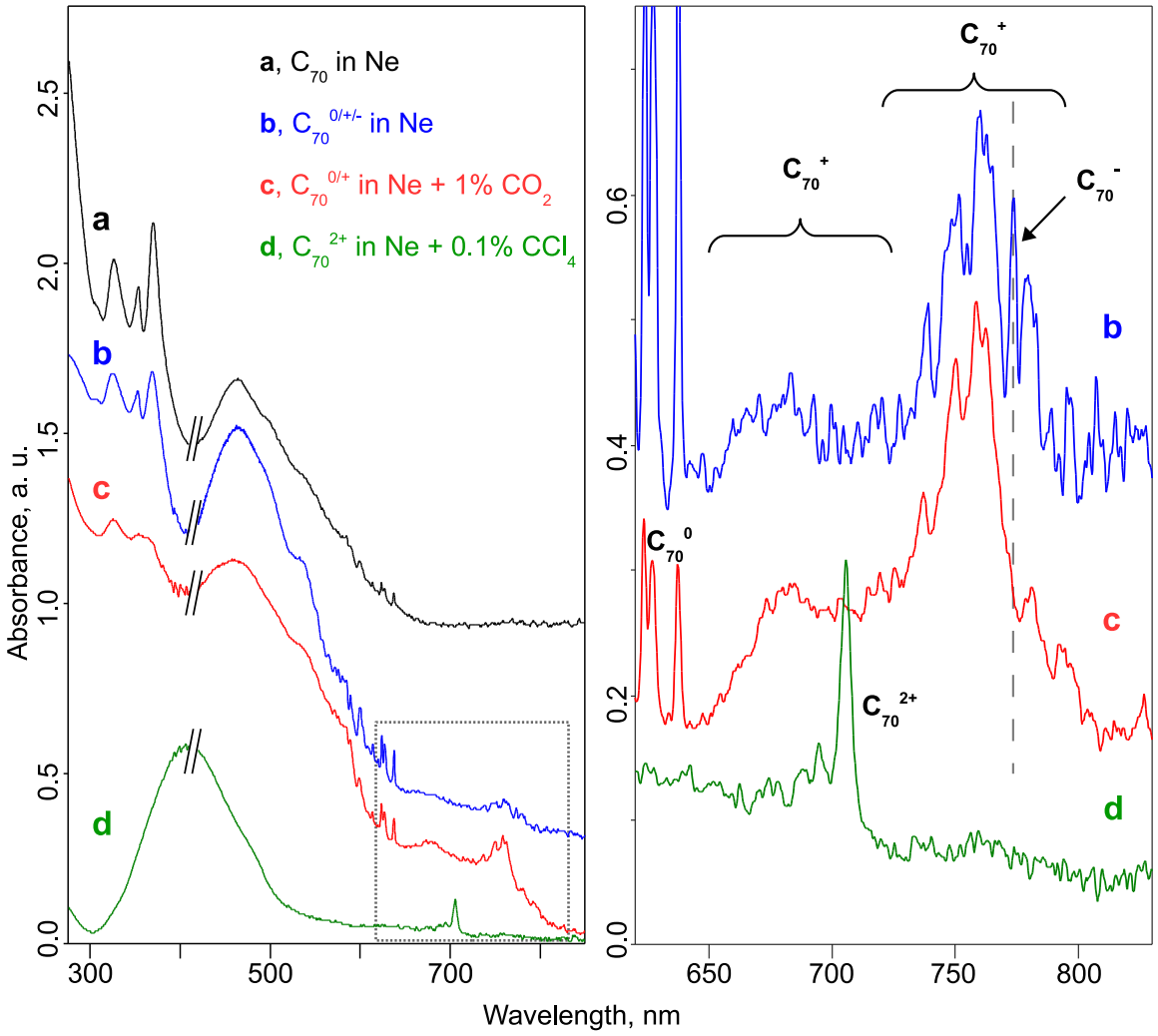

Figure 3.20: Left: UV-vis spectra of neutral C_{70} in Ne (a), a mixture of $C_{70}^{0/+/-}$ in Ne (b), $C_{70}^{0/+}$ in Ne + 1% CO_2 (c), and C_{70}^{2+} in Ne + 0.1% CCl_4 (d). Th UV region is measured with a deuterium discharge light source, the vis-NIR range with a halogen lamp. Right: Detail of the marked region, the transitions of C_{70}^{+} (785 nm, 715 nm), C_{70}^{-} (773.5 nm), and C_{70}^{2+} (705.7 nm) are labeled.

estimated to be at 685 nm [150], which is close to the measured wavelength of approximately 715 nm. The identification of the band origin of this feature is complicated by its overlap with the $^2E_1' \leftarrow {}^2E_1''$ transition. The agreement with theory is not expected to be as good as for the first absorption, given that the photoelectron spectrum [149] does not show a distinctive peak in the corresponding region [9], in contrast to the first absorption.

The additional electronic transitions of C_{70}^+ from the $^2E_1''$ ground state ($^2E_2'' \leftarrow {}^2E_1''$ and $^2E_2' \leftarrow {}^2E_1''$) are calculated to be around 1900 nm and 1300 nm, respectively, and are not in the spectral range of the detector used in this experiment.

In the region below 625 nm, no additional characteristic features of $C_{70}^{+/-}$ are detected. The broadness of the features with half-widths around 3000 cm^{-1} hinders identification of any single transition. TD-DFT calculations predict close-lying electronic transitions in the UV range for the different charge states of C_{70} investigated. As for C_{60}, the similarity between the UV absorptions of C_{70} and its ions originates in the plasmonic nature of these transitions, the excitation is carried by several delocalized electrons.

The integrated molar absorptivity of C_{70} and its ions could not be determined in the UV-vis region. Annealing of the sample did not lead to appreciable changes of the absorption intensities in the UV-vis. Also, IR and UV-vis measurements are done with different setups, therefore the IR absorbance cannot be used to deduce the absorptivity in the UV.

3.3.2 Dications of C_{70}

C_{70}^{2+} is generated by electron impact ionization and deposited into Ne + 1% CO_2 and Ne + 0.15% CCl_4 matrixes with a charge current of 5 nA, corresponding to an ion beam intensity which is 1/30 of the monocation. Deposition time for IR measurements is two to three days. Due to its high electron affinity, it can only be studied in matrixes with electron scavengers. In pure neon matrixes, the deposition results in the capture of secondary electrons by C_{70}^{2+}, preventing the accumulation of sufficient material for IR spectroscopy.

The ionization energies of C_{70} are comparable to those of C_{60} (experimental ionization energies of C_{70}: 7.48 eV (first), 11.36 eV (second), 16.46 eV (third) [145]).

Results

Vibrational Spectra

IR spectra of C_{70}^{2+} isolated in Ne + 1% CO_2 and Ne + 0.15% CCl_4 matrixes are shown in figures 3.21 and 3.22. Weak features, previously identified as C_{70}^0 and C_{70}^+ ab-

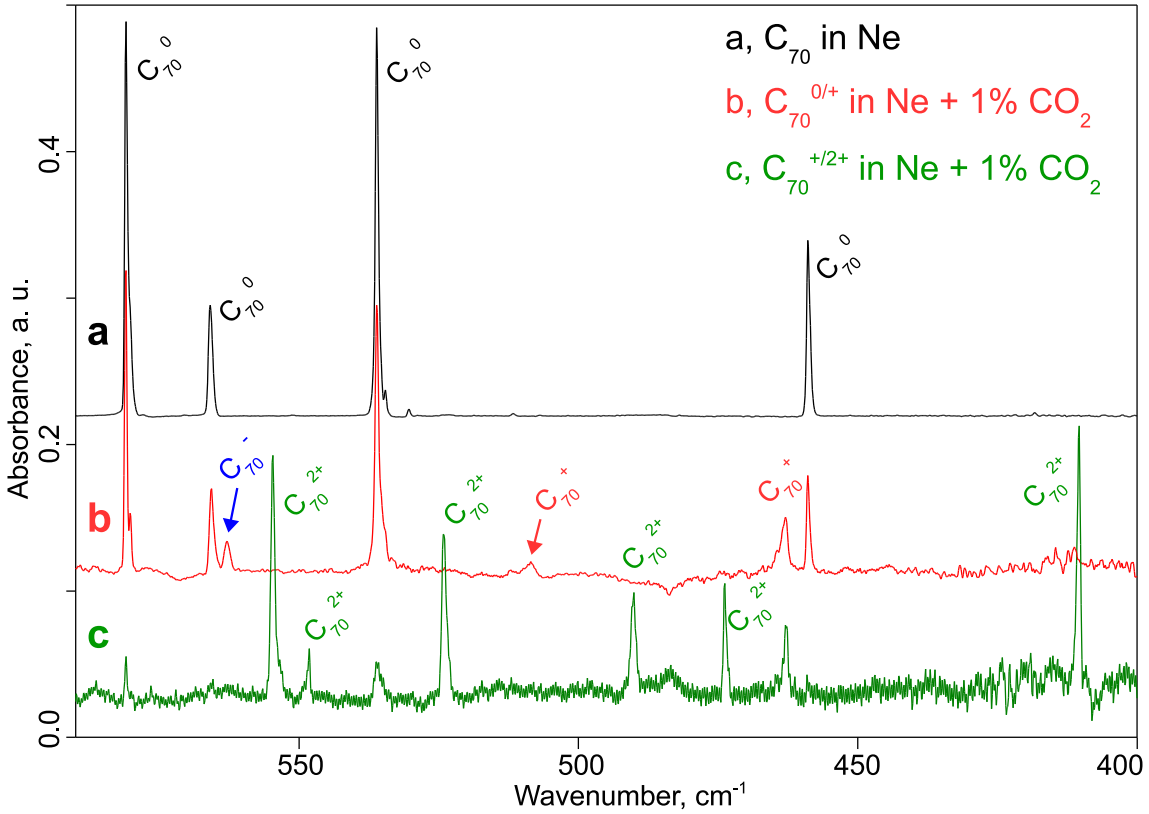

Figure 3.21: Comparison of the far-IR absorptions of neutral C_{70} in Ne (a), $C_{70}^{0/+}$ in Ne + 1% CO_2 (b) with weak features of C_{70}^{-} present, and $C_{70}^{+/2+}$ in Ne + 1% CO_2 (c). Spectra are scaled for similar intensity of the neutral or cationic absorptions.

sorptions, as well as several new features are observed, which are identified as C_{70}^{2+} absorptions. The region between 800 and 600 cm^{-1} is dominated by strong absorptions of CO_2 or CCl_4, hindering the identification of C_{70}^{2+} absorptions possibly present. Absorptions in this range, and very weak absorptions in general, are assigned tentatively.

The *fwhm* of the identified absorptions of C_{70}^{2+} is less than 2 cm^{-1} in the region below 900 cm^{-1}. At higher wavelengths, some of the absorptions are broader, with a halfwidth of more than 5 cm^{-1}.

Electronic Spectra

In the UV-vis range, deposition of C_{70}^{2+} into Ne + 1% CO_2 and Ne + 0.15% CCl_4 matrixes leads to the emergence of additional absorption features, most prominently a sharp peak at 705.7 nm with several weaker features in the range of 705-670 nm.

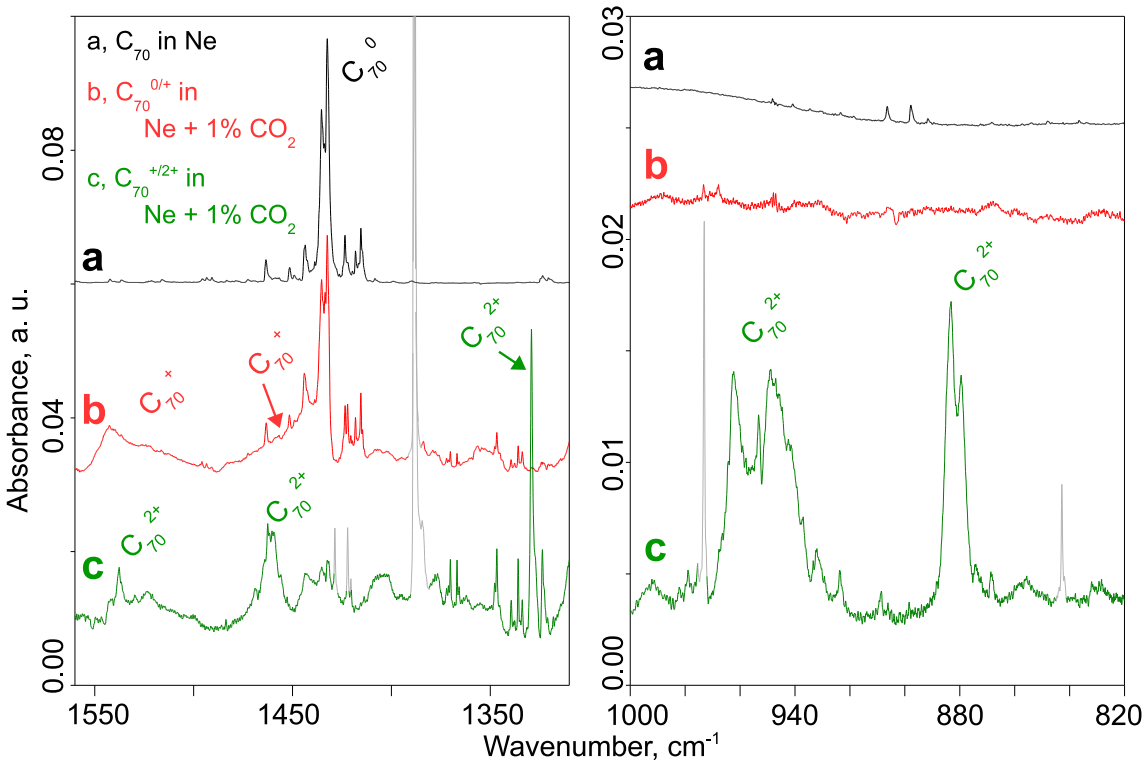

Figure 3.22: Comparison of the mid-IR absorptions of neutral C_{70} in Ne (a), $C_{70}^{0/+}$ in Ne + 1% CO_2 (b), and $C_{70}^{+/2+}$ in Ne + 1% CO_2 (c). Spectra are scaled for similar intensity of the neutral or cationic absorptions. Strong CO_2 absorptions are shown in reduced contrast.

Since these absorptions only occur in samples with C_{70}^{2+}, and not with any other species investigated in this work, they are assigned to transitions of C_{70}^{2+}.

In the range from 300 to 500 nm, a broad feature is present (fig. 3.20 (d)). The poor quality of the matrix, due to the long deposition time, results in too much light scattering for the measurement of clear spectra. No distinct absorptions of the fullerene C_{70} species present in the matrix are observed in the UV range.

Discussion

Vibrational Spectra

For comparison with calculations, the IR spectrum of C_{70}^{2+} is extracted by substituting the regions between identified absorptions with straight lines, while the position, intensity and *fwhm* of the absorptions remain unchanged. Absorption features, for which no unambiguous assignment is possible, are marked (fig. 3.23).

RI-DFT calculations (Turbomole [33], BP86/def2-SV(P)) are performed for C_{70}^{2+} for different ground state symmetries (C_1, C_s, C_{2v}, C_{5v}, and D_{5h}) in singlet and triplet state.

For C_{70}^{2+}, a D_{5h} triplet ground state symmetry is identified. Its energy is close to the calculated minimum (+0.01 eV, corresponding to C_{5v} symmetry). However, the small energy difference is well within the error of the calculation. Since the calculated spectra for D_{5h} and C_{5v} symmetry are close to identical, the ground state of C_{70}^{2+} is assigned to the state with the higher symmetry, D_{5h}. The other symmetries, as well as the singlet state, do not reproduce the experimental spectrum.

The comparison of the calculated triplet D_{5h} spectrum with the experimental extracted spectrum is shown in figure 3.23.

The calculated frequencies of the triplet D_{5h} C_{70}^{2+} absorptions are in good agreement with the experimental results. Below 600 cm^{-1}, the calculated spectrum fits to the number of detected absorptions, although the relative intensity of the absorption at 524.1 cm^{-1} is not predicted correctly. For the absorption at 554.2 cm^{-1}, no corresponding calculated normal mode is identified. In the 800 - 600 cm^{-1} range, strong absorptions of the electron scavengers CO_2 and CCl_4 hinder the identification of C_{70}^{2+} features. In figure 3.23, this range is marked in gray. In the range from 1250 - 1100 cm^{-1}, the calculation predicts several transitions (E_1'(14, 15, 16)), which are not detected in the experiment. The calculated intensities of these absorptions are probably overestimated.

As for C_{60}^{2+}, a rough estimation of the integrated molar absorptivity of C_{70}^{2+} is done by two different approaches, by the deposited number of ions and the intensity of the absorptions of counterions.

Table 3.8: Assignment of the identified absorptions of C_{70}^{2+} by comparison to DFT (D_{5h} triplet): their experimental frequency, full width at half maximum (*fwhm*), and integrated molar absorptivity A_{Ne} in neon matrixes, and the calculated frequency and integrated molar absorptivity A_{calc}.

	experiment			*theory*	
mode	ν, [a] cm^{-1}	*fwhm*, cm^{-1}	A_{Ne}, $km \cdot mol^{-1}$	ν, cm^{-1}	A_{calc}, $km \cdot mol^{-1}$
$A_2''(10)$; $E_1'(21)$ [b]	1537.6	2	5.4±2	1537.1; 1531.8	106; 218
$E_1'(20)$	1459.5	7.3	18±7	1460.3	411
$E_1'(17)$	*1328.8*; 1323.5	1.4	30±12	1304.8	305
$E_1'(13)$	962.8; 952.8 *948.7* 945.8	3.1	64±26	986.0	1341
$E_1'(12)$	*883.2* 879.5	1.7	44±18	870.1	440
$E_1'(9)$	712.0 [c]	0.6	1.3±0.5	687.3	71
$E_1'(7)$	642.3	0.6	8±3	620.3	177
- [d]	554.2	0.7	7±3	-	-
$E_1'(6)$	524.1	0.9	4.5±2	530.7	6.8
$E_1'(5)$	490.1	0.7	2±0.8	499.2	143
$E_1'(4)$	473.6	0.6	2.3±1	478.0	236
$E_1'(3)$	410.4	0.6	5.5±2	379.3	111

[a] Site effect in neon matrixes, most intense line set in italics, *fwhm* of most intense line, A_{Ne} integrated over all absorptions; [b] No clear assignment to calculated normal mode; [c] Absorption only identified in Ne + 0.15% CCl_4 matrix; [d] No normal mode could be identified.

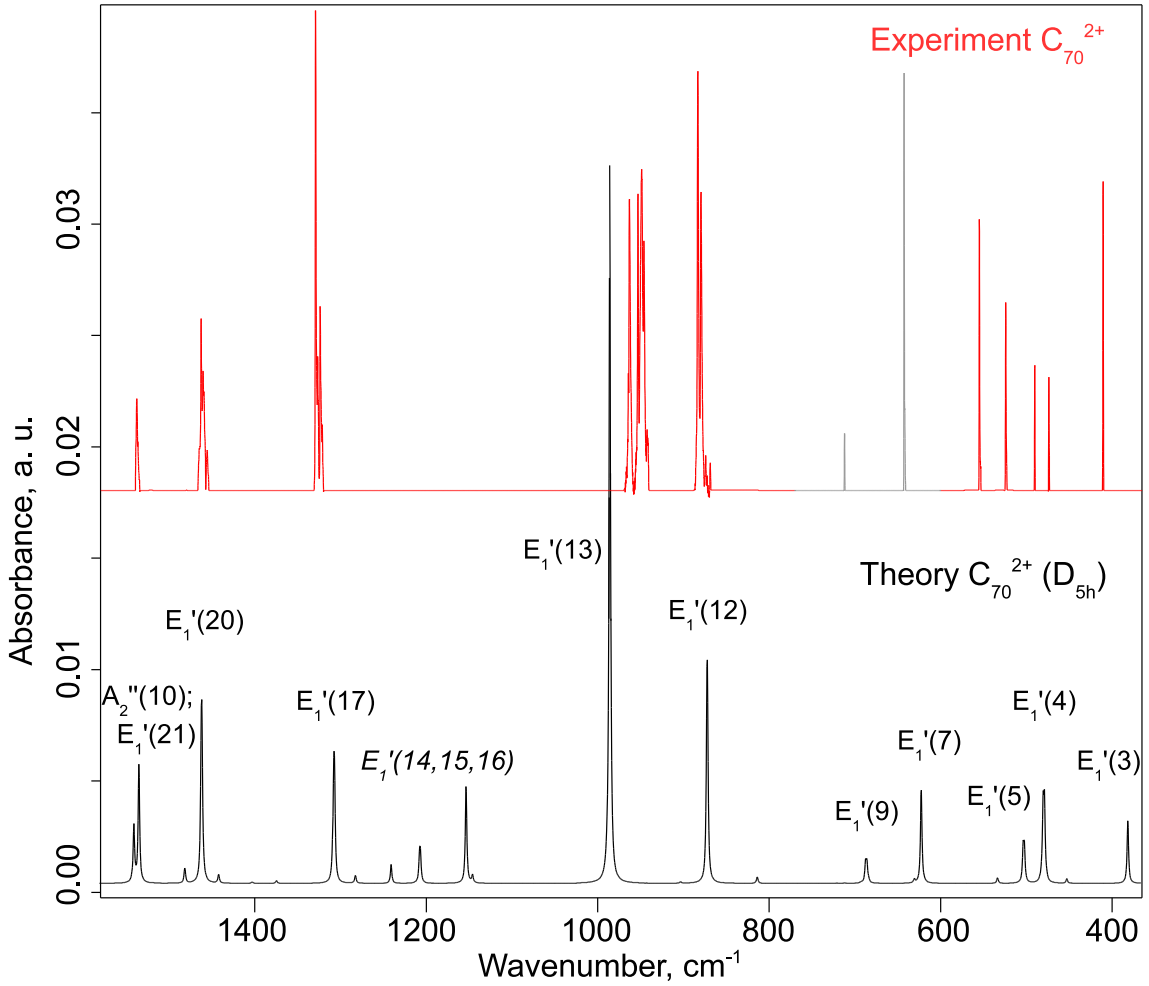

Figure 3.23: Comparison of the 'extracted' IR absorption spectrum of C_{70}^{2+} to RI-DFT calculations for triplet D_{5h} C_{70}^{2+}. Normal modes not observed in the experimental data are labeled in italics. In the 800 - 600 cm^{-1} range (marked gray), strong absorptions of CO_2 and CCl_4 hinder the unambiguous assignment. The calculated frequencies are unscaled. Details see text.

The total amount of deposited C_{70}^{2+} is estimated from the integrated ion current corrected for the charge state. For the second approach, the absorption intensity of the $CCl_3 \cdot\cdot Cl^-$ counterions [67] is estimated from samples of C_{70}^+ in Ne + 0.15% CCl_4 and known absorptivity values for C_{70}^+, to approximate the total charge present in the matrix. Both approaches lead to roughly the same values of the integrated molar absorptivity of C_{70}^{2+}, the overall accuracy is estimated to be around $\pm 40\%$.

For the identified absorptions of C_{70}^{2+}, the experimental and calculated frequencies and integrated molar absorptivities, and the assignment according to DFT are listed in table 3.8.

Similar to C_{60}^+ and C_{60}^-, C_{70}^{2+} exhibits sharp absorptions with a halfwidth of less than $2\,cm^{-1}$ in the wavelength region below $900\,cm^{-1}$. At higher energies, the *fwhm* increases, indicating a dynamic Jahn-Teller effect for vibrational modes with a tangential motion.

Electronic Spectra

In figure 3.20, the absorption features of C_{70}^+, C_{70}^-, and C_{70}^{2+} in the visible range are shown.

The strong absorption feature of C_{70}^{2+} at 705.7 nm is assigned to the band origin of the $4^3E_1' \leftarrow X^3A_1'$ transition by comparison to TD-DFT calculations. With a displacement of 227 and $377\,cm^{-1}$ respectively, the distinct, but weaker absorptions at 694.6 and 687.4 nm are assigned as vibronic excitations.

In previous measurements by Fulara *et al.* [9], the band origin was identified as a transition of C_{70}^+. Apparently, the sample preparation by irradiating a matrix containing neutral C_{70} with Ne I radiation leads to the formation of traces of C_{70}^{2+}, along with C_{70}^+ and C_{70}^-. The integrated molar absorptivity for the $4^3E_1' \leftarrow X^3A_1'$ transition of C_{70}^{2+} could not be established.

Since this absorption of C_{70}^{2+} lies in the absorption range relevant for astronomy, it may be a candidate for a carrier of diffuse interstellar bands, and would indicate the presence of C_{70}^{2+} in interstellar space. As was shown for C_{60}^+ in section 3.2, only a small matrix shift is expected in neon matrixes. The neon matrix wavelength of 705.7 nm is thus a good first approximation of the gas phase frequency of the transition until further measurements are performed, either in matrixes using different noble gases or in gas-phase.

In the UV-vis range, a broad feature is observed from 300 to 500 nm. Whether this feature is an absorption of C_{70}^{2+}, or a scattering effect of the matrix, could not be determined. Further measurements are required.

3.3.3 Summary

Electronic and vibrational spectra of neutral C_{70}, C_{70}^-, C_{70}^+, and C_{70}^{2+} isolated in cryogenic matrixes were recorded.

The integrated molar absorptivity of the most intense absorptions of neutral C_{70} was determined.

For C_{70}^- and C_{70}^+, the IR absorptions were measured for the first time in noble gas matrixes. Several absorptions were identified in the IR to UV-vis range, and the integrated molar absorptivity of the IR absorptions was estimated. Deposition of C_{70}^+ into argon matrixes allowed the estimation of the IR gas-phase absorption frequencies of neutral C_{70}, C_{70}^-, and C_{70}^+.

In the UV-vis, the assignment of absorptions of C_{70}^+ was revised, two features previously assigned to vibronic transitions of C_{70}^+ are re-assigned to C_{70}^- (773.5 nm) and C_{70}^{2+} (705.7 nm). A new electronic transition of C_{70}^+ was identified at 715 nm.

In the UV-vis range below 500 nm, no difference between the absorptions of $C_{70}^{0/+/-}$ was observed. This is consistent with TD-DFT calculations, and indicates plasmon-like excitations of the delocalized electrons.

Both C_{70}^+ and C_{70}^- were established as non-Born-Oppenheimer systems. Electronic potentials with intersections at energies of less than 1000 cm^{-1} are suggested. Calculations of the IR spectra of the ions in the correct electronic potential are ongoing in collaboration with Dr. E. Gromov, Dr. S. Klaiman, and Prof. L. Cederbaum [153].

C_{70}^{2+} was measured spectroscopically for the first time. In the IR, several vibrations were identified and their integrated molar absorptivities were estimated. From comparison with DFT calculations, a D_{5h} ground state for C_{70}^{2+} was suggested. In the UV-vis, an electronic transition with vibronic sidebands was identified at 705.7 nm.

3.4 Non-IPR C_{58} and its Ions

Classical fullerenes smaller than C_{60} always have a 'non-IPR' structure with adjacent pentagon rings (see page 27). Non-IPR sites increase the strain of the fullerene cage, thereby reducing the stability of the species. Furthermore, they act as defect sites, leading to an increased reactivity. Extraction of these non-IPR species from carbon soot by solvent extraction is not possible due to polymerization, which is hindering their experimental study.

Non-IPR fullerenes have been studied mostly theoretically, for example their structure has been calculated with DFT [154, 155]. For C_{58}, a C_{3v} ground state symmetry

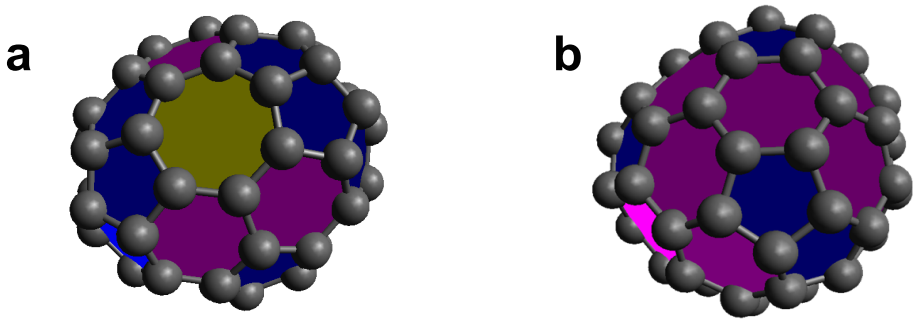

Figure 3.24: The two C_{58} isomers of lowest energy [156]. (a) C_s symmetry, showing the heptagon ring, and (b) C_{3v} symmetry, showing one of the three pairs of adjacent pentagons.

is predicted [156]. However, the energy difference of the non-classical C_s isomer is only around 0.03 eV for the neutral [156] and 0.05 eV for the cation [157], which is well within the accuracy of DFT calculations [23].

Experimental studies of C_{58} are scarce. Electronic, vibrational, thermodynamic, and mechanical properties of thin films prepared by deposition of mass-selected ion beams have been studied [158, 159, 160]. However, polymerization of the reactive C_{58} cages in thin films masks the properties of the isolated molecules. So far, only one experimental study of single C_{58} molecules, adsorbed on a Au(111) surface and studied with STM, has been reported [84]. No unambiguous experimental determination of the molecular symmetry of C_{58} or its ions has been achieved as yet.

In the following sections, the first optical spectroscopy measurements on isolated C_{58} and its ions are presented. The experimental data is compared to DFT calculations, and the assignment of the ground state symmetry is discussed.

3.4.1 Neutral and Monoionic C_{58}

C_{58}^+ is produced by electron impact ionization and fragmentation of C_{60}. Fragmentation takes place via C_2 loss. The resulting C_{58}^+ ions are separated from the parent ion and other fragments with a quadrupole mass filter. An ion current of up to 9 nA is produced and maintained for several hours.

The mass-selected C_{58}^+ ions are co-deposited with an excess of matrix gas onto the cold substrate. Samples are created using pure neon and Ne + 1% CO_2 as matrix gas. Addition of the electron scavenger CO_2 suppresses the formation of neutral and anionic C_{58}. The deposition time for the samples was around 8 days, resulting in thick samples of low optical quality due to increased light scattering.

Absorption features are identified by the comparison of Ne and Ne + 1% CO_2 matrixes, containing different ratios of C_{58}^+, C_{58}, and C_{58}^-. Features with an increased relative intensity are identified as cationic, with a decreased relative intensity as anionic, and features, whose relative intensity remains constant as neutral features. Measurements of samples with different electron scavengers are planned.

To improve the signal-to-noise ratio, all spectra are averaged over 12 000 to 18 000 single scans.

Direct sublimation of neutral C_{58} is possible only after prior accumulation of large amounts of C_{58}^+ on a surface and subsequent thermal desorption of neutral C_{58}. However, most of the accumulated bulk material cannot be desorbed. Instead, it forms a stable polymeric phase which remains on the surface [158]. Currently, the amount of mass-selected C_{58} that can be produced is too low to enable optical spectroscopy on re-desorbed neutral C_{58} isolated in cryogenic matrixes.

Results

Vibrational Spectra

Upon deposition of mass selected C_{58}^+ into pure neon matrixes, several characteristic IR absorption features emerge. In addition to these absorptions, weak features of C_{60} and its ions are present (fig. 3.25). The low resolution setting of the mass spectrometer of approximately $^{m}/_{\Delta m}$ = 25 leads to some contamination of the C_{58}^+ ion beam with approximately 5% of C_{60}^+, as is estimated from mass spectra measured prior to the deposition. This approach was chosen because it results in an increase of the ion current of roughly 10%, which saves approximately one day of deposition time.

In the IR spectrum obtained after co-deposition of C_{58}^+ with Ne + 1% CO_2, almost all features observed in pure Ne are still present. The relative change in absorption intensity in matrixes with electron scavengers enables the identification of neutral and ionic features. The neutral absorptions are identified by comparing the intensities of the C_{58} features to the known absorptions of C_{60}^0. Features of C_{58}, that have a similar relative intensity to the C_{60}^0 absorptions in Ne and Ne + 1% CO_2 are assigned as absorptions of C_{58}^0. The absorptions of C_{58}^+ gain in relative intensity in Ne + 1% CO_2 matrixes, absorptions of C_{58}^- almost completely vanish. All absorptions assigned to the same charge state ($C_{58}^{0/+/-}$) have the same relative intensity in Ne and Ne + 1% CO_2 matrixes. The identified absorptions are listed in table 3.9.

In the range from 800 to 600 cm^{-1}, strong CO_2 absorptions prevent the identification of any weak absorption. The unambiguous assignment to a charge state of C_{58} for more intense absorptions is hindered in this range.

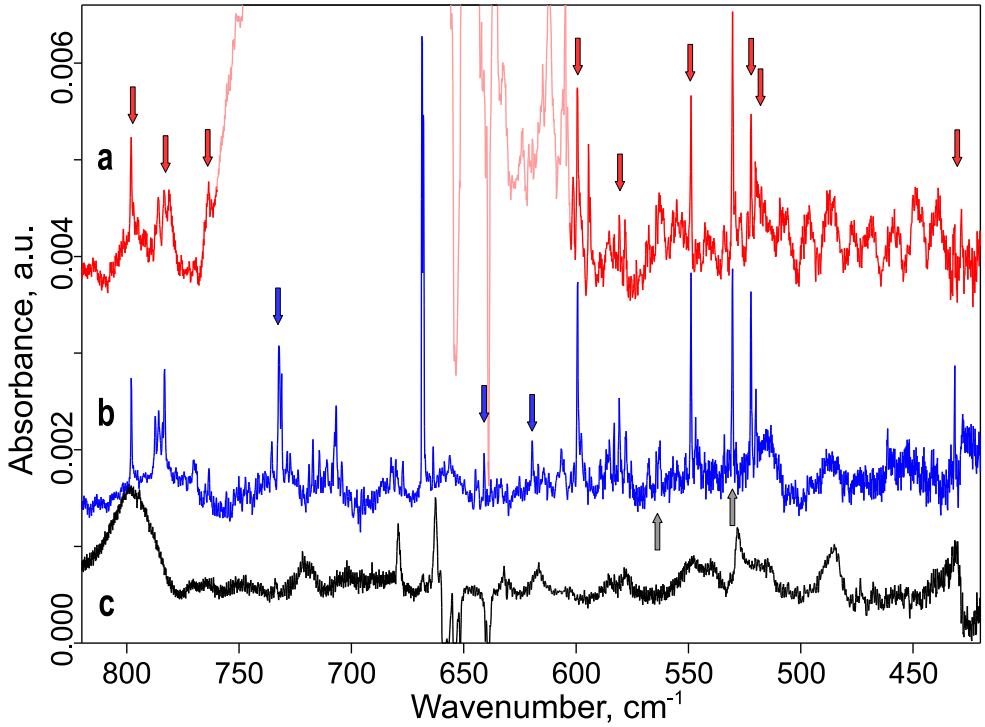

Figure 3.25: IR spectrum of C_{58}^{+} deposited into Ne + 1% CO_2 (a) and pure neon (b) and the spectrum of the residual material after removal of the matrix gas (measured at 50 K) (c). Red arrows mark identified absorptions of C_{58} and its ions, blue arrows mark absorptions masked by CO_2 absorptions and therefore not confirmed, and gray arrows mark absorptions from C_{60} impurities. Additional features are identified as CO_2 or $(CO_2)_n$ absorptions. Strong CO_2 absorptions are shown in reduced contrast, the spectra are offset for clarity.

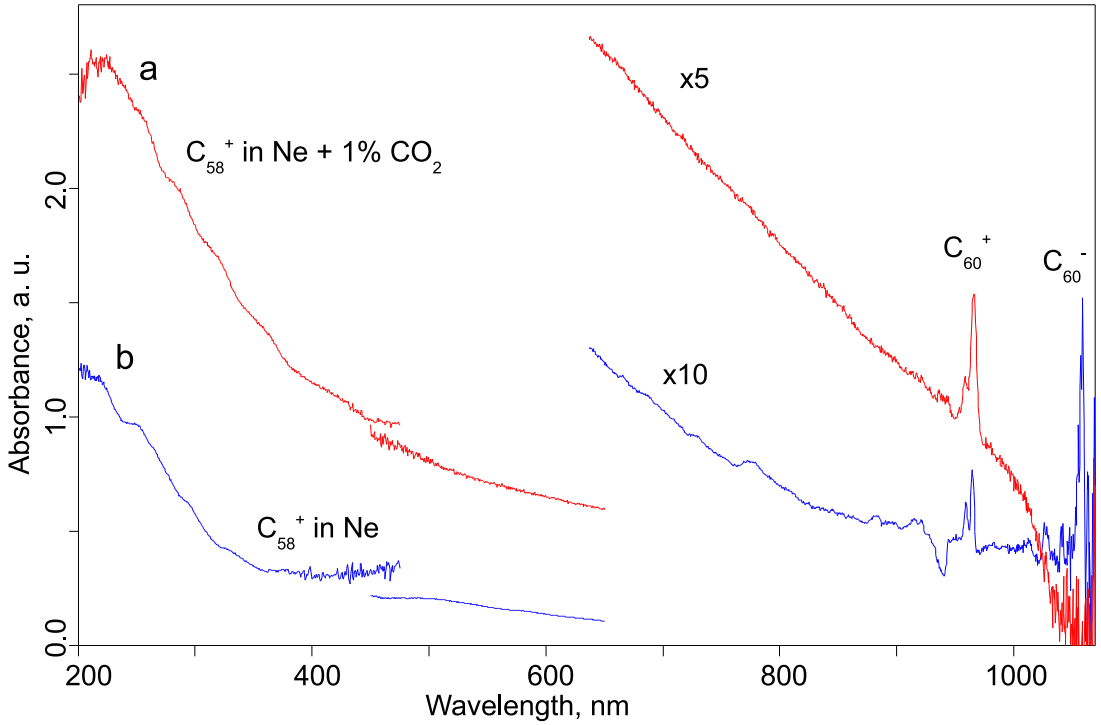

Figure 3.26: UV-vis spectra of C_{58}^+ deposited into Ne + 1% CO_2 (a) and pure neon (b). Absorptions of $C_{60}^{+/-}$ are visible in the NIR (intensities scaled as noted). In the UV, a broad absorption is observed, starting from roughly 400 nm. The weak structure in the UV is probably due to interference effects. The UV range is measured with a deuterium discharge lamp, the vis-NIR region with a halogen lamp.

Neutralization of the C_{58} ions in the matrix by annealing to roughly 10 K does not lead to detectable changes in the spectrum. A further slow increase of the temperature to roughly 50 K completely removes the matrix gas while a residual film of molecules remains. The IR spectrum of this film at 50 K is shown in figure 3.25 c, it shows only broad, non-distinctive absorptions.

Electronic Spectra

In the NIR region, the well-known absorptions of C_{60}^+ are visible at 964.5 and 958 nm, and at 1057 nm weak absorptions of C_{60}^- (fig. 3.26 a). In the spectrum measured for the Ne + 1% CO_2 sample, no NIR absorptions of C_{60}^- are present (fig. 3.26 b).

As shown in figure 3.26, a broad absorption in the UV, beginning from approximately 400 nm is the only feature besides the NIR absorptions of the C_{60} ions. No distinct C_{58} related features are identified.

Discussion

Vibrational Spectra

The presence of C_{60} and its ions in the matrixes does not hinder the identification of C_{58} features, and is instead quite useful as it allows to probe for the presence of charged species in the matrixes.

As previously described, comparison of the experimental absorption intensities in Ne versus Ne + 1% CO_2 matrixes allows the assignment of the features to specific charge states. The assignment is tentative, because only one kind of electron scavenger is used for C_{58}.

The integrated molar absorptivities of the absorptions of C_{58} and its ions could not be determined directly. However, the $T_{1u}(1)$ absorption of neutral C_{60} has roughly the same intensity as the strong absorptions of C_{58}. From mass spectra, the contamination of the C_{58}^+ ion beam with C_{60}^+ is measured to be less than 5%. Therefore, the integrated molar absorptivity of the strongest absorptions of matrix isolated C_{58} and its ions in the range of 1600-400 cm^{-1} is estimated to be at least one order of magnitude smaller than the integrated molar absorptivity of the C_{60} $T_{1u}(1)$ mode ($A_{Ne}(T_{1u}(1))$ = 27$\pm$2 km·mol^{-1}, see table 3.1).

The full width at half maximum (*fwhm*) of the identified C_{58} absorptions is less than 2 cm^{-1} in the whole IR range. In contrast to the measurements of the ions of C_{60}, no broadening of the C_{58} features is observed above 1000 cm^{-1}. This indicates, that for the dominant C_{58} isomer no close-lying electronic states exist, which would lead to a dynamic Jahn-Teller effect.

As can be seen in figure 3.25 and table 3.9, only four strong absorption features can confidently be assigned to neutral C_{58} (522.2 , 548.9 , 599.4 , and 798.0 cm^{-1}). Probably only one isomer with a symmetry higher than C_1 dominated the spectrum. The presence of several different isomers of C_{58} would lead to a much richer spectrum. However, the presence of isomers with lower IR absorptivity cannot be excluded.

To determine the ground state symmetry of the deposited C_{58} species, all C_{58} cage isomers with any possible number of pentagons and hexagons[5], and up to one heptagon were generated with the CaGe program package [162]. The geometries of all 23 994 isomers were optimized with neutral and cationic charge, and the ground state energy was calculated on a semi-empirical level (PM7) using MOPAC [163]. The ten C_{58}^0 and the ten C_{58}^+ isomers with lowest ground state energies were selected for further DFT treatment. For each of the 20 geometries, the vibrational spectrum of the neutral molecule is calculated with Turbomole [33].

[5]The classical (only pentagons and hexagons) C_{58} cage has 12 pentagons and $^n/_2$-10=19 hexagons, the non-classical isomers with one heptagon consist of 1 heptagon, 13 pentagons, and 17 hexagons.

Table 3.9: Frequency of the identified absorption lines of C_{58} and its ions in neon matrixes at 5 K, full width at half maximum (*fwhm*), intensity, and tentative assignment to specific charge states.

ν, cm^{-1}	*fwhm*, cm^{-1}	intensity [a]	tentative assignment
1277.8	0.8	*s*	– [b]
1071.4	0.7	*w*	C_{58}^0
798.0	0.7	*m*	C_{58}^0
787.4; 784.0 [c]	0.6	*w*	C_{58}^-
783.2	0.7	*w*	C_{58}^0
763.4	0.8	*w*	C_{58}^+
732.3; 731.1 [c]	1	*m*	– [b]
640.9	0.7	*w*	– [b]
619.6	0.7	*m*	C_{58}^0
616.8	0.6	*w*	– [b]
599.4	0.9	*s*	C_{58}^0
585.2	1.4	*w*	C_{58}^0
583.1	0.7	*w*	C_{58}^-
580.8	0.8	*m*	C_{58}^0
573.1	0.7	*vw*	C_{58}^+
567.8	1	*w*	C_{58}^0
562.9; 564.2 [c]	1.1	*m*	C_{58}^0
556.9	1	*vw*	C_{58}^0
551.4	0.5	*vw*	C_{58}^0
548.9; 546.8 [c]	0.6	*s*	C_{58}^0
542.9	0.9	*vw*	C_{58}^+
526.5	1.3	*w*	C_{58}^+
522.2	0.9	*s*	C_{58}^0
520.0	0.7	*m*	C_{58}^+
461.4	0.7	*w*	C_{58}^-
431.5	0.6	*m*	C_{58}^0
428.4	1.9	*w*	C_{58}^+

[a] *s* – strong, *m* – medium, *w* – weak, *vw* – very weak; [b] Masked by strong CO_2 absorptions, no assignment possible; [c] Site effect in Ne matrix

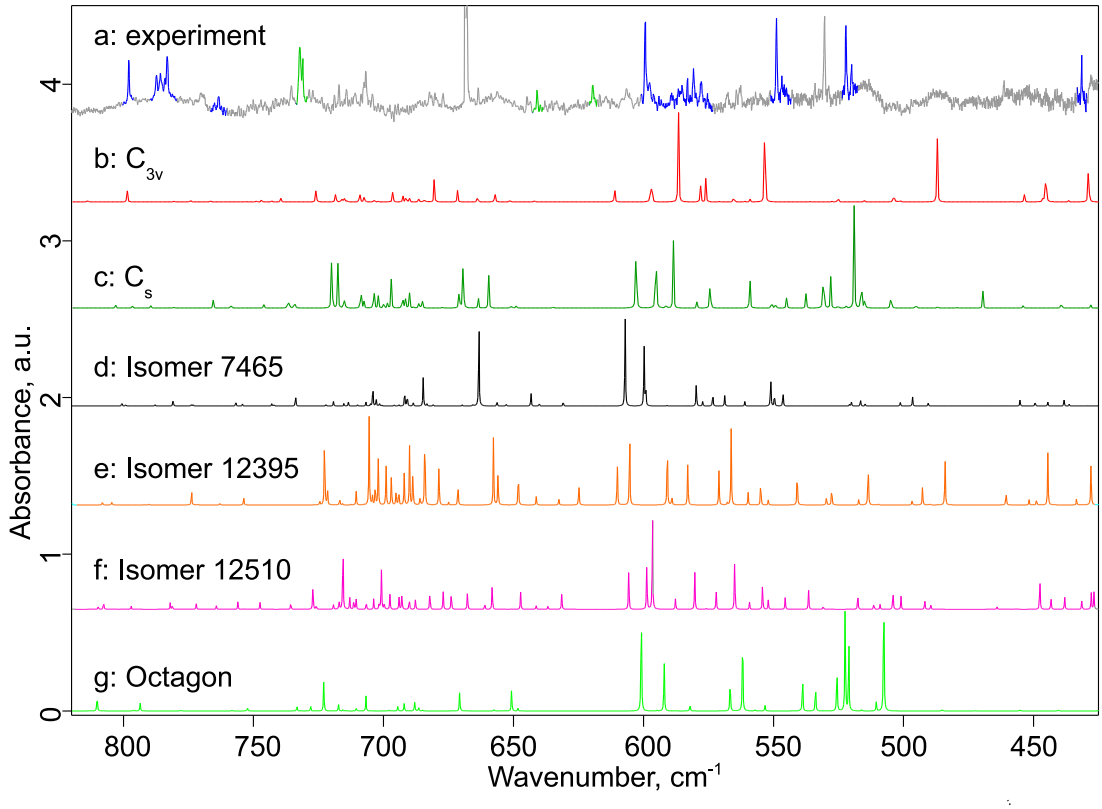

Figure 3.27: Comparison of experimental C_{58}^0 absorptions (marked in blue, green features are assigned tentatively) to calculated spectra of different neutral isomers in the 800-450 cm^{-1} region. Experimental data (a), calculated spectra of C_{3v} (b) and C_s (c) symmetry, isomers of energies close to the global minimum (d, e, f), and an isomer with an octagon (g) [161]. Details see text.

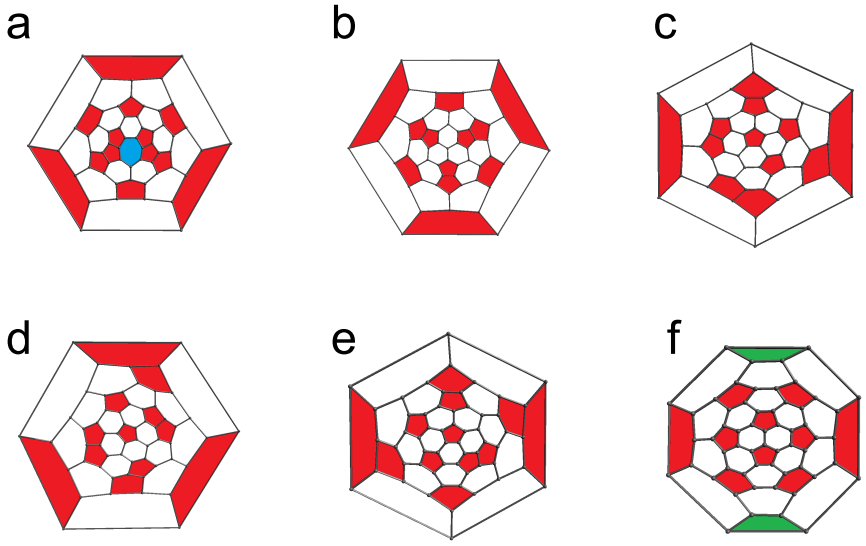

Figure 3.28: Schlegel diagrams of the C_{58}^0 isomers, for which the spectra are shown in figure 3.27, (a) isomer with C_s symmetry, (b) isomer with C_{3v} symmetry, (c) isomer 7465, (d) isomer 12395, (e) isomer 12510, (f) isomer with an octagon. For details of the calculations see text.

Additionally, a C_{58} isomer with an octagon is calculated. This structure is formed by removing one C_2 unit from C_{60}, without allowing for reconstruction of the cage - the simplest route by which C_{58} can be formed by fragmentation of C_{60}.

All calculations are done by Dr. D. Strelnikov [161].

Figure 3.27 shows the comparison of the experimental spectrum with the calculated spectra for six of the C_{58}^0 isomers. The Schlegel diagrams of these isomers are shown in figure 3.28. None of the calculated spectra fit the experimental results, therefore the ground state symmetry of neutral C_{58} remains unknown.

The determination of the ground state symmetry of the C_{58} ions is postponed until measurements with different electron scavengers allow for an unambiguous assignment of the absorption features.

The absorption frequencies of C_{58} and its ions are listed in table 3.9 along with their *fwhm*, their intensity, and a tentative assignment to specific charge states. Strong absorptions from CO_2 in the Ne + 1% CO_2 matrix prevent the identification of some absorption features, an assignment to specific charge states is therefore not carried out for these features.

Further measurements are in progress.

Electronic Spectra

In the NIR, only absorption features of C_{60}^+ and C_{60}^- can be identified (fig. 3.26). As expected, the C_{60}^- features are not present in spectra measured for Ne + 1% CO_2 matrixes. Assuming a similar cation-to-anion ratio for C_{58} as can be seen for C_{60}, roughly equal amounts of C_{58}^+ and C_{58}^- are expected in pure neon matrixes, no C_{58}^- is expected to be present in Ne + 1% CO_2.

A broad absorption feature is present in all spectra, starting at approximately 400 nm (fig. 3.26). The presence of C_{60} and its ions in the matrix hinders the assignment of the UV absorption to any specific species. Additionally, the low optical quality of the matrixes due to the long deposition time leads to interference fringes in the UV range.

3.4.2 Summary

The non-IPR fullerene ion C_{58}^+ was deposited into cryogenic matrixes. For the first time, optical spectra were measured for the isolated neutral species and its ions. Several IR absorption features were identified.

For neutral C_{58}, only four strong absorptions were clearly identified in the IR. This low number of absorptions indicates that one isomer dominates the IR absorptions. DFT calculations of the vibrational spectrum of the 20 lowest ground state energy isomers do not allow an assignment of the experimental spectrum. Comparing the intensity of the most intense C_{58} absorptions to the C_{60} $T_{1u}(1)$ absorption, present due to a contamination of the C_{58}^+ ion beam, the integrated molar absorptivity of C_{58} was estimated to be at least one order of magnitude smaller than that of the C_{60} $T_{1u}(1)$ mode.

The assignment of ionic absorptions remained tentative, because only CO_2 is used as electron scavenger and the assignment could not yet be confirmed using other types of electron scavengers.

In the UV-vis range, no clear absorptions of C_{58} and its ions were detected.

3.5 The Azafullerene $C_{59}N$ and its Ions

By replacing one or more carbon atoms in a fullerene cage with nitrogen, one obtains the so-called azafullerenes, which have a modified geometry and electronic properties [101]. These properties are presently being explored concerning possible applications of $C_{59}N$ derived materials. Of special interest is the intrinsic doping with electrons to form a metallic and superconducting phase, as is observed in alkali or alkaline earth metal doped C_{60} [164, 165, 166]. The first azafullerene to be

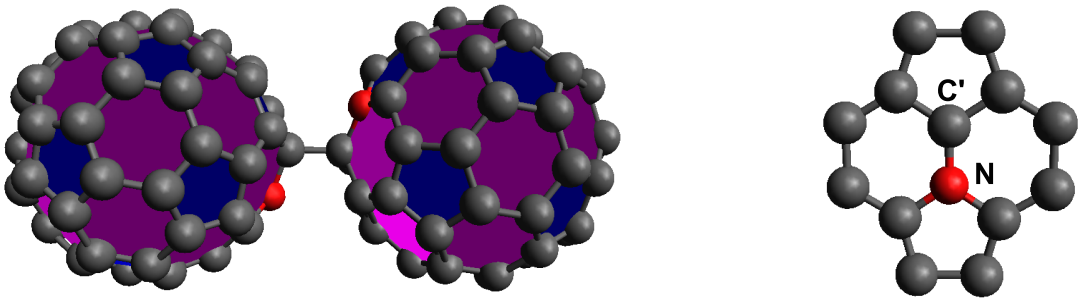

Figure 3.29: Left: The azafullerene dimer $(C_{59}N)_2$ with C_{2h} symmetry. Right: Detail of the cage showing its connection site to the other cage (via the carbon atom marked as C′).

experimentally addressed was $C_{59}N$ [167], which has one additional electron compared to C_{60}, and is therefore isoelectric to C_{60}^-.

However, first experiments [167] showed that $C_{59}N$ is a highly reactive radical, which readily forms the $(C_{59}N)_2$ dimer (shown in figure 3.29) or $C_{59}HN$. Through this reaction, all molecular orbitals are fully occupied and the open-shell structure of the azafullerene is lost. Even though synthesis of $(C_{59}N)_2$ is possible in bulk quantities [168], no industrial application of azafullerenes is reported so far. First experiments showed that the $C_{59}N$ monomer forms a molecular rectifier on isolating surfaces [169]. Furthermore, organic solar cells with azafullerene acceptors have been reported, although with lower efficiency than can be achieved for fullerene acceptors [170, 171].

Quantum chemical calculations [172] and photoemission experiments [173, 174] show that $(C_{59}N)_2$ is nonmetallic with a band gap of 1.4 eV. The dimer is formed by a single C-C bond between the carbon atoms next to the nitrogen atoms, see figure 3.29. The additional electron is localized at the nitrogen [175]. The dimer exhibits a *trans*-configuration, which reduces the repulsion of the electron clouds [175], resulting in a C_{2h} symmetry. For the monomer, DFT calculations have been reported, which suggest a C_s ground state symmetry of $C_{59}N$ [176].

Among other measurements, thin films of the $(C_{59}N)_2$ dimer have been studied by Raman and IR spectroscopy [177, 178, 179], UPS, XPS, and EELS [174], and photoemission spectroscopy [180]. These measurements have established numerous electronic and vibrational properties of $(C_{59}N)_2$ at room temperature and above. The species has been measured to be stable up to 550 K, with irreversible degradation into disordered graphite at higher temperatures [178]. Heating of $(C_{59}N)_2$ to 825 K leads to the sublimation of the radical monomer [181, 178].

The vibrational properties and thermal stability have also been measured of thin films of the hydrogenated $C_{59}HN$ monomer [178, 179].

While some fingerprint lines of $(C_{59}N)_2$ and $C_{59}HN$ were identified in the IR absorption spectrum recorded of thin films at room temperature around 800 cm^{-1} and 1100 cm^{-1}, most of the IR vibrations of the two species could not be distinguished.

Measurements on the isolated monomer are rare, for it is highly reactive and easily dimerizes or attaches a hydrogen atom. However, the isolated monomer has been studied by scanning tunneling microscopy on silicon substrates [181] and on isolating self-assembled monolayers [169]. From these measurements, the electronic properties of the monomer were established, but vibrations have not been probed.

The cation of the $C_{59}N$ monomer, being isoelectric to C_{60}, was expected to be a stable species [182]. $C_{59}N^+$ was isolated as a carborane anion salt, and IR and UV-vis spectra have been measured [182]. While the carborane counterion is inert, the sourroundings are expected to induce a large shift and a broadening of the $C_{59}N^+$ IR absorption frequencies, complicating the comparison to gas-phase frequencies.

The goal of the experiments presented in this section is the identification of infrared fingerprint and UV-vis absorptions of $(C_{59}N)_2$ and $C_{59}N$ isolated in cryogenic neon matrixes, as well as the spectrum of the monomer ions. The material for the experiment was provided by Dr. R. Eigler of the group of Prof. A. Hirsch [183]. The synthesis is described in Ref. [168]. To prevent degradation, the synthesized $(C_{59}N)_2$ was kept under a protective argon atmosphere as a precaution.

3.5.1 Neutral $C_{59}N$ and $(C_{59}N)_2$

For measurements of matrix isolated neutral $C_{59}N$ and $(C_{59}N)_2$, the azafullerene monomer is deposited by direct sublimation from a Knudsen cell and studied in pure neon matrixes. Samples are formed with different dilution ratios of the deposited species. High concentrations of $C_{59}N$ lead to the formation of $(C_{59}N)_2$ dimers in the matrix. Deposition of $C_{59}N^+$ from the ion beam results in very dilute samples, therefore no dimerization is expected. By comparing the spectra of samples with different monomer to dimer ratios, the infrared absorptions of both species in cryogenic neon matrixes can be identified.

Spectra are measured in the IR from 4000 to 400 cm^{-1}, and in the UV-vis from 200 to 1100 nm.

No optical spectroscopy of matrix isolated $(C_{59}N)_2$ or of the radical monomer $C_{59}N$ has so far been reported in the literature.

Results

Vibrational Spectra

The abundance of $(C_{59}N)_2$ can be inferred from the intensity of the fingerprint absorptions at 820 and 840 cm^{-1}. In this region, characteristic stretching modes of C-C and C-N bonds in pentagon rings are present, which are strongly enhanced due to dimerization [179].

Figure 3.30 shows IR spectra obtained from matrixes with lower (fig. 3.30 a) and higher (fig. 3.30 b) dilution ratios. For comparison, the spectrum measured after deposition of $C_{59}N^+$ is shown (fig. 3.30 c, d), where no $(C_{59}N)_2$ features are visible.

Features only occurring after deposition of mass selected $C_{59}N^+$ are due to ionic absorptions and will be discussed in the following section (3.5.2).

Electronic Spectra

NIR absorption spectra were measured after deposition of neutral $C_{59}N$ into cryogenic neon matrixes with different concentrations. Previously not observed features are present in the regions from 920 - 800 nm and 800 - 660 nm (fig. 3.32).

In the UV-vis range below 500 nm, scattering of the matrixes and interference effects hinder the clear identification of absorption features (fig. 3.32). Absorptions are present at the position of previously measured absorption features of $(C_{59}N)_2$ at 433 , 322 , and 250 nm [168].

Discussion

Vibrational Spectra

The features of the monomer and dimer species can be identified in the IR range with the help of the known fingerprint absorptions of $(C_{59}N)_2$ at 819.9 and 841.3 cm^{-1}. The most intense absorptions are listed in table 3.10 and 3.11.

Subtraction of two spectra containing different ratios of neutral $(C_{59}N)_2$ and $C_{59}N$ in a way, that either the monomer or dimer absorptions vanish, results in the extracted spectra shown in figure 3.31 a and c, respectively. The formation of larger clusters, for example trimers or tetramers, is not detected. In all spectra, only absorptions of two different species (i.e. $(C_{59}N)_2$ and $C_{59}N$) are present. All strong absorption features present in the extracted spectrum of the monomer species are also present in the spectrum measured after deposition of the monomer cation.

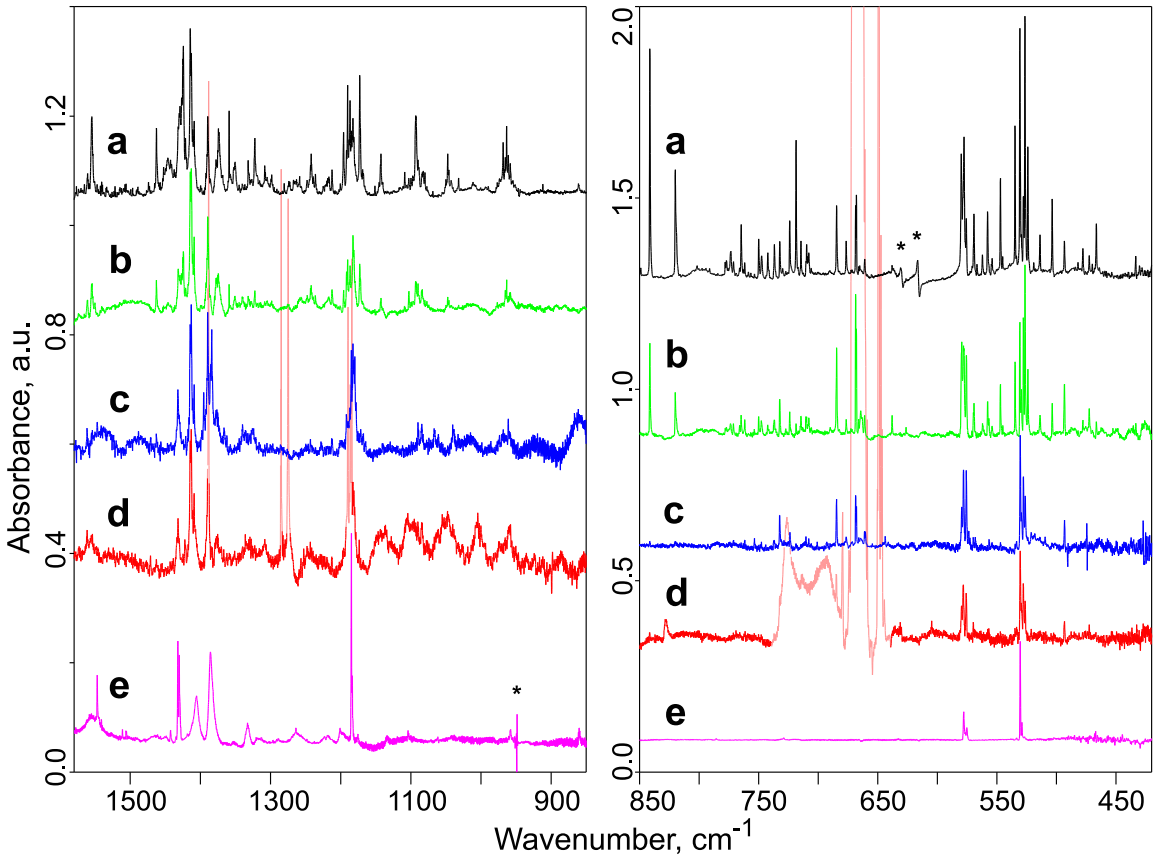

Figure 3.30: Measured IR spectra of $C_{59}N$ and $(C_{59}N)_2$ in Ne with more (a) and less (b) dimers, IR spectra after deposition of $C_{59}N^+$ in Ne (c) and Ne + 1% CO_2 (d, strong CO_2 features in reduced contrast), spectrum of $C_{60}^{0/+/-}$ for comparison (e). Spectra are scaled for similar intensity at 1415 cm^{-1} ($C_{59}N$). MIR range measured with MCT detector, FIR range with CuGe detector. Measurement artifacts are marked (*).

Table 3.10: Assignment of the identified absorptions of the $C_{59}N$ monomer according to DFT (C_s symmetry), frequency, full width at half maximum (*fwhm*) and intensity in neon matrix at 5 K, calculated frequency and integrated molar absorptivity A_{calc}.

	experiment			*theory*	
mode	ν, cm^{-1}	*fwhm*, cm^{-1}	Intensity [a]	ν, cm^{-1}	A_{calc}, $km \cdot mol^{-1}$
A′(89)	1561.4	1.1	w	1575.0	8.8
A′(79);	1432.1	2.7	m	1450.0	9.8
A′′(77) [c]				1447.1	4.8
A′(75)	1414.4; *1413.0* [b]	1.1	vs	1433.2	36.9
A′′(74)	1408.8	0.8	m	1431.2	38.5
A′(74)	1389.6	1.5	s	1401.2	30.5
A′(73)	1376.5	5.7	m	1383.7	22.2
A′(58)	1191.9	2.4	m	1201.2	7.6
A′(56)	*1182.5*; 1181.3 [b]	0.8	s	1191.4	6.8
A′(53)	1089.8	0.7	w	1101.1	2.6
A′(51)	1084.4	1.6	w	1088.7	5.9
A′(39)	732.4	0.6	m	715.2	3.7
A′(29)	684.6	0.7	vs	668.8	9.7
A′(25)	579.5	0.7	vs	578.9	17.8
A′′ (23)	578.1	0.7	s	577.3	20.4
A′(24)	575.6	0.7	vs	574.9	23.5
A′(19);	527.7	0.6	vs	512.8	7.2
A′′(16) [c]				512.4	9.6
A′(18)	526.2	0.5	vs	509.6	5.0
A′(15)	493.2	0.8	s	485.0	5.9

[a] vs - very strong; s - strong; m - medium; w - weak. Very weak absorptions are not included. [b] Site effect in Ne matrix, strongest feature set in italics. [c] Normal mode could not be assigned.

Table 3.11: Assignment of the identified absorptions of the $(C_{59}N)_2$ dimer according to DFT (C_{2h} symmetry), frequency, full width at half maximum (*fwhm*) and intensity in neon matrix at 5 K, calculated frequency and integrated molar absorptivity A_{calc}.

	experiment			*theory*	
mode	ν, cm^{-1}	*fwhm*, cm^{-1}	Intensity [a]	ν, cm^{-1}	A_{calc}, $km \cdot mol^{-1}$
$A_u(82)$	1554.9	2.3	m	1551.8	18.9
$B_u(81)$	1462.6	1.5	w	1480.3	41.0
$B_u(75)$	1429.4; *1424.3* [b]	2.1	m	1431.9	67.9
$B_u(74)$	1373.6	2.9	m	1365.4	55.4
$B_u(73)$; $A_u(74)$ [c]	1359.0	0.5	m	1357.7	2.7
$B_u(72)$	1350.7	2.2	w	1344.7	34.2
$B_u(71)$	1322.4	1.1	w	1329.2	47.6
$B_u(61)$	1190.2	0.8	m	1207.6	21.7
$B_u(60)$	1186.7	0.7	w	1203.2	13.0
$A_u(58)$; $B_u(58)$ [c]	1172.8	1.1	m	1189.0	29.7
$B_u(55)$	1108.8	0.5	w	1104.0	14.7
$B_u(53)$	1092.9	2.6	m	1091.0	16.6
$B_u(50)$	965.4; *963.5* [b]	0.6	w	965.3	32.7
$B_u(47)$	841.3	0.8	vs	826.5	213.8
$B_u(46)$	820.0	0.6	s	800.8	29.3
$B_u(42)$	749.9	0.8	w	747.3	31.7
$B_u(41)$	736.7	0.7	w	734.1	5.8
$B_u(40)$	723.8	0.7	m	723.9	28.1
$B_u(26)$	580.0	0.7	s	579.8	28.2
$A_u(25)$	577.6	0.8	s	577.9	24.4
$B_u(25)$	569.3	0.6	m	570.5	24.7
$B_u(24)$	557.9	0.7	m	559.3	7.5
$B_u(22)$	547.0	0.7	m	546.9	21.8
$B_u(20)$	534.8	0.5	s	528.3	13.1
$A_u(18)$	530.7	0.8	vs	517.5	21.8
$B_u(19)$; $A_u(17)$ [c]	526.5	0.6	vs	512.3	36.2
$B_u(18)$	524.0	0.6	s	510.6	37.5
$A_u(16)$	519.1	0.4	w	506.5	2.6
$B_u(16)$	503.6	0.6	m	480.8	2.9
$B_u(14)$	466.4	0.6	m	456.2	6.8

[a] vs - very strong; s - strong; m - medium; w - weak. Very weak absorptions are not included. [b] Site effect in Ne matrix, strongest feature in italics. [c] Frequency and intensity are taken from the strongest calculated mode.

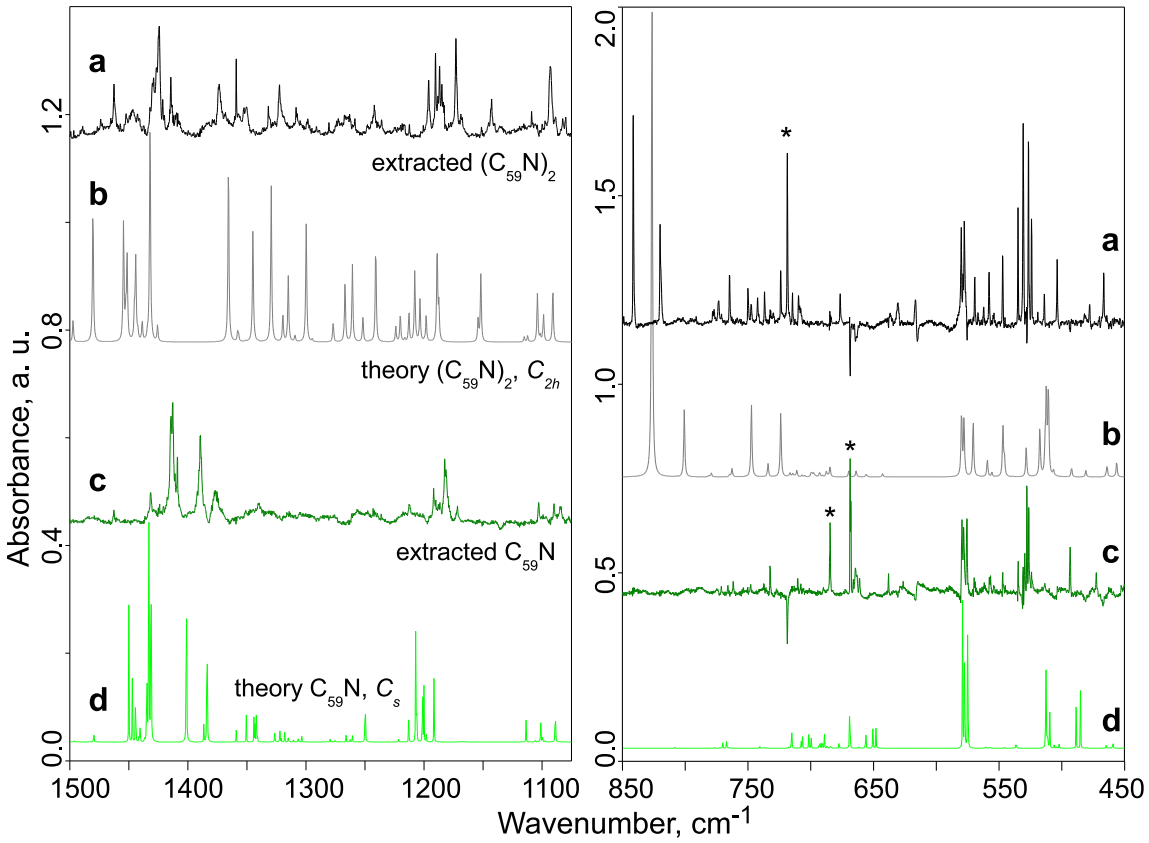

Figure 3.31: Extracted IR spectra of $(C_{59}N)_2$ (a) and $C_{59}N$ (c) with the simulated spectra of $(C_{59}N)_2$ in C_{2h} symmetry (b) and $C_{59}N$ in C_s symmetry (d). MIR range measured with MCT detector, FIR range with CuGe detector. Absorptions of impurities are marked (*).

Compared to the four IR active T_{1u} modes of C_{60} (1432.1 , 1184.8 , 577.8 , and 530.4 cm^{-1} in solid neon at 5 K), the IR spectra of $(C_{59}N)_2$ and $C_{59}N$ show many absorptions. The absorptions derived from the C_{60} T_{1u} modes are the most intense due to the complete removal of degeneracy [178]. While in thin films the difference between IR spectra of $(C_{59}N)_2$ and the hydrogenated monomer $C_{59}HN$ is small [178], the difference of IR spectra of matrix isolated $(C_{59}N)_2$ and $C_{59}N$ is pronounced. The sharp absorption features allow for the assignment of almost all absorptions to a specific species (see tables 3.10 and 3.11).

Similar to the ions of C_{60}, a broadening of the $(C_{59}N)_2$ and $C_{59}N$ absorptions is observed at higher energies. While absorptions below 1000 cm^{-1} have a *fwhm* of less than 1 cm^{-1}, features in the range of 1000 - 1550 cm^{-1} are broadened to around 2 cm^{-1}, possibly due to a Jahn-Teller distortion from tangential cage vibrations.

RI-DFT calculations (Turbomole [33], BP86/def2-SV(P)) are performed to simulate the measured IR spectra. A comparison of the measured and calculated spectra is

shown in figure 3.31.

For the dimer, calculations are performed in C_{2h} symmetry. The geometry was established in previous measurements [175]. The experimentally established transitions of the dimer are reproduced in the region from 1000 to 400 cm^{-1}, especially the fingerprint absorptions at 819.9 and 841.3 cm^{-1}. In the range from 1600 to 1000 cm^{-1}, a multitude of absorption features complicates the assignment of the measured absorptions to calculated vibrational modes. However, the most intense absorptions are reproduced by the calculations.

For the monomer, DFT calculation are performed in C_s symmetry, which has previously been calculated to be the ground state structure [176]. The calculated vibrational transitions reproduce the measured spectrum to a high degree. As can be seen in figure 3.31 c and d, all strong $C_{59}N$ absorption features close to the C_{60} T_{1u} modes are assigned to calculated normal modes.

The assignment of the transitions according to DFT calculations, the absorption frequencies and the *fwhm* in neon matrixes, as well as the calculated frequencies and calculated integrated molar absorptivities are listed in table 3.10 for $C_{59}N$ and in table 3.11 for $(C_{59}N)_2$.

Electronic Spectra

In the NIR, the samples of matrix isolated $(C_{59}N)_2$ and $C_{59}N$ show several absorptions in the range of 660 - 920 nm, the strongest absorptions are at 796.5 nm and 910.8 nm. As can be seen in figure 3.32, the absorptions in the range from 660 - 800 nm are strongest in matrixes containing high concentrations of $(C_{59}N)_2$, therefore they are assigned to the dimer. Absorptions of the monomer are identified in the 800 - 920 nm region.

For the monomer, all further features are within 1400 cm^{-1} to the blue from the most intense absorption at 910.8 nm. Therefore, the absorption at 910.8 nm is assigned to the band origin, and the additional weaker absorptions to vibronic bands. The energy difference to the first vibronic feature is approximately 265 cm^{-1}, roughly corresponding to a radial cage vibration frequency.

For the dimer, the absorption at 796.5 nm is assigned as the band origin, with a less intense vibronic progression within 2100 cm^{-1}. The energy difference of the first vibronic feature at 790.8 nm to the band origin is only 80 cm^{-1}. From DFT calculations, the $A_g(1)$ and $B_g(1)$ modes are expected in this energy range. However, a site effect in neon matrixes, or an additional electronic transition, cannot be ruled out.

TD-DFT calculations support this assignment with an electronic transition of the monomer ($2^1A' \leftarrow X^1A'$) at 980 nm, and of the dimer ($3^1B_u \leftarrow X^1A_g$) at 873 nm.

The UV-vis absorption spectra of matrix isolated $(C_{59}N)_2$ and $C_{59}N$ are similar to the previous measurements of $(C_{59}N)_2$ in cyclohexane solution [168]. In matrix, pronounced maxima are found at 433 , 322 , and 250 nm (fig. 3.32). No clear differences are observed in the UV region for the monomer and the dimer. The different overall intensity of the measured absorptions is due to the different amount of $(C_{59}N)_2$ and $C_{59}N$ deposited into the matrixes.

The absorption at 433 nm, previously identified in solution [168], is pronounced in matrixes with high concentrations of $(C_{59}N)_2$ (fig. 3.32 a and b). In matrixes with no $(C_{59}N)_2$, the 433 nm feature is not observed (fig. 3.32 c and d). The low absorbance in matrixes produced with mass selected ions hinders the unambiguous observation of the 433 nm feature in these samples. Still, the feature at 433 nm is tentatively assigned to the $(C_{59}N)_2$ dimer.

TD-DFT calculations predict close-lying electronic transitions in the UV range for both $(C_{59}N)_2$ and $C_{59}N$. The halfwidth of the measured absorptions is about 3000 cm^{-1}, which hinders the identification of any single transition. The absorption spectra of $(C_{59}N)_2$ and $C_{59}N$ are almost identical to UV absorption spectra of C_{60}. The main difference is the azafullerene absorption at 433 nm. UV-vis spectra of the different species are shown in figure 3.32.

The similar UV spectra of $(C_{59}N)_2$, $C_{59}N$, and C_{60} indicate plasmonic-like excitations of fullerenes and azafullerenes, which are only weakly influenced by small changes of the cage symmetry and by the addition or removal of a single electron.

3.5.2 The Ions of $C_{59}N$

$C_{59}N^+$ is produced by electron impact ionization of sublimated $(C_{59}N)_2$. As was already mentioned, heating of $(C_{59}N)_2$ leads to the sublimation of the $C_{59}N$ monomer. An ion current of roughly 15 nA is co-deposited with an excess of Ne or Ne + 1% CO_2, which are used as matrix gases.

During deposition, the hydroazafullerene ion $C_{59}HN^+$, if present, cannot be rejected by the mass filter due to the small difference in mass. However, fingerprint IR absorptions of neutral $C_{59}HN$ in thin films have previously been measured at 611 and 1127 cm^{-1} [178]. In matrixes formed by deposition of $C_{59}N^+$, no absorptions are observed close to either wavenumber. Therefore, the presence of $C_{59}HN^+$ in concentrations relevant for spectroscopy is excluded.

Due to the low ion current, deposition over three to five days is necessary to observe weak absorptions. Comparing the spectra measured from the different matrixes allows to identify the $C_{59}N^+$ and $C_{59}N^-$ absorptions. Absorption features of neutral $C_{59}N$ are identified after its direct deposition (see section 3.5.1).

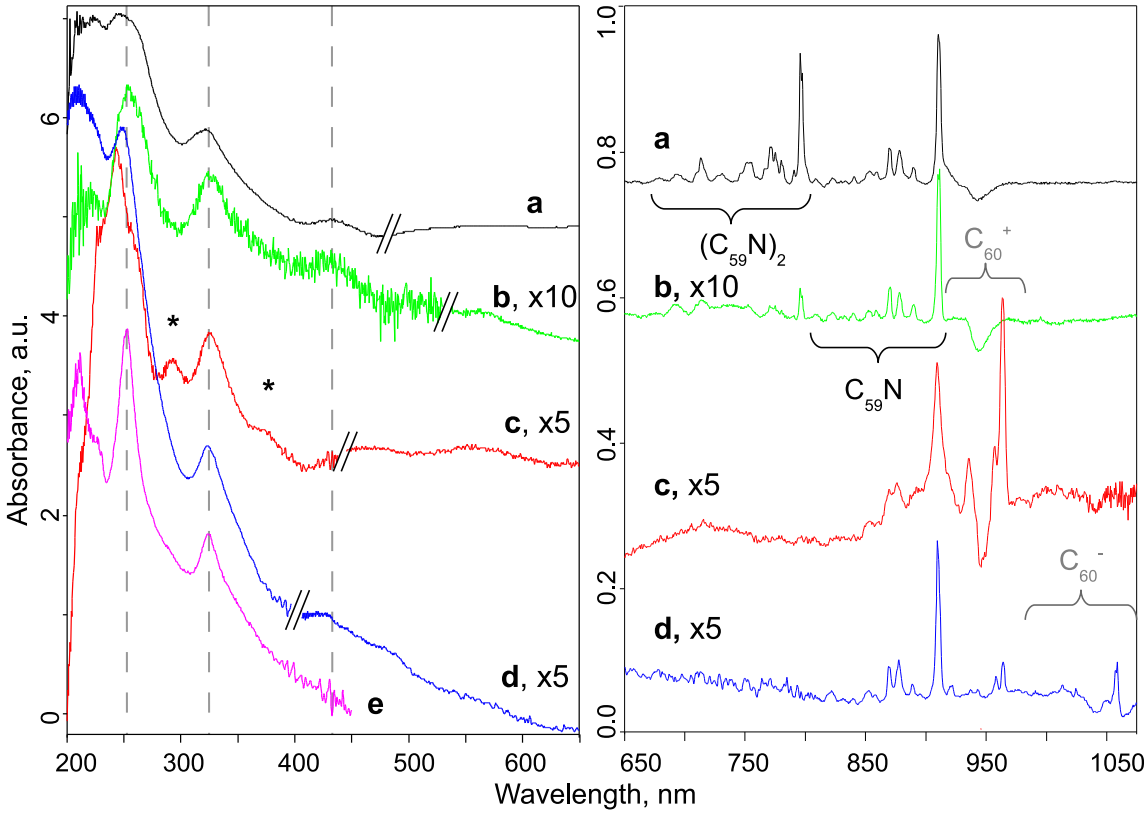

Figure 3.32: Measured UV-NIR spectra of $C_{59}N$ and $(C_{59}N)_2$ in Ne with high (a) and low (b) concentration of dimers, UV-NIR spectra upon deposition of $C_{59}N^+$ in Ne + 1% CO_2 (c) and in Ne (d), spectrum of C_{60}^0 for comparison (e). UV range measured with deuterium light source, vis-NIR range with halogen lamp. Interference effects are marked (*). The intensities of the spectra are scaled for clarity.

The matrixes formed by deposition of mass-selected $C_{59}N^+$ show impurities from $C_{60}^{0/+/-}$. The mass resolution used for the deposition is not sufficient to separate C_{60}^+ and $C_{59}N^+$. The C_{60}^+ ions in the beam are probably generated in the electron impact ionization source: C_{60} previously adsorbed on the walls of the vacuum chamber is sublimed and subsequently ionized.

Spectra are measured in the IR in the range from 4000 to 400 cm^{-1}, and in the UV-NIR from 200 to 1100 nm.

Results

Vibrational Spectra

In figure 3.33, the IR spectra of $C_{59}N^+$ in Ne (b) and in Ne + 1% CO_2 (c) are shown. Several previously not observed absorption features are present in addition to absorptions of the neutral $C_{59}N$ monomer and of $C_{60}^{0/+/-}$.

In the range of 800 - 600 cm^{-1}, strong absorptions of CO_2 hinder the assignment of ionic absorptions. Some absorptions in other regions are masked by sharp features of CO_2, $(CO_2)_n$, and their anions.

Electronic Spectra

In the NIR, no additional features are present following the deposition of $C_{59}N^+$, as can be seen in figure 3.32 c and d. The NIR absorption features of neutral $C_{59}N$ and C_{60}^+ are visible in all measurements, C_{60}^- is only present in pure neon matrixes. No absorptions of the dimer can be observed in the 660 - 800 nm range.

In the region of 200 - 500 nm, the spectra of matrixes containing $C_{59}N$ neutrals and ions in different ratios are close to identical to the spectra of neutral $C_{59}N$ in neon matrixes.

Discussion

Vibrational Spectra

Only few ionic absorptions can be identified, and most of the features exhibit a low intensity. The absorptions of $C_{59}N^-$ at 1395.3 and 1383.8 cm^{-1} are the most intense ionic absorptions observed. In the Ne + 1% CO_2 matrix the features of $C_{59}N^-$ vanish, while the features of $C_{59}N^+$ roughly double their relative intensity. However, the spectrum is still dominated by absorptions of the neutral $C_{59}N$ monomer.

The presence of $C_{59}N^+$ in the matrix is inferred from the absorptions of CO_2^- and $(CO_2)_n^-$ at 1660 and 1860 cm^{-1}, respectively [126].

It is possible to roughly approximate the integrated molar absorptivity of $C_{59}N^+$. From IR spectra measured for C_{60}^+ deposited in Ne + 1% CO_2, the absorptivity of the CO_2^- and $(CO_2)_2^-$ absorptions at 1660 and 1860 cm^{-1} can be estimated. Under the assumption, that the positive charge of C_{60}^+ is completely compensated by CO_2^- and $(CO_2)_2^-$ counterions: $N(C_{60}^+) = N_1(CO_2^-) + N_2((CO_2)_2^-)$, the estimated integrated molar absorptivities are: $A_{CO_2^-} = (460 \pm 150)$ km·mol^{-1} and $A_{(CO_2)_2^-} = (490 \pm 160)$ km·mol^{-1}. With this value, the integrated molar absorptivity of $C_{59}N^+$ can be estimated, assuming that no counter-ions other than CO_2^- and $(CO_2)_2^-$ are present: $N(C_{59}N^+) = N_1(CO_2^-) + N_2((CO_2)_2^-)$.

The integrated molar absorptivity of the $C_{59}N^-$ anions is estimated within the assumption, that no counter-ions besides $C_{59}N^-$ are present in Ne matrixes. Therefore, the anionic integrated molar absorptivity is likely to be a lower limit to the actual value.

The accuracy of the approximation is taken to be around $\pm$50%, because no direct measurement of the integrated molar absorptivity of $C_{59}N^+$ and $C_{59}N^-$ is achieved. Other counter-ions, for example H_2O^- or CO^-, are not considered in the approximation, but are expected to be present in the matrixes. The estimated integrated absorptivities for the IR absorptions of $C_{59}N^{+/-}$ are listed in table 3.12.

For neutral $C_{59}N$, no integrated molar absorptivity is given. Annealing of the matrix does not lead to a change in the absorption intensities of $C_{59}N^{0/+/-}$, therefore no integrated molar absorptivities could be estimated for the neutral species.

DFT calculations (Turbomole [33], BP86/def2-SVP) are performed for $C_{59}N^+$ and $C_{59}N^-$ in C_1 symmetry. The most intense modes are calculated to be in the proximity of the C_{60} T_{1u} frequencies.

As shown in figure 3.33, the calculated IR transitions of $C_{59}N^+$ do not match the experimentally identified absorptions: the strong absorptions calculated around 1450 , 1200 , and 580 cm^{-1} are not identified in the experiment. Possibly the absorptions of $C_{59}N^+$ coincide with the more intense absorptions of the neutral monomer, and are thus masked. It is also possible, that calculations of $C_{59}N^+$ in a higher symmetry than C_1 reproduce the experimental spectrum to a higher degree. In DFT calculations, no higher symmetry is identified.

For $C_{59}N^-$, the calculations reproduce the main features of the experimental spectrum. The calculated integrated molar absorptivities are overestimated by a factor of 5 to 10.

All calculated values are listed in table 3.12.

Some of the identified $C_{59}N^-$ absorptions exhibit a large *fwhm*, indicating a Jahn-Teller distortion. However, unlike in C_{60}^-, this effect can not be observed for all

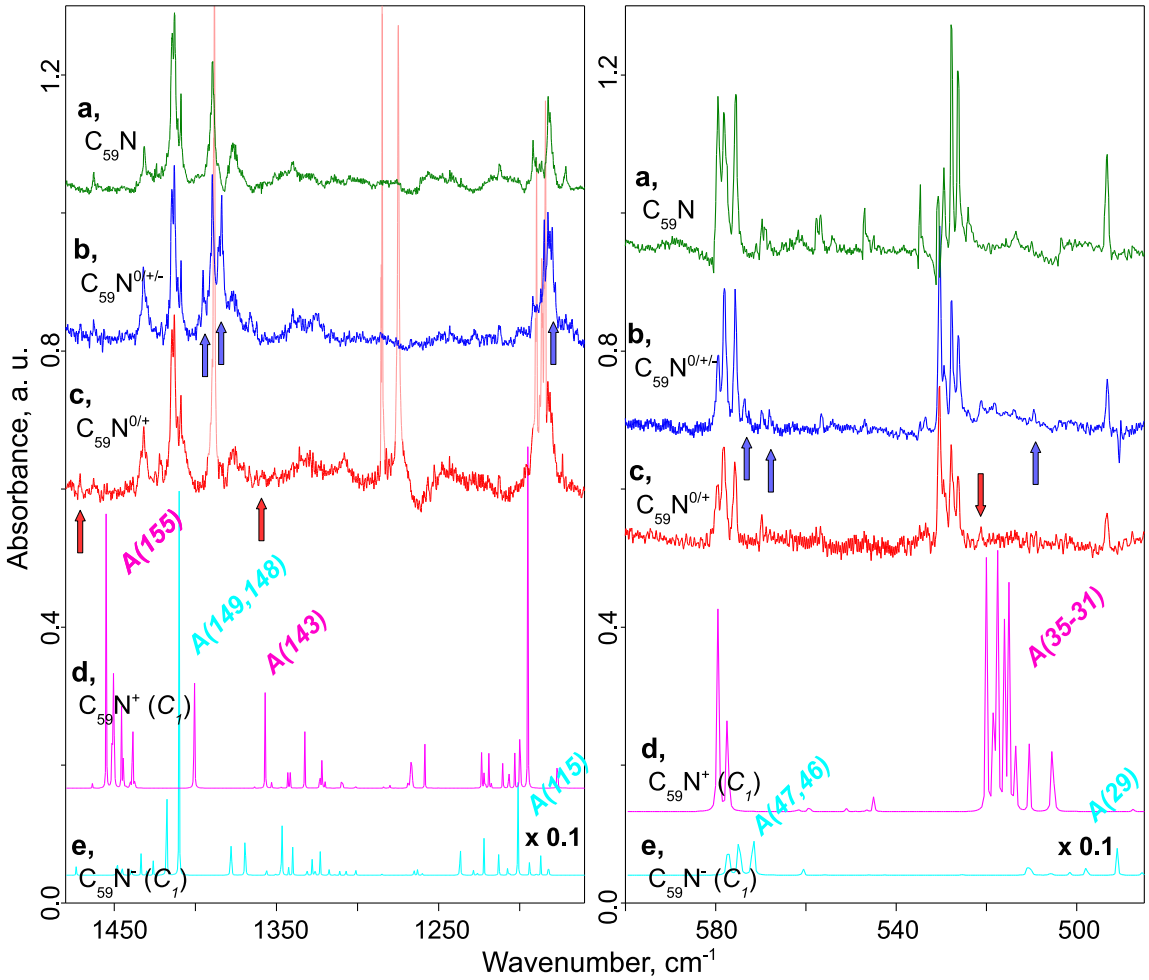

Figure 3.33: Extracted IR spectra of $C_{59}N$ (a), IR spectrum of $C_{59}N^+$ in Ne (b) and in Ne + 1% CO_2. Identified ionic absorptions are marked with arrows (cations: red, anions: blue). Calculated spectra of the cation (d) and anion (e). Only the most intense calculated features are visible in the spectra.

Table 3.12: Assignment of the identified absorption lines of $C_{59}N^+$ and $C_{59}N^-$ according to DFT, frequency, full width at half maximum (*fwhm*) and integrated molar absorptivity A_{Ne} in neon matrix at 5 K, calculated frequency and integrated molar absorptivity A_{calc}.

		experiment			*theory*	
	mode	ν, cm^{-1}	*fwhm*, cm^{-1}	A_{Ne}, $km{\cdot}mol^{-1}$	ν, cm^{-1}	A_{calc}, $km{\cdot}mol^{-1}$
$C_{59}N^+$	- [a]	1471.2	1.0	2±1	-	-
$C_{59}N^+$	A(143)	*1366.2*; 1362.2 [b]	1.5	3±1.5	1356.9	4.3
$C_{59}N^+$	A(31-35) [c]	521.2	0.7	3±1.5	517.6	14
$C_{59}N^-$	A(149)	1395.3	0.7	11±5.5	1417.7	86
$C_{59}N^-$	A(148)	*1383.8*; 1385.2 [b]	1.1	29±15	1410.0	134
$C_{59}N^-$	A(115)	1179.9	0.8	3±1.5	1201.1	45
$C_{59}N^-$	A(108)	1066.6	2.5	3±1.5	1118.5	2.4
$C_{59}N^-$	A(104)	1060.7	1.6	2±1	1096.3	6.0
$C_{59}N^-$	A(102)	1039.5	4.0	13±6.5	1073.5	24
$C_{59}N^-$	A(98, 99) [c]	961.1	0.7	3±1.5	977.1	3.6
$C_{59}N^-$	A(47)	573.6	0.7	4±2	574.8	43
$C_{59}N^-$	A(46)	568.1	1.0	2±1	571.7	44
$C_{59}N^-$	A(29)	509.5	0.6	2±1	491.0	9.2

[a] No normal mode could be assigned, details see text; [b] Site effect in Ne matrix, most intense line is set in italics; [c] Frequency and intensity are taken from the most intense calculated mode.

features at higher energies. For $C_{59}N^+$ only three absorptions are identified, the presence of distortions in the spectrum can only be speculated on.

Electronic Spectra

As is seen in figure 3.32, no additional absorptions of the $C_{59}N$ ions are visible in the NIR. The visible features result from electronic and vibronic transitions of fullerene C_{60} anions (1060 to 970 nm, not in Ne + 1% CO_2), cations (970 to 900 nm), and neutral $C_{59}N$ monomers (920 to 800 nm). Transitions of the $(C_{59}N)_2$ dimer are not present. The presence of $C_{60}^{+/-}$ in the matrixes is a result of the low resolution of the mass filter. Heating of the source chamber leads to sublimation and ionization of C_{60}, which was previously adsorbed to the walls of the vacuum chamber.

Comparing the $C_{59}N$ species to the corresponding isoelectronic C_{60} species, a trend regarding electronic transitions in the NIR is observed: while for $C_{59}N$ and C_{60}^- NIR transitions are detected, no transitions occur for $C_{59}N^+$ and C_{60}. However, while for $C_{59}N^-$ no NIR absorptions are detected, NIR transitions of the isoelectronic C_{60}^{2-} have been reported [144].

While no IR features of the C_{60} ions are present, their NIR absorptions exhibit approximately the same intensity as the NIR absorptions of $C_{59}N$, which is readily identified in the IR. Therefore, the ratio of the integrated molar absorptivity of the IR and NIR absorption of $C_{59}N$ is estimated to be at least one order of magnitude less than for C_{60}.

In the UV-vis range, absorptions are visible at 322 and 250 nm after the deposition of $C_{59}N^+$. With a *fwhm* of the features of around 3000 cm^{-1}, no difference in the absorption position is visible. The absorption at 433 nm, which is detected in matrixes after the deposition of neutral $C_{59}N$, is not observed after $C_{59}N^+$ deposition. The low signal-to-noise ratio, due to the low density of the species, hinders an unambiguous assignment, tentatively the absorption at 433 nm is assigned to the $(C_{59}N)_2$ dimer.

The spectrum of $C_{59}N^+$ in the Ne + 1% CO_2 matrix exhibits additional features in the range from 400 to 200 nm. These features are interference fringes, which could not be subtracted completely. Additional absorptions of $C_{59}N^+$ may be masked.

TD-DFT calculations of the azafullerene $C_{59}N$ ions predict close-lying electronic transitions in the UV range, consistent with the measurements. The similarity of the calculated and measured spectra of the azafullerene dimer, monomer, and its ions in the UV can be rationalized by plasmon-like excitations.

3.5.3 Summary

The azafullerene $(C_{59}N)_2$ and its radical monomer $C_{59}N$, as well as the monomer ions, were measured by optical spectroscopy isolated in cryogenic matrixes. The isolated monomer and its ions were measured for the first time in a weakly interacting environment.

In the IR, fingerprint absorptions of the neutral monomer and dimer were identified. For the ions, only few absorptions were identified. Broadening of the identified absorption features at frequencies above 1000 cm^{-1} indicates a dynamic Jahn-Teller distortion for all species.

For $C_{59}N^+$, no strong IR absorptions were identified, either because the absorptions have an unexpectedly low integrated molar absorptivity, or because the cationic absorptions coincide with intense absorptions of the $C_{59}N$ monomer. The identified absorptions of $C_{59}N^-$ have larger integrated molar absorptivites. The most intense

$C_{59}N^-$ absorption is about ten times more intense than the identified absorptions of $C_{59}N^+$.

The absorptivities of $C_{59}N^{+/-}$ are estimated from the absorptions of CO_2^- at 1660 cm^{-1} and $(CO_2)_2^-$ at 1860 cm^{-1}. The estimated integrated molar absorptivities of the absorptions of the counterions are $A_{CO_2^-}$ = (460 ± 150) km·mol^{-1} and $A_{(CO_2)_2^-}$ = (490 ± 160) km·mol^{-1}.

DFT calculations of the neutral $(C_{59}N)_2$ in C_{2h} symmetry and $C_{59}N$ in C_s symmetry reproduce the experimental spectra very well. The calculated spectrum of $C_{59}N^+$ in C_1 symmetry could not reproduce the experiment, either because not all absorptions were identified in the experiment, or because the ground state symmetry was not determined correctly. Calculations for $C_{59}N^-$ in C_1 symmetry reproduced the main absorption features in the IR correctly.

In the NIR, electronic transitions with vibronic bands were identified for $C_{59}N$ and $(C_{59}N)_2$ with band origins at 910.8 nm ($2^1A' \leftarrow X^1A'$) and 796.5 nm ($3^1B_u \leftarrow X^1A_g$), respectively.

In the UV range, broad absorption bands with maxima at 250 , 322 , and 433 nm were identified for the dimer, which are similar to absorptions measured in solution [168, 182]. For the monomer and its ions no additional features were observed. The 433 nm absorption was not observed in matrixes containing none, or small amounts, of the dimeric species. The absorption at 433 nm was tentatively assigned as a characteristic transition of the $(C_{59}N)_2$ dimer.

The identified UV absorptions of $(C_{59}N)_2$ and $C_{59}N^{0/+/-}$ coincide with the absorptions of C_{60} and its ions. Neither electronic nor geometric changes strongly affect the plasmonic-like electronic transitions.

4 Lanthanoid Diketonates in Cryogenic Matrixes

4.1 Introduction

Photophysical characterization of species by luminescence spectroscopy is used for a wide range of different systems and different properties. The luminescence characteristics of a system are often altered by their environment or charge state: the exchange of a counterion, the charge of a ligand or of a coordinated metal atom, or even variations in the protonation site can lead to significant changes of the molecular electronic states, and thus to the light emission of the systems. Such variations are difficult to quantify in condensed phase measurements, where different charge states and geometries are superimposed. Furthermore, not all species of interest can be stabilized in condensed phase. In solution, elusive species can often be produced, however, the stoichiometry and geometry of the emitting species is determined by poorly controllable solution equilibria.

In gas phase, the stoichiometry and the charge can easily be selected by mass spectrometry, selection of different isomers is also possible, but more difficult. Comparison to theoretical calculations is facilitated, because no environmental effects have to be taken into account. Consequently, such well-defined gas-phase species may be regarded as model systems, for which energy transfer within the molecule, the electronic states, and charge effects can be studied in detail [184, 185].

However, gas phase measurements have to compensate for two disadvantages, which complicate the measurement of some species: energy dissipation via non-radiative processes is slow, which often leads to photofragmentation, and the space-charge limit (ca. 10^6 ions per cm^{-3}) prevents the accumulation of large numbers of ions, which effectively prevents the measurement of weakly absorbing and/or emitting species.

To avoid these limitations, and nonetheless keep most of the advantages of gas phase experiments (i.e. selectivity, isolation, and measurement on elusive species), the ionic species of interest can be isolated in cryogenic noble gas matrixes. While the interactions with the solid noble gas are small in most cases, energy dissipation is facilitated, and the ion density may be orders of magnitude larger than in gas phase, due to the presence of counterions.

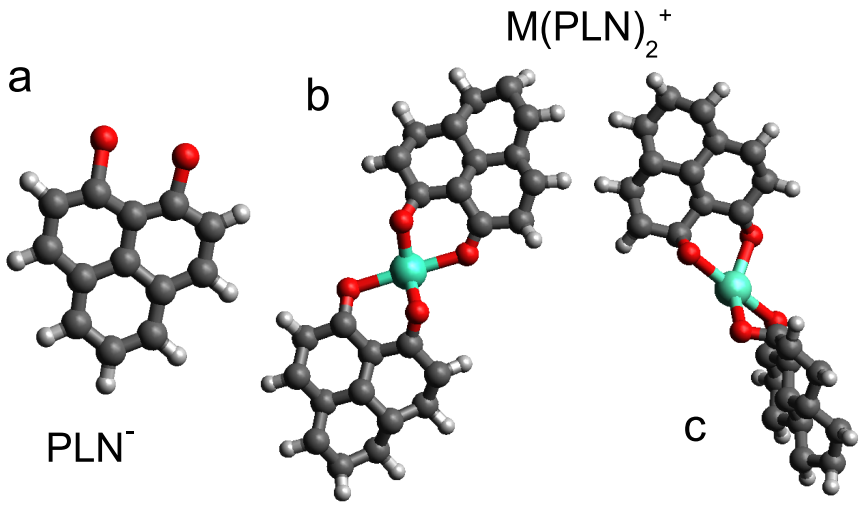

Figure 4.1: Representation of the deprotonated, and consequently anionic, 9-hydroxyphenalen-1-one (PLN^-) ligand (a) and of a lanthanoid diketonate complex ($Ln(PLN)_2^+$) in D_{2h} (b, planar complex) and D_{2d} (c, ligands perpendicular) symmetry. Calculations suggest a lower ground state energy for the D_{2d} symmetry isomer [189].

In this work, lanthanoid coordination complexes are presented, which have a wide range of applications, for example as active material in light emitting diodes [186], memory devices [187], and downconversion layers, for improving the efficiency of solar cells [188]. Lanthanoids are used for their luminescence over a wide spectral range, from the NIR to the UV. The optical transitions of the lanthanoids involve the shielded $4f$ orbitals with parity forbidden $4f$-$4f$ transitions, resulting in long lifetimes of the excited states and narrow emission bands. This results in low absorption coefficients, and narrow absorption features of the lanthanoids. To enhance the absorption, strongly absorbing antennas are coordinated to the lanthanoids: Such antennas absorb energy over a wide spectral range, and are able to transfer the energy efficiently to the lanthanoid. For the presented measurements, diketonate complexes have been used as antennas. An example of the systems is shown in figure 4.1.

The luminescence of neutral, uncomplexed 9-hydroxyphenalen-1-one (HPLN) upon UV photoexcitation has been studied in neon matrixes [190]. Primarily fluorescence of the first excited singlet state S_1 was observed with a radiative lifetime of less than 10 ns, and band origins at 430.9 and 432.2 nm. The splitting occurs due to a proton transfer at the oxygen sites. Additionally, weak phosphorescence from the lowest-lying triplet state T_1 was observed. This triplet state has a lifetime of around 25 ms with the band origin at 575 nm. Both singlet and triplet state emissions show rich vibronic sidebands at lower energies.

To understand the properties of metal diketonate complexes and the energy trans-

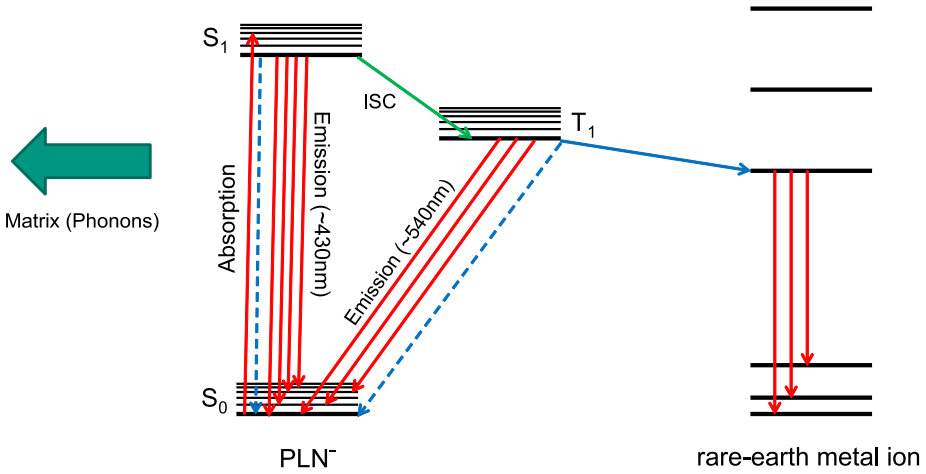

Figure 4.2: Jablonski diagram showing possible energy transfer steps following the $S_0 \rightarrow S_1$ excitation of the ligand (ISC: intersystem crossing). The process strongly depends on the available energy states of the metal ion. Blue arrows mark possible radiationless transitions, the excess energy is dissipated via matrix phonons.

fer from the ligand to the central metal atoms, simple systems have to be investigated which can be modelled by theory. The systems studied in this work are anionic deprotonated 9-hydroxyphenalen-1-one (PLN) ligands complexed to emitting cationic lanthanoid (III) atoms. The PLN ligands are known to effectively sensitize lanthanoid emitters at wavelength regions from the UV to the visible [191]. As outlined in figure 4.2, the energy transfer from the absorbing antenna to the complexed metal atoms is achieved via the PLN triplet state. For the energy transfer to be effective, the acceptor energy state of the metal has to be slightly lower in energy than the PLN triplet donor state, to prevent back transfer.

To systematically characterize the energy transfer from the ligand to the central lanthanoid ion, and to supply data against which theoretical calculations can be tested, different metal atoms are used for the simplest monocationic clusters, composed of one trivalent metal center and two anionic PLN ligands. For more complex systems, Eu^{3+} is used as the emitter, because its $^5D_0$ state can be efficiently populated by energy transfer from the PLN ligand, and it shows a hypersensitive $^5D_0 \rightarrow ^7F_2$ emission [191, 192].

A large number of results have previously been reported for the luminescence properties of rare-earth metals and their ions. An overview of the electronic energies of the different ionic states is given in Martin *et al.* [193]. The reports cited in the following to compare the measured data to published results are chosen so as to allow easy comparison to the results presented in this work. No complete overview of previous measurements for each lanthanoid is given.

In the experiment, the mass-selected lanthanoid diketonate ion current does not

exceed 300 pA for any species, therefore the ions are well separated in the matrixes, with an estimated ratio of guest species to matrix atoms of 1:10^5 to 1:10^7. All ions are produced with the electrospray ionization source (details see chapter 2.2.3). The solvent used for all species is dimethyl sulfoxide (DMSO).

All systems studied in this work were synthesized by Dr. B. Schäfer in the group of Prof. M. Ruben [194] (description of synthesis: [195]). Calculations were done by J. Chmela and Dr. M. Harding in the group of Prof. W. Klopper [189]. The presented gas phase data were measured by Dr. J.-F. Greisch [196].

For gas-phase measurements, ions were produced by a nanoES ion source, mass selected, and then injected into an electrostatic Paul ion trap held at 83 K. The ions were stored on a timescale of 50 to 90 s under a helium pressure of 0.2 mbar, to achieve thermalization. Each bunch of ions was irradiated with an argon-ion laser, either with the 476.5 nm or the 458 nm line. A detailed description of the apparatus, and previously published results of the gas phase measurements, are found in refs. [184] and [192].

4.2 Matrix Effects of Lanthanoid Diketonates

To quantify the effect of matrix isolation for the luminescence spectra of lanthanoid diketonate complexes, and to establish matrix isolation of electrosprayed ions as an additional experimental method for the investigation of weakly emitting species, several preliminary experiments are performed.

The influence of the matrix environment on different test systems with different energy transfer processes and covering a large $^m/_z$-range is studied. Different electron scavengers are added to the matrix gas to assess whether neutralization of the species significantly affects the measurements. The complexation with different molecules, either in gas phase, or in matrix, is studied. Argon is used as matrix gas to study the consequences of providing a more strongly interacting environment.

The species used to quantify matrix effects on lanthanoid diketonate complexes are $Gd(PLN)_2^+$, $[Gd(PLN)_3Na]^+$, $[Gd_9(PLN)_{16}(OH)_{10}]^+$, and $[Eu_9(PLN)_{16}(OH)_{10}]^+$, with the deposited amounts being in each case on the order of femto- to picomoles.

All of these species have been studied in gas phase [192, 196]. For the gadolinium complexes, no energy transfer from the ligands to the central metal atoms was observed, the first excited Gd^{3+} state ($^6P_{7/2}$) lies approximately 32 000 cm^{-1} above its ground state. The emitting state of these complexes was the PLN triplet state. For Eu^{3+}, on the other hand, energy transfer from the PLN triplet state to the Eu^{3+} $^5D_0$ state was observed. Emissions from the $^5D_0 \rightarrow {}^7F_J$ transitions were detected.

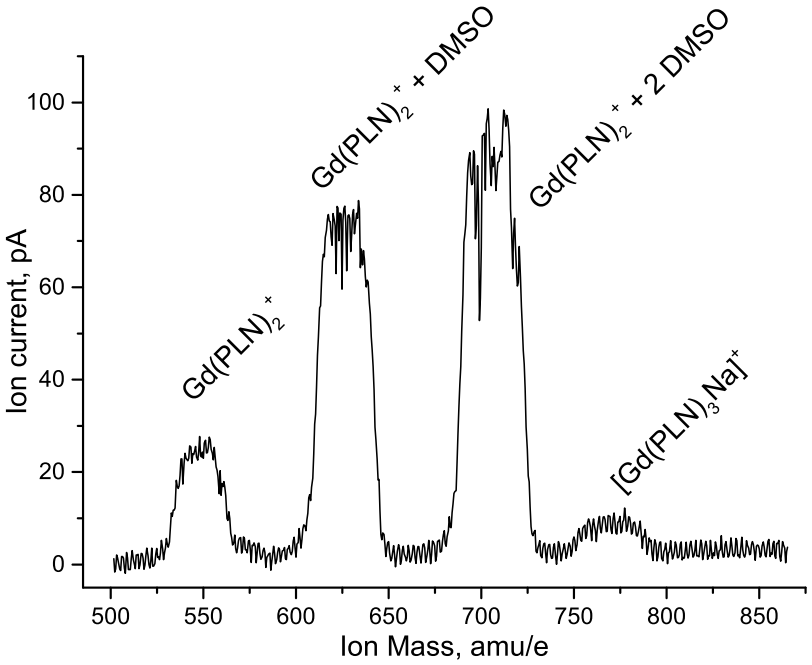

Figure 4.3: Mass spectrum of $Gd(PLN)_4Na$ electrosprayed from DMSO solution. The ratio of the different cationic species changes with the spraying conditions.

$Gd(PLN)_2^+$

$Gd(PLN)_2^+$ is deposited in mass resolving mode, the measured mass spectrum is shown in figure 4.3[6]. $Gd(PLN)_2^+$ is deposited in pure Ne and Ar matrixes, and in neon matrixes with different ratios of electron scavengers: Ne + 0.01% CCl_4, Ne + 0.1% CO_2, Ne + 0.3% CO_2, and Ne + 0.7% CO_2. Furthermore, the addition of one or two dimethyl sulfoxide solvent molecules to the $Gd(PLN)_2^+$ complex is studied in Ne matrixes.

As can be seen in figure 4.4, $Gd(PLN)_2^+$ exhibits sharp, vibronically resolved emissions from the PLN $T_1 \rightarrow S_0$ phosphorescence. The presence of the heavy central metal increases the intersystem crossing rate, efficiently quenching the PLN $S_1 \rightarrow S_0$ emissions [197, 198]. The gas-phase and neon matrix luminescence spectra (fig. 4.4 a and d) are close to identical. In the matrix, the band origin of the PLN triplet emission is shifted to 553 nm, which corresponds to a red-shift of 20 cm^{-1}. The vibronic progression is almost identical, with a slight increase of the red-shift to 50 cm^{-1} for the last clearly distinguishable vibronic emission feature. The emission lines of $Gd(PLN)_2^+$ in neon matrixes at 5 K are slightly narrower than in gas phase at 83 K. Apparently, the lower temperature and better thermalization in matrixes overcompensates the expected matrix induced broadening.

[6]Mass spectra of different $M(PLN)_2^+$ species are similar.

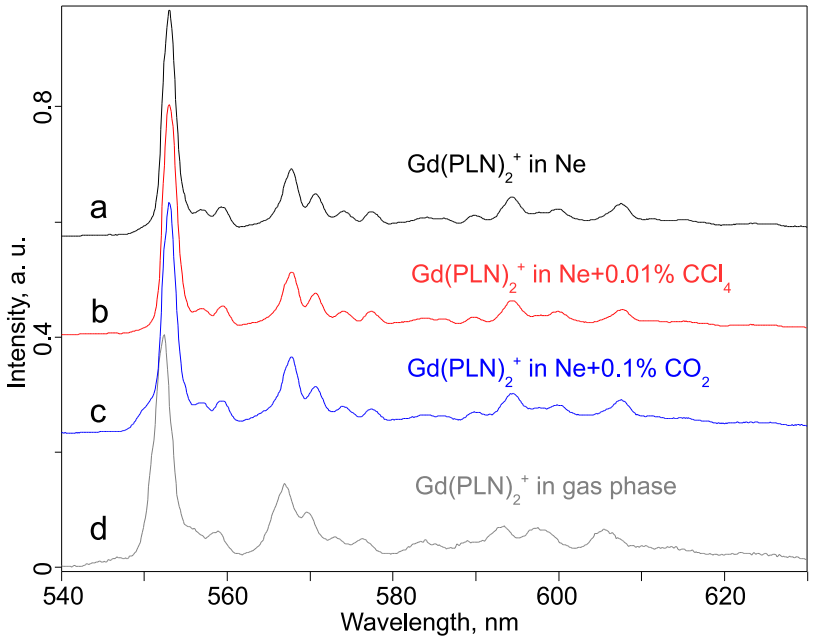

Figure 4.4: Emission spectra of $Gd(PLN)_2^+$ in Ne (a), Ne + 0.01% CCl_4 (b), Ne + 0.1% CO_2 (c), and in gas phase (d). No strong influence of the matrix occurs, the neutral species is not detected. Experimental parameters: (a), (b), (c): $\lambda_{excitation}$= 375 nm, 200 $^W/_{cm^2}$, T = 5 K; (d): $\lambda_{excitation}$= 458 nm, 400 $^W/_{cm^2}$, T = 83 K.

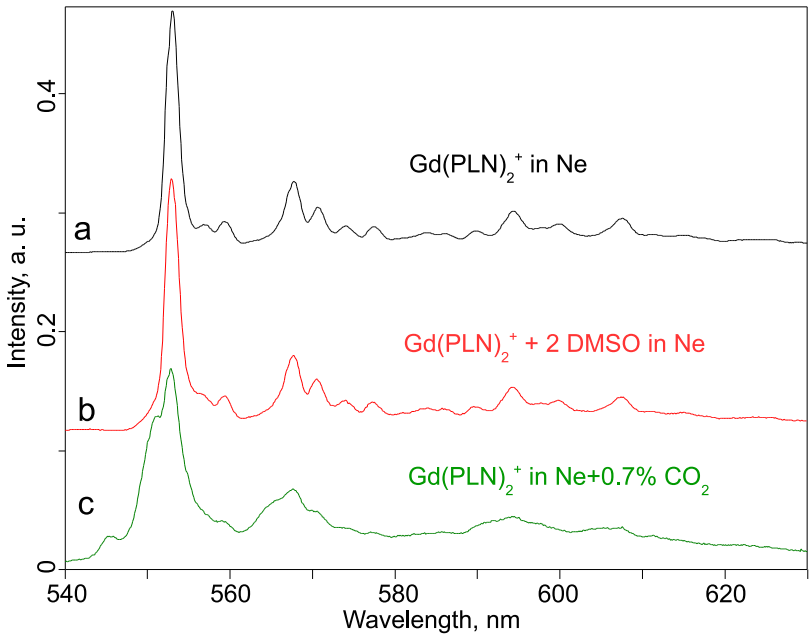

Figure 4.5: Comparison of the emission spectrum of $Gd(PLN)_2^+$ in Ne (a) to complexes with 2 DMSO adducts (b), and complex formation in the matrix with increased concentration of CO_2 (0.7%) (c). Experimental parameters: (a), (b), (c): $\lambda_{excitation}$= 375 nm, 200 $^W/_{cm^2}$, T = 5 K.

Upon addition of electron scavengers in low concentrations to the matrix gas (Ne + 0.01% CCl_4, Ne + 0.1% CO_2), the emission spectra remain unchanged (fig. 4.4 b and c), indicating that no other charge state contributes to the emission. This is also confirmed by comparison to gas-phase spectra, where the charge state is unambiguously known.

The complexation of small molecules to the $Gd(PLN)_2^+$ ions is possible in the matrix by increasing the concentration of CO_2 in the matrix gas (Ne + 0.3% CO_2, Ne + 0.7% CO_2), or by deposition of the solvent adducts, $Gd(PLN)_2^+$ + DMSO and $Gd(PLN)_2^+$ + 2 DMSO. In the CO_2 containing matrixes, distinct shoulders emerge, best seen at the band origin (fig. 4.5 c). For the DMSO adducts, only a slight broadening is detected, best seen at 556 nm (fig. 4.5 b). No shift of the PLN $T_1 \rightarrow S_0$ band origin emission is detected for the adducts. By changing the matrix gas mixture, adduct ions of the mass selected species and different molecules can be studied, which cannot be generated easily in the gas phase.

Codeposition of $Gd(PLN)_2^+$ with argon results in some changes of the PLN emission spectrum, which are shown in figure 4.6 b and c. As expected in an environment, which interacts more strongly with the deposited species, broadening of the emission features occurs. In fact, some of the weaker vibronic lines are not distinguishable at all.

In the argon environment, a further red-shift of the $T_1 \rightarrow S_0$ emission of 65 cm^{-1}

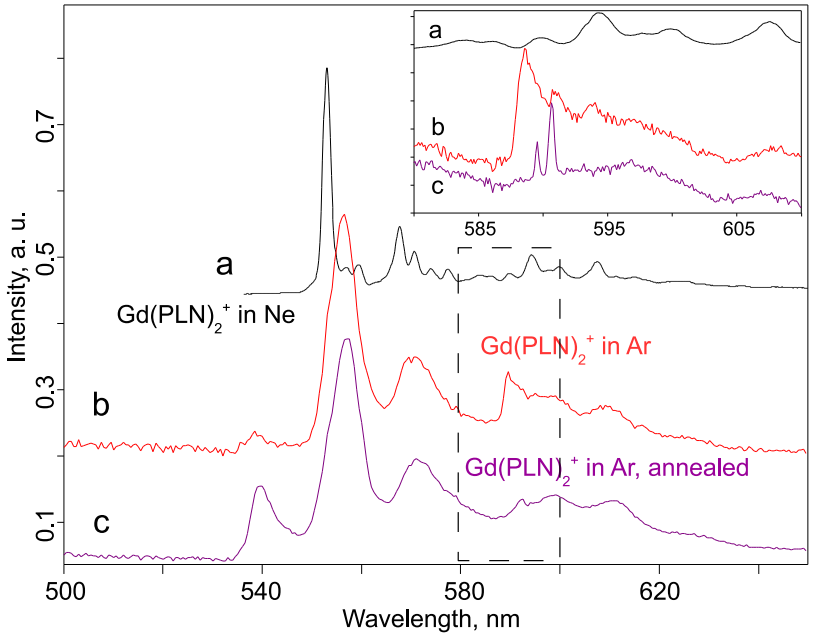

Figure 4.6: Comparison of the emission spectrum of $Gd(PLN)_2^+$ in Ne (a) and in Ar after the deposition (b) and after subsequent annealing of the matrix at 20 K for 5 minutes (c). The inset shows the marked range of the so far unidentified emissions in higher resolution. Experimental parameters: (a): $\lambda_{excitation}$= 375 nm, 200 $^W/_{cm^2}$, T = 5 K; (b), (c): $\lambda_{excitation}$= 405 nm, 1000 $^W/_{cm^2}$, T = 5 K

is measured relative to neon matrixes, the PLN $T_1 \rightarrow S_0$ emission is centered at 555 nm (fig. 4.6). The increasing red-shift is due to the increased interaction of the $Gd(PLN)_2^+$ with the environment. Extrapolation of the gas phase emission frequency from argon and neon spectra reproduces the measured frequency within 2 cm^{-1}.[7]

Additionally, two new emission features emerge, one at 540 nm, and one around 590 nm. Both new features are only detected when the sample is irradiated with the 405 nm diode laser, they do not occur with the 375 nm laser. Upon annealing of the sample at 20 K, the feature at 540 nm gains in relative intensity to the 555 nm emission (fig. 4.6 b, c) while the 588 nm decreases. Two very narrow emissions at 589.6 and 590.7 nm appear after annealing (fig. 4.6, inset).

The similar broadness of the 540 and 555 nm feature indicates that both originate from the PLN triplet state. At the same time, the different relative intensities of the 555 and 540 nm emissions at different excitation wavelengths, and after annealing of the argon matrix at 20 K indicate that two different PLN species are present in Ar matrixes.

[7]Corresponding to 0.1 nm in this wavelength region, which is within the experimental accuracy.

A possible reason for the presence of two different PLN species in argon matrixes is a change of the $Gd(PLN)_2^+$ symmetry. Two different symmetries can lead to two different PLN conformers, with different absorption cross-sections at 375 nm and 405 nm. Stabilization of a different symmetry also accounts for the relative increase of the 540 nm emission feature after annealing of the sample. However, another possible reason is the neutralization of $Gd(PLN)_2^+$ during deposition. While in neon matrixes, no signal of the neutral $Gd(PLN)_2$ is detected, it is expected to be present. Possibly, the neutral species exhibits laser-induced phosphorescence in argon matrixes. However, a similar feature is observed for the $[Gd(PLN)_3Na]^+$ species (see page 111), which is deposited in Ne + 0.01% CCl_4. Here, neutralization can be ruled out. For $Gd(PLN)_2^+$ in Ar, no measurement with the addition of electron scavengers are performed yet.

The emisison feature at 588.6 nm and the very narrow 589.6 and 590.7 nm emissions are probably caused by a contamination in the argon matrix. Possibly, the narrow emissions are Na D-line emissions, which are shifted in argon relative to the gas phase values of 588.9950 nm (D_2) and 589.5924 nm (D_1) [199]. However, while $Gd(PLN)_2^+$ is electrosprayed from $Gd(PLN)_4Na$ in DMSO solution, the sodium adduct species are rejected by the mass filter. No corresponding features are detected in other matrixes. So far, no conclusive explanation can be given regarding the origin of these two emission features.

The interaction of the deposited $Gd(PLN)_2^+$ with the argon matrix environment gives rise to two new emission bands. While these features have yet to be understood, it is demonstrated that the preparation of samples with different matrix materials is possible. Also, extrapolating the gas phase emission wavelength of the PLN $T_1 \rightarrow S_0$ transition in $Gd(PLN)_2^+$ is possible.

To estimate the signal enhancement that can be achieved in matrix isolation, increasing amounts of $Gd(PLN)_2^+$ are deposited at a constant dilution ratio (1:10^5) for a total duration of 22.75 hours. The laser-induced phosphorescence is measured at various times during the deposition (375 nm, 200 W/cm^2, 10 s acquisition time) (fig. 4.7). The integrated emission intensity increases linearly with the number of deposited ions (linear regression: R^2= 0.998), no saturation of the signal occurs over more than two orders of magnitude of deposited ions. Increasing the signal further is possible by additional deposition, or increasing the measurement time, or the irradiance.

$[Gd(PLN)_3Na]^+$

In gas phase, the $[Gd(PLN)_3Na]^+$ complex photofragments upon irradiation to the strongly luminescent $Gd(PLN)_2^+$, whose signal covers any emissions of$Gd(PLN)_3Na^+$. In Ne matrixes, even after prolonged photoexcitation, the signal intensity is

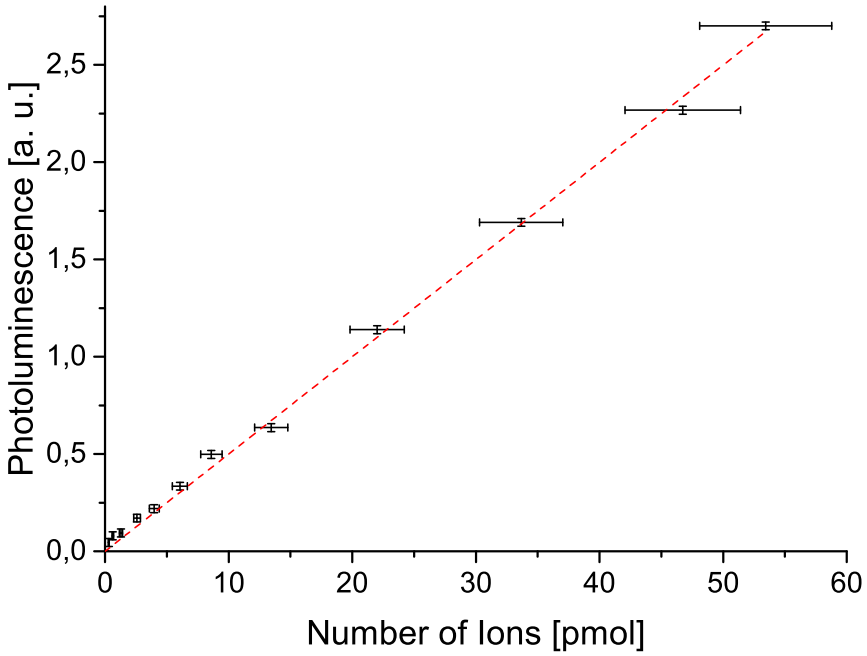

Figure 4.7: Integral photoluminescence of $Gd(PLN)_2^+$ for various numbers of deposited ions embedded in Ne + 0.01% CCl_4 at constant dilution ratio of about 1:10^5. The integral photoluminescence increases linearly with the number of deposited ions (linear regression: R^2 = 0.998). Experimental parameters: $\lambda_{excitation}$= 375 nm, 200 $^W/_{cm^2}$, T = 5 K.

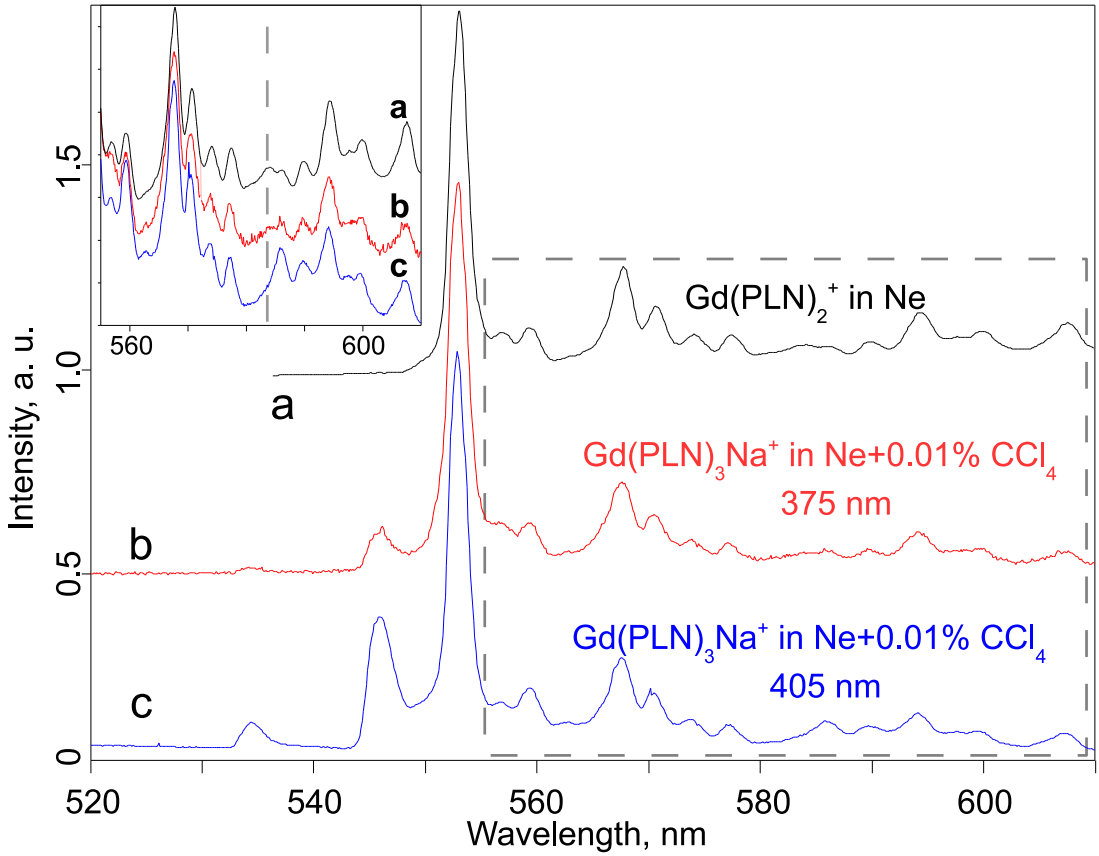

Figure 4.8: Emission spectra of $Gd(PLN)_2^+$ in Ne (a) and $[Gd(PLN)_3Na]^+$ in Ne + 0.01% CCl_4 irradiated at 375 nm (b) and 405 nm (c). While the relative intesity of the 545.9 and 534.4 nm features is constant, the 553 nm emission does not correlate. In the inset, the missing vibronic feature is marked (see text for details). Experimental parameters: (a), (b): $\lambda_{excitation}$= 375 nm, 200 $^W/_{cm^2}$, T = 5 K; (c): $\lambda_{excitation}$= 405 nm, 1000 $^W/_{cm^2}$, T = 5 K.

not decreasing: The faster energy dissipation in cryogenic matrixes enables laser-induced luminescence spectroscopy of $[Gd(PLN)_3Na]^+$.

$[Gd(PLN)_3Na]^+$ is deposited into a Ne + 0.01% CCl_4 matrix. In the emission spectra measured upon irradiation at 375 or 405 nm, several differences occur relative to the spectrum of $Gd(PLN)_2^+$ (fig. 4.8).

Next to the emission at 553 nm, which is also present for $Gd(PLN)_2^+$, two features, which were not observed for $Gd(PLN)_2^+$ are present at 545.9 and 534.4 nm. Changing the irradiation wavelength, or annealing the sample at 9 K, does not change the relative intensities of the 545.9 and 534.4 nm features. However, the intensity of the 553 nm emission does not correlate.

The lineshape of the 545.9 and 534.4 nm emissions, and a weak vibronic progres-

sion, indicate that both features originate in the PLN $T_1 \rightarrow S_0$ emission. As is the case for $Gd(PLN)_2^+$ in Ar matrixes, apparently different PLN conformers occur. Also, the shift of the 534.4 nm feature compared to the band origin at 553 nm for $[Gd(PLN)_3Na]^+$ is close to the shift of the additional feature of $Gd(PLN)_2^+$ in argon (fig. 4.6).

Interestingly, while the band origin of the PLN $T_1 \rightarrow S_0$ transition is identical to $Gd(PLN)_2^+$ (within the experimental resolution), a difference is identified in the vibronic progression: one vibronic feature at 584 nm is not observed in the spectrum of $[Gd(PLN)_3Na]^+$ (fig. 4.8 inset), indicating a slightly changed geometry of the PLN ligand. All other vibronic features are identical.

As for the measurement of $Gd(PLN)_2^+$ in argon matrixes, the origin of the different PLN conformers is unknown. Again, one can speculate about fragmentation of the $[Gd(PLN)_3Na]^+$ complex during deposition, forming for example neutral $Gd(PLN)_3$ and Na^+, or $Gd(PLN)_2^+$ and NaPLN. Neutralization of the $[Gd(PLN)_3Na]^+$ complex is also possible, although in the presence of an electron scavenger neutralization of the deposited cation is not expected to contribute strongly. Another possibility is, that in the case of $[Gd(PLN)_3Na]^+$, the different PLN species are due to different binding sites of the ligands to the Gd^{3+} and Na^+ metal ions.

While the origin of the additional PLN $T_1 \rightarrow S_0$ transitions is not understood, no fragmentation is detected upon irradiation of the sample. This demonstrats, that laser-induced photoemission measurements in cryogenic matrixes are possible without photofragmentation. Whether fragmentation of $[Gd(PLN)_3Na]^+$ occurs during deposition or not can be investigated by changing the kinetic energy of the ions for the deposition in further experiments.

$[Gd_9(PLN)_{16}(OH)_{10}]^+$ and $[Eu_9(PLN)_{16}(OH)_{10}]^+$

In gas phase, $[Gd_9(PLN)_{16}(OH)_{10}]^+$ and $[Eu_9(PLN)_{16}(OH)_{10}]^+$ have been studied in detail by Greisch *et al.* [192], showing that for the gadolinium complex the PLN $T_1 \rightarrow S_0$ emission occurs, while in the europium complex strong emissions from the Eu^{3+} were measured. The molecular structure of $[Eu_9(PLN)_{16}(OH)_{10}]^+$ (RI-BP/def2-SVP, [189]) is shown in figure 4.9, the structure of $[Gd_9(PLN)_{16}(OH)_{10}]^+$ is similar.

Both species are co-deposited with neon without mass selection, the cut-off mass in RF-only mode is set to the highest value (1000 $^{amu}/_{e}$) to reduce contamination of the sample. By electrospray ionization of the solution containing the respective pure substance, more than 95% of the ions produced are the desired nonanuclear species. All samples are irradiated with a 375 nm/20 mW diode laser, the spectra are shown in figures 4.10 and 4.11.

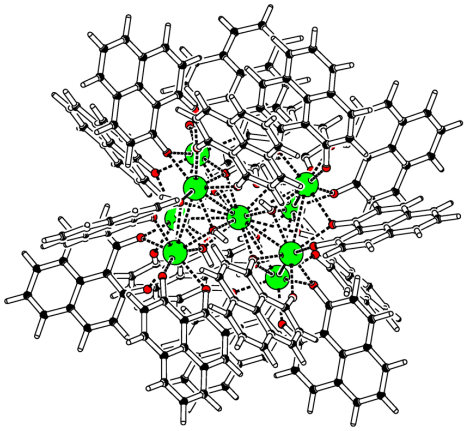

Figure 4.9: Molecular structure of the nonanuclear $[Eu_9(PLN)_{16}(OH)_{10}]^+$ ion (RI-B-P/def2-SVP) [189]. The central Eu^{3+} ions are shown in green, oxygen in red, carbon in black, and hydrogen as empty globes.

In the emission spectrum of matrix-isolated $[Gd_9(PLN)_{16}(OH)_{10}]^+$, a broad feature with a halfwidth of 900 cm^{-1}, centered at 581 nm and two shoulders at 625 and 680 nm occurs (fig. 4.10).

These features are assigned to the PLN $T_1 \rightarrow S_0$ triplet emission. No further emission band is detected. While the spectra of isolated $Gd(PLN)_2^+$ and $[Gd(PLN)_3Na]^+$ show resolved vibronic emissions of the ligand, this is not the case for the broad emission of $[Gd_9(PLN)_{16}(OH)_{10}]^+$. No superposition of ligand emissions in different binding geometries can be detected. Therefore, the broad spectrum of the nonanuclear complex is rationalized by a collective excitation and emission process of the whole ligand shell, mediated by a partial stacking of the planar ligands.

Comparing the spectrum obtained by matrix isolation with the one from gas-phase measurements, a shift of the PLN emission of $[Gd_9(PLN)_{16}(OH)_{10}]^+$ is detected [192]. In the gas phase, the emission feature is centered at 568 nm, with the first shoulder at 617 nm and the second shoulder below detection limit. The emission features in neon matrixes are red-shifted by 400 and 200 cm^{-1}, respectively.

In the spectrum of matrix-isolated $[Eu_9(PLN)_{16}(OH)_{10}]^+$ (fig. 4.11), very clear emissions from the Eu(III) transitions are seen ($^5D_0 \rightarrow ^7F_0$ (582 nm), $^5D_0 \rightarrow ^7F_1$ (590 - 597 nm), $^5D_0 \rightarrow ^7F_2$ (610 - 627 nm), $^5D_0 \rightarrow ^7F_3$ (650 - 658 nm), and $^5D_0 \rightarrow ^7F_4$ (685 - 710 nm)) [200], dominated by the hypersensitive $^5D_0 \rightarrow ^7F_2$ band, without any contributions from PLN emissions: The energy transfer from the PLN ligand triplet state to the central Eu^{3+} is not affected by the matrix environment.

For $[Eu_9(PLN)_{16}(OH)_{10}]^+$, the Eu^{3+} emission wavelengths are almost unaffected by the noble gas matrix surroundings, the matrix shift of the emission features does not exceed 30 cm^{-1} for any emission, and is smaller for most.

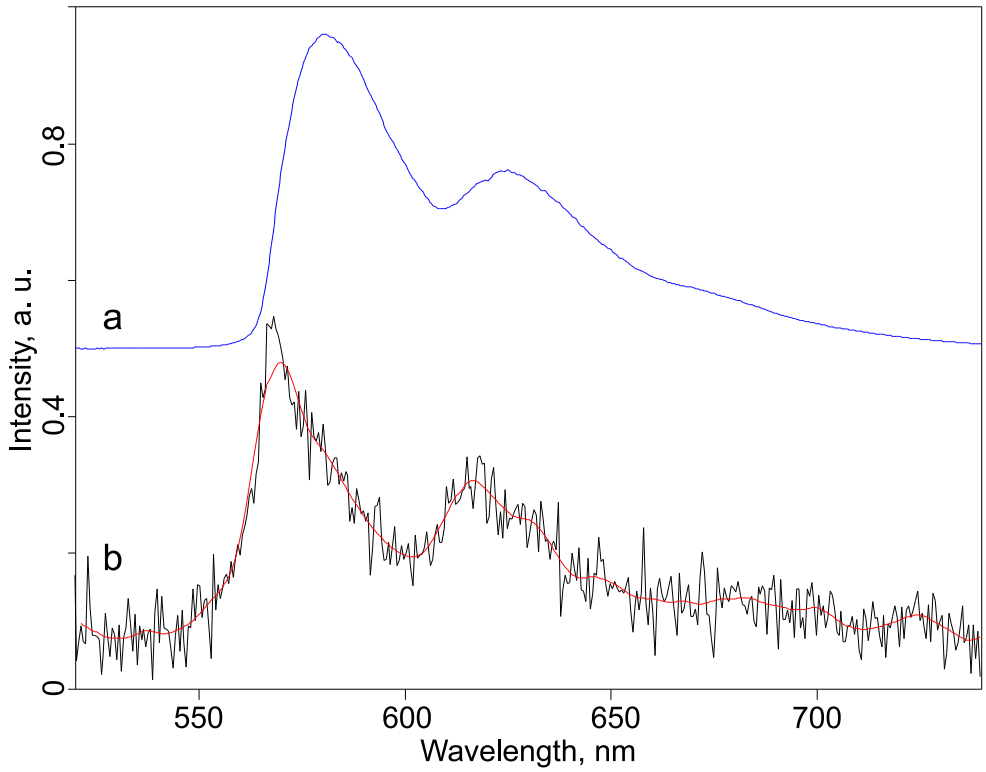

Figure 4.10: Emission spectrum of $[Gd_9(PLN)_{16}(OH)_{10}]^+$: (a) after deposition in neon matrix at 5 K, excitation at 375 nm, and (b) in gas phase at 83 K, excitation at 476.5 nm, the corresponding smoothed spectrum (low pass FFT filter) is shown in red. Experimental parameters: (a): $\lambda_{excitation}$= 375 nm, 200 $^W/_{cm^2}$, T = 5 K; (b): $\lambda_{excitation}$= 476.5 nm, 1975 $^W/_{cm^2}$, T = 83 K.

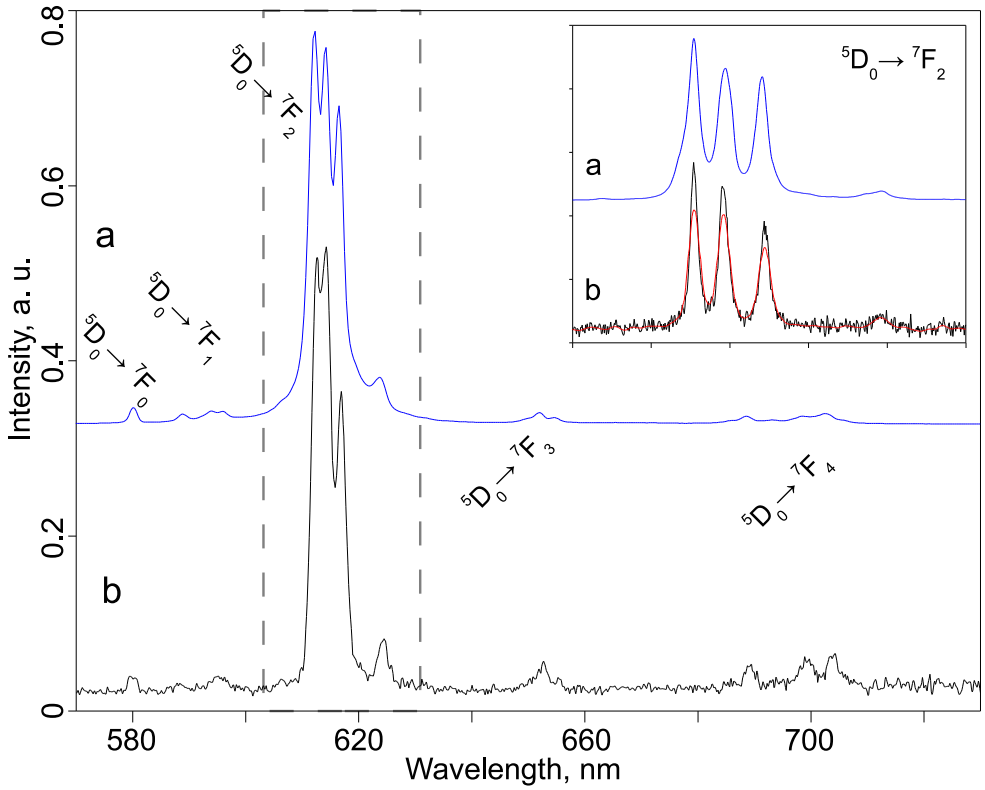

Figure 4.11: Emission spectrum of $[Eu_9(PLN)_{16}(OH)_{10}]^+$: (a) after deposition in neon matrix at 5 K, excitation at 375 nm, and (b) in gas phase at 83 K, excitation at 476.5 nm. The inset shows in detail the $^5D_0 \rightarrow {}^7F_2$ transition, top: neon matrix, bottom: gas phase, smoothed spectrum (low pass FFT filter) is shown in red. Experimental parameters: (a): $\lambda_{excitation}$= 375 nm, 200 $^W/_{cm^2}$, T = 5 K; (b): $\lambda_{excitation}$= 476.5 nm, 1975 $^W/_{cm^2}$, T = 83 K.

For both species, the signal-to-noise ratio is improved compared to the gas-phase measurements.

4.3 Study of $M(PLN)_2^+$ and $[Eu(PLN)_3A]^+$

To understand the energy transfer from the diketonate ligand to the central metal ions, simple systems have to be investigated, which can be modeled by theory. For the studied lanthanoid diketonate complexes, the simplest monoionic system consists of a lanthanoid Ln^{3+} cation, complexed with two deprotonated 9-hydroxyphenalen-1-one (PLN) anions, forming a monocationic $Ln(PLN)_2^+$ complex.

Different lanthanoids and also other trivalent metallic ions (Al^{3+}, In^{3+}) are characterized regarding their emission processes, emission intensities, and wavelength. For systems sufficiently luminescent for gas phase measurements ($Gd(PLN)_2^+$ and $Lu(PLN)_2^+$), a comparison between gas phase and matrix isolation measurements is also presented. Most species studied only exhibit a weak luminescence, especially so the emitting lanthanoids, with the exception of Eu^{3+}. The relative emission intensities of the species are listed in table 4.1.

All samples are irradiated with 375 and 405 nm diode lasers. For most species, no qualitative difference is observed in the emission spectra, therefore the excitation wavelength is only explicitly mentioned when necessary. For each shown spectrum, the experimental details are listed in the corresponding caption.

Most spectra show an emission at 696 nm, originating from the Al_2O_3 substrate. This feature will be marked in the presented spectra.

Aluminum: $Al(PLN)_2^+$

$Al(PLN)_2^+$ cations are mass selected and deposited into a neon matrix. The emission spectrum of the aluminum complex shows sharp vibronic features from the PLN $S_1 \rightarrow S_0$ singlet and $T_1 \rightarrow S_0$ triplet transitions, with origins at 448.4 and 534.6 nm, respectively (fig. 4.12 b). No emissions from the Al^{3+} ion are detected.

Measuring the lifetime of the emitting states is not possible with the setup. However, an afterglow of several seconds, originating from the PLN triplet emission at 534.6 nm, is visible with the naked eye. The long lifetimes of the excited states are further supported by the sharp emission lines.

For other central metal ions apart from aluminum, no emissions from the PLN $S_1 \rightarrow S_0$ transition are measured. Quenching of the PLN singlet emission is based on the spin-orbit coupling of the PLN with the heavy central metal ions, leading to an increase of the $S_1 \rightarrow T_1$ intersystem crossing rate, and thus to a loss of emission from the S_1 state [197, 198].

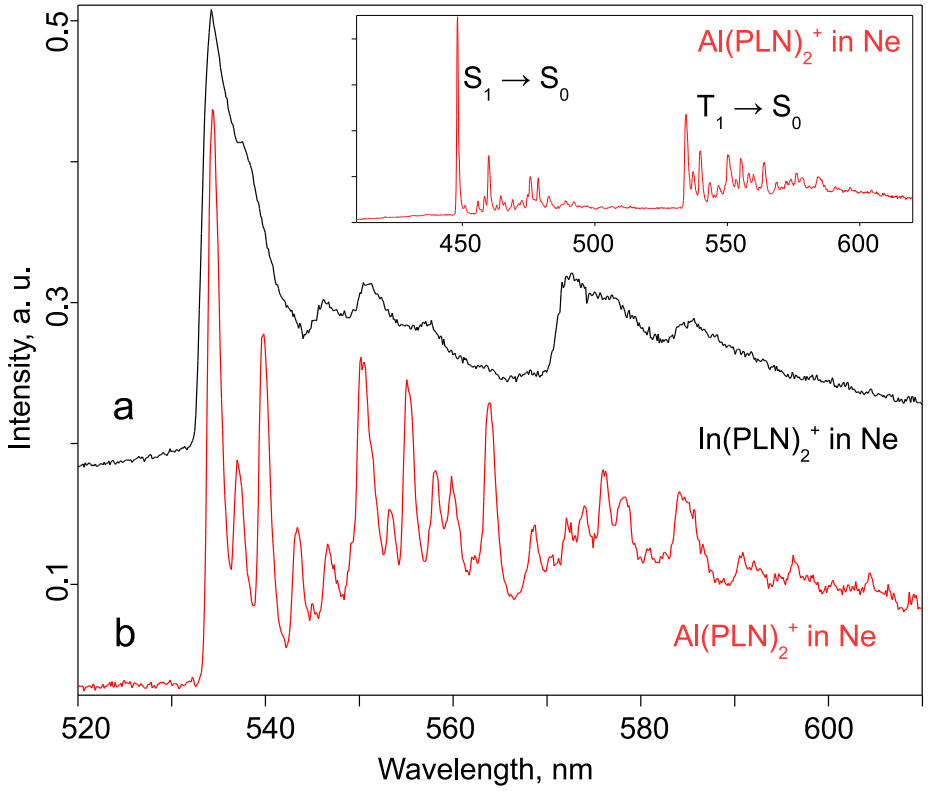

Figure 4.12: PLN $T_1 \rightarrow S_0$ emission spectra of $In(PLN)_2^+$ (a) and $Al(PLN)_2^+$ (b). For both species, ligand emissions are detected, for $Al(PLN)_2^+$ from the S_1 and T_1 states (shown in the inset), for $In(PLN)_2^+$ only from the T_1 state. Experimental parameters: (a), (b): $\lambda_{excitation}$= 375 nm, 200 $^{W}/_{cm^2}$, T = 5 K.

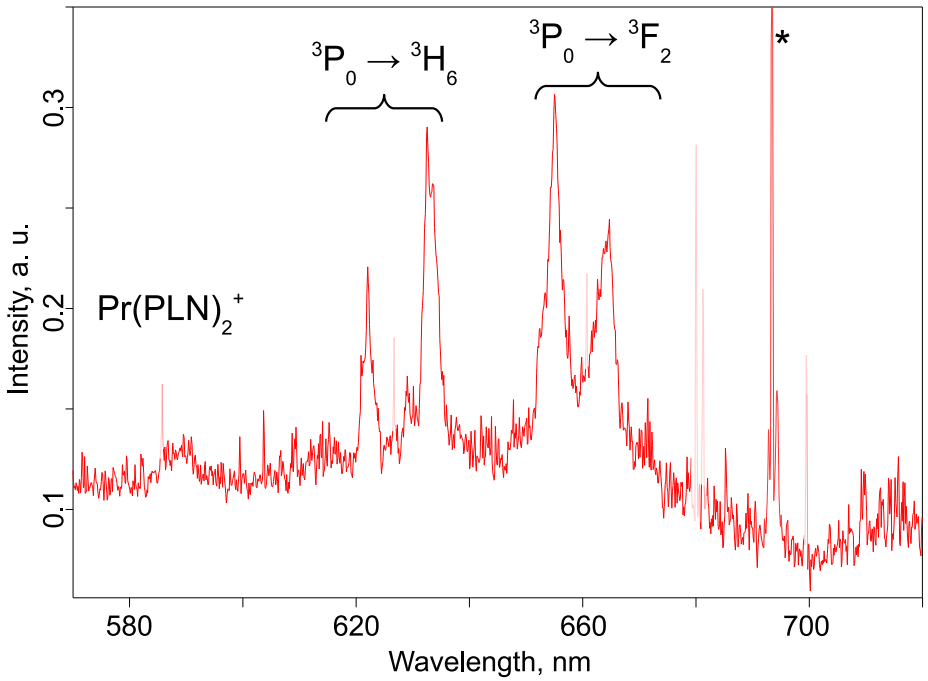

Figure 4.13: Emission spectrum of $Pr(PLN)_2^+$ with emissions from the Pr^{3+} $^3P_0 \rightarrow {}^3H_6$ and $^3P_0 \rightarrow {}^3F_2$ transitions. Masked features are background noise. The strong marked feature (*) is an emission from the substrate. Experimental parameters: $\lambda_{excitation}$= 375 nm, 200 $^W/_{cm^2}$, T = 5 K.

Indium: $In(PLN)_2^+$

For $In(PLN)_2^+$ isolated in cryogenic neon matrixes, only the PLN triplet emission occurs, with the band origin at 534.3 nm and vibronic sidebands (fig. 4.12 a). As can be seen in figure 4.12, the emission lines of $In(PLN)_2^+$ are much broader than for $Al(PLN)_2^+$, but still similar vibronic bands can be identified. No additional emissions from the central In^{3+} ions are detected.

Praseodymium: $Pr(PLN)_2^+$

The emission spectra from samples of isolated $Pr(PLN)_2^+$ show four strong emission features at 622 , 632.5 , 655.1 , and 664.7 nm, and several weaker features in the same range (fig. 4.13).

The strong emissions result from the $^3P_0 \rightarrow {}^3H_6$ (632.5 nm) and the $^3P_0 \rightarrow {}^3F_2$ (655.1 nm) transitions of the Pr^{3+} ion [201]. In solids, a splitting of the Pr^{3+} emission bands is observed for different sites. Also, the intensities of the atomic transitions of praseodymium depend on the symmetry of the environment, the temperature, and the excitation wavelength [202].

Emissions from states of higher energies, for example the strong $^3P_0 \rightarrow ^3H_4$ transition at roughly 480 nm [201], cannot be populated from the PLN triplet state and are therefore not present in the spectrum.

The emission features of $Pr(PLN)_2^+$ only occur for irradiation with the 375 nm diode laser. When exciting the sample with the 405 nm diode laser, even with higher laser power, no clear emission lines can be identified. This suggests a low absorption cross-section of the PLN ligands in the $Pr(PLN)_2^+$ complex at 405 nm.

Europium: $Eu(PLN)_2^+$

Matrix-isolated $Eu(PLN)_2^+$ exhibits emissions from the PLN triplet state with the band origin at 540.5 nm and a vibronic progression at lower energies. Additionally, a broad absorption around 620 nm with a fine structure, and some weaker emission features are observed in neon matrixes upon irradiation at 405 nm (fig. 4.14 a). Upon irradiation at 375 nm, or in matrixes containing electron scavengers, only the PLN $T_1 \rightarrow S_0$ emission is detected, the broad emission is lost (fig 4.14 b). The different emission spectra for different excitation wavelength indicate, that two different species are present as carriers of the 540.5 and 620 nm emissions, respectively.

Energy transfer is possible from the PLN T_1 state to the Eu^{3+} $^5D_0$ state, with following $^5D_0 \rightarrow ^7F_J$ emissions. The broad emission feature of matrix isolated $Eu(PLN)_2^+$ is assigned to the $^5D_0 \rightarrow ^7F_2$ transition, the weaker emissions correspond to transitions to other ^7F_J states. As can be seen in figure 4.14, all expected emissions of Eu^{3+} are detected.

In matrixes containing electron scavengers, no emissions from the central Eu^{3+} are observed, indicating a charge effect as cause of the different species present. However, a complete neutralization of the complex is excluded, because the observed emissions cannot be explained by Eu^{2+} emissions, which exhibits a broad emission in the range from 400 to 500 nm [203]. Instead, it is suggested, that electrons are localized at the ligands without charge transfer to the central Eu^{3+} ion, forming a $^{2-}PLN\cdot\cdot Eu^{3+} \cdot\cdot PLN^-$ complex. This localized charge reduces the symmetry of the $Eu(PLN)_2^+$ complex, and allows for symmetry-forbidden Eu^{3+} emissions to occur [203]. In matrixes containing CCl_4, the secondary electrons are scavenged before they can reach the $Eu(PLN)_2^+$ complexes, hence no symmetry reduction and no Eu^{3+} emissions are detected.

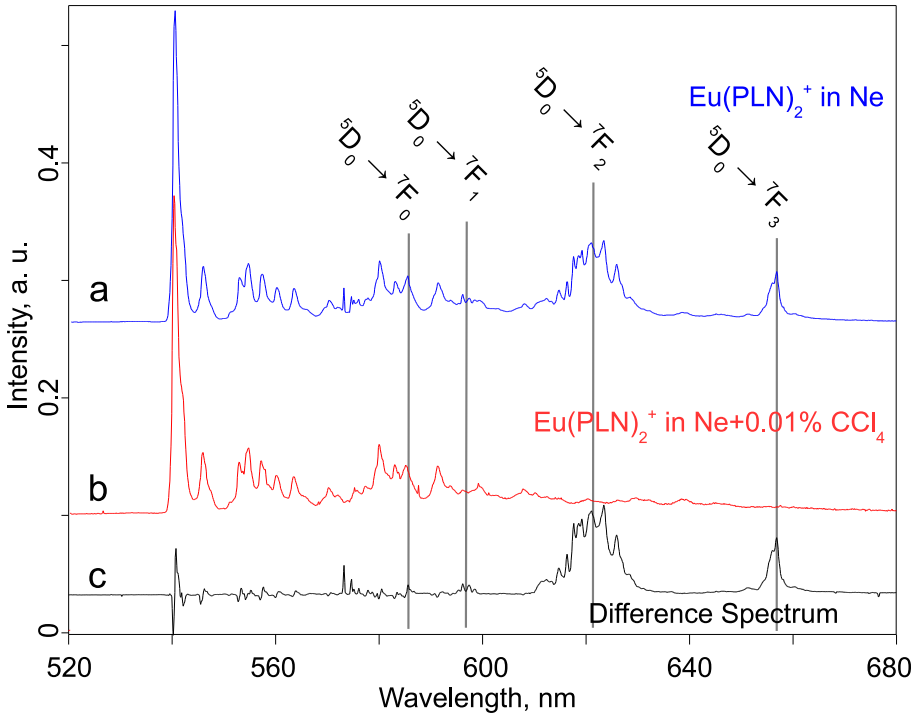

Figure 4.14: Emission spectrum of $Eu(PLN)_2^+$ in pure neon matrix (a), and in Ne + 0.01% CCl_4 (b). In the difference spectrum (c), only the Eu^{3+} emissions are observed. Vibronic features with the origin at 540.5 nm are from the PLN triplet state, the marked features are emissions from the Eu^{3+} $^5D_0 \rightarrow {}^7F_J$ transitions. Experimental parameters: (a): $\lambda_{excitation}$= 405 nm, 500 $^W/_{cm^2}$, T = 5 K; (b): $\lambda_{excitation}$= 375 nm, 200 $^W/_{cm^2}$, T = 5 K.

Gadolinium: $Gd(PLN)_2^+$

A detailed discussion of the $Gd(PLN)_2^+$ complex is presented in the previous section 4.2.

In short, in the $Gd(PLN)_2^+$ complex, emissions are observed from the PLN triplet state, with the band origin at 553.0 nm and vibronic features. No emissions of the central Gd^{3+} ion are detected.

For the band origin of the PLN $T_1 \rightarrow S_0$ transition, a red-shift of 20 cm^{-1} compared to gas-phase measurements occurs. The following vibronic progression is close to identical.

Terbium: $Tb(PLN)_2^+$

In the spectrum of $Tb(PLN)_2^+$ in figure 4.15 a and b, several emission features occur in the range from 550 to 800 nm, with the most intense features at 550.9 and 580.4 nm.

The first emission feature is assigned as emission from the PLN triplet state. The halfwidth of this emission, and the vibronic sidebands, correspond to PLN emissions in other lanthanoid complexes. The assignment of the emissions at lower energy, 565.2 and 580.4 nm, is less clear. Emissions of different PLN ligands at different matrix sites are possible, or different geometries of the $Tb(PLN)_2^+$ complex are present. Charge effects as cause of the different emissions in the spectrum of $Tb(PLN)_2^+$ can be ruled out, co-depositon with electron scavengers does not alter the spectrum (fig. figure 4.15 b).

The emission features in the 615 - 800 nm range cannot be explained by PLN emission. Tb^{3+} can also be ruled out as the emitting species, because the observed emissions do not fit the previously reported Tb^{3+} emission spectrum [204]. Additionally, the energetically closest state of Tb^{3+}, the $^5D_4$ state, is higher in energy than the PLN T_1 state. Therefore, no energy transfer from the PLN is expected.

Instead, a mixture of different rare earth metals in the sample, which are not rejected by the mass filter due to the low resolution, could be responsible for the emissions. However, the lanthanoids adjacent to terbium are europium and gadolinium at lower, and dysprosium and holmium at higher mass. The measured emission features of $Eu(PLN)_2^+$, $Gd(PLN)_2^+$, and $Dy(PLN)_2^+$ do not show any agreement with the 615 - 800 nm features measured for $Tb(PLN)_2^+$. For Ho^{3+}, previously reported emission spectra do not match the emission features in this experiment [205]. Lanthanoid complexes with a larger difference in mass are rejected by the mass filter.

The assignment of the emission features in the 615 - 800 nm range is currently not possible.

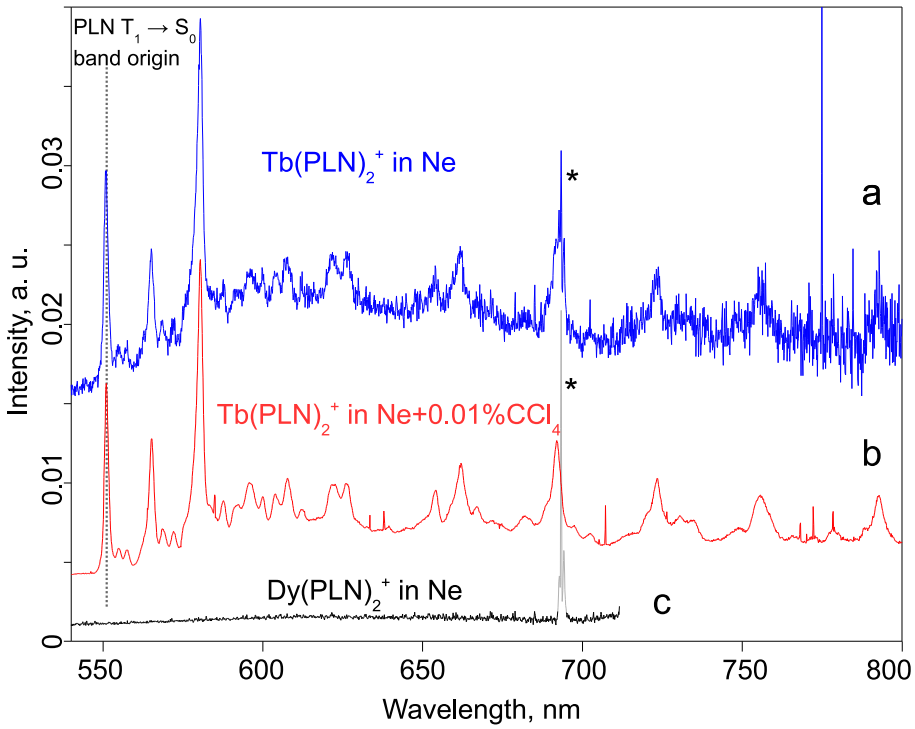

Figure 4.15: Emission spectra of $Tb(PLN)_2^+$ in Ne (a) and Ne + 0.01% CCl_4 (b), and $Dy(PLN)_2^+$ in Ne (c). For $Tb(PLN)_2^+$, the emissions in the 615 - 800 nm range cannot be explained by PLN or Tb^{3+} emissions. The strong emission from the Al_2O_3 substrate is marked. Experimental parameters: (a), (b), (c): $\lambda_{excitation}$= 375 nm, 200 $^W/_{cm^2}$, T = 5 K.

Dysprosium: Dy(PLN)$_2^+$

Dy(PLN)$_2^+$ cations are co-deposited with neon. No emissions from the deposited species is detected in the range from 400 to 850 nm (fig. figure 4.15 c). The sample is irradiated with 20 mW at 375 nm, the total measurement time is 600 s.

The Dy^{3+} $^4F_{9/2}$ state is too high in energy to be populated by energy transfer from the PLN triplet state. An energy transfer to the $^6F_{1/2}$ state and relaxation by emissions in the NIR is possible [206, 207]. For this sample, no NIR spectra were obtained.

Another possibility is a vanishing absorption cross-section for the ligands in the Dy(PLN)$_2^+$ complex, or a very effective energy transfer from the PLN to matrix phonons, and thus a radiationless relaxation.

Ytterbium: Yb(PLN)$_2^+$

In samples produced from co-deposition of Yb(PLN)$_2^+$ with neon, irradiation at 375 nm results in two emission regions (fig. 4.16). In the first region around 540 nm, two separate broad emission features with center wavelengths of 537 and 550 nm occur. In the second region, an emission at 982 nm, with a shoulder at 974 nm, is detected.

No emissions from the PLN triplet state are detected. No emissions occur for irradiation at 405 nm.

The emission features at 974 and 982 nm are readily identified as the split Yb^{3+} $^2F_{5/2} \rightarrow {}^2F_{7/2}$ transition. Energy transfer from the PLN triplet state to the central Yb^{3+} ion occurs.

The emissions at 537 and 550 nm are identified as the Er^{3+} $^2H_{11/2} \rightarrow {}^4I_{15/2}$ and $^4S_{3/2} \rightarrow {}^4I_{15/2}$ transitions [208]. Er(PLN)$_2^+$ is present in the sample due to the difficulty in separating different rare-earth metals prior to synthesis, and the low mass resolution of the experimental setup. Typically, the mass filter is set to $^m/_{\Delta m}$ = 30, for an efficient separation of Yb(PLN)$_2^+$ and Er(PLN)$_2^+$ a resolution of $^m/_{\Delta m}$ = 100 is required. By increasing the mass resolution to 50, and shifting the transmitted mass to higher values (569 $^{amu}/_z$ instead of 566 $^{amu}/_z$), Er(PLN)$_2^+$ can be rejected, as is shown in the inset of figure 4.16, b. However, the ion beam intensity is reduced by a factor of two.

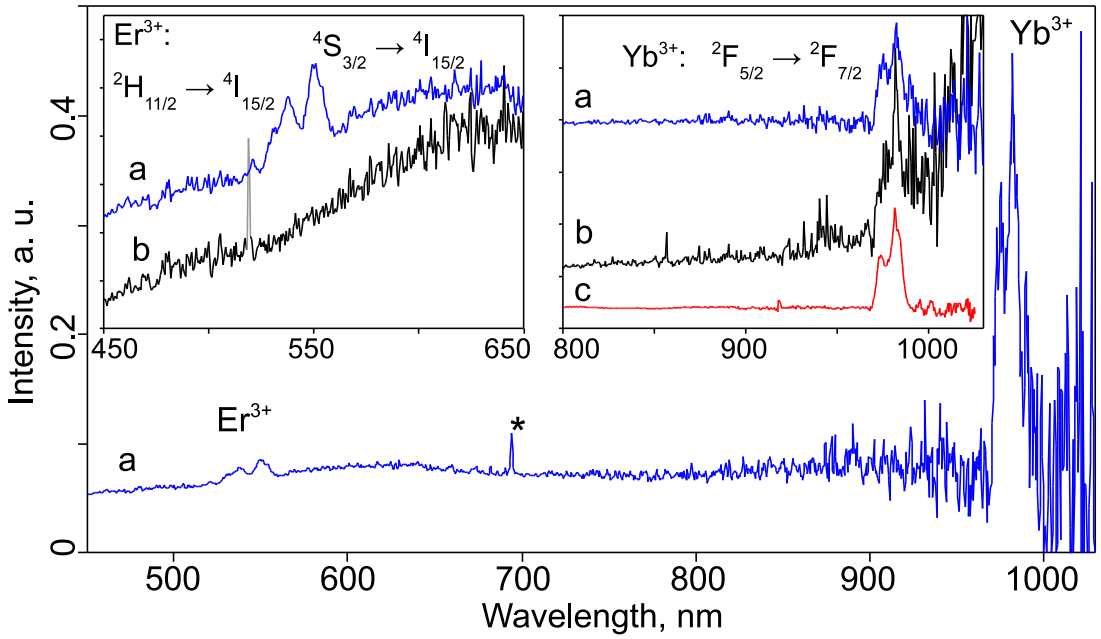

Figure 4.16: Emission spectra of $Yb(PLN)_2^+$ in Ne (a) and (c), and Ne + 0.01% CCl_4 with higher resolution of the mass filter during deposition (b). Emission at 537 and 550 nm, which are present in spectrum (a), are assigned to Er^{3+} transitions. At 980 nm, the emission from the Yb^{3+} $^2F_{5/2} \rightarrow ^2F_{7/2}$ transition can be seen. (c) is measured with a detector optimized for the NIR. In the insets, the emissions of the lanthanoid ions are shown in detail. The marked feature (*) is an emission from the Al_2O_3 substrate. Experimental parameters: (a), (b), (c): $\lambda_{excitation}$= 375 nm, 200 $^W/_{cm^2}$, T = 5 K.

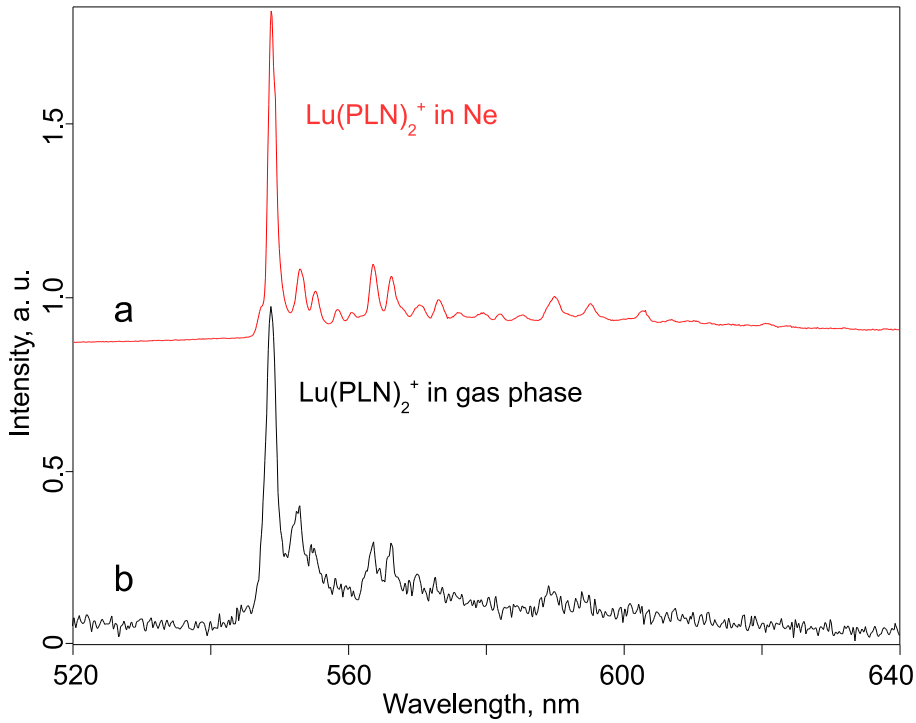

Figure 4.17: Emission spectra of $Lu(PLN)_2^+$ in Ne (a), and in gas phase (b). The emission spectra agree within the experimental accuracy. Experimental parameters: (a): $\lambda_{excitation}$= 375 nm, 200 $^{W}/_{cm^2}$, T = 5 K; (b): $\lambda_{excitation}$= 458 nm, 400 $^{W}/_{cm^2}$, T = 83 K.

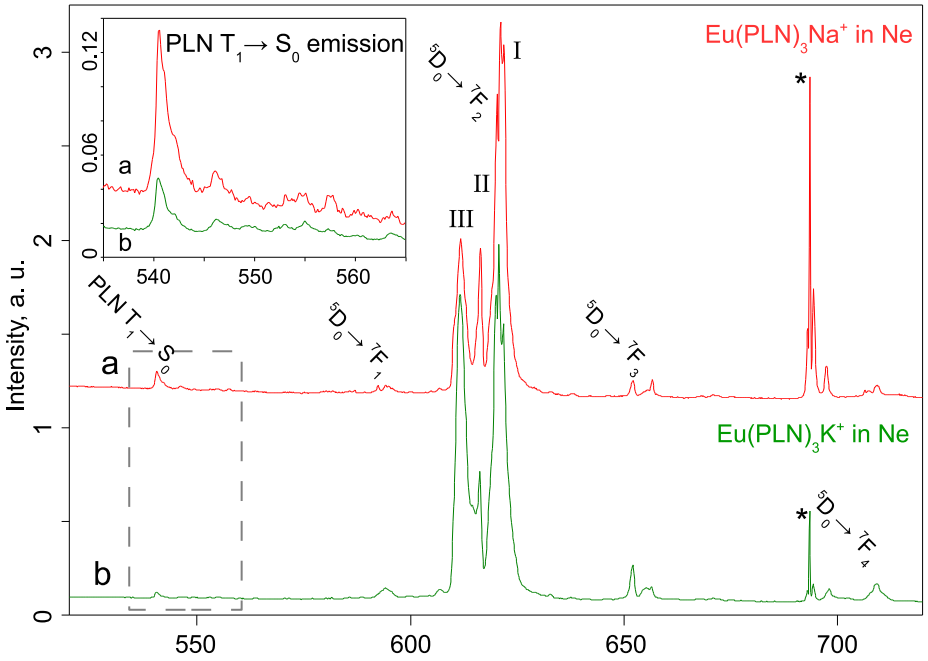

Figure 4.18: Emission spectra of $[Eu(PLN)_3Na]^+$ (a) and $[Eu(PLN)_3K]^+$ (b) isolated in neon, showing emissions from the Eu^{3+} $^5D_0 \rightarrow ^7F_J$ transitions. The inset shows the PLN $T_1 \rightarrow S_0$ transition, the marked feature (*) is an emission from the Al_2O_3 substrate. I and II are $^5D_0 \rightarrow ^7F_2$ emissions, III is likely related to the $^5D_0 \rightarrow ^7F_J$ transition (see text). Experimental parameters: (a), (b): $\lambda_{excitation}$= 405 nm, 1000 $^W/_{cm^2}$, T = 5 K.

Lutetium: $Lu(PLN)_2^+$

The emission spectrum of isolated $Lu(PLN)_2^+$ shows a strong emission from the PLN triplet state, with the band origin at 548.8 nm and a vibronic progression. No emissions from the Lu^{3+} ion are detected.

$Lu(PLN)_2^+$ emissions have been measured in gas phase. The comparison of the gas phase to the matrix isolation spectrum is shown in figure 4.17. The PLN $T_1 \rightarrow S_0$ emissions agree within the experimental accuracy. In matrix isolation, the lower temperature results in a smaller linewidth.

$[Eu(PLN)_3Na]^+$ and $[Eu(PLN)_3K]^+$

Samples of matrix isolated $[Eu(PLN)_3Na]^+$ and $[Eu(PLN)_3K]^+$ show similar emission spectra. As can be seen in figure 4.18, the main differences are the relative intensities of the emissions.

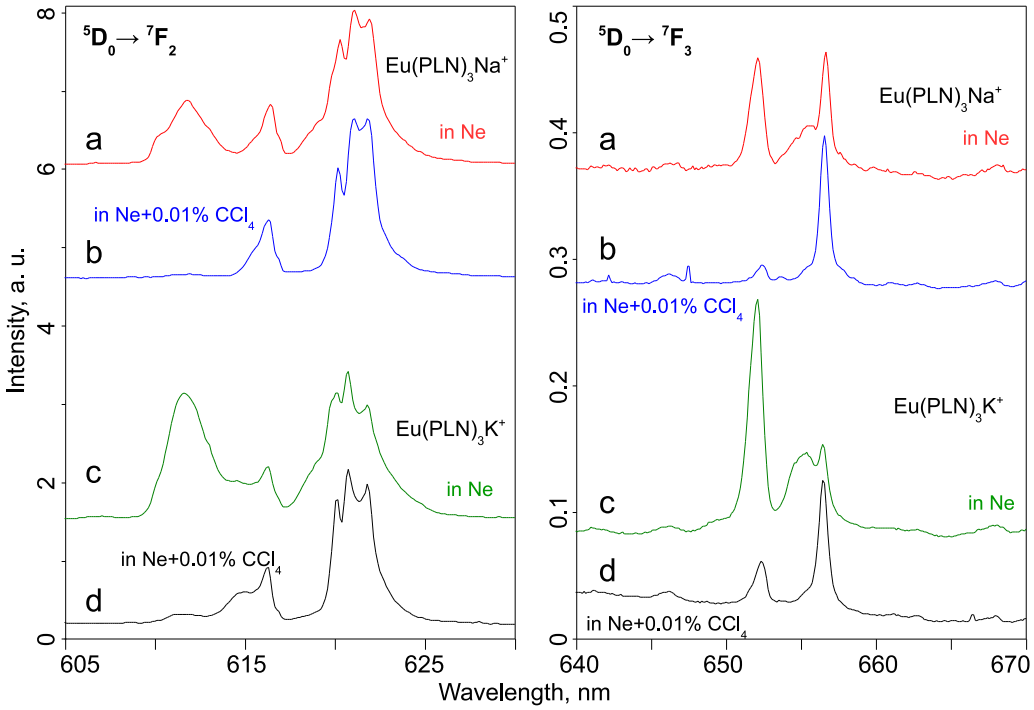

Figure 4.19: Emission spectra of $[Eu(PLN)_3Na]^+$ in Ne (a) and Ne + 0.01% CCl_4 (b), and $[Eu(PLN)_3K]^+$ in Ne (c) and Ne + 0.01% CCl_4 (d). Left: $^5D_0 \rightarrow {}^7F_2$ transition, right: $^5D_0 \rightarrow {}^7F_3$ transition. In matrixes containing electron scavengers, some features are suppressed. Experimental parameters: (a), (b), (c), (d): $\lambda_{excitation}$= 405 nm, 1000 W/cm^2, T = 5 K.

The $^5D_0 \rightarrow {}^7F_J$ transitions of the central Eu^{3+} ion are prominent, dominated by the hypersensitive $^5D_0 \rightarrow {}^7F_2$ emission at 616.4 and 621.1 nm (emissions I and II in fig. 4.18) [200]. Weak emissions from the PLN triplet state are present at 540.5 nm, the same wavelength that is observed for $Eu(PLN)_2^+$ emissions. Additionally, a broad, featureless emission is visible at 611.7 nm, which is likely related to the $^5D_0 \rightarrow {}^7F_2$ band (emission III in fig. 4.18).

Co-deposition of the species with Ne + 0.01% CCl_4 results in an almost complete disappearance of the 611.7 nm feature and a weaker feature at 652.1 nm (fig. 4.19). Besides these features, no further differences in the emission spectra are observed for matrixes containing electron scavengers.

The strong feature at 611.7 nm was not observed in gas phase spectra of $[Eu(PLN)_3Na]^+$ and $[Eu(PLN)_3K]^+$ [195], or in matrix isolation spectra of $Eu(PLN)_2^+$ or $[Eu_9(PLN)_{16}(OH)_{10}]^+$. However, a strong feature around 610 nm has been observed in gas phase emission spectra of $[Eu_2(PLN)_6Na]^+$ and $[Eu_2(PLN)_7Na_2]^+$ [196]. Here, this feature was assigned to the Eu^{3+} $^5D_0 \rightarrow {}^7F_2$ transition, which is shifted because of the reduced symmetry of the Eu^{3+} environment.

In matrixes, a similar symmetry reduction is suggested. While in the case of $[Eu_2(PLN)_6Na]^+$ and $[Eu_2(PLN)_7Na_2]^+$ this change is induced by additional ligands, in matrixes a charge effect can be responsible. Similar to the proposed local charge of $Eu(PLN)_2^+$ in matrixes, an electron is attached to a PLN ligand in $[Eu(PLN)_3Na]^+$ and $[Eu(PLN)_3K]^+$. This results in a change of the binding geometry, and thus a symmetry change in the Eu^{3+} environment. Apparently, the electron stays localized on a ligand. Charge transfer to the central europium atom does not occur: Eu^{2+} exhibits a broad emission in the range from 400 to 500 nm [203], which is not detected in the experiment. The added CCl_4 in the matrix gas efficiently scavenges secondary electrons before they reach a lanthanoid complex. Therefore, complexes with an added electron are scarce, and the emissions from the complexes with reduced symmetry are suppressed.

The weaker feature at 652.1 nm, which exhibits the same decrease in intensity in Ne + 0.01% CCl_4 matrixes, is assigned to the $^5D_0 \rightarrow ^7F_3$ transition in the reduced symmetry. The energy difference relative to the undisturbed Eu^{3+} emission is similar for this feature and the 611.7 nm emission.

Whether the presence of the PLN $T_1 \rightarrow S_0$ emission indicates fragmentation of the $[Eu(PLN)_3A]^+$ complexes, or incomplete energy transfer from the PLN to the Eu^{3+} occurs, could not be conclusively established.

Discussion

The relative luminescence intensity of the deposited species (corresponding to absorption cross section at 375 nm times luminescence quantum yield) is estimated based on the deposited amount and the measurement time, with the intensity of $Gd(PLN)_2^+$ set to 1. A possible difference in the absorption cross-section of the PLN ligands is not taken into account. The estimated relative intensities are listed in table 4.1.

The most intense luminescing $M(PLN)_2^+$ species are $Gd(PLN)_2^+$ and $Lu(PLN)_2^+$, with an intensity ratio of 5:1 in neon matrixes. A similar ratio is found in gas phase. The other species show a much weaker luminescence, which did not allow for gas phase measurements. In noble gas matrixes, photoemissions can be measured for species with a wide range of luminescence intensity, for the $M(PLN)_2^+$ species, the ratio of the strongest ($Gd(PLN)_2^+$) and the weakest ($Pr(PLN)_2^+$) emitter is roughly 3000:1.

The energy of the PLN ligand triplet state is influenced by the central metal ion. While the vibronic features are close to identical for all studied species, the band origin is shifted by several hundred wavenumbers, even for central metal ions with similar properties. A purely geometric effect based on different ionic radii is ruled out: as can be seen in figure 4.20 a, the PLN triplet emission wavelength and the

Table 4.1: Summary of the deposited mononuclear ionic complexes, the emitting species and the transitions, and the relative emission intensity. For emissions from the PLN triplet state, the emission wavelength is given. The relative emission intensity is corrected for deposited number of ions and measurement time.

complex	emitting species	transition	relative emission intensity [a]
$Al(PLN)_2^+$	PLN	$S_1 \rightarrow S_0$ (448.4 nm)	0.09
	PLN	$T_1 \rightarrow S_0$ (534.6 nm)	0.03
$In(PLN)_2^+$	PLN	$T_1 \rightarrow S_0$ (534.3 nm)	0.09
$Pr(PLN)_2^+$	Pr^{3+}	$^3P_0 \rightarrow ^3H_6$;	
		$^3P_0 \rightarrow ^3F_2$	3×10^{-4}
$Eu(PLN)_2^+$	PLN	$T_1 \rightarrow S_0$ (540.5 nm)	0.03
	Eu^{3+}	$^5D_0 \rightarrow ^7F_J$	
$Gd(PLN)_2^+$	PLN	$T_1 \rightarrow S_0$ (553.0 nm)	1 [b]
$Tb(PLN)_2^+$	PLN	$T_1 \rightarrow S_0$ (550.9 nm)	1.5×10^{-3}
	- [c]		
$Dy(PLN)_2^+$	-	-	0
$Yb(PLN)_2^+$	Yb^{3+}	$^2F_{5/2} \rightarrow ^2F_{7/2}$	- [d]
$Er(PLN)_2^+$	Er^{3+}	$^2H_{11/2} \rightarrow ^4I_{15/2}$	- [d]
$Lu(PLN)_2^+$	PLN	$T_1 \rightarrow S_0$ (548.8 nm)	0.2 [b]

[a] Emission intensity of $Gd(PLN)_2^+$ is set to 1; [b] Only the emission intensities of $Gd(PLN)_2^+$ and $Lu(PLN)_2^+$ are large enough to allow gas phase measurements under analogous excitation conditions; [c] Further emitting species are present but could not be assigned; [d] Relative intensity could not be estimated.

ionic radius of the central metal ion do not correlate. Instead, the electronic configuration of the PLN ligands can explain the trend. Plotting the PLN triplet emission wavelength versus the ionization potential (IP) of the central metal ion, an almost linear correlation is found, higher ionization potentials of the metal ion are associated with an increase in the triplet state energy of the PLN (fig. 4.20 b). This trend is also seen for HPLN, when using the first IP of hydrogen.

So far, no conclusive explanation for this correlation can be given. A possible reason is, that the local electron density at the oxygen atoms of the anionic ligands is influenced by the local field due to the central metal trication, which is apparently related to its third ionization potential. A related possibility is, that the metal-ligand bond lengths are influenced by corresponding electrostatic interactions. Further studies and theoretical calculations are required to explain the energy shift of emissions from the PLN triplet state in proximity to the various ionic species.

4.4 Summary

The combination of electrospray ionization, laser-induced luminescence, and matrix isolation was demonstrated using lanthanoid diketonate ions. The accumulation of some femto- to picomoles of mass-selected ions into a cryogenic noble gas matrix at about 5 K allowed measurements on highly reactive or elusive species, whose properties are typically masked in standard condensed-phase measurements. The obtained spectra displayed sharp emission lines. The influence of the matrix on the isolated species was assessed via comparison with laser-induced luminescence measurements of gas-phase ions stored in a Paul trap, and by the use of different matrix gases. The remarkable agreement between the results obtained using both techniques suggests, that the neon matrix often induces only a negligible geometrical and electronic perturbation of the studied species. Even vibronic bands were close to identical. By contrast, the perturbation was increased in argon matrixes. Measurements with further matrix gases (e.g. CO_2, N_2, or H_2O) enable the systematic assessment of environmental effects in future.

Complexation with CO_2 in the matrix and with DMSO prior to deposition was specifically studied to demonstrate the potential of such measurements. A broadening of the emission lines, and the emergence of shoulders, was observed for $Gd(PLN)_2^+$.

Thanks to the higher ion density achievable for matrix isolation measurements, the accessible signal-to-noise ratio was drastically improved relative to ion trap experiments. Consequently, species inaccessible to gas-phase studies were measured. Furthermore, lower irradiance and higher thermalization rates allowed the study of molecules which photofragment in gas phase.

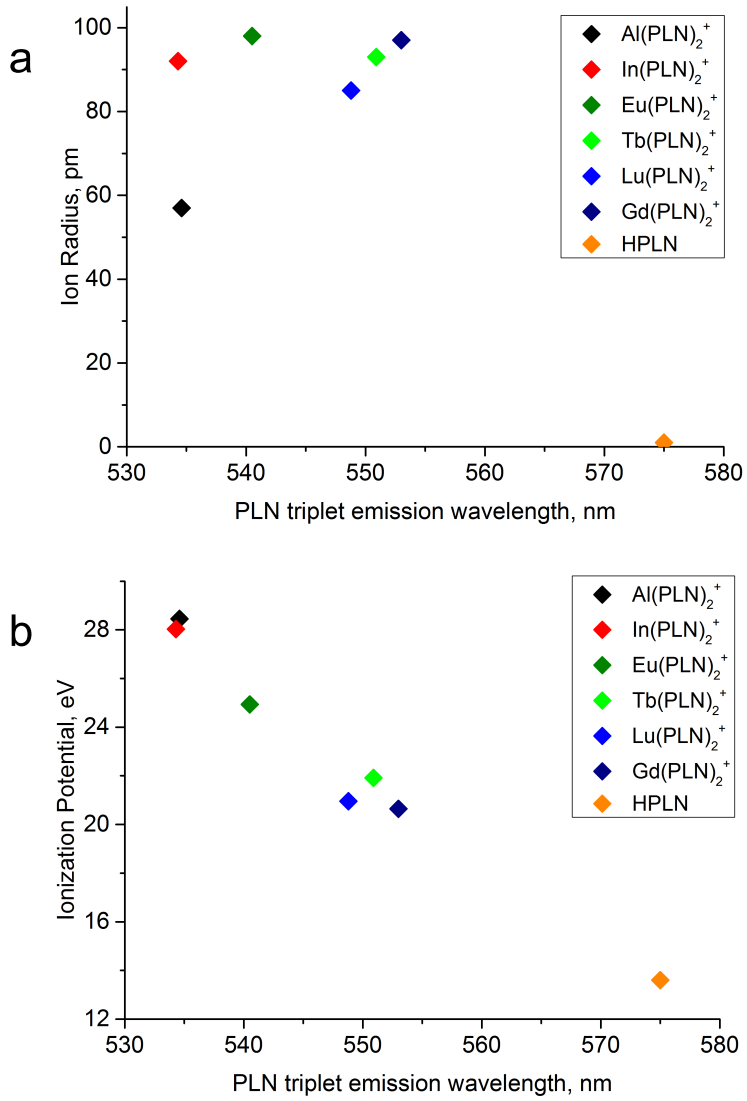

Figure 4.20: (a) No correlation is present for the emission wavelength and the ionic radius [209]. (b) Plotting the wavelength of the PLN triplet emission versus the ionization potential of the metal ions [193] and hydrogen a correlation is found.

A series of different metal diketonates was studied, with the main focus on the simple $M(PLN)_2^+$ species.

For metal ions without an acceptor state for energy transfer from the PLN triplet state (Al^{3+}, In^{3+}, Gd^{3+}, and Lu^{3+}), no emission from the metal was observed. For systems, where energy transfer is possible (Pr^{3+}, Eu^{3+}, Tb^{3+}, Dy^{3+}, Yb^{3+}, and Er^{3+}), emissions from the metal ions were detected for most lanthanoids. For Dy^{3+}, no emissions were detected, for the Tb^{3+} sample, the emitting species could not be identified.

The emission wavelength of the PLN triplet emission was shifted, depending on the central metal ion. A correlation between the third ionization potential of the metal and the emission wavelength was found.

For the Eu^{3+} containing species, the emissions from the lanthanoid ions were influenced by the presence of negative charges. For the $Eu(PLN)_2^+$ complex, Eu^{3+} emissions were suppressed by addition of electron scavengers. For $[Eu(PLN)_3Na]^+$ and $[Eu(PLN)_3K]^+$ in Ne, a side feature of the $^5D_0 \rightarrow {}^7F_2$ transition emerged (approximately 10 nm to the blue). This feature was suppressed in Ne + 0.01% CCl_4. Electrons, localized on the PLN ligands, are suggested to induce a reduction of the local symmetry of the Eu^{3+}, resulting the emergence of symmetry forbidden transitions or a splitting of the transitions.

5 STM Study of C_{60} and $H_2@C_{60}$

5.1 Endohedral Fullerenes

The study of elusive species by scanning tunneling microscopy (STM) is hindered by the necessary direct contact of the substrate and the species of interest. For dihydrogen, only the lower *para* spin state could be identified on nickel and gold surfaces, the interaction with the metal surfaces prevents the appearance of the *ortho* spin state of H_2 [210, 211].

One elegant way of isolating molecules or clusters in elusive states is incorporation into fullerenes. Using this approach, the endohedral species are effectively isolated, and for most molecular species only weak van der Waals interactions with the carbon cage occur, while interaction with the environment is suppressed.

Molecules and clusters, for example noble gases [212, 213], nitrogen [214], water [17] or metal clusters [12, 215], can be inserted into the cavity of the fullerene cage. This can be done during the formation process by arc discharge, by ion bombardment, or high-pressure and high-temperature treatment. However, the yield of these procedures is around one endohedral cage per one million fullerenes [212]. More efficient, and more elegant, is the synthetic way of 'molecular surgery' established by Komatsu *et al.* [16, 216]. Here, the fullerene is opened chemically, the molecule or cluster of interest inserted, and the cage is closed again. This method leads to yields of around 90%, and milligram quantities.

The interest in endohedral fullerenes lies in the possibility to tune their properties, for example the band gap, to form 'semiconducting' or 'metallic' molecules [217], and in the study of the isolated molecules inside the highly symmetrical fullerene environment. $N@C_{60}$, for example, is studied with regard to possible applications in quantum computing. The advantage of the endohedral nitrogen atom lies in its long relaxation times ($T_1 \approx 100$ - 1000 ms, $T_2 \approx 20\,\mu s$) [218]. Another example are endohedral gadolinium complexes, which are discussed as MRI contrast agents [219].

In the case of molecular hydrogen, the insertion into the fullerene cage allows for the study of the symmetric *ortho*- and the antisymmetric *para*-H_2 allotropes, shown schematically in figure 5.1. The interconversion time of *ortho*- and *para*-H_2 in C_{60} at room temperature is around 7 days [220], because interconversion requires highly forbidden simultaneous changes in the nuclear and rotational quantum numbers

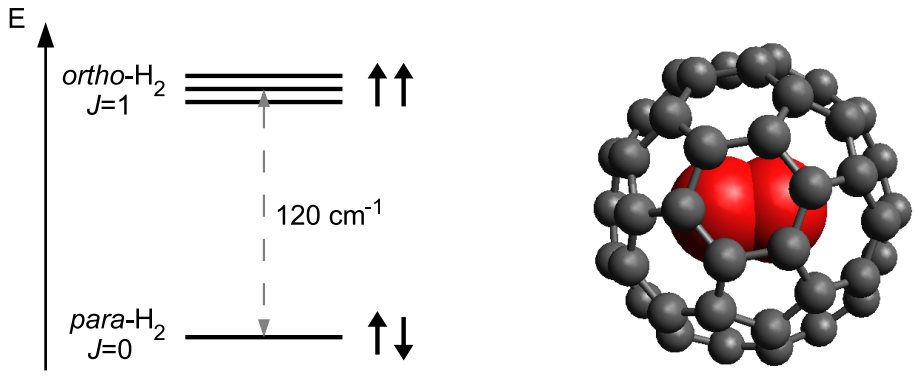

Figure 5.1: Left: Energy diagram for the two spin states of H_2. The ground state of *para*-H_2 (J=0) is 120 cm^{-1} lower in energy than *ortho*-H_2 (J=1). Right: Drawing of $H_2@C_{60}$.

[221, 222]. In the presence of a paramagnetic spin catalyst, the interconversion is much faster. The *para* state is about 120 cm^{-1} lower in energy, the equilibrium *ortho*:*para* ratio at room temperature is 3:1, reflecting the ratio of possible spin states. At temperatures below 170 K, the *para* state is favored.

Endohedral $H_2@C_{60}$ has been studied extensively by NMR spectroscopy [223, 224, 225, 226, 227], IR spectroscopy [228, 222], and inelastic neutron scattering (INS) [229]. An overview of these measurements is presented by Mamone *et al.* [21]

The main focus of previous measurements have been studies of the *ortho-para* conversion [225], and the translational, rotational, and vibrational transitions of the endohedral hydrogen molecule at different temperatures [228, 222].

All previous spectroscopic measurements have been performed on bulk samples, no single $H_2@C_{60}$ molecules were probed.

For inelastic electron tunneling spectroscopy (IETS) measurements of C_{60}, the electron-phonon coupling of the vibrational modes has to be considered. A theoretical description of Jahn-Teller distortions of adsorbed C_{60} during STM measurements is given in Lakin *et al.* [230]. In short, by ionizing the adsorbed C_{60} to C_{60}^-, the additional electron occupies the LUMO T_{1u} state. From simple considerations of the symmetry of the allowed dipole coupling for C_{60}, the H_g, A_g, and T_{1g} modes are expected to give a contribution to the IETS signal. Each mode results in a different nuclear displacement, giving rise to a Jahn-Teller effect and electron-vibration coupling. However, because of relaxation on the surface, and different possible charge states, it is expected that different modes can also be excited by IETS.

The empty fullerene C_{60} has been studied extensively by STM and IETS on different substrates [77, 78, 79, 80, 81]. It was shown that all Jahn-Teller active H_g modes of C_{60} can be excited on metallic substrates [81].

However, the appearance of inelastic features strongly depends on the position of the lowest unoccupied molecular orbital (LUMO) relative to the Fermi energy E_F. Only on Pb(111) are all eight H_g modes, and one A_g or T_{1u} mode of C_{60} detected, on Ag(111) only one mode ($H_g(2)$) was excited, while on Cu(111) no vibrations of C_{60} could be excited [81]. It was suggested that on Cu(111) the fullerene C_{60} molecules show an on-resonance electron transport, resulting in a quick damping of the molecular vibrations [231, 232], leading to a broadening of the transitions [233]. It was also suggested, that introduction of thin insulating films between C_{60} and the metallic substrate decreases the overlap of the molecular orbitals with the substrate [233, 234]. This should lead to narrow molecular resonances of all Jahn-Teller active modes. However, while experiments on C_{60} on thin alumina films did indeed show very sharp molecular resonances, only few vibronic modes were excited [77, 78].

For rotations of dihydrogen molecules on surfaces, two STM measurements have been reported [210, 211]. In the first experiment by Natterer *et al.* [210], dihydrogen was adsorbed on a monolayer of boron nitride on Ni(111). The rotational excitation spectra of the dihydrogen shows a transition at 43.7 meV, corresponding to the $J = 0 \rightarrow 2$ transition of *para*-H_2. No signal of *ortho*-H_2 was detected, probably due to fast conversion to the spin of lowest lowest nuclear energy on the surface. The number of dihydrogen molecules contributing to the measurement is estimated to be 60 ± 30. In the experiment by Li *et al.* [211], the STM tip was kept above a gold substrate, prepared with a sub-monolayer of dihydrogen. Under these conditions, the weakly physisorbed molecules were diffusing into and out of the tunneling junction, with the average lifetime of the trapped molecule being shorter than the response time of the STM. The signal originated from the average of several different diffusion and trapping processes. For the *para*-hydrogen molecule, the $J = 0 \rightarrow 2$ transition was measured at 42 meV. No signal from *ortho*-H_2 was reported. These measurements showed for the first time, that the detection of molecular rotations is possible with STM, although in both experiments, it was not possible to measure the spectrum of only one single hydrogen molecule in a fixed position on the sample.

No STM measurements of single endohedral H_2@C_{60} fullerenes have been reported so far.

5.2 IETS of C_{60} and H_2@C_{60} on CuN

In the measurements presented, an attempt is made to study the excitations of single endohedral *ortho*- and *para*-H_2 molecules. First, the vibronic spectrum of C_{60} on an insulating Cu{100}-$c(2 \times 2)$N (referred to as CuN) substrate [235, 236] is measured to assess whether the molecules are sufficiently decoupled from the surface, to enable the measurement of single transitions. Second, the rotation of hydrogen encapsulated in endohedral H_2@C_{60} is measured on CuN, in order to distinguish

the *ortho* and *para* state, and to enable the investigation of one single hydrogen molecule which is not adsorbed on the surface. IETS spectra are measured in the range from -110 to +110 mV and from -700 to -400 mV. Vibronic excitations of C_{60}, as well as the first rotational excitation of the encapsulated hydrogen molecule are expected in the first region. In the latter region, the coupled rotational-vibrational transitions of *ortho*- and *para*-H_2 are expected [228].

The sample of $H_2@C_{60}$ used for the measurements was provided by Dr. Murata [237]. Fullerene C_{60} was bought from SES Research (99.5% purity).

The CuN substrate is prepared by sputtering the Cu(100) substrate first with Ar^+ (U= 3 kV, I= 3 μA, t= 30 min) to clean the surface, followed by annealing at 720K to reduce the strain, and second with nitrogen ions (U= 0.65 kV, I= 0.15 μA, t= 20 min), followed by heating to 570K, to form a layer of isolating CuN. A low dosage of N_2 leads to unsaturated surfaces of copper nitride islands of roughly $5\times5\,nm^2$, separated by trenches of bare copper. At high dosages, the surface is fully covered by an insulating CuN layer. The molecules are deposited onto the CuN surface by sublimation from a ceramic crucible after thorough degassing at 570 K for one hour to remove residual solvent[8]. Deposition time of the molecules is 1 to 6 minutes at 610 to 630 K. Both $H_2@C_{60}$ and C_{60} do not decompose at the sublimation temperatures used [216]. Following the deposition of $H_2@C_{60}$, the residual material from the crucible is analyzed by mass spectroscopy (LTQ XL Orbitrap, Thermo Scientific, electrospray ionization) to confirm the stability of the molecule. The mass spectrum of a 80:20 sample of $H_2@C_{60}$:C_{60} is shown in figure 5.2. No escape of molecular hydrogen can be observed after heating to 640 K.

The molecules are deposited onto unsaturated and saturated layers of CuN. The topography of the samples is studied in constant current mode, the vibronic excitations of the molecules are measured by IETS. The experimental details are listed for each measurement. All measurements are carried out at sample temperatures of less than 1 K.

5.2.1 Results

On unsaturated CuN, both C_{60} and $H_2@C_{60}$ mainly adsorb on the bare copper trenches separating the CuN islands (figure 5.3). After deposition onto the saturated CuN surface, the molecules form large islands. For C_{60}, almost no single molecules are present on the surface (fig. 5.4 a), while for $H_2@C_{60}$ smaller islands and more single molecules can be seen (fig. 5.4 b). At low coverages of approximately 0.01 monolayer (ML), almost no ordered structures are present for $H_2@C_{60}$, as can be seen in figure 5.4 c.

[8] No mass selection is used for this experiment. The residual solvent is often not completely removed by degassing, while the deposition of mass selected ions allows for very clean samples [84].

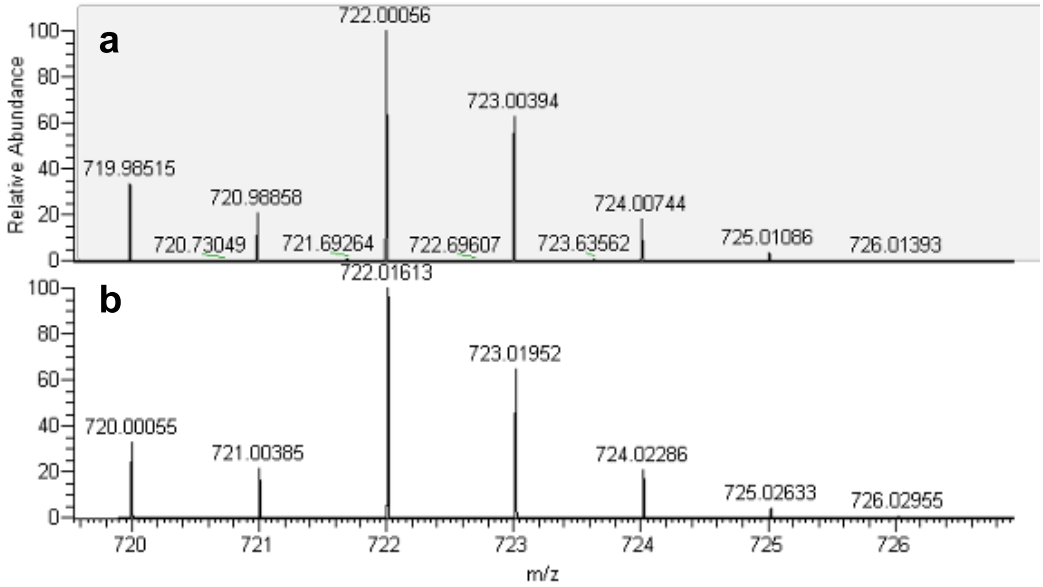

Figure 5.2: (a) Measured mass spectrum of a sample of 80:20 $H_2@C_{60}$:C_{60} after heating to 360 °C, (b) simulated mass spectrum for 75% $H_2@C_{60}$ + 25% C_{60}, assuming a natural carbon isotope abundance.

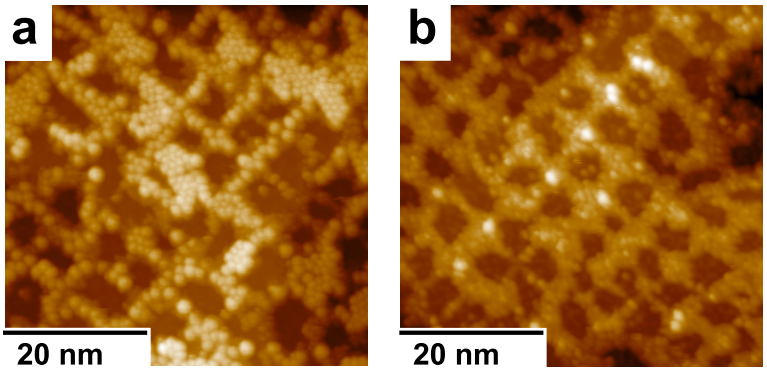

Figure 5.3: C_{60} (a) and $H_2@C_{60}$ (b) on an unsaturated CuN surface. The molecules mainly adsorb on the bare copper trenches. Experimental parameters: (a) $V = 0.51$ V, $I = 20$ pA; (b) $V = 1$ V, $I = 50$ pA

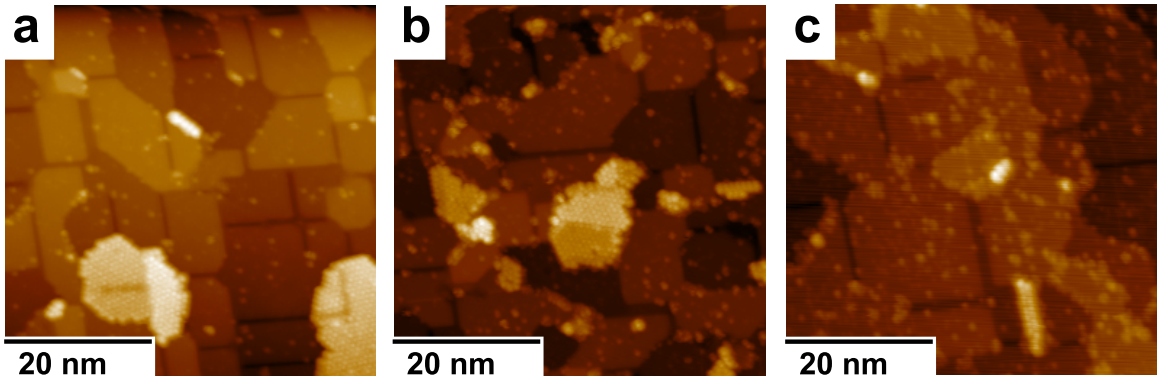

Figure 5.4: C_{60} (a) and $H_2@C_{60}$ (b, c) on a saturated CuN surface. C_{60} forms large, well ordered islands, for $H_2@C_{60}$ a higher density of smaller islands is observed. At low coverages (around 0.01 ML), almost no ordered structures are present for $H_2@C_{60}$ (c). Experimental parameters: (a) $V = 1\,\mathrm{V}$, $I = 100\,\mathrm{pA}$; (b) $V = 1\,\mathrm{V}$, $I = 100\,\mathrm{pA}$; (c) $V = 1\,\mathrm{V}$, $I = 50\,\mathrm{pA}$

For both C_{60} and $H_2@C_{60}$ the inelastic excitation spectra were measured. In the range from -110 to +110 mV, several sharp peaks are observed, which are mostly antisymmetric to the origin (fig. 5.5). In the range from -700 to -400 mV, no clear features can be distinguished in either species (fig. 5.8). IETS is performed solely on molecules adsorbed on CuN.

5.2.2 Discussion

The interaction of C_{60} and $H_2@C_{60}$ with the copper substrate is stronger than with CuN. Therefore, the molecules are pinned to the copper sites on the unsaturated CuN surface. On the saturated CuN surface, defect sites or contaminations act as trapping sites for the molecules, diffusion of the molecules on the surface leads to the aggregation of larger and well ordered islands.

The evident difference in mobility of $H_2@C_{60}$ on CuN, which leads to the appearance of more single molecules on the substrate, cannot be attributed to the molecule itself. Although the separation by high performance liquid chromatography indicates a different interaction of C_{60} and $H_2@C_{60}$ to the chromatography substrate, the difference is negligible: the difference in retention time is only 1% [216]. The mobility of the deposited molecules on the substrates at elevated temperatures (approximately 320 to 340 K) is expected to be large enough for both species to form well-ordered islands. Therefore, the presence of single $H_2@C_{60}$ is attributed to contaminations of the surface by residual solvent molecules, which are not completely removed by the degassing procedure (see footnote on p. 138).

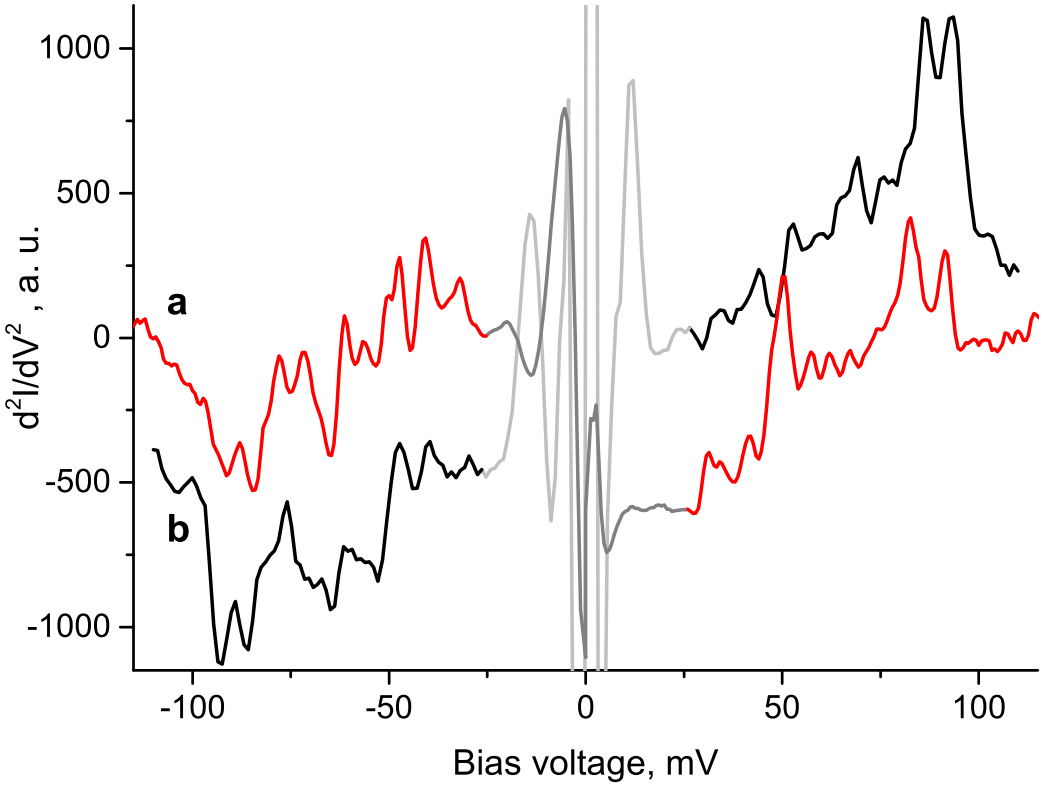

Figure 5.5: Inelastic tunneling spectrum of $H_2@C_{60}$ (a, red) and C_{60} (b, black) embedded in small islands on CuN. The signal is recorded as the second harmonic frequency with a lock-in amplifier. Experimental parameters: (a) $I = 10\,\text{nA}$ at $120\,\text{mV}$, $V_{mod} = 1.4\,\text{mV}$, $f = 2.97\,\text{kHz}$, 50 scans averaged (6 min each scan); (b) $I = 5\,\text{nA}$ at $110\,\text{mV}$, $V_{mod} = 2.5\,\text{mV}$, $f = 2.97\,\text{kHz}$, 200 scans averaged (3 min 20 s each scan). The strong inelastic features around zero, which are also present on the bare substrate, are shown in reduced contrast.

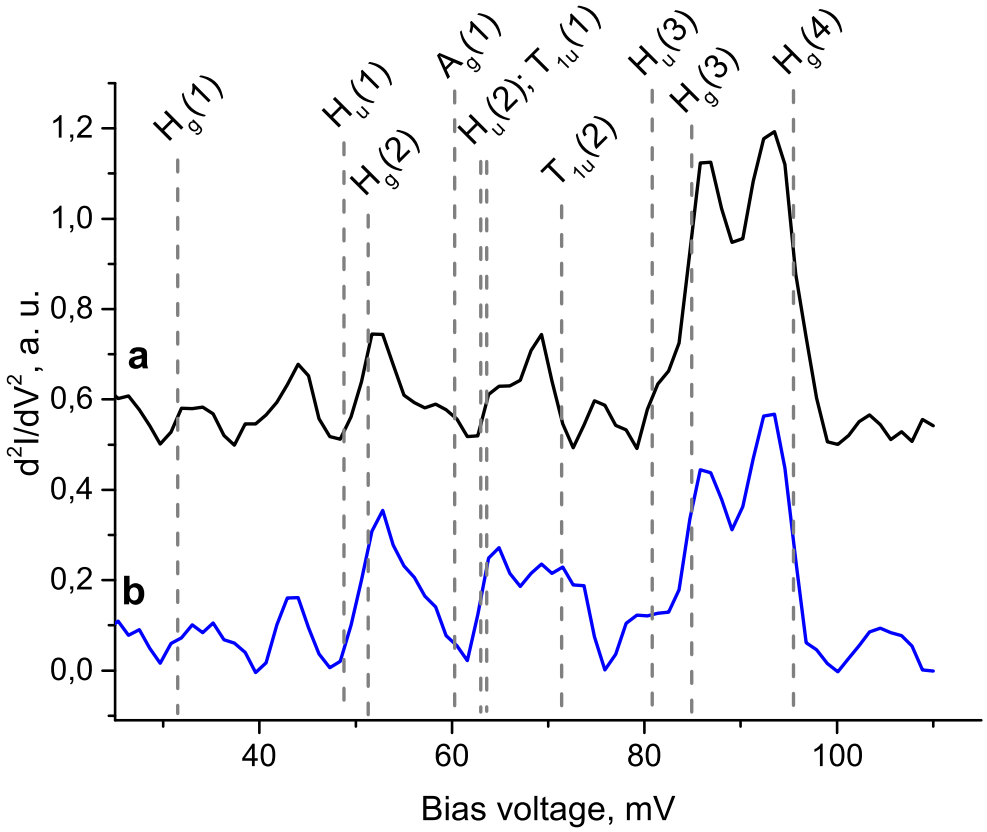

Figure 5.6: Inelastic tunneling spectra of C_{60} at positive bias (a) and at negative bias after antisymmetrization (b), in each case after background subtraction. The dashed lines indicate the energies of the corresponding vibrational modes of a free C_{60} molecule according to DFT. Experimental parameters: $I = 5\,\text{nA}$ at $110\,\text{mV}$, $V_{mod} = 2.5\,\text{mV}$, $f = 2.97\,\text{kHz}$, 200 scans averaged.

For the analysis of the IETS signal of C_{60}, the background is subtracted. The spectrum at positive voltage, and the spectrum at negative voltage after antisymmetrization, are shown in figure 5.6 a and b. In total nine vibrational features are identified. The noise level of background spectra of the bare CuN surface is shown in figure 5.7 d.

In previous experiments on Pb(111) and Al_2O_3 surfaces, excitations of the Jahn-Teller active modes have been identified in IETS. On Pb(111), an experiment similar to the one presented in this work has been done: C_{60} was deposited on the substrate, and the IETS spectrum was recorded from - 200 to + 200 mV. The H_g vibrational modes have been identified, as well as a feature which has been assigned to either a A_g or T_{1u} mode [81]. On Al_2O_3, vibronic progressions have been measured with a constant separation of the features. The separation was correlated to the vibronic excitations of the molecule. In this experiment, the bias voltage was varied from 0 to + 2.5 V. Here, the $A_g(1)$ and $H_g(4)$ modes have been identified [77]. On CuN, no IETS measurements of C_{60} have been reported previously.

Out of the nine identified features on CuN, four correspond to the Jahn-Teller active H_g(1-4) modes expected in this energy region. The additional four H_g modes (H_g(5-8)), which are expected for C_{60}, are out of range in this experiment. Only one of the A_g modes, $A_g(1)$, is inside the experimental range. These Jahn-Teller actice modes are assigned to the measured vibrations, which are closest in energy. The assignment is shown in figure 5.6 and table 5.1.

The assignment of the remaining features is more complicated. The additional vibrational modes of C_{60} are close-lying, and do usually not exhibit electron-vibration coupling. Based on theoretical transition energies, the experimentally identified features are tentatively assigned (table 5.1). Note that due to the high number of vibrations of C_{60}, 46 vibrational states in 10 irreducible representations of the I_h point group, the assignment based on the energy of the vibrations is somewhat uncertain. A shift of the theoretical or experimental energy of less than 5 meV leads to a complete change of the assignment. Additionally, the H_u, T_{1g}, and T_{1u} modes show no electron-vibration coupling in gas phase. However, a relaxation of the molecular symmetry on the surface could allow the nonactive modes to be excited [81].

On CuN, the identified vibronic features of C_{60} have a smaller width than those of C_{60} on Pb(111) [81], which were measured at a comparable temperature of 5 K. A longer lifetime of the excited states on an insulating substrate is suggested. A long lifetime of the vibration increases the possibility of interaction with other states - in the case of endohedral H_2@C_{60}, we hope that a coupling of the vibrational excitation of C_{60} to the H_2 rotation is detectable. The rotation of *para*-dihydrogen on metallic substrates has previously been identified at approximately 43 meV [210, 211].

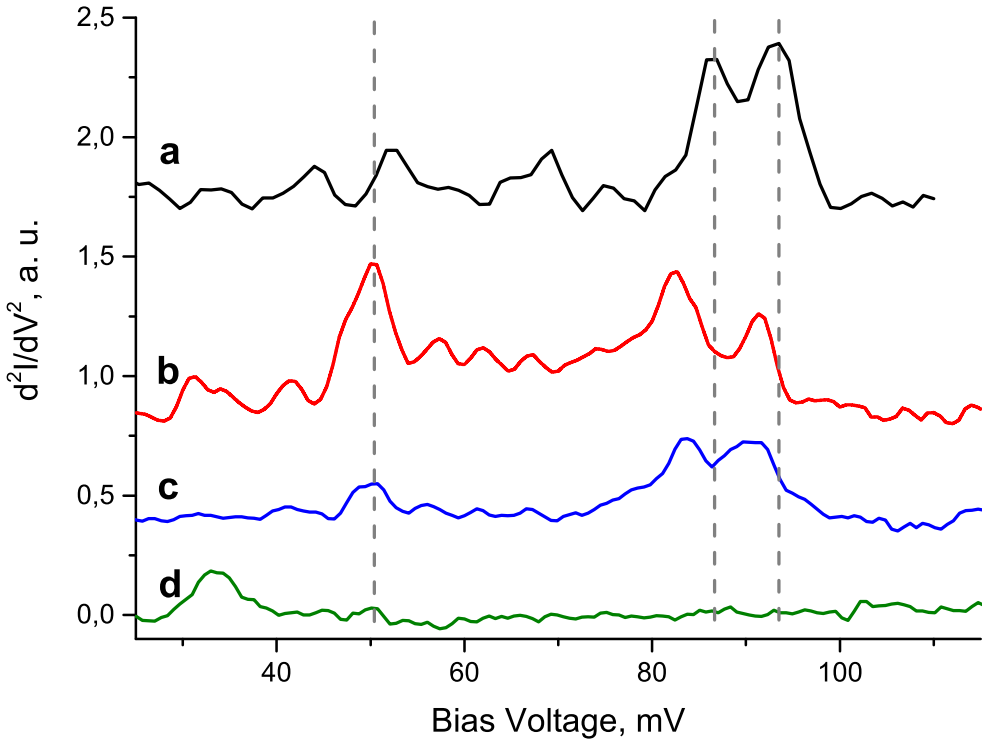

Figure 5.7: Inelastic tunneling spectra of C_{60} and $H_2@C_{60}$ at positive bias after background subtraction. (a) C_{60}, (b) and (c) different molecules of the sample of $H_2@C_{60}$, (d) bare CuN substrate, showing the noise level of the measurements. The dashed lines are to guide the eye. Experimental parameters: (a) $I = 5\,\text{nA}$ at 110 mV, $V_{mod} = 2.5\,\text{mV}$, $f = 2.97\,\text{kHz}$, 200 scans averaged, (b), and (c) $I = 10\,\text{nA}$ at 120 mV, $V_{mod} = 1.4\,\text{mV}$, $f = 2.97\,\text{kHz}$, 50 scans averaged, (d) $I = 1\,\text{nA}$ at 120 mV, $V_{mod} = 1.4\,\text{mV}$, $f = 2.97\,\text{kHz}$, 50 scans averaged.

Table 5.1: Experimental energy of the vibrational modes detected in IETS of C_{60} on CuN, tentatively assigned symmetry, and calculated energy according to DFT [33].

experiment	*literature* [a]	*theory*	
$\hbar\omega_\nu$, meV	$\hbar\omega_\nu$, meV	mode	$\hbar\omega_{calc}$, meV
34 ± 2	34 ± 2	$H_g(1)$	31.5
44 ± 2		$H_u(1)$	48.9
53 ± 2	52 ± 2	$H_g(2)$	51.3
60 ± 2		$A_g(1)$	60.4
65 ± 2	67 ± 2	$H_u(2)$; $T_{1u}(1)$ [b]	63.2; 63.6
69 ± 2		$T_{1u}(2)$	71.4
80 ± 2		$H_u(3)$	80.9
86 ± 2	87 ± 2	$H_g(3)$	84.9
94 ± 2	97 ± 3	$H_g(4)$	95.5

[a] Values of IETS of C_{60} on Pb(111), by Franke *et al.* [81]; [b] No clear assignment possible.

In IETS spectra of endohedral H_2@C_{60} in the energy region from -110 to +110 mV, the C_{60} $H_g(3)$ and $H_g(4)$ vibrations are clearly observed (fig. 5.7), though a shift in the excitation energy of roughly 2.5 mV occurs. The vibronic modes with lower intensities are also shifted.

A prominent peak occurs in the spectra of some H_2@C_{60} molecules at 50 mV, which is not detected in IET spectra of C_{60}. This feature is present in several measurement of different molecules. However, a weak feature at the same energy is present on the bare CuN substrate. Also, this feature is only detected at positive bias. Even though asymmetric IETS spectra have been recorded for graphene [238], the most likely explanation for this feature is an inelastic excitation of the tip. Still, one could speculate about its sole presence at positive bias being due to a direction dependance of the H_2@C_{60}-electron coupling on the surface.

A possible explanation for the energy shift of the H_2@C_{60} vibrations are different adsorption geometries, or solvent molecules, which interact with the cage, thus lowering the vibrational energy levels. Also, a small bias offset for the experiment cannot be excluded, either from the calibration, or by the insulating substrate. An influence of the endohedral H_2 is unlikely: the shift of the vibrations in the experiment (2.5 meV/20 cm^{-1}) is much larger than the shift, which has been observed for other endohedral systems. For thin films of Ar@C_{60} and Kr@C_{60}, the A_g, H_g, and T_{1u} modes were measured to be within 0 - 5 cm^{-1} of the pure C_{60} frequencies [239]. Even in (Li@C_{60})$_2$, the main Raman features ($H_g(1)$ and $A_g(1,2)$ modes) are close to identical to (C_{60})$_2$ [240].

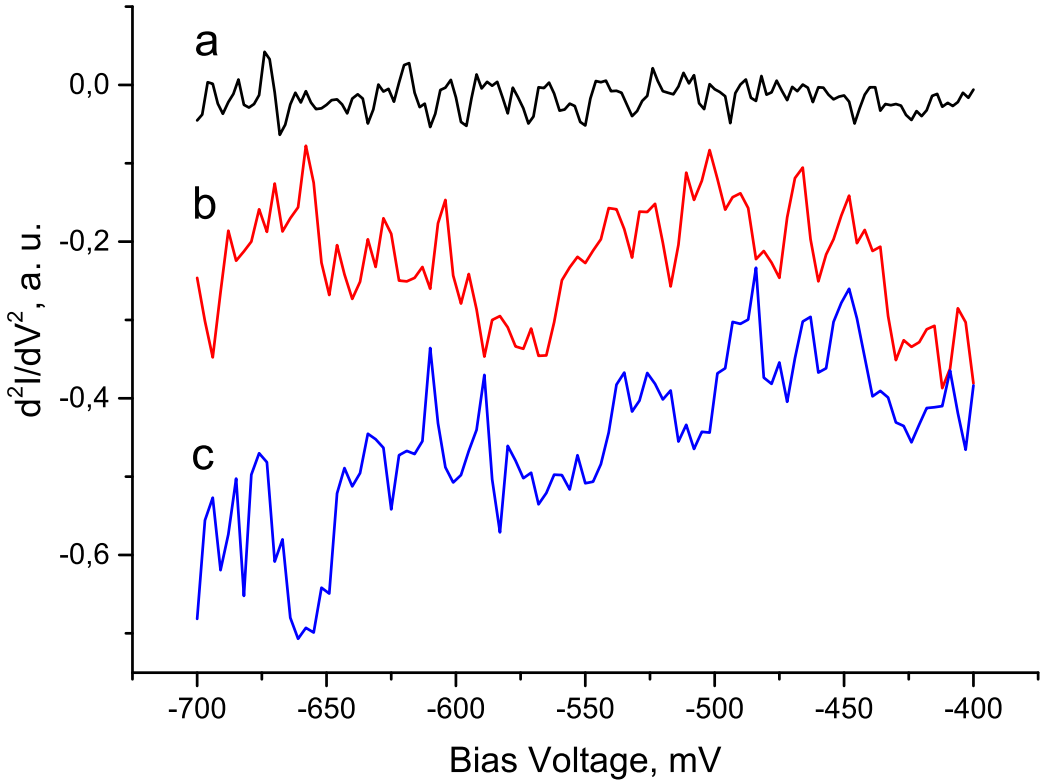

Figure 5.8: Inelastic tunneling spectrum in the range of the S(0) and S(1) transitions of *ortho*- and *para*-H_2. (a) CuN background, (b) and (c) $H_2@C_{60}$ on CuN. The signal is recorded as the second harmonic signal with a lock-in amplifier. Experimental parameters: (a) $I = 11\,\text{nA}$ at -700 mV, $V_{mod} = 3\,\text{mV}$, $f = 2.92\,\text{kHz}$, 10 scans averaged ; (b) and (c) $I = 3\,\text{nA}$ at -700 mV, $V_{mod} = 3\,\text{mV}$, $f = 2.92\,\text{kHz}$, 10 scans averaged. The spectra are offset for clarity.

IET spectra in the range of $H_2@C_{60}$ in the range from -700 to -400 mV do not show any excitations, as can be seen in figure 5.8. For C_{60}, no vibrational transitions are expected in this energy range. For $H_2@C_{60}$, the coupled rotational-vibrational transitions of *ortho*- and *para*-H_2 are expected in this region. The S(0) transitions of *para*- and the S(1) transition of *ortho*-H_2 differ enough in energy to be distinguished by IETS spectroscopy. By IR spectroscopy, the energies of these transitions are determined to be 569 meV and 595 meV, respectively [228]. However, in the IETS spectra shown in figure 5.8, no excitation of the endohedral H_2 molecule is observed.

A probable cause for the absence of detectable hydrogen excitations is, that the hydrogen inside the fullerene cage is electronically shielded from the environment. The charge transport in organic materials and C_{60} occurs mainly through the π molecular orbitals [241, 242]. The π orbitals are mainly localized on the cage of C_{60}, no strong coupling to endohedral molecules is expected. This leads to an inherently weak signal from any can der Waals interacting molecule inside the fullerene cage. On Cu(111), it was shown that C_{60} can form atomlike molecular orbitals at bias voltages of around 3.5 V, which have s, p, and d character [243]. These orbitals are core-centered and can hybridize with species in the center of the cage, as was shown for $Li@C_{60}$ [243] and $La@C_{82}$ [244], while the π orbitals do not show any hybridization. No IETS measurements at a bias above 1 V are performed yet.

The existence of weak hydrogen transitions below the detection limit of the experimental setup is possible. In this case, the signal intensity is at least one order of magnitude lower than the signal intensity of the $H_g(3)$ and $H_g(4)$ modes of C_{60}. It is also possible, that the lifetime of the hydrogen excitations is very short due to the interaction of the adsorbed $H_2@C_{60}$ with the CuN substrate, leading to very broad spectral features which cannot be distinguished from the background.

5.3 Summary

C_{60} and endohedral $H_2@C_{60}$ were deposited onto an insulating CuN surface. The topography and the inelastic excitations of the molecules were measured.

The topography of samples of pure C_{60} showed well-ordered islands, while for $H_2@C_{60}$ smaller islands, clusters and single molecules occured. The difference in adsorption energy between C_{60} and $H_2@C_{60}$ is negligible and cannot be the cause of this discrepancy. The presence of residual solvent molecules from the purification of $H_2@C_{60}$ was suggested.

For the first time, the vibrational spectrum of C_{60} adsorbed on insulating CuN surface was measured by IETS. In contrast to measurements on an insulating Al_2O_3 substrate, all Jahn-Teller active modes were identified [77]. Several additional Jahn-Teller inactive modes were observed. The relaxation of the molecular symmetry on the surface probably enhances electron-vibration coupling effects.

In $H_2@C_{60}$, a shift of the vibrations to lower energies is observed. However, no conclusive explanation of this shift could be given so far.

No transitions of the endohedral H_2 were found in IET spectra of $H_2@C_{60}$ in the studied energy range (from -700 to -400 meV, and from -110 to +110 meV). This result was rationalized by the small intrusion of the electronic wave functions of C_{60} into the cage [243], effectively isolating the hydrogen molecule from the tunneling electrons. Further experiments at higher bias voltages ($U > 2$ V) are suggested.

6 Summary and Outlook

In this thesis, elusive molecular species were studied with optical spectroscopy in cryogenic noble gas matrixes and with low-temperature STM. For the optical spectroscopy measurements, the existing apparatus for isolating elusive and reactive species in cryogenic matrixes was improved, especially regarding the optical range and the ion current intensity. The improved setup enabled the study of previously inaccessible, mass-selected fullerene and azafullerene ions in unusual charge states. The frequency of vibrational and electronic transitions was determined. For ionic species of astrophysical interest, the gas phase absorption frequencies were extrapolated and the integrated molar absorptivities were established.

The combination of electrospray ionization and matrix isolation was demonstrated for the first time. From the ion source to the deposition chamber, the pressure was reduced by a factor of 10^{12}, allowing for a deposition time of up to several hours without sample degradation or the accumulation of appreciable amounts of contaminations. The photoluminsecent properties of electrosprayed lanthanoid diketonate complexes were determined, which previously could not be determined in gas phase or in condensed phase.

STM was used to study vibronic excitations of single C_{60} and $H_2@C_{60}$ molecules on CuN surfaces. With $H_2@C_{60}$, a system was studied in which the endohedral hydrogen molecule is quasi-free, with only weak interactions to the surrounding fullerene cage, while still being addressable as a single molecule by STM.

In summary, fullerenes, azafullerenes and their ions were investigated with optical spectroscopy. The measurement range extended from 200 nm in the UV to 400 - 200 cm^{-1} in the far-IR. All species studied were isolated in noble gas matrixes at $\approx$ 5 K. Cations were generated by electron impact ionization, anions during deposition by electron capture.

For C_{60}^+ and C_{60}^-, several previously unidentified IR absorptions were detected. For the first time, C_{60}^{2+} and C_{60}^{3+} were studied by optical spectroscopy. The integrated molar absorptivities of all identified IR absorptions, and the oscillator strengths of the NIR absorptions of C_{60}^+, C_{60}^-, and C_{60}^{3+} were established. For C_{60}^+ and C_{60}^-, the oscillator strengths were found to be significantly larger than previously accepted values. In combination with the extrapolated gas phase IR absorption frequencies,

these results are of interest for the identification of fullerene C_{60} species in stellar objects.

For the first time, the IR spectra of C_{70}^+, C_{70}^-, and C_{70}^{2+} were measured. Both C_{70}^+ and C_{70}^- were identified as non-Born-Oppenheimer systems, showing a large electron-vibration coupling. In the IR, the integrated molar absorptivities of the matrix isolated species were established. For $C_{70}^{+/-}$, the IR gas phase absorption frequencies were extrapolated. The electronic transitions of C_{70}^+ in the visible range were revised. Absorptions previously assigned to C_{70}^+ were re-assigned to C_{70}^- and C_{70}^{2+}. Moreover, an additional electronic transition of C_{70}^+ was observed. As for $C_{60}^{+/-}$, the measured spectra of $C_{70}^{+/-/2+}$ are of interest for astronomy.

The non-IPR fullerene C_{58} was studied for the first time as the isolated monomer. In the IR, several absorptions were identified and tentatively assigned to the specific charge states $C_{58}^{0/+/-}$. Only four strong absorptions of C_{58}^0 could clearly be identified in the IR, indicating that only one dominant isomer was generated by electron impact fragmentation of C_{60}. The integrated molar absorptivities of the C_{58} IR absorptions was estimated to be at least one order of magnitude smaller than the integrated molar absorptivity of the C_{60} $T_{1u}(1)$ mode. No clear absorptions of $C_{58}^{0/+/-}$ were detected in the UV to NIR range.

The neutral azafullerene dimer $(C_{59}N)_2$, and the monomer $C_{59}N$ radical, were studied for the first time as isolated species in cryogenic noble gas matrixes. For both species, IR fingerprint absorptions were identified. In the NIR, electronic transitions with vibronic progressions were observed for both the monomer and the dimer. The monomer ions $C_{59}N^{+/-}$ were also studied. For the cation $C_{59}N^+$, only few and unexpectedly weak IR absorptions were identified, while for the anion $C_{59}N^-$, several clear IR absorptions were observed, with intensities comparable to those of the ions of the fullerene C_{60}. In the NIR, no absorptions were observed for the charged azafullerene monomers.

Different photoluminescing lanthanoid diketonate complexes were deposited in cryogenic matrixes and studied by laser-induced luminescence spectroscopy. The combination of nano-electrospray ionization, mass-to-charge selection, and soft-landing into cryogenic noble gas matrixes was demonstrated for the first time.

Matrix effects of isolated lanthanoid diketonate complexes were studied by comparison to gas phase measurements and different matrix environments. All species studied showed a good overall agreement between gas phase and matrix isolation spectra, even vibronic bands of the PLN triplet emission in $Gd(PLN)_2^+$ were close to identical. The ion density, and thus also the signal intensity, could be enhanced by several orders of magnitude in matrix isolation relative to space charge limited gas phase measurements.

Different trivalent metal centers in the $M(PLN)_2^+$ complexes were studied systematically. For some species, emissions from the PLN anion $T_1 \rightarrow S_0$ transition were observed. For Pr^{3+}, Eu^{3+}, Yb^{3+}, and Er^{3+} as central metal ions, energy transfer from the PLN anion triplet state to the metal ion, and subsequent emissions of the metal ion, were detected. For the wavelengths of the PLN triplet emissions, a linear correlation to the third ionization potential of the central metal ion, and the first ionization potential of hydrogen in HPLN, was found.

The spectra of diketonate complexes with Eu^{3+} was influenced by the presence of electron scavengers in the matrixes. For $Eu(PLN)_2^+$, the symmetry forbidden $^5D_0 \rightarrow ^7F_J$ emissions were observed in pure Ne matrixes, while they were not detected in matrixes with electron scavengers. For $[Eu(PLN)_3Na]^+$ and $[Eu(PLN)_3K]^+$, the $^5D_0 \rightarrow ^7F_2$ emission in Ne matrixes was shifted by 10 nm to the blue compared to gas phase measurements. In matrixes with electron scavengers, the gas phase spectra was reproduced. The formation of $PLN^{2-} \cdot\cdot Eu^{3+} \cdot\cdot PLN^-$ complexes with reduced symmetry was suggested.

To study the excitations of single quasi-free hydrogen molecules encapsulated in C_{60} cages, C_{60} and endohedral $H_2@C_{60}$ were studied by low-temperature scanning tunneling microscopy. For the first time, vibronic features of C_{60} were studied on a CuN substrate. In the bias range from -110 to +110 mV nine vibronic modes were resolved. Jahn-Teller active H_g and A_g modes, as well as Jahn-Teller inactive H_u and T_{1u} modes were observed, showing a symmetry reduction on the substrate.

For $H_2@C_{60}$, excitations of the endohedral dihydrogen were not detected. In the studied energy range (from -700 to -400 meV, and from -110 to +110 meV), the excitations of endohedral hydrogen are estimated to be at least one order of magnitude weaker than the vibronic excitations of the fullerene C_{60} cage on CuN. The measurement of the H_2 *ortho* state by STM, and the measurement of rotational spectra of addressable molecules, remains a task for further experiments.

Future improvements for the absorption measurement setup are a diamond beam splitter for the FTIR, as well as diamond vacuum windows, which will enable routine measurements from the visible to the far-infrared region, without changing the setup, i.e. without having to break the vacuum, readjust the optical setup, and make a new sample. Molecular iodine is planned to be used as electron scavenger. This will facilitate IR measurements of ionic species, because I_2 produces no IR absorptions.

Species for further studies are mass- and charge-selected polyaromatic hydrocarbons, diamondoids, hydrogenated fullerenes, and fullerene fragments, which are of relevance for astronomy and astrochemistry.

For luminescence measurements, the use of a tunable excitation laser system would allow for the study in different wavelength regions. The ion intensity of the ESI source could be improved by multi-capillary nanoES or similar techniques. Only deposition of cationic species is possible as yet, neutralization of the matrix via secondary electrons does not work for the deposition of anions. Simultaneous deposition of the anion of interest and a cationic counterion could allow for the study negatively charged species, which are inaccessible in the current setup. Also, the addition of an ion mobility spectrometer is suggested, to select different molecular isomers prior to the deposition.

In future experiments, the scope of molecular ions studied can be expanded. A systematic study of different elusive charge states and the interaction with different environments can be performed.

To improve the STM measurements of H_2@C_{60}, deposition of the molecules with mass-selection and subsequent soft-landing on the substrate is suggested. By this, contamination of the substrate by residual solvent molecules can be prevented. Furthermore, the excitation of atomlike molecular orbitals of C_{60} and H_2@C_{60} at higher bias voltages (U>2 V) is suggested for additional measurements. Hybridization with the endohedral hydrogen is expected to increase the interaction of the tunneling electron with the isolated H_2.

Acknowledgment

I would like to express my gratitude to the following people. The presented work would not have been possible without them. I want to thank

Prof. Dr. Wulf Wulfhekel for giving me the opportunity for this thesis, for his patience, motivation, and help throughout the work,

Prof. Dr. Manfred M. Kappes for the continuous support, his insightful comments and encouragement, and his immense knowledge he was always willing to share,

Dr. Dmitry Strelnikov for the great time I had working with him and his constant support in all things related to matrix isolation spectroscopy,

Dr. Jean-François Greisch for his enthusiasm and the stimulating discussions about luminescence,

Dr. Hironari Isshiki, Jinjie Chen, and Dr. Toshio Miyamachi for their support and advice with the STM measurements,

Dr. Artur Böttcher and Dr. Patrick Weis for helping with the experimental setup and with all the small and not so small problems,

all former and present group members of the Institute of Physical Chemistry and Institute of Physics for their moral support and the great atmosphere,

Dr. Regina Eigler and Prof. Andreas Hirsch for the synthesis of the azafullerene $(C_{59}N)_2$,

Dr. Bernhard Schäfer and Prof. Dr. Mario Ruben for the synthesis of the lanthanoid diketonates,

Dr. Michihisa Murata and Prof. Dr. Yasujiro Murata for the synthesis of the endohedral $H_2@C_{60}$,

Holger Halberstadt and Klaus Stree for everything they constructed and repaired over the years,

Dieter Walz and his team in the mechanical workshop for the quick and competent fabrication all special requests,

and my family and friends, and especially Ella, for their loving support and motivation over the last years.

Bibliography

[1] E. Whittle, D. A. Dows, and G. C. Pimentel. Matrix Isolation Method for the Experimental Study of Unstable Species. *J. Chem. Phys.*, 22:1943, 1954.

[2] H. E. Hallam, editor. *Vibrational Spectroscopy of Trapped Species*. John Wiley & Sons, New York, 1973.

[3] S. Cradock and A. J. Hinchcliffe. *Matrix Isolation: A Technique for the Study of Reactive Inorganic Species*. Cambridge University Press, New York, 1975.

[4] J. A. Glasel. Near-Infrared Absorption Spectra of *ortho*- and *para*-H_2O in Solid Xenon and Argon. *J. Chem. Phys.*, 33:252, 1960.

[5] P. H. Kasai and D. McLeod. Electron Spin Resonance Study of Molecular Anions Generated in Argon Matrix at 4K: ESR Spectrum of $B_2H_2^-$. *J. Chem. Phys.*, 51:1250, 1969.

[6] W. Harbich. 'Soft landing' of size-selected clusters in chemically inert substrates. *Philos. Mag. B*, 79(9):1307–1320, 1999.

[7] J. P. Maier. Spectroscopic characterization of mass-selected ions. *Mass Spectrom. Rev.*, 11(8):119–135, 1992.

[8] J. Fulara, M. Jakobi, and J. P. Maier. Electronic and Infrared Spectra of C_{60}^+ and C_{60}^- in Neon and Argon Matrices. *Chem. Phys. Lett.*, 211:227–234, 1993.

[9] J. Fulara, M. Jakobi, and J. P. Maier. Electronic spectra of the C_{70} molecule and C_{70}^+, C_{70}^- ions in neon matrices. *Chem. Phys. Lett.*, 206(1-4):203–209, 1993.

[10] J. B. Fenn, M. Mann, C. K. Meng, S. F. Wong, and C. M. Whitehouse. Electrospray Ionization for Mass Spectrometry of Large Biomolecules. *Science*, 246(4926):64–71, October 1989.

[11] G. Binnig, H. Rohrer, Ch. Gerber, and E. Weibel. Surface Studies by Scanning Tunneling Microscopy. *Phys. Rev. Lett.*, 49:57–61, 1982.

[12] J. R. Heath, S. C. O'Brien, Q. Zhang, Y. Liu, R. F. Curl, F. K. Tittel, and R. E. Smalley. Lanthanum complexes of spheroidal carbon shells. *J. Am. Chem. Soc.*, 107(25):7779–7780, 1985.

[13] D. S. Bethune, R. D. Johnson, J. R. Salem, and C. S. de Vries, M. S.and Yannoni. Atoms in carbon cages: the structure and properties of endohedral fullerenes. *Nature*, 366:123–128, 1993.

[14] Z. Ge, J. C. Duchamp, T. Cai, H. W. Gibson, and H. C. Dorn. Purification of Endohedral Trimetallic Nitride Fullerenes in a Single, Facile Step. *J. Am. Chem. Soc.*, 127(46):16292–16298, 2005.

[15] S. Stevenson, J. P. Phillips, J. E. Reid, M. M. Olmstead, S. P. Rath, and A. L. Balch. Pyramidalization of Gd_3N inside a C_{80} cage. The synthesis and structure of $Gd_3N@C_{80}$. *Chem. Commun.*, pages 2814–2815, 2004.

[16] K. Komatsu, M. Murata, and Y. Murata. Encapsulation of Molecular Hydrogen in Fullerene C_{60} by Organic Synthesis. *Science*, 307(5707):238–240, 2005.

[17] K. Kurotobi and Y. Murata. A Single Molecule of Water Encapsulated in Fullerene C_{60}. *Science*, 333(6042):613–616, 2011.

[18] R. Klingeler, G. Kann, I. Wirth, S. Eisebitt, P. S. Bechthold, M. Neeb, and W. Eberhardt. La@C_{60}: A metallic endohedral fullerene. *J. Chem. Phys.*, 115(15):7215–7218, 2001.

[19] T. Huang, J. Zhao, M. Feng, A. A. Popov, S. Yang, L. Dunsch, and H. Petek. A Molecular Switch Based on Current-Driven Rotation of an Encapsulated Cluster within a Fullerene Cage. *Nano Lett.*, 11(12):5327–5332, 2011.

[20] J. Jiang, B. Gao, Z. P. Hu, Wei Lu, Z. Y. Wu, J. L. Yang, and Y. Luo. Identification of metal-cage coupling in a single metallofullerene by inelastic electron tunneling spectroscopy. *Appl. Phys. Lett.*, 96(25):253110, 2010.

[21] S. Mamone, J. Y.-C. Chen, R. Bhattacharyya, M. H. Levitt, R. G. Lawler, A. J. Horsewill, T. Rõõm, Z. Bačić, and N. J. Turro. Theory and spectroscopy of an incarcerated quantum rotor: The infrared spectroscopy, inelastic neutron scattering and nuclear magnetic resonance of H_2@C_{60} at cryogenic temperature. *Coord. Chem. Rev.*, 255(7–8):938 – 948, 2011.

[22] P. Hohenberg and W. Kohn. Inhomogeneous Electron Gas. *Phys. Rev. B*, 136:864 – 871, 1964.

[23] V. N. Staroverov, G. E. Scuseria, J. Tao, and J. P. Perdew. Comparative assessment of a new nonempirical density functional: Molecules and hydrogen-bonded complexes. *J. Chem. Phys.*, 119(23):12129–12137, 2003.

[24] J. P. Perdew, J. Tao, V. N. Staroverov, and G. E. Scuseria. Meta-generalized gradient approximation: Explanation of a realistic nonempirical density functional. *J. Chem. Phys.*, 120(15):6898–6911, 2004.

[25] A. Bérces, R. M. Dickson, L. Fan, H. Jacobsen, D. Swerhone, and T. Ziegler. An implementation of the coupled perturbed Kohn-Sham equations: pertubation due to nuclear displacements. *Comput. Phys. Commun.*, 100:247–262, 1997.

[26] H. Jacobsen, A. Bérces, D. P. Swerhone, and T. Ziegler. Analytic second derivatives of molecular energies: a density functional implementation. *Comput. Phys. Commun.*, 100:263–276, 1997.

[27] David Sholl and Janice A. Steckel. *Density Functional Theory: A Practical Introduction*. John Wiley & Sons, New York, 2011.

[28] D. J. Tozer and N. C. Handy. On the determination of excitation energies using density functional theory. *Phys. Chem. Chem. Phys.*, 2:2117–2121, 2000.

[29] M. C. M. O'Brien and C. C. Chancey. The Jahn–Teller effect: An introduction and current review. *Am. J. Phys.*, 61(8):688–697, 1993.

[30] R. Gopalan. *Concise Coordination Chemistry*. Vikas Publishing House Pvt Limited, 1st edition, 2001.

[31] W. Domcke, H. Köppel, and L. S. Cederbaum. Spectroscopic effects of conical intersections of molecular potential energy surfaces. *Mol. Phys.*, 43(4):851–875, 1981.

[32] F. Negri, G. Orlandi, and F. Zerbetto. Quantum-chemical investigation of Franck-Condon and Jahn-Teller activity in the electronic spectra of Buckminsterfullerene. *Chem. Phys. Lett.*, 144(1):31–37, 1988.

[33] TURBOMOLE V7.0 2015, a development of University of Karlsruhe and Forschungszentrum Karlsruhe GmbH, 1989-2007, TURBOMOLE GmbH, since 2007; available from http://www.turbomole.com.

[34] A. D. Becke. Density-functional exchange-energy approximation with correct asymptotic behavior. *Phys. Rev. A*, 38:3098–3100, 1988.

[35] J. P. Perdew. Density-functional approximation for the correlation energy of the inhomogeneous electron gas. *Phys. Rev. B*, 33:8822–8824, 1986.

[36] A. Schäfer, H. Horn, and R. Ahlrichs. Fully optimized contracted gaussian basis sets for atoms Li to Kr. *J. Chem. Phys.*, 97(4):2571–2577, 1992.

[37] E. D. Becker and G. C. Pimentel. Spectroscopic Studies of Reactive Molecules by the Matrix Isolation Method. *J. Chem. Phys.*, 25(2):224–228, 1956.

[38] H. W. Brown and G. C. Pimentel. Photolysis of Nitromethane and of Methyl Nitrite in an Argon Matrix; Infrared Detection of Nitroxyl, HNO. *J. Chem. Phys.*, 29:883, 1958.

[39] M. Moskovits and J. E. Hulse. The ultraviolet-visible spectra of diatomic, triatomic, and higher nickel clusters. *J. Chem. Phys.*, 66:3988, 1977.

[40] Ian R. Dunkin. *Matrix Isolation Technique: A Practical Approach*. Oxford University Press, Oxford, New York, 1998.

[41] C. M. Lovejoy and D. J. Nesbitt. High sensitivity, high-resolution IR laser spectroscopy in slit supersonic jets: Application to N_2HF ν_1 and $\nu_5 + \nu_1 - \nu_5$. *J. Chem. Phys.*, 86:3151, 1987.

[42] D. W. Kohn, H. Clauberg, and P. Chen. Flash pyrolysis nozzle for generation of radical in a supersonic jet expansion. *Rev. Sci. Instrum.*, 63:4003, 1992.

[43] M. E. Jacox. The spectroscopy of molecular reaction intermediates trapped in the solid rare gases. *Chem. Soc. Rev.*, 31:108–115, 2002.

[44] D. Strelnikov, R. Reusch, and W. Krätschmer. Infrared and Ultraviolet Absorptions of Matrix Isolated C_6O_2. *J. Phys. Chem. A*, 110(45):12395–12399, 2006.

[45] D. Strelnikov, R. Reusch, and W. Krätschmer. Oxides of long carbon chains: Results obtained on IR and UV-vis absorptions. *J. Mol. Spectrosc.*, 243:189–193, 2007.

[46] R. M. Ludwig and D. T. Moore. Formation of ionic complex in cryogenic matrices: A case study using co-deposition of Cu^- with rare gas cations in solid argon. *J. Chem. Phys.*, 139:244202, 2013.

[47] M. Grutter, P. Freivogel, D. Forney, and J. P. Maier. Diffusion of mass-selected carbon atoms and molecules in argon and neon matrices. *J. Chem. Phys.*, 107(14):5356–5360, 1997.

[48] A. J. Barnes, J. B. Davies, H. E. Hallam, G. F. Scrimshaw, G. C. Hayward, and R. C. Milward. Interferometric study of rotational motion of hydrogen halides trapped in low-temperature matrices. *J. Chem. Soc. D*, 19:1089–1090, 1969.

[49] J. T. Godbout, T. M. Halasinski, G. E. Leroi, and J. Allison. Matrix Isolation of Mass-Selected Cations: Are Counterions Present and How Are They Formed? *J. Phys. Chem.*, 100(8):2892–2899, 1996.

[50] D. Forney, M. Jakobi, and J. P. Maier. Absorption spectroscopy of mass-selected ions in neon matrices. *J. Chem. Phys.*, 90:600–601, 1989.

[51] P. Freivogel, M. Grutter, D. Forney, and J. P. Maier. Infrared bands of mass-selected carbon chains C_n (n=8-12) and C_n^- (n=5-10, 12) in neon matrices. *J. Chem. Phys.*, 216(3):401–406, 1997.

[52] M. S. Sabo, J. Allison, J. R. Gilbert, and G. E. Leroi. Bridging the Gap between What Mass Spectrometrists Want and What Spectroscopists Can Do: An Instrument for Spectroscopic Investigation of Matrix-Isolated, Mass-Selected Ions. *Appl. Spectrosc.*, 45(4):535–542, 1991.

[53] M. Kasha. Characterization of electronic transitions in complex molecules. *Discuss. Faraday Soc.*, 9:14–19, 1950.

[54] Bastian Kern. *Aufbau und Inbetriebnahme einer neuen Apparatur zur Deposition massenselektierter Cluster in Edelgasmatrices*. Diploma thesis, Karlsruhe Institute of Technology, 2011.

[55] E. Kolodney, B. Tsipinyuk, and A. Budrevich. Thermal energy dependence (10-20eV) of electron impact induced fragmentation of C_{60} in molecular beams: experiment and model calculation. *J. Chem. Phys.*, 102:9263–9275, 1995.

[56] D. Hathiramani, K. Aichele, W. Arnold, K. Huber, E. Salzborn, and P. Scheier. Electron-Impact Induced Fragmentation of Fullerene Ions. *Phys. Rev. Lett.*, 85(17):3604–3607, 2000.

[57] C. W. Walter, Y. K. Bae, D. C. Lorents, and J. R. Peterson. Production and stability of multiply charged C_{60} and C_{70} fullerene ions. *Chem. Phys. Lett.*, 195:543–550, 1992.

[58] H.-S. Kim and R. J. Saykally. An ion beam reflectron/single-photon infrared emission spectrometer for the study of gas-phase polycyclic aromatic hydrocarbon ions: Testing proposed carriers of the unidentified infrared emission bands. *Rev. Sci. Instrum.*, 74(4):2488–2494, 2003.

[59] Angela Bihlmeier. *Untersuchung des Adsorptions- und Desorptionsverhaltens der Fullerene C_n $(50 < n < 60)$ auf HOPG*. Diploma thesis, University of Karlsruhe, 2004.

[60] Chr. Hamann, R. Woltmann, I-Po Hong, N. Hauptmann, S. Karan, and R. Berndt. Ultrahigh vacuum deposition of organic molecules by electrospray ionization. *Rev. Sci. Instrum.*, 82, 2011.

[61] S. Rauschenbach, R. Vogelsang, N. Malinowski, J. W. Gerlach, M. Benyoucef, G. Costantini, Z. Deng, N. Thontasen, and K. Kern. Electrospray Ion Beam Deposition: Soft-Landing and Fragmentation of Functional Molecules at Solid Surfaces. *ACS Nano*, 3(10):2901–2910, 2009.

[62] J. Laskin, P. Wang, and O. Hadjar. Soft-landing of peptide ions onto self-assembled monolayer surfaces: an overview. *Phys. Chem. Chem. Phys.*, 10:1079–1090, 2007.

[63] S. A. Shaffer, K. Tang, G. A. Anderson, D. C. Prior, H. R. Udseth, and R. D. Smith. A Novel Ion Funnel for Focusing Ions at Elevated Pressure Using Electrospray Ionization Mass Spectrometry. *Rapid Commun. Mass Spectrom.*, 11:1813–1817, 1997.

[64] W. Paul and H. Steinwedel. Ein neues Massenspektrometer ohne Magnetfeld. *Z. Naturforsch. A*, 8(7):448–450, 1953.

[65] V. E. Bondybey and T. A. Miller. Absorption and laser induced fluorescence spectra of $C_6F_6^+$ inert gas matrices. *J. Chem. Phys.*, 73:3053–3059, 1980.

[66] P. O. Staneke, G. Groothuis, S. Ingemann, and N. M. M. Nibbering. Formation, stability and structure of radical anions of chloroform, tetrachloromethane and fluorotrichloromethane in the gas phase. *Int. J. Mass Spectrom. Ion Processes*, 142(1-2):83–93, 1995.

[67] C. L. Lugez, M. E. Jacox, and R. D. Johnson. Matrix Isolation Study of the Interaction of Excited Neon Atoms with CCl_4: Infrared Spectra of the Ion Products and of $Cl_2CCl \cdot\cdot Cl$. *J. Chem. Phys.*, 109:7147–7156, 1998.

[68] J. A. Paulino and R. R. Squires. Carbene thermochemistry from collision-induced dissociation threshold energy measurements. The heats of formation of $\tilde{X}^1A_1$ CF_2 and $\tilde{X}^1A_1$ CCl_2. *J. Am. Chem. Soc.*, 113(15):5573–5580, 1991.

[69] G. Tammann. *Lehrbuch der Metallkunde*. Verlag Voss, Berlin, 1929.

[70] J. Tersoff and D. R. Hamann. Theory of the scanning tunneling microscope. *Phys. Rev. B*, 31:805–813, 1985.

[71] C. J. Chen. Origin of atomic resolution on metal surfaces in scanning tunneling microscopy. *Phys. Rev. Lett.*, 65(4):448–451, 1990.

[72] J. Lambe and R. C. Jaklevic. Molecular Vibration Spectra by Inelastic Electron Tunneling. *Phys. Rev.*, 165:821–832, 1968.

[73] J. Klein, A. Léger, M. Belin, D. Défourneau, and M. J. L. Sangster. Inelastic-Electron-Tunneling Spectroscopy of Metal-Insulator-Metal Junctions. *Phys. Rev. B*, 7:2336–2348, 1973.

[74] B. C. Stipe, M. A. Rezaei, and W. Ho. Single-Molecule Vibrational Spectroscopy and Microscopy. *Science*, 280(5370):1732–1735, 1998.

[75] N. Lorente and M. Persson. Theory of Single Molecule Vibrational Spectroscopy and Microscopy. *Phys. Rev. Lett.*, 85:2997–3000, 2000.

[76] A. Troisi and M. A. Ratner. Molecular Transport Junctions: Propensity Rules for Inelastic Electron Tunneling Spectra. *Nano Lett.*, 6(8):1784–1788, 2006.

[77] N. A. Pradhan, N. Liu, and W. Ho. Vibronic Spectroscopy of Single C_{60} Molecules and Monolayers with the STM. *J. Phys. Chem. B*, 109(17):8513–8518, 2005.

[78] N. Liu, N. A. Pradhan, and W. Ho. Vibronic states in single molecules: C_{60} and C_{70} on ultrathin Al_2O_3 films. *J. Chem. Phys.*, 120(24):11371–11375, 2004.

[79] J. I. Pascual, J. Gómez-Herrero, D. Sánchez-Portal, and H.-P. Rust. Vibrational spectroscopy on single C_{60} molecules: The role of molecular orientation. *J. Chem. Phys.*, 117(21):9531–9534, 2002.

[80] M. Grobis, K. H. Khoo, R. Yamachika, Xinghua Lu, K. Nagaoka, Steven G. Louie, M. F. Crommie, H. Kato, and H. Shinohara. Spatially Dependent Inelastic Tunneling in a Single Metallofullerene. *Phys. Rev. Lett.*, 94:136802, 2005.

[81] K. J. Franke, G. Schulze, and J. I. Pascual. Excitation of Jahn-Teller Active Modes during Electron Transport through Single C_{60} Molecules on Metal Surfaces. *J. Phys. Chem. Lett.*, 1(2):500–504, 2010.

[82] L. Zhang, T. Miyamachi, T. Tomanić, R. Dehm, and W. Wulfhekel. A compact sub-Kelvin ultrahigh vacuum scanning tunneling microscope with high energy resolution and high stability. *Rev. Sci. Instrum.*, 82(10):103702, 2011.

[83] Lei Zhang. *Sub-Kelvin scanning tunneling microscopy on magnetic molecules*. PhD thesis, Karlsruhe Institute of Technology, 2012.

[84] N. Bajales, S. Schmaus, T. Miyamashi, W. Wulfhekel, J. Wilhelm, M. Walz, M. Stendel, A. Bagrets, F. Evers, S. Ulas, B. Kern, A. Böttcher, and M. M. Kappes. C_{58} on Au(111): A scanning tunneling microscopy study. *J. Chem. Phys.*, 138(10):104703, 2013.

[85] P. W. Fowler and D. E. Manolopoulos. *An Atlas of Fullerenes*. Dover Books on Chemistry, 1995.

[86] H. W. Kroto. The stability of fullerenes C_n, with n = 24, 28, 32, 36, 50, 60 and 70. *Nature*, 329:529–531, 1987.

[87] K. Yu. Amsharov, K. Ziegler, A. Mueller, and M. Jansen. Capturing the Antiaromatic $^{6094}C_{68}$ Carbon Cage in the Radio-Frequency Furnace. *Chem. - Eur. J.*, 18(30):9289–9293, 2012.

[88] Y.-Z. Tan, S.-Y. Xie, R.-B. Huang, and L.-S. Zheng. The stabilization of fused-pentagon fullerene molecules. *Nature Chemistry*, 1:450–460, 2009.

[89] R. C. Haddon. Chemistry of the Fullerenes: The Manifestation of Strain in a Class of Continuous Aromatic Molecules. *Science*, 261(5128):1545–1550, 1993.

[90] H. W. Kroto, J. R. Heath, S. C. O'Brien, R. F. Curl, and R. E. Smalley. C_{60}: Buckminsterfullerene. *Nature*, 318:162–163, 1985.

[91] E. A. Rohlfing, D. M. Cox, and A. Kaldor. Production and characterization of supersonic carbon cluster beams. *J. Chem. Phys.*, 81(7):3322–3330, 1984.

[92] S. Maruyama, L. R. Anderson, and R. E. Smalley. Direct injection supersonic cluster beam source for FT-ICR studies of clusters. *Rev. Sci. Instrum.*, 61(12):3686–3693, 1990.

[93] W. Krätschmer, Lowell D. Lamb, K. Fostiropoulos, and Donald R. Huffman. Solid C_{60}: a new form of carbon. *Nature*, 347:354–358, 1990.

[94] G. von Helden, N. G. Gotts, and M. T. Bowers. Experimental evidence for the formation of fullerenes by collisional heating of carbon rings in the gas phase. *Nature*, 363:60–63, 1993.

[95] G. von Helden, M. T. Hsu, N. Gotts, and M. T. Bowers. Carbon cluster cations with up to 84 atoms: structures, formation mechanism, and reactivity. *J. Phys. Chem.*, 97(31):8182–8192, 1993.

[96] Y. Rubin, M. Kahr, C. B. Knobler, F. Diederich, and C. L. Wilkins. The higher oxides of carbon $C_{8n}O_{2n}$ (n = 3-5): synthesis, characterization, and x-ray crystal structure. Formation of cyclo[n]carbon ions C_n^+ (n = 18, 24), C_n^- (n = 18, 24, 30), and higher carbon ions including C_{60}^+ in laser desorption Fourier transform mass spectrometric experiments. *J. Am. Chem. Soc.*, 113(2):495–500, 1991.

[97] T. Wakabayashi, K. Kikuchi, H. Shiromaru, S. Suzuki, and Y. Achiba. Ring-stacking consideration on higher fullerene growth. *Z. Phys. D Atom. Mol. Cl.*, 26(1):258–260, 1993.

[98] J. Hutter, H. P. Lüthi, and F. Diederich. Structures and vibrational frequencies of the carbon molecules C_2-C_{18} calculated by density functional theory. *J. Am. Chem. Soc.*, 116(2):750–756, 1994.

[99] S. D. Khan and S. Ahmad. Modelling of C_2 addition route to the formation of C_{60}. *Nanotechnology*, 17(18):4654, 2006.

[100] A. Chuvilin, U. Kaiser, E. Bichoutskaia, N. A. Besley, and A. N. Khlobystov. Direct transformation of graphene to fullerene. *Nature Chemistry*, 2:450–453, 2010.

[101] W. Andreoni, F. Gygi, and M. Parrinello. Impurity states in doped fullerenes: $C_{59}B$ and $C_{59}N$. *Chem. Phys. Lett.*, 190(3-4):159–162, 1992.

[102] J. Cami, J. Bernard-Salas, E. Peeters, and S. E. Malek. Detection of C_{60} and C_{70} in a Young Planetary Nebula. *Science*, 329(5996):1180–1182, 2010.

[103] B. H. Foing and P. Ehrenfreund. Detection of two interstellar absorption bands coincident with spectral features of C_{60}^+. *Nature*, 369:296–298, 1994.

[104] J. P. Maier. Interstellar detection of C_{60}^+. *Nature*, 370:423–424, 1994.

[105] P. Jenniskens, G. Mulas, I. Porceddu, and P. Benvenuti. Diffuse interstellar bands near 9600 $\AA$: not due to C_{60}^+ yet. *Astron. Astrophys.*, 327:337–341, 1997.

[106] B. H. Foing and P. Ehrenfreund. New evidences for interstellar C_{60}^+. *Astron. Astrophys.*, 319:L59–L62, 1997.

[107] E. K. Campbell, M. Holz, D. Gerlich, and J. P. Maier. Laboratory confirmation of C_{60}^+ as the carrier of two diffuse interstellar bands. *Nature*, 523:322–323, 2015.

[108] Z. Gasyna, L. Andrews, and P. Schatz. Near-Infrared Absorption Spectra of Fullerene (C_{60}) Radical Cations and Anions Prepared Simultaneously in Solid Argon. *J. Phys. Chem.*, 96:1525–1527, 1992.

[109] C. A. Reed, K.-C. Kim, R. D. Bolskar, and L. J. Mueller. Taming Superacids: Stabilization of the Fullerene Cations HC_{60}^+ and $C_{60}^+\cdot$. *Science*, 289(5476):101–104, 2000.

[110] T. Kato, T. Kodama, and T. Shida. Spectroscopic studies of the radical anion of C_{60}. Detection of the fluorenscence and reinvestigation of the ESR spectrum. *Chem. Phys. Lett.*, 205(4–5):405 – 409, 1993.

[111] P. Kupser, J. D. Steill, J. Oomens, G. Meijer, and G. von Helden. IR Spectroscopy of Gas-Phase C_{60}^-. *Phys. Chem. Chem. Phys.*, 10:6862–6866, 2008.

[112] S. Tomita, J. U. Andersen, E. Bonderup, P. Hvelplund, B. Liu, S. B. Nielsen, U. V. Pedersen, J. Rangama, K. Hansen, and O. Echt. Dynamic Jahn-Teller Effects in Isolated C_{60}^- Studied by Near-Infrared Spectroscopy in a Storage Ring. *Phys. Rev. Lett.*, 94:053002, 2005.

[113] U. Kadhane, J. U. Andersen, E. Bonderup, B. Concina, P. Hvelplund, M.-B. Suhr Kirketerp, B. Liu, S. Brøndsted Nielsen, S. Panja, J. Rangama, K. Støchkel, S. Tomita, H. Zettergren, K. Hansen, A. E. K. Sundén, S. E. Canton, O. Echt, and J. S. Forster. Near-infrared photoabsorption by C_{60} dianions in a storage ring. *J. Chem. Phys.*, 131:014301, 2009.

[114] W. Krätschmer, K. Fostiropoulos, and Donald R. Huffman. The infrared and ultraviolet absorption spectra of laboratory-produced carbon dust: evidence for the presence of the C_{60} molecule. *Chem. Phys. Lett.*, 170(2-3):167–170, 1990.

[115] K.-A. Wang, A. M. Rao, P. C. Eklund, M. S. Dresselhaus, and G. Dresselhaus. Observations of Higher-Order Infrared Modes in Solid C_{60} Films. *Phys. Rev. B*, 48:11375–11380, 1993.

[116] Dmitry Strelnikov. *IR spectroscopy of neutral C_{60} isolated in argon matrixes*. Personal correspondence.

[117] E. Blaisten-Barojas and M. Allavena. IR absortion spectrum of molecules trapped in matrices: I. The libron-phonon coupling in 1D. *J. Phy. C: Solid State*, 9(16):3121, 1976.

[118] M. Frankowski, M. Algarra, P. Rodrigues, M. T. Barros, M. N. D. S. Cordeiro, B. S. Fox, A. M. Smith-Gicklhorn, M. K. Beyer, M. L. Costa, and V. E. Bondybey. Matrix-isolation FTIR study of azidoacetone and azidoacetonitrile. *Low Temp. Phys.*, 29(9-10):870–875, 2003.

[119] S. Iglesias-Groth, F. Cataldo, and A. Manchado. Infrared Spectroscopy and Integrated Molar Absorptivity of C_{60} and C_{70} Fullerenes at Extreme Temperatures. *Mon. Not. R. Astron. Soc.*, 413:213–222, 2011.

[120] R. E. Haufler. Efficient Production of C_{60} (Buckminsterfullerene), $C_{60}H_{36}$, and the Solvated Buckide ion. *J. Phys. Chem.*, 94:8634–8636, 1990.

[121] N. Sogoshi, Y. Kato, T. Wakabayashi, T. Momose, S. Tam, M. E. DeRose, and M. E. Fajardo. High-Resolution Infrared Absorption Spectroscopy of C_{60} Molecules and Clusters in Parahydrogen Solids. *J. Phys. Chem. A*, 104:3133–3742, 2000.

[122] S. E. Canton, A. J. Yencha, E. Kukk, J. D. Bozek, M. C. A. Lopes, G. Snell, and N. Berrah. Experimental Evidence of a Dynamic Jahn-Teller Effect in C_{60}^+. *Phys. Rev. Lett.*, 89(4):045502, 2002.

[123] M. Saito. Electron-phonon coupling of electron- or hole-injected C_{60}. *Phys. Rev. B*, 65:220508, 2002.

[124] L. Nemes, R. S. Ram, P. F. Bernath, F. A. Tinker, M. C. Zumwalt, L. D. Lamb, and D. R. Huffman. Gas-phase infrared emission spectra of C_{60} and C_{70}. Temperature-dependent studies. *Chem. Phys. Lett.*, 218(4):295 – 303, 1994.

[125] G. von Helden, I. Holleman, G. M. H. Knippels, A. F. G. van der Meer, and G. Meijer. Infrared Resonance Enhanced Multiphoton Ionization of Fullerenes. *Phys. Rev. Lett.*, 79:5234–5237, 1997.

[126] M. E. Jacox. The vibrational energy levels of small transient molecules isolated in neon and argon matrices. *Chem. Phys.*, 189:149–170, 1994.

[127] D. Strelnikov, B. Kern, A. Böttcher, and M. M. Kappes. Laboratory and Space Infrared Detection of C_{60}^+. In *PRAHA2012, 22nd Int. Conf. High Res. Mol. Spec.*, 2012.

[128] O. Berné, G. Mulas, and C. Joblin. Interstellar C_{60}^+. *Astron. Astrophys.*, 550:L4, 2013.

[129] G. C. Sloan, E. Lagadec, A. A. Zijlstra, K. E. Kraemer, A. P. Weis, M. Matsuura, K. Volk, E. Peeters, W. W. Duley, J. Cami, J. Bernard-Salas, F. Kemper, and R. Sahai. Carbon-rich Dust Past the Asymptotic Giant Branch: Aliphatics, Aromatics, and Fullerenes in the Magellanic Clouds. *Astrophys. J.*, 791(1):28, 2014.

[130] D. Strelnikov, B. Kern, and M. M. Kappes. On observing C_{60}^+ and C_{60}^{2+} in laboratory and space. *Astron. Astrophys.*, 584(A55), 2015.

[131] V. S. Langford and B. E. Williamson. Magnetic Circular Dichroism of C_{60}^+ and C_{60}^- Radicals in Argon Matrixes. *J. Phys. Chem. A*, 103(33):6533–6539, 1999.

[132] T. Kato, T. Kodama, T. Shida, T. Nakagawa, Y. Matsui, S. Suzuki, H. Shiromaru, K. Yamauchi, and Y. Achiba. Electronic absorption spectra of the radical anions and cations of fullerenes: C_{60} and C_{70}. *Chem. Phys. Lett.*, 180(5):446 – 450, 1991.

[133] A. Sassara, G. Zerza, M. Chergui, and S. Leach. Absorption Wavelengths and Bandwidths for Interstellar Searches of C_{60} in the 2400-4100 $\AA$ Region. *Astrophys. J. Suppl. S.*, 135(2):263–273, 2001.

[134] D. K. Bohme. Buckminsterfullerene Cations: New Dimensions in Gas-Phase Ion Chemistry. *Mass Spectrom. Rev.*, 28:672–693, 2009.

[135] M. Riccò, D. Pontiroli, M. Mazzani, F. Gianferrari, M. Pagliari, A. Goffredi, M. Brunelli, G. Zandomeneghi, B. H. Meier, and T. Shiroka. Fullerenium Salts: A New Class of C_{60}-Based Compounds. *J. Am. Chem. Soc.*, 132:2064–2068, 2010.

[136] B. Kern, D. Strelnikov, P. Weis, A. Böttcher, and M. M. Kappes. IR, NIR, and UV Absorption Spectroscopy of C_{60}^{2+} and C_{60}^{3+} in Neon Matrixes. *J. Phys. Chem. Lett.*, 5:457–460, 2014.

[137] R. Wörgötter, B. Dünser, P. Scheier, and T. D. Märk. Appearance and Ionization Energies of C_{60-2m}^{z+} and C_{70-2m}^{z+} Ions (with z and m up to 4) Produced by Electron Impact Ionization of C_{60} and C_{70}, Respectively. *J. Chem. Phys.*, 101:8674–8679, 1994.

[138] S.G. Lias. *"Ionization Energy Evaluation" in NIST Chemistry WebBook, NIST Standard Reference Database Number 69.* Eds. Linstrom, P. J.; Mallard, W. G. National Institute of Standards and Technology, Gaithersburg MD, 20899. http://webbook.nist.gov, (retrieved June 16, 2015).

[139] J. Bradley, Z. R. Dai, R. Erni, N. Browning, G. Graham, P. Weber, J. Smith, I. Hutcheon, H. Ishii, S. Bajt, C. Floss, F. Stadermann, and S. Sandford. An Astronomical 2175 $\AA$ Feature in Interplanetary Dust Particles. *Science*, 307(5707):244–247, 2005.

[140] F. Cataldo, S. Iglesias-Groth, and Y. Hafez. On the molar extinction coefficients of the electronic absorption spectra of C_{60} and C_{70} fullerenes radical cation. *Eur. Chem. Bull.*, 2(12):1013–1018, 2013.

[141] S. Pfuetzner, J. Meiss, A. Petrich, M. Riede, and K. Leo. Improved bulk heterojunction organic solar cells employing fullerenes. *Appl. Phys. Lett.*, 94:223307, 2009.

[142] D. S. Bethune, G. Meijer, W. C. Tang, H. J. Rosen, W. G. Golden, H. Seki, C. A. Brown, and M. S. de Vries. Vibrational Raman and infrared spectra of chromatographically separated C_{60} and C_{70} fullerene clusters. *Chem. Phys. Lett.*, 179(1–2):181 – 186, 1991.

[143] D. R. Lawson, D. L. Feldheim, C. A. Foss, P. K. Dorhout, C. M. Elliott, C. R. Martin, and B. Parkinson. Near-IR Absorption Spectra for the C_{70} Fullerene Anions. *J. Phys. Chem.*, 96(18):7175–7177, 1992.

[144] F. Cataldo, S. Iglesias-Groth, and A. Manchado. On the Radical Anion Spectra of Fullerenes C_{60} and C_{70}. *Fuller. Nanotub. Car. N.*, 21(6):537–548, 2013.

[145] S. Matt, O. Echt, R. Wörgötter, V. Grill, P. Scheier, C. Lifshitz, and T.D. Märk. Appearance and ionization energies of multiply-charged C_{70} parent ions produced by electron impact ionization. *Chem. Phys. Lett.*, 264(1-2):149–156, 1997.

[146] C. W. Bauschlicher. The infrared spectra of nonplanar polycyclic aromatic hydrocarbons with five- or seven-membered rings. *Chem. Phys.*, 448:43 – 52, 2015.

[147] A. Sassara, G. Zerza, and M. Chergui. Assignment of the Lowest Excited States of C_{70} and Evidence for Fluorescence from the S_2 State. *J. Phys. Chem. A*, 102(18):3072–3077, 1998.

[148] J. P. Hare, H. W. Kroto, and R. Taylor. Preparation and UV visible spectra of fullerenes C_{60} and C_{70}. *Chem. Phys. Lett.*, 177(4–5):394 – 398, 1991.

[149] D. L. Lichtenberger, M. E. Rempe, and S. B. Gogosha. The He I valence photoelectron spectrum of C_{70} in the gas phase. *Chem. Phys. Lett.*, 198(5):454 – 460, 1992.

[150] G. E. Scuseria. The equilibrium structure of C_{70}. An ab initio Hartree-Fock study. *Chem. Phys. Lett.*, 180(5):451 – 456, 1991.

[151] H. Hase and Y. Miyatake. Electronic spectra of C_{70} anions produced in γ-irradiated organic glasses at 77 K. *Chem. Phys. Lett.*, 215(1–3):141 – 143, 1993.

[152] A.S. Lobach, N.F. Goldshleger, M.G. Kaplunov, and A.V. Kulikov. Near-IR and ESR studies of the radical anions of C_{60} and C_{70} in the system fullerene-primary amine. *Chem. Phys. Lett.*, 243(1–2):22 – 28, 1995.

[153] Evgeniy Gromov, Shachar Klaiman, and Lutz Cederbaum. Group of Prof. Cederbaum, Theoretical Chemistry, University of Heidelberg, http://www.pci.uni-heidelberg.de/cms/index.html. Contact: evgeniy.gromov@pci.uni-heidelberg.de.

[154] S. Díaz-Tendero, M. Alcamí, and F. Martín. Theoretical study of ionization potentials and dissociation energies of C_n^{q+} fullerenes (n=50–60, q=0, 1 and 2). *J. Chem. Phys.*, 119(11):5545–5557, 2003.

[155] G. Sánchez, S. Díaz-Tendero, M. Alcamí, and F. Martín. Size dependence of ionization potentials and dissociation energies for neutral and singly-charged C_n fullerenes (n = 40–70). *Chem. Phys. Lett.*, 416(1–3):14 – 17, 2005.

[156] D.-L. Chen, W. Q. Tian, J.-K. Feng, and C.-C. Sun. Structures, Stabilities, and Electronic and Optical Properties of C_{58} Fullerene Isomers, Ions, and Metallofullerenes. *ChemPhysChem*, 8(7):1029–1036, 2007.

[157] S. Díaz-Tendero, M. Alcamí, and F. Martín. Structure and electronic properties of highly charged C_{60} and C_{58} fullerenes. *J. Chem. Phys.*, 123(18):1840306, 2005.

[158] A. Böttcher, P. Weis, A. Bihlmeier, and M. M. Kappes. C_{58} on HOPG: Soft-landing adsorption and thermal desorption. *Phys. Chem. Chem. Phys.*, 6:5213–5217, 2004.

[159] A. Böttcher, P. Weis, S.-S. Jester, D. Löffler, A. Bihlmeier, W. Klopper, and M. M. Kappes. Solid C_{58} films. *Phys. Chem. Chem. Phys.*, 7:2816–2820, 2005.

[160] D. Löffler, S. Ulas, S.-S. Jester, P. Weis, A. Böttcher, and M. M. Kappes. Properties of non-IPR fullerene films versus size of the building blocks. *Phys. Chem. Chem. Phys.*, 12:10671–10684, 2010.

[161] Dmitry Strelnikov. *Thorough search for $C_{58}^{0/+}$ structure of minimal energy*. Contact: dmitry.strelnikov@kit.edu, 2015.

[162] G. Brinkmann, O. Delgado Friedrichs, S. Lisken, A. Peeters, and N. Van Cleemput. CaGe - a Virtual Environment for Studying Some Special Classes of Plane Graphs - an Update. *MATCH Commun. Math. Comput. Chem.*, 63(3):533–552, 2010.

[163] James J. P. Stewart. MOPAC2012, http://openmopac.net.

[164] R. C. Haddon, A. F. Hebard, M. J. Rosseinsky, D. W. Murphy, S. J. Duclos, K. B. Lyons, B. Miller, J. M. Rosamilia, R. M. Fleming, A. R. Kortan, S. H. Glarum, A. V. Makhija, A. J. Muller, R. H. Eick, S. M. Zahurak, R. Tycko, G. Dabbagh, and F. A. Thiel. Conducting films of C_{60} and C_{70} by alkali-metal doping. *Nature*, 350:320–322, 1991.

[165] A. F. Hebard, M. J. Rosseinsky, R. C. Haddon, D. W. Murphy, S. H. Glarum, T. T. M. Palstra, A. P. Ramirez, and A. R. Kortan. Superconductivity at 18 K in potassium-doped C_{60}. *Nature*, 350:600–601, 1991.

[166] K. Tanigaki, T. W. Ebbesen, S. Saito, J. Mizuki, J. S. Tsai, Y. Kubo, and S. Kuroshima. Superconductivity at 33 K in $Cs_xRb_yC_{60}$. *Nature*, 352:222–223, 1991.

[167] J. C. Hummelen, B. Knight, J. Pavlovich, R. González, and F. Wudl. Isolation of the Heterofullerene $C_{59}N$ as Its Dimer $(C_{59}N)_2$. *Science*, 269(5230):1554–1556, 1995.

[168] B. Nuber and A. Hirsch. A new route to nitrogen heterofullerenes and the first synthesis of $(C_{69}N)_2$. *Chem. Commun.*, 12:1421–1422, 1996.

[169] J. Zhao, C. Zeng, X. Cheng, K. Wang, G. Wang, J. Yang, J. G. Hou, and Q. Zhu. Single $C_{59}N$ Molecule as a Molecular Rectifier. *Phys. Rev. Lett.*, 95:045502, 2005.

[170] Z. Xiao, D. He, C. Zuo, L. Gan, and L. Ding. An azafullerene acceptor for organic solar cells. *RSC Adv.*, 4:24029–24031, 2014.

[171] C. D. Wessendorf, R. Eigler, S. Eigler, J. Hanisch, A. Hirsch, and E. Ahlswede. Investigation of pentaarylazafullerenes as acceptor systems for bulk-heterojunction organic solar cells. *Sol. Energ. Mat. Sol. C.*, 132:450 – 454, 2015.

[172] W Andreoni. Computational approach to the physical chemistry of fullerenes and their derivatives. *Annu. Rev. Phys. Chem.*, 49:405, 1998.

[173] T. Pichler, M. Knupfer, M. S. Golden, S. Haffner, R. Friedlein, J. Fink, W. Andreoni, A. Curioni, M. Keshavarz-K, C. Bellavia-Lund, A. Sastre, J.-C. Hummelen, and F. Wudl. On-Ball Doping of Fullerenes: The Electronic Structure of $C_{59}N$ Dimers from Experiment and Theory. *Phys. Rev. Lett.*, 78:4249–4252, 1997.

[174] S. Haffner, T. Pichler, M. Knupfer, B. Umlauf, R. Friedlein, M.S. Golden, J. Fink, M. Keshavarz-K., C. Bellavia-Lund, A. Sastre, J.C. Hummelen, and F. Wudl. The electronic structure of $(C_{59}N)_2$ from high energy spectroscopy. *Eur. Phys. J. B*, 1(1):11–17, 1998.

[175] W. Andreoni, A. Curioni, K. Holczer, K. Prassides, M. Keshavarz-K., J.-C. Hummelen, and F. Wudl. Unconventional Bonding of Azafullerenes: Theory and Experiment. *J. Am. Chem. Soc.*, 118(45):11335–11336, 1996.

[176] H. Bai, W. Ji, X. Liu, L. Wang, N. Yuan, and Y. Ji. Doping the Buckminsterfullerene by Substitution: Density Functional Theory Studies of $C_{59}X$ (X = B, N, Al, Si, P, Ga, Ge, and As). *J. Chem.*, 2013:571709, 2013.

[177] H. Kuzmany, W. Plank, J. Winter, O. Dubay, N. Tagmatarchis, and K. Prassides. Raman spectrum and stability of $(C_{59}N)_2$. *Phys. Rev. B*, 60:1005–1012, 1999.

[178] M. Krause, S. Baes-Fischlmair, R. Pfeiffer, W. Plank, T. Pichler, H. Kuzmany, N. Tagmatarchis, and K. Prassides. Thermal Stability and High Temperature Graphitization of Bisazafullerene $(C_{59}N)_2$ As Studied by IR and Raman Spectroscopy. *J. Phys. Chem. B*, 105(48):11964–11969, 2001.

[179] N. Tagmatarchis, T. Pichler, M. Krause, H. Kuzmany, and H. Shinohara. Infra-red and Raman spectroscopic study on the thermal stability and high temperature transformation of hydroazafullerene $C_{59}HN$. *Carbon*, 44(8):1420–1424, 2006.

[180] F. H. Jones, M. J. Butcher, B. N. Cotier, P. Moriarty, P. H. Beton, V. R. Dhanak, K. Prassides, K. Kordatos, N. Tagmatarchis, and F. Wudl. Oscillations in the valence-band photoemission spectrum of the heterofullerene $C_{59}N$: A photoelectron interference phenomenon. *Phys. Rev. B*, 59:9834–9837, 1999.

[181] M. J. Butcher, F. H. Jones, P. H. Beton, P. Moriarty, B. N. Cotier, M. D. Upward, K. Prassides, K. Kordatos, N. Tagmatarchis, F. Wudl, V. Dhanak, T. K. Johal, C. Crotti, C. Comicioli, and C. Ottaviani. $C_{59}N$ Monomers: Stabilization through Immobilization. *Phys. Rev. Lett.*, 83:3478–3481, 1999.

[182] K.-C. Kim, F. Hauke, A. Hirsch, P. D. W. Boyd, E. Carter, R. S. Armstrong, P. A. Lay, and C. A. Reed. Synthesis of the $C_{59}N^+$ Carbocation. A Monomeric Azafullerene Isoelectronic to C_{60}. *J. Am. Chem. Soc.*, 125(14):4024–4025, 2003.

[183] Regina Eigler. Synthesis done in the group of Prof. A. Hirsch, Organic Chemistry, University Erlangen, http://www.hirsch.chemie.uni-erlangen.de/en/welcome.html.

[184] M. Kordel, D. Schooss, C. Neiss, L. Walter, and M. M. Kappes. Laser-Induced Fluorescence of Rhodamine 6G Cations in the Gas Phase: A Lower Bound to the Lifetime of the First Triplet State. *J. Phys. Chem. A*, 114(17):5509 – 5514, 2010.

[185] Q. Bian, M. W. Forbes, F. O. Talbot, and R. A. Jockusch. Gas-phase fluorescence excitation and emission spectroscopy of mass-selected trapped molecular ions. *Phys. Chem. Chem. Phys.*, 12:2590–2598, 2010.

[186] J. Kido and Y. Okamoto. Organo Lanthanide Metal Complexes for Electroluminescent Materials. *Chem. Rev.*, 102(6):2357–2368, 2002.

[187] J. Fang, H. You, J. Chen, J. Lin, and D. Ma. Memory Devices Based on Lanthanide (Sm^{3+}, Eu^{3+}, Gd^{3+}) Complexes. *Inorg. Chem.*, 45(9):3701–3704, 2006.

[188] T. Trupke, M. A. Green, and P. Würfel. Improving solar cell efficiencies by down-conversion of high-energy photons. *J. Appl. Phys.*, 92(3):1668–1674, 2002.

[189] Jiří Chmela and Michael E. Harding. Calculations of different PLN systems using Turbomole and hotFCHT, Group of Prof. W. Klopper. Contact: jiri.chmela@kit.edu, michael.harding@kit.edu.

[190] V. E. Bondybey, R. C. Haddon, and J. H. English. Fluorescence and phosphorescence of 9-hydroxyphenalenone in solid neon and its hydrogen tunneling potential function. *J. Chem. Phys.*, 80(11):5432–5437, 1984.

[191] R. Van Deun, P. Nockemann, P. Fias, K. Van Hecke, L. Van Meervelt, and K. Binnemans. Visible light sensitisation of europium(III) luminescence in a 9-hydroxyphenal-1-one complex. *Chem. Commun.*, 5:590–592, 2005.

[192] J.-F. Greisch, M. E. Harding, B. Schäfer, M. Ruben, M. M. Kappes, and D. Schooss. Characterization of Nonanuclear Europium and Gadolinium Complexes by Gas-Phase Luminescence Spectroscopy. *J. Phys. Chem. Lett.*, (5):1727 – 1731, 2014.

[193] W. C. Martin, R. Zalubas, and L. Hagan. Atomic Energy Levels - The Rare-Earth Elements. *NSRDS-NBS*, 60, 1978. U.S. Department of Commerce: Washington, DC.

[194] Bernhard Schäfer. Synthesis done in the group of Prof. M. Ruben, Institute for Nanotechnology, KIT Karlsruhe, http://www.int.kit.edu/ruben.php. Contact: bernhard.schaefer@kit.edu.

[195] J.-F. Greisch, M. E. Harding, B. Schäfer, M. Rotter, M. Ruben, W. Klopper, M. M. Kappes, and D. Schooss. Substitutional Photoluminescence Modulation in Adducts of a Europium Chelate with a Range of Alkali Metal Cations: A Gas-Phase Study. *J. Phys. Chem. A*, 118(1):94–102, 2014.

[196] Jean-François Greisch. Gas phase spectra measured with TLIF apparatus, Group of Prof. M. M. Kappes, Institute for Nanotechnology, KIT. Contact: jean-francois.greisch@kit.edu.

[197] J. A. Kemlo and T. M. Shepherd. Quenching of excited singlet states by metal ions. *Chem. Phys. Lett.*, 47(1):158 – 162, 1977.

[198] Douglas A. Skoog, F. James Holler, and Stanley R. Crouch. *Principles of instrumental analysis*. Brooks/Cole, Belmont CA, 6. ed. edition, 2007. ISBN: 0-495-12570-9.

[199] Yu. Ralchenko, A. E. Kramida, J. Reader, and NIST ASD Team. NIST Atomic Spectra Database (ver. 5.2). [Online], 2014.

[200] A. F. Kirby, D. Foster, and F. S. Richardson. Comparison of $^7F_J \leftarrow ^5D_0$ emission spectra for Eu(III) in crystalline environments of octahedral, near-octahedral and trigonal symmetry. *Chem. Phys. Lett.*, 95(6):507–512, 1983.

[201] H. Wu, Y. Hu, F. Kang, N. Li, G. Ju, Z. Mu, and Z. Yang. Luminescent properties of Praseodymium in $CaWO_4$ Matrix. *J. Am. Ceram. Soc.*, 95(10):3214–3219, 2012.

[202] E. van der Kolk, P. Dorenbos, and C. W. E. van Eijk. Vacuum ultraviolet excitation of $^1S_0$ and $^3P_0$ emission of Pr^{3+} in $Sr_{0.7}La_{0.3}Al_{11.7}Mg_{0.3}O_{19}$ and SrB_4O_7. *J. Phys.: Condens. Matter*, 13(23):5471, 2001.

[203] C. R. Ronda, T. Jüstel, and H. Nikol. Rare earth phosphors: fundamentals and applications. *J. Alloys Compd.*, 275-277:669–676, 1998.

[204] C. A. Kodaira, H. F. Brito, E. E. S. Teotonio, M. C. F. C. Felinto, O. L. Malta, and G. E. S. Brito. Photoluminescence behavior of the Sm^{3+} and Tb^{3+} ions doped into the $Gd_2(WO_4)_3$ matrix prepared by the Pechini and ceramic methods. *J. Braz. Chem. Soc.*, 15:890 – 896, 12 2004.

[205] J. Zhang, Y. Wang, L. Guo, and P. Dong. Up-conversion luminescence and near-infrared quantum cutting in $Y_6O_5F_8$:RE^{3+} (RE = Yb, Er, and Ho) with controllable morphologies by hydrothermal synthesis. *Dalton Trans.*, 42:3542–3551, 2013.

[206] M. Tsvirko, S. Meshkova, G. Kiriiak, and V. Gorodnyuk. Detection of dysprosium (III) in the presence of terbium (III) by using the time-resolved luminescence. *J. Phys. Conf. Ser.*, 79(1):012007, 2007.

[207] E. M. Chan. Combinatorial approaches for developing upconverting nanomaterials: high-throughput screening, modeling, and applications. *Chem. Soc. Rev.*, 44:1653–1679, 2015.

[208] E. A. Gouveia, M. T. de Araujo, and A. S. Gouveia-Neto. Thermal effects on light emission in Yb^{3+}-sensitized rare-earth doped optical glasses. *Braz. J. Phys.*, 31:89 – 101, 2001.

[209] P. D'Angelo, A. Zitolo, V. Migliorati, G. Chillemi, M. Duvail, P. Vitorge, S. Abadie, and R. Spezia. Revised Ionic Radii of Lanthanoid(III) Ions in Aqueous Solution. *Inorg. Chem.*, 50(10):4572–4579, 2011.

[210] F. D. Natterer, F. Patthey, and H. Brune. Distinction of Nuclear Spin States with the Scanning Tunneling Microscope. *Phys. Rev. Lett.*, 111:175303, 2013.

[211] S. Li, A. Yu, F. Toledo, Z. Han, H. Wang, H. Y. He, R. Wu, and W. Ho. Rotational and Vibrational Excitations of a Hydrogen Molecule Trapped within a Nanocavity of Tunable Dimension. *Phys. Rev. Lett.*, 111:146102, 2013.

[212] M. Saunders, H. A. Jiménez-Vázquez, R. J. Cross, and R. J. Poreda. Stable Compounds of Helium and Neon: He@C_{60} and Ne@C_{60}. *Science*, 259(5100):1428–1430, 1993.

[213] M. Saunders, H. A. Jiménez-Vázquez, R. J. Cross, S. Mroczkowski, M. L. Gross, D. E. Giblin, and R. J. Poreda. Incorporation of helium, neon, argon, krypton, and xenon into fullerenes using high pressure. *J. Am. Chem. Soc.*, 116(5):2193–2194, 1994.

[214] H. Mauser, A. Hirsch, N. J. R. van Eikema Hommes, T. Clark, B. Pietzak, A. Weidinger, and L. Dunsch. Stabilization of Atomic Nitrogen Inside C_{60}. *Angew. Chem. Int. Edit.*, 36(24):2835–2838, 1997.

[215] L. Dunsch and S. Yang. Metal Nitride Cluster Fullerenes: Their Current State and Future Prospects. *Small*, 3(8):1298–1320, 2007.

[216] M. Murata, Y. Murata, and K. Komatsu. Synthesis and Properties of Endohedral C_{60} Encapsulating Molecular Hydrogen. *J. Am. Chem. Soc.*, 128(24):8024–8033, 2006.

[217] A. Strózecka, K. Muthukumar, A. Dybek, T. J. Dennis, J. A. Larsson, J. Mysliveček, and B. Voigtländer. Modification of the conductance of single fullerene molecules by endohedral doping. *Appl. Phys. Lett.*, 95(13):133118, 2009.

[218] W. Harneit, M. Waiblinger, K. Lips, S. Makarov, and A. Weidinger. N@C_{60} for quantum computing. *AIP Conf. Proc.*, 544(1):207–212, 2000.

[219] R. D. Bolskar, A. F. Benedetto, L. O. Husebo, R. E. Price, E. F. Jackson, S. Wallace, L. J. Wilson, and J. M. Alford. First Soluble M@C_{60} Derivatives Provide Enhanced Access to Metallofullerenes and Permit in Vivo Evaluation of Gd@C_{60}[$C(COOH)_2$]$_{10}$ as a MRI Contrast Agent. *J. Am. Chem. Soc.*, 125(18):5471–5478, 2003.

[220] M. Frunzi, S. Jockusch, J. Y.-C. Chen, R. M. Krick Calderon, X. Lei, Y. Murata, K. Komatsu, D. M. Guldi, R. G. Lawler, and N. J. Turro. A Photochemical On-Off Switch for Tuning the Equilibrium Mixture of H_2 Nuclear Spin Isomers as a Function of Temperature. *J. Am. Chem. Soc.*, 133(36):14232–14235, 2011.

[221] J. Y.-C. Chen, Y. Li, M. Frunzi, X. Lei, Y. Murata, R. G. Lawler, and N. J. Turro. Nuclear spin isomers of guest molecules in $H_2@C_{60}$, $H_2O@C_{60}$ and other endofullerenes. *Philos. T. Roy. Soc. A*, 371(1998), 2013.

[222] M. Ge, U. Nagel, D. Hüvonen, T. Rõõm, S. Mamone, M. H. Levitt, M. Carravetta, Y. Murata, K. Komatsu, J. Y.-C. Chen, and N. J. Turro. Interaction potential and infrared absorption of endohedral H_2 in C_{60}. *J. Chem. Phys.*, 134(5):054507, 2011.

[223] E. Sartori, M. Ruzzi, N. J. Turro, J. D. Decatur, D. C. Doetschman, R. G. Lawler, A. L. Buchachenko, Y. Murata, and K. Komatsu. Nuclear Relaxation of H_2 and $H_2@C_{60}$ in Organic Solvents. *J. Am. Chem. Soc.*, 128(46):14752–14753, 2006.

[224] J. Y.-C. Chen, A. A. Martí, N. J. Turro, K. Komatsu, Y. Murata, and R. G. Lawler. Comparative NMR Properties of H_2 and HD in Toluene-d_8 and in H_2/HD@C_{60}. *J. Phys. Chem. B*, 114(45):14689–14695, 2010.

[225] N. J. Turro, A. A. Martí, J. Y.-C. Chen, S. Jockusch, R. G. Lawler, M. Ruzzi, E. Sartori, S.-C. Chuang, K. Komatsu, and Y. Murata. Demonstration of a Chemical Transformation Inside a Fullerene. The Reversible Conversion of the Allotropes of $H_2@C_{60}$. *J. Am. Chem. Soc.*, 130(32):10506–10507, 2008.

[226] M. Carravetta, O. G. Johannessen, M. H. Levitt, I. Heinmaa, R. Stern, A. Samoson, A. J. Horsewill, Y. Murata, and K. Komatsu. Cryogenic NMR spectroscopy of endohedral hydrogen-fullerene complexes. *J. Chem. Phys.*, 124(10), 2006.

[227] M. Carravetta, A. Danquigny, S. Mamone, F. Cuda, O. G. Johannessen, I. Heinmaa, K. Panesar, R. Stern, M. C. Grossel, A. J. Horsewill, A. Samoson, M. Murata, Y. Murata, K. Komatsu, and M. H. Levitt. Solid-state NMR of endohedral hydrogen-fullerene complexes. *Phys. Chem. Chem. Phys.*, 9:4879–4894, 2007.

[228] S. Mamone, Min Ge, D. Hüvonen, U. Nagel, A. Danquigny, F. Cuda, M. C. Grossel, Y. Murata, K. Komatsu, M. H. Levitt, T. Rõõm, and M. Carravetta. Rotor in a cage: Infrared spectroscopy of an endohedral hydrogen-fullerene complex. *J. Chem. Phys.*, 130(8), 2009.

[229] A. J. Horsewill, S. Rols, M. R. Johnson, Y. Murata, M. Murata, K. Komatsu, M. Carravetta, S. Mamone, M. H. Levitt, J. Y.-C. Chen, J. A. Johnson, X. Lei, and N. J. Turro. Inelastic neutron scattering of a quantum translator-rotator encapsulated in a closed fullerene cage: Isotope effects and translation-rotation coupling in $H_2@C_{60}$ and HD@C_{60}. *Phys. Rev. B*, 82:081410, 2010.

[230] A. J. Lakin, H. S. Alqannas, and J. L. Dunn. Theoretical modelling of Jahn-Teller distorted C_{60} anions on a surface. *J. Phys. Conf. Ser.*, 428(1):012001, 2013.

[231] G. Schulze, K. J. Franke, and J. I. Pascual. Resonant heating and substrate-mediated cooling of a single C_{60} molecule in a tunnel junction. *New J. Phys.*, 10(6):065005, 2008.

[232] B. N. J. Persson and M. Persson. Vibrational lifetime for CO adsorbed on Cu(100). *Solid State Commun.*, 36(2):175 – 179, 1980.

[233] K. J. Franke and J. I. Pascual. Effects of electron-vibration coupling in transport through single molecules. *J. Phys.: Condens. Matter*, 24(39):394002, 2012.

[234] G. V. Nazin, S. W. Wu, and W. Ho. Tunneling rates in electron transport through double-barrier molecular junctions in a scanning tunneling microscope. *Proc. Natl. Acad. Sci. U.S.A.*, 102(25):8832–8837, 2005.

[235] F. M. Leibsle, C. F. J. Flipse, and A. W. Robinson. Structure of the Cu{100}- *c*(2x2)N surface: A scanning-tunneling-microscopy study. *Phys. Rev. B*, 47:15865–15868, 1993.

[236] F. M. Leibsle, S. S. Dhesi, S. D. Barrett, and A. W. Robinson. STM observations of Cu(100)-c(2×2)N surfaces: evidence for attractive interactions and an incommensurate c(2×2) structure. *Surf. Sci.*, 317(3):309–320, 1994.

[237] M. Murata and Y. Murata. Synthesis done at Kyoto University, Institute for Chemical Research, Group of Prof. Y. Murata, http://www.scl.kyoto-u.ac.jp/ kouzou/index.html. Contact: mmurata@scl.kyoto-u.ac.jp.

[238] F. D. Natterer, Y. Zhao, J. Wyrick, Y.-H. Chan, W.-Y. Ruan, M.-Y. Chou, K. Watanabe, T. Taniguchi, N. B. Zhitenev, and J. A. Stroscio. Strong Asymmetric Charge Carrier Dependence in Inelastic Electron Tunneling Spectroscopy of Graphene Phonons. *Phys. Rev. Lett.*, 114:245502, 2015.

[239] F. Cimpoesu, S. Ito, H. Shimotani, H. Takagi, and N. Dragoe. Vibrational properties of noble gas endohedral fullerenes. *Phys. Chem. Chem. Phys.*, 13:9609–9615, 2011.

[240] A. Gromov, N. Krawez, A. Lassesson, D. I. Ostrovskii, and E. E. B. Campbell. Optical properties of endohedral Li@C_{60}. *Curr. Appl. Phys.*, 2(1):51 – 55, 2002.

[241] V. Coropceanu, J. Cornil, D. A. da Silva Filho, Y. Olivier, R. Silbey, and J.-L. Brédas. Charge Transport in Organic Semiconductors. *Chem. Rev.*, 107(4):926–952, 2007.

[242] F. S. Tautz. Structure and bonding of large aromatic molecules on noble metal surfaces: The example of PTCDA. *Prog. Surf. Sci.*, 82(9-12):479–520, 2007.

[243] M. Feng, J. Zhao, and H. Petek. Atomlike, Hollow-Core-Bound Molecular Orbitals of C_{60}. *Science*, 320(5874):359–362, 2008.

[244] M. Feng, Y. Shi, C. Lin, J. Zhao, F. Liu, S. Yang, and H. Petek. Energy stabilization of the s-symmetry superatom molecular orbital by endohedral doping of C_{82} fullerene with a lanthanum atom. *Phys. Rev. B*, 88:075417, 2013.